Doctoral theses at NTNU, 2013:118

Reza Firoozkoohi

Experimental, numerical and analytical investigation of the effect of screens on sloshing

ISBN 978-82-471-4337-7(printed version)
ISBN 978-82-471-4338-4(electronic version)
ISSN 1503-8181

NTNU
Norwegian University of Science and Technology
Thesis for the degree of Philosophiae Doctor
Faculty of Engineering Science and Technology
Department of Marine Technology

NTNU – Trondheim
Norwegian University of
Science and Technology

Doctoral Thesis

Reza Firoozkoohi

Doctoral theses at NTNU, 2013:118

NTNU

NTNU – Trondheim
Norwegian University of
Science and Technology

Reza Firoozkoohi

Experimental, numerical and analytical investigation of the effect of screens on sloshing

Thesis for the degree of philosophiae doctor

Trondheim, May 2013

Norwegian University of Science and Technology
Faculty of Engineering Science and Technology
Department of Marine Technology

NTNU – Trondheim
Norwegian University of
Science and Technology

NTNU
Norwegian University of Science and Technology

Thesis for the degree of philosophiae doctor

Faculty of Engineering Science and Technology
Department of Marine Technology

ISBN 978-82-471-4337-7(printed version)
ISBN 978-82-471-4338-4(electronic version)
ISSN 1503-8181

Doctoral Theses at NTNU, 2013:118

Printed by Skipnes Kommunikasjon as

Acknowledgments

I am and always will be thankful to Professor Odd Faltinsen, my supervisor and my best teacher. It was in the beginning of my PhD, when a friend came to me and said "You are a lucky guy. He is a real teacher, coming to you, asking about your progress and supporting you for the better performance and faster progress". Well, today I can confirm that opinion.

In my opinion, *Marinteknisk senter* is a national treasure; not because of the computers and the big library but because of the brilliant researchers doing great jobs. More than 70 PhD students working on different topics collected in one place are worth tons of gold. I had this chance to be among these researchers taking advantage of having nice discussions with them. Babak Ommani, Tufan Arslan, Bjørn Abrahamsen, Maxime Thys, Trygve Kristiansen, Arnt Fredriksen, and Mia Prsic are a small group of them that I could ask my questions to and share my thoughts and opinions with.

Professor Timokha is strongly acknowledged here for his help regarding development of non-linear modal theory for sloshing. I have received unique insights into modal analysis of sloshing specialized for screen problem through incredible discussions with him.

My special thanks go to Professor Sverre Steen who provided me with extra computer resources that I used for accelerating my numerical simulations.

This dissertation work is dedicated to my parents and my brothers and sisters: Hamid, Saeed, Masoome and Zahra.

Abstract

This thesis describes an investigation of two-dimensional steady-state sloshing in a rectangular tank with small breadth-to-length ratio b/l equipped with a slat screen in the tank middle. The tools used for performing the investigations are experiments, numerical simulations using Computational Fluid Dynamics (CFD) and potential-flow based theoretical method.

Experiments are carried out in non-dimensional finite, $h/l = 0.35$ and 0.4, and shallow water, $h/l = 0.12$ and 0.125, depths. The tank motion in the longitudinal direction follows a periodic sinusoidal motion. The measured physical variable is the instantaneous wave elevation at the vertical tank walls. The solidity ratio is varied between 0 and 1. The range of the forcing frequencies includes the first three natural sloshing frequencies of the tank without screens.

Very small forcing amplitude-to-tank length ratio $\varepsilon = 0.001$ in finite water depth is used to achieve closely-linear free-surface conditions. Non-linear sloshing is achieved by applying relatively small non-dimensional forcing amplitude $\varepsilon = 0.01$ in finite water depth. Larger non-linear free-surface effects appear in experiments by applying larger forcing amplitudes, for instance with $\varepsilon = 0.03$ in the depth $h/l = 0.35$ close to the theoretical critical depth $h/l = 0.3368$. Wave breaking (spilling), free-surface overturning at the vertical walls and free-surface fragmentations as results of large forcing amplitude are categorized as a function of forcing frequency for each solidity ratio.

One goal is to determine which solidity ratio causes minimum wave responses in the whole tested forcing frequency range for constant forcing amplitude. Experiments reveal that increasing the forcing amplitude decreases the solidity ratio that causes the minimum wave response.

Strong free-surface non-linearities are examined by running experiments for $h/l = 0.12$ and 0.125 with $\varepsilon = 0.01$ and 0.05, respectively. Influence of screen and its solidity ratio on previously-reported impact events on the vertical walls in the literature is demonstrated ($h/l = 0.125$ and $\varepsilon = 0.05$). Estimation of high pressures due to some of the impact events occurred on the vertical walls are made using pressure impulse theory. The impact events on the wall (and on screen) are categorized based on the forcing frequency and solidity ratio of the screen.

Linear and non-linear multimodal methods which are derived from potential flow theory are employed. These methods are combined with a pressure drop condition and continuity of relative horizontal velocity in the middle of the tank to account for the presence of the screen. Depending on the solidity ratio an empirical pressure drop is enforced in the governing equations. Conditions where these methods are working are determined by making comparison with produced experimental results in this thesis.

Validation and details of the theoretical work can be found in the Appendix section of this thesis.

Numerical simulations based on an incompressible laminar model are conducted for $\varepsilon = 0.01$ and $h/l = 0.12$. The simulations are performed using an open-source CFD software called OpenFOAM. The interface between water and air, i.e. the free surface, is captured and located by transporting Volume Of Fluid (VOF) fractions. The ability of the software to capture non-linear non-violent free-surface effects is tested. Large wave breakings accompanied with over-turnings, liquid fragmentations and screen-caused jet flows traveling in the air/gas hitting the underlying free-surface are examples of violent free-surface effects.

Nomenclatures

General rules

- Only the most used nomenclatures are listed. Those ones which have been defined and used locally and not used in several places in the thesis are not included here.
- Sometimes the same symbols are used for different quantities
- Vectors and tensors are represented by bold-face letters

Subscripts

a	Amplitude of motion or wave response
b	Baffle
d	Drag
f	Face of a numerical cell or control volume
i	Number of a natural frequency
r	Relative
rm	Relative velocity amplitude in the Middle of the tank
S	Surface
t	Total area of a screen. Also time
2	Sway or y-direction

Superscripts

$*$	Natural frequency of the clean tank. Also First corrected pressure or velocity
$**$	Natural frequency of a compartment of half the length of the clean tank
-1	Inverse of a matrix

Roman letters

A	Area
b	Tank breadth normal to the direction of excitation
C_d	Drag coefficient
Co	Courant number
D	Averaged work done by the drag force in one period of oscillation. Also diameter
h	Water Depth
i_{2k}	Non-dimensional frequency corresponding to secondary resonance of $2kth$ mode of clean-tank sloshing
i_{2k+1}	Non-dimensional frequency corresponding to secondary resonance of $(2k+1)th$ mode of clean-tank sloshing
k	kth harmonic of forcing frequency. Also counting cumber
K	Empirical pressure loss coefficient
KC	Keulegan-Carpenter number
l	Tank length in the excitation direction
l_b	Length of a baffle. Also height of the screen supports normal to lateral vertical walls

p	Pressure
$p_{-\rho gh}$	Pressure minus hydrostatic pressure part
rad	Radians
Re	Reynolds number
Si	Vertical line at non-dimensional ith natural frequency
S	Seconds
Sn	Solidity ratio of screen
T	Period of forced oscillation
U_r	Uniform average horizontal approach velocity in the middle of the tank
U_{rm}	Amplitude of relative horizontal approach velocity in the middle of the tank
V	Volts and also volume.
x	Horizontal spatial direction perpendicular to forcing direction
y	Horizontal spatial direction. Also Sway direction
z	Vertical spatial direction

Greek letters

α	Modulus of decay; Volume of fluid fraction
Δt	Time step
ε	Non-dimensional forcing amplitude η_{2_a}/l
ζ_{1st}	Amplitude of the first Fourier harmonic of the measured wave elevation
ζ_{2nd}	Amplitude of the second Fourier harmonic of the measured wave elevation
ζ_{3rd}	Amplitude of the third Fourier harmonic of the measured wave elevation
ζ_{max}	Maximum steady-state wave elevation
η_{2_a}	Forcing amplitude
λ	Wave length
ν	Kinematic viscosity
ξ	Damping coefficient
ρ	Fluid density
σ	Forcing frequency
σ_i^*	ith Natural frequency of sloshing in a clean tank
σ_i^{**}	ith Natural frequency of sloshing in a compartmented tank
σ_0	An exemplary natural frequency
ϕ	Fluid flux at a numerical cell face

Bold-face letters

$\boldsymbol{a_o}$	Linear acceleration of coordinate system
$\boldsymbol{g}$	Gravitational acceleration
$\boldsymbol{n_f}$	Unit normal vector of a numerical cell face
$\boldsymbol{u}$	Velocity vector
$\boldsymbol{v_o}$	Linear velocity of coordinate system
$\boldsymbol{\tau}$	Laminar stress tensor
$\boldsymbol{\omega}$	Rotational velocity of coordinate system

Abbreviations

CFD	Computational Fluid Dynamics

CFL	Courant–Friedrichs–Lewy condition
CV	Control Volume
FFT	Fast Fourier Transform
L	“Left” side of the tank
PISO	Pressure-Implicit Splitting of Operators
QL0	Quasi-linear modal theory version 0
QL1	Quasi-linear modal theory version 1
QL2	Quasi-linear modal theory version 2
R	“Right” side of the tank
std	Standard deviation
TLD	Tuned Liquid Damper
VOF	Volume Of Fluid

Mathematical operators

∇	Gradient
$\nabla\cdot$	Divergence
$\lvert\ \rvert$	Absolute value

Contents

1 Introduction

1.1 Overview of the problem

Large liquid responses in partially filled tanks of ships (commonly called sloshing) can occur if ship motions excite the tank-liquid system at its lowest natural frequencies. Sloshing causes impact loads on the tank walls in low fillings and on the tank roof in high fillings when the free surface of the waves hits them with high velocity. High pressure loads can lead to structural damage of the tank structure. These loads should be avoided especially in LNG tanks because of their weak structure. Internal structures such as columns, plates perpendicularly joined to the walls (baffles), wired or mesh screens and swash (wash) bulkheads (perforated plates) cause damping of resonant liquid motions and reduce the risk of high pressure loads (Figure 1-1). The main damping source is the large turbulent diffusion in the shear layers of shed vortices due to flow separation from either the smooth boundaries of columns, wired screens, tubular ventilated structures or sharp edges of baffles, perforated plates and swash bulkheads. Viscous dissipation associated with breaking waves and in the boundary layer of the flow attached to the structure boundaries are other damping sources.

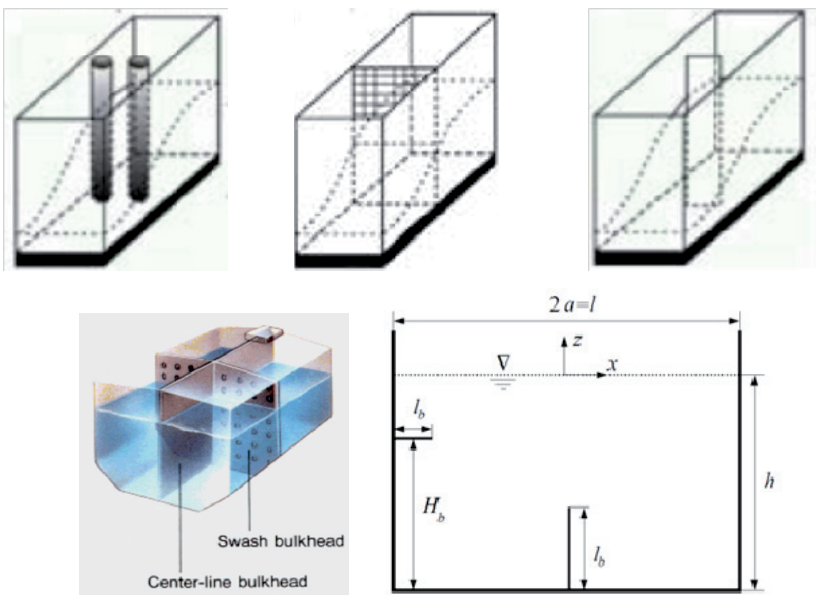

Figure 1-1. Internal structures in a liquid tank. Top: from left to right: columns, screen, and vertical plate, bottom right: Baffles (Faltinsen & Timokha, Sloshing, 2009); bottom left: swash bulkhead (IHI, 2000)

An important parameter for a submerged perforated structure is the solidity ratio Sn. Solidity ratio is the ratio between the submerged solid area of a perforated structure and its submerged total area including the perforations. If Sn is sufficiently large, the

resonant sloshing frequencies can increase to a frequency domain with less severe wave-induced ship velocities and accelerations.

For a fixed Sn, a perforated plate or screen with sufficiently large cross-flow produces more hydrodynamic damping relative to the other structures presented in Figure 1-1 due to the increased flow separation at the sharp edges of the perforations. An important goal here is to find an optimum solidity ratio providing smallest wave responses in a wide enough frequency range that typically covers the first three lowest natural frequencies of sloshing in a clean tank. This optimum Sn is a function of the tank motion magnitude and liquid depth.

1.2 Previous studies

Suppression of sloshing forces also matters in space craft applications to avoid unwanted induced motions of the space craft. Abramson, 1966 refers to numerous works in which the effect of viscosity and surface tension, tank shapes, baffles and perforated sectored tanks on resonant sloshing frequencies and damping have been investigated. The effect of perforated walls on sloshing has been studied experimentally by Garza (1964) and Abramson and Garza (1965) (Faltinsen & Timokha, Sloshing, 2009) for forced horizontal excitation of a vertical circular tank that is compartmented into sectors by means of radial walls corresponding to 45°, 60° and 90° sector tanks. The tank is excited to oscillate laterally with small amplitudes. Figure 1-2 presents a three-dimensional plot that shows the complex effect of the excitation amplitude X_0 and the open area percentage i.e. $\left(\frac{flow\ area}{total\ area}\right) * 100\%$ $(= (1 - Sn) * 100\%)$ on damping and the first resonant sloshing frequency in a sectored cylindrical tank. The liquid depth is constant at $h/d = 1.0$, where d is the tank diameter. The tank is divided into 45° perforated sectored tanks to gain more hydrodynamic damping and to shift up the lowest resonant frequency of the non-sectored tank close to the resonant frequency of the sectored tank without perforated tanks. As shown in Figure 1-2, the up-shifting of the resonance frequency needs smaller forcing amplitude at larger solidity ratios. The variation of damping against the solidity ratio is similar for the two lower forcing amplitudes. For the largest forcing amplitude, the damping ratio curve contains a clear peak point at $Sn \cong 0.78$. This difference shows the clear nonlinear effects due to amplitude of motion. However, the damping ratio for the three values of X_0 is largest when $0.76 < Sn < 0.84$. In addition the exact value of the compartmented resonant frequency when $Sn \to 1$ is also depending on the amount of damping and forcing amplitude. In Figure 1-2 the damping ratio γ is computed from free-decay tests.

As a rule-of thumb Dodge (2000) gives that if the solidity ratio exceeds 0.9, the liquid tends to slosh between the compartments and the slosh natural frequency tends to approach the value of a compartmented tank. This guideline is relevant in space applications where the expected motion amplitudes are much smaller than representative wave-induced ship motions. In ship applications, classification societies have rules regarding the solidity ratio of the swash bulkheads. For instance, Germanischer Lloyd (GL, 2003) expresses that the perforation area should be between 5 and 10 percent of the whole bulkhead area in oil cargo tanks. However, we do not know what the basis is for this recommendation by GL.

Damping of sloshing is also desirable in partially filled rectangular tanks of tall buildings (Tuned Liquid Dampers or TLD) or in anti-rolling tanks of ships. The sloshing motion is used to damp out the large responses of their carrying structure. These tanks are normally equipped with a screen of (roughly) $Sn \leq 0.5$ to experience less violent fluid motions and less non-linear behavior for better control. An important design requirement here is to match the lowest resonant frequency of sloshing in the tank with the natural frequency of interest of the structure. Therefore large solidity ratios are not of interest because they affect the lowest resonant frequency as discussed above.

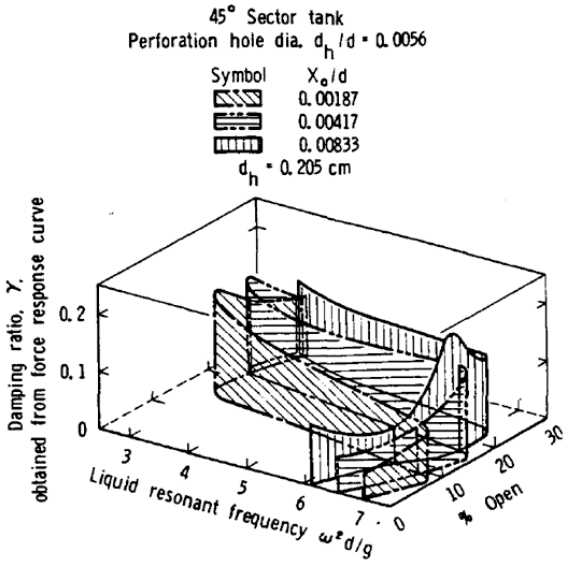

Figure 1-2. Effect of forcing amplitude and solidity ratio on resonant frequency and damping of sloshing in a vertical 45^o sectored circular tank (Abramson, 1966). X_0: forcing amplitude, d: tank diameter, d_h:perforations diameter, ω: forcing parameter, γ: damping ratio. Water depth $h/d = 1.0$.

1.2.1 Modeling of sloshing in a screen-equipped tank

A theoretical model for the investigated problem must couple the hydrodynamic effect of the screen in the middle of the tank with the sloshing. Forced harmonic lateral tank motions are considered. In most fluid dynamics applications, a thin perforated structure such as a gauze or slat screen or a perforated plate is considered as a local discontinuity with an average effect expressed as a pressure loss in the direction of the flow. Laws & Livesey 1978 studied the flow through gauze screens of small solidity ratios ($Sn < 0.5$). They showed that the screen's pressure loss is quadratically related to the approach velocity U_r at the screen, i.e. $\Delta p = \frac{1}{2}\rho K|U_r|U_r$. Here K is a pressure loss coefficient (non-dimensional). Experimental values of K for a variety of screens or structures made of an array of small bluff bodies can be found in the hand books by Blevins (2000) and Idelchik (1996). Molin (2010) confirms in a review paper that the quadratic pressure loss assumption is sufficient to explain the hydrodynamics of perforated structures in infinite oscillatory fluid and in waves. Important conditions for

applicability of this model are that the screen should be thin, number of perforations should be numerous and the size of the perforations should be very small. Under the mentioned conditions, an important conclusion from Molin (2010) is that the solidity ratio matters a lot more than the size and shape of the perforations. In this thesis the quadratic model of the pressure loss is used in the theoretical approaches. The pressure loss coefficients are taken from empirical calculations, for instance, by Blevins (2000) or Baines and Peterson (1951).

For the current study, a theoretical method should be able to capture the resonant behavior of sloshing in a screen-equipped tank as a function of the following physical parameters:

- Non-dimensional sway forcing amplitude: $\varepsilon = \eta_{2_a}/l$
- Non-dimensional forcing frequency:σ/σ_1^*
- Non-dimensional water depth: h/l
- Solidity ratio of the screen: Sn.

Here l is the tank length in the direction of excitation and σ_1^* is the lowest natural sloshing frequency of the clean tank. ε may be as high as 0.1 in ship applications. Most of the existing theories are developed for solidity ratios smaller than 0.5. These theories are used for analysis of sloshing in cylindrical and rectangular TLDs with submerged nets or slat screens. As long as the solidity ratio is less than 0.5 theories developed by Kaneko & Ishikawa (1999) and Kaneko and Mizota (2000), Tait et al., 2005, Love and Tait (2010) and J. Love, M. Tait , and H.Toopchi-Nezhadare (2011) are applicable. A short review of their work will be informative here.

Kaneko and Ishikawa (1999) studied the shallow, intermediate and finite water depth ($0.05 \leq h/l \leq 0.281$) sloshing in a rectangular TLD with a net in the middle section. Based on the definition by Faltinsen and Timokha (2009) shallow, intermediate, finite and deep water depth are corresponding to $h/l \leq 0.1$, $0.1 \leq h/l \leq 0.2 - 0.25$, $0.2 - 0.25 \leq h/l \leq 1$ and $h/l \geq 1$. Kaneko and Ishikawa (1999) modified the nonlinear shallow water theory proposed by Lepelletier and Raichlen (1988) to account for a screen using a one-dimensional finite difference model. The screen is modeled as a local pressure drop that causes a wave elevation difference across the net. The boundary layer damping is incorporated as a linear damping term in the shallow water equations. They measured the sloshing forces in the experiments for four solidity ratios, smaller than 0.5, and very small forcing amplitude ($\varepsilon = 0.0025$). Their results agree well with experiments.

Kaneko and Mizota (2000) developed a third-order nonlinear modal theory in terms of non-dimensional forcing amplitude ε for finite water depth in a vertical circular cylindrical tank with a submerged net. The three lowest sloshing modes are assumed to be sufficient for the simulations. The net effect is described as a quadratic damping term in the modal equations implying that the modes are preserved and not affected by the presence of the net. The net effect is only adopted for the first mode of sloshing in their model but a linear damping model of the boundary layer is included in all modal equations. Their experimental results agree very well with the results of their modal approach for very small amplitude of excitation $\varepsilon = 0.0025$. They did not study the effect of different excitation amplitudes and all the tested solidity ratios are smaller than 0.5.

Tait et al., (2005) investigated a rectangular TLD with single and multiple slat screens with $Sn \leq 0.5$ by carrying out experimental and theoretical approaches. They examined the effect of small and large forcing amplitudes in three different water depths varying between shallow and intermediate depths using linear and nonlinear shallow water theories developed by Fediw et al., (1995) and Kaneko and Ishikawa (1999), respectively. Their comparison concludes that the linear model is insufficient for large excitation amplitudes. They present very good results in time and frequency domain by applying the nonlinear model of Kaneko and Ishikawa (1999). The screen solidity ratio was equal to 0.42. An important contribution from their study is that the pressure loss coefficients for a slat screen calculated in steady-uniform flow is applicable in oscillatory flow when the Keulegan-Carpenter number (KC) is larger than 15. KC defines the non-dimensional distance a free-stream particle travels in one cycle of an oscillatory flow. Here $KC = U_{rm}T/D$ is defined based on the height of a slat (D) and amplitude of relative horizontal approach velocity (U_{rm}). T is the period of forced oscillation.

Love and Tait (2010) modified the adaptive modal theory of Faltinsen and Timokha (2001) to account for a slat screen with $Sn < 0.5$ as a quadratic damping term in modal equations similar to the work of Kaneko and Mizota (2000). The novelty relative to the work of Kaneko and Mizota (2000) was to consider finite, intermediate and shallow water depth. However, the forcing amplitudes are small and the accuracy of the results decreases in shallow depths. They conclude that the nonlinearity of the free surface can be important.

Faltinsen and Timokha (2009) calculated damping coefficients of the lowest sloshing mode in a two-dimensional tank with a wire mesh screen mounted in the tank middle with solidity ratios $Sn = 0.29$ and 0.48. The selected water depths are $h/l = 0.2$ and 0.3. A strip theory approach was used for calculation of forces on individual wire elements. They defined a drag coefficient for the screen based on empirical formulas depending on the KC number and related it to solidity ratio of the screen. Boundary layer damping at the tank walls was also included. They calculated the damping coefficient of the first mode of sloshing by relating the rate of dissipation of total potential and kinetic energy contaiend in the first mode of sloshing to the work done by the drag force imposed on the screen in one cycle of forcing. They compared their results with experiments. The accuracy of their results are good for $Sn = 0.29$ for very small and small forcing amplitudes, i.e. $0.001\ m < A < 0.021\ m$. For $Sn = 0.48$, the result are poor for very small forcing amplitude, $A \cong 0.001\ m$ but it improves with increasing the forcing amplitude. Their method is simple and applicable for $Sn < 0.5$ (roughly speaking). However, their method breaks down for large solidity ratios, i.e. $Sn > 0.75$ and it does not account for changing of the natural sloshing modes and frequencies when the solidity ratio of the screen is large.

Faltinsen and Timokha (2009) consider $0.5 < Sn < 1$ by decomposing the tank into two theoretical compartments with flow between the compartments. Two velocity potential functions representing the flow in each domain are found by matching them at the screen position using two transmission conditions: (A). The relative horizontal approach velocity U_r stays continuous ; (B). Pressures on both sides of the screen are related by an empirical pressure loss coefficient $K = \Delta p/(\frac{1}{2}\rho|U_r|U_r)$ (quadratic relation

between Δp and U_r). The horizontal velocity is assumed to be uniform over the depth. The latter assumption decreases the accuracy of the theory in predicting the natural frequencies which is more pronounced when the exponential decay of the velocity over the depth matters, i.e. deep water or higher natural frequencies. The proposed model uses linear free-surface conditions. The problem is transformed to a modal approach by modal representation of the potential functions and water wave elevations. The combination of linear free-surface conditions and nonlinear (quadratic in velocity) pressure loss model of the screen leads to a quasi-linear modal method (QL0). QL0 accounts for the changes in the natural frequencies and modes as $Sn \to 1$ as a function of forcing amplitude and water depth. In fact it confirms the trend observed in Figure 1-2. Firoozkoohi and Faltinsen (2010) examined the QL0 against experiments in finite water depth for very small ($\varepsilon = 0.001$) and small forcing amplitudes ($\varepsilon = 0.01$). The theoretical results were not in a good agreement with the experiments from a quantitative point of view. One objective in the experiments by Firoozkoohi and Faltinsen (2010) was to find the solidity ratio that causes the lowest wave response in the frequency range including the three lowest natural frequencies. This objective is well predicted by the theory for $\varepsilon = 0.001$ and $\varepsilon = 0.01$.

QL0 is modified to account for exponential decay in the velocity profile by Faltinsen, Firoozkoohi and Timokha (J Eng Math, 2011) (QL1). This modification improves the accuracy of the predicted linear natural frequencies. Another modification is applied in the definition of potential functions where the anti-symmetric sloshing modes in the clean tank are assumed unaffected by the screen but responsible for cross flow through the screen. The results agree better with experiments compared to Firoozkoohi and Faltinsen (2010) from a damping point of view, i.e. the amplitude of resonance peaks are closer to experiments. In general, QL1 performs better for lower solidity ratios and forcing amplitudes. This must be due to the assumption that the anti-symmetric modes are unaffected even for large solidity ratios. Due to the linear free-surface assumption, QL1 gives very large responses at natural frequencies of a compartment for solidity ratio of 1.

Solidity ratio and geometrical properties of the slat screen such as number of submerged slat/slots, the position and height of the slats at the free-surface zone and their effect on linear anti-symmetric natural sloshing frequencies and modes are investigated by Faltinsen and Timokha (2011). They use domain-decomposition and employ potential flow theory with linear free-surface boundary conditions and zero forcing. The flow does not separate from the slat edges and therefore the velocity potential contains singular points at the screen edges that describe the screen's local flow properties. The effect of increasing the solidity ratio is found to be a decrement in the natural frequencies of the clean tank.

Faltinsen, Firoozkoohi and Timokha (Phys Fluids, 2011a) presented a new quasi-linear modal model (QL2) that includes local pressure and velocity fields depending on the screen's solidity ratio and geometrical properties. These local fields affect the anti-symmetric modes and asymptotically vanish away from the screen. The even (symmetric) modes that are responsible for tangential liquid motions at the screen remain unchanged. The final equations are solved for screen-modified odd (anti-symmetric) modes. For $\varepsilon = 0.001$ the results are very good for almost all solidity ratios. Still infinite responses are seen at natural frequencies of sloshing in a compartment due

to the linear free-surface assumption. For the larger forcing amplitude $\varepsilon = 0.01$ the theory gives good results at forcing frequencies far from resonance. The theory cannot predict the new screen-caused resonant peak points observed in the experiments. The results for the largest forcing amplitude are of qualitative nature. Most of the differences between theory and experiments are probably due to nonlinear free-surface effects that are not accounted for.

Larger forcing amplitudes amplify the nonlinearity in the free surface leading to generation of new resonant peak points in the steady-state wave elevation response curves associated with secondary resonance of higher modes of sloshing in the clean tank. Secondary resonance is a consequence of the fact that super-harmonics associated with the liquid flow is close to a higher sloshing natural frequency. In order to include the free-surface nonlinearity Faltinsen, Firoozkoohi and Timokha (Phys Fluids, 2011b) used the adaptive nonlinear modal theory and modified it to include the screen effect. The nonlinear adaptive multimodal method requires derivation of the polynomial-type modal system, i.e., the system of ordinary differential equations which keeps nonlinearities up to the third-order in terms of generalized coordinates. These generalized coordinates are time-dependent functions that describe the time-dependence of sloshing modes. The adaptive modal method is a generalization of Moiseev-type theory. Moiseev type theories assume the lowest mode to be dominant while an adaptive modal method can account for more than one dominant mode. Both odd and even modes are coupled due to the free-surface nonlinearity. However, the screen-caused damping terms appear only in modal equations responsible for the odd modes. The modified adaptive nonlinear modal theory shows its ability to predict and capture the new resonant points associated with secondary resonance quantitatively.

The articles including experimental validations of the quasi-linear theory and its modifications QL0(Firoozkoohi & Faltinsen, 2010), QL1 (Faltinsen, Firoozkoohi, & Timokha, J Eng Math, 2011) and QL2 (Faltinsen, Firoozkoohi, & Timokha, Phys Fluids, 2011a) and the non-linear adaptive modal method modified for screen problem (Faltinsen, Firoozkoohi, & Timokha, Phys Fluids, 2011b) can be found in the Appendix section. The author has contributed to these articles by performing experimental study and analysis. These analyses cover discussions on various phenomena found in the experimental tests. New phenomena discovered in the experiments in connection with the present problem are categorized and reported in the above-mentioned papers.

Sloshing has been extensively simulated and reported by many authors using Computational Fluid Dynamics (CFD). A noteworthy work related to the present investigation was done by Maravani and Hamed (2010) where a screened-TLD was studied using a laminar Navier-Stokes solver coupled with the Volume Of Fluid free-surface capturing method. The VOF model works based on the original donor-acceptor method of Hirt and Nichols (1981). They have used finite difference discretization. A partial cell treatment method takes care of the presence of the screen. A cell may be filled partially or fully with a solid part of the screen at the screen position. They have examined their algorithm for random and sinusoidal excitation against experiments. Their results for very small ($\varepsilon = 0.0026$) and small ($\varepsilon = 0.013$) excitation amplitudes show excellent agreement with experiments. They compared steady and transient wave elevation and sloshing forces.

1.3 Objectives and scope of the thesis

The main objective is to study the steady-state resonant sloshing due to periodic horizontal excitation in a rectangular tank equipped with a screen. The investigation starts by performing experiments in order to analyze the effect of the main physical parameters $\varepsilon, h/l, Sn, \sigma/\sigma_1^*$ on sloshing. The results of the analysis are the basic information used as reference to establish theoretical investigations. The effect of screens with $0.45 < Sn < 0.96$ on the resonant frequencies and the amplitude of the steady –state sloshing waves for fixed forcing amplitude and in a constant water depth are considered while the frequency of the tank motion is varying. The motion-frequency range covers the first three natural frequencies of sloshing in a clean tank, i.e. $\sigma_1^* < \sigma < \sigma_3^*$ and the water depth is limited to finite and shallow water depths. For such conditions one goal is to find the solidity ratio with minimum wave responses.

The experiments are carried out in a narrow rectangular tank to avoid developing three-dimensional flow in the direction perpendicular to the direction of excitation. The effect of the amplitude of the motion (that largely influences the nonlinearity of the sloshing waves) is tested for both finite and shallow water depths. In finite water depth the tank is excited with very small, small and relatively large forcing amplitudes. The effect of large amplitude sloshing is tested in shallow water to study the effect of screen on suppressing violent shallow water phenomena like hydraulic jump. The experimental investigation is done by analysis of the measured wave elevations at both vertical end walls and by taking photographs and videos. Forces on the screen and the pressures on the walls were not measured. Roof impact does not occur for all the tested experimental cases. The screen as well as the tank structure is assumed to be completely rigid, i.e. hydroelasticity is not considered here.

Analytical investigation (excluding numerically based methods such as CFD or BEM) is used to better understand and describe the physics observed in the experiments. The theoretical analysis is based on the multimodal method, derived from potential flow theory for an incompressible liquid; the method is modified to include the screen effect. It is applied in finite water depths $h/l = 0.4$ and 0.35. Considering free-surface boundary conditions, a linear assumption is examined by applying the quasi-linear modal method of Faltinsen and Timokha (2009) (QL0) and its modifications QL1 and QL2. These quasi-linear theories are examined against experimental results. QL2 (the most complete modification) can predict resonant frequencies and their corresponding steady-state amplitudes for $\varepsilon = 0.001$ accurately for low to high solidity ratios. Non-linearity of the free surface at resonance is non negligible for $\varepsilon \geq 0.01$ and for all tested depths. The results of the quasi-linear approach are in qualitative agreement with experiments for $\varepsilon \geq 0.01$. Amplification of second and third harmonics of the forcing motion at resonance leading to secondary resonance needs nonlinear free-surface conditions considered in the governing equations. A non-linear adaptive modal method that couples even and odd modes is examined for small forcing amplitude $\varepsilon \geq 0.01$ (but large enough for triggering the mentioned nonlinearities). This nonlinear model produces results quantitatively comparable to experiments. The forcing frequency range covers the first two natural frequencies of the clean tank.

The effect of relatively large forcing amplitudes with important free-surface nonlinearities is further examined by considering $\varepsilon = 0.03$ and $\varepsilon = 0.05$ in finite and shallow water depths. The experiments show sloshing waves with special free-surface

nonlinearities that cannot be simulated by the multi-modal theory. Examples are breaking waves (overturning free surface), thick wave run-ups on the vertical end walls and on the screen (non-perpendicular free surface at vertical boundary) and free-surface fragmentation at the screen (discontinuous free surface). For instance, the nonlinear adaptive multi-modal method does not produce satisfactory results for $\varepsilon = 0.03$ at $h/l = 0.35$ due to the phenomena stated above. This depth is close to the critical depth $h/l = 0.3368$, where a change from a hard spring to a soft spring nonlinear theoretical response occurs (Faltinsen and Timokha, 2009).

The detailed description of the theoretical models and their properties can be found in the articles attached in the Appendix section. These articles include comparisons made between the theoretical and experimental results. Conditions where the theoretical models are applicable are mentioned and discussed in detail.

Small and relatively large amplitude sloshing in shallow water is studied experimentally. While the small amplitude excitation generates almost standing waves for all the solidity ratios, the larger amplitude causes very violent flows that include all the special free surface non-linearities stated in the above paragraph with much more amplification. Because of these special phenomena the modal method is not applied for shallow water.

Equality of the steady-state wave amplitudes at the vertical end walls is considered by measuring the wave heights at both sides of the tank. Mainly this is used to assure that the wave elevations are accurately measured. Experiments show that two different steady-state wave amplitudes on the two sides of the tank, the two compartments, may occur, in author's opinion, when the following conditions are met:

a. The forcing amplitude must be sufficiently large, for instance $\varepsilon \geq 0.01$.
b. The tank-liquid system should be close to resonance. The resonance may be due to primary resonance at natural sloshing frequencies of clean tank or one compartment or due to secondary resonance. The difference in responses is, in general, smaller in case of secondary resonance.
c. The largest differences in responses occur when solidity ratio is close to 1 and the responses in the two sides of the screen become almost isolated (compartmantation). This is due to smaller damping and multiple solutions for sloshing in either sides of the screen. A more in-detail explanation regarding compartmentaion and unequal responses can be found in section 3.2.4.
d. Relatively small unequal responses on either sides of the screen may occur due to violent flow behavior. Violent flows are mostly seen for relatively large forcing amplitudes. Experimental conditions $h/l = 0.35$, $\varepsilon = 0.03$ and $\frac{h}{l} = 0.125$, $\varepsilon = 0.05$ are accompanied with violent flows such as large wave breaking with wave overturning and liquid-to-gas jet flows through screen openings (slots) hitting the underlying free-surface.

An open-source CFD package called OpenFoam that employs laminar Navier-Stokes equations and the volume-of-fluid (VOF) free-surface capturing method is used for numerical simulations in shallow water for $h/l = 0.12$ and $\varepsilon = 0.01$. Finite Volume Method is used for solving the governing equations. Simulations are done in a tank-fixed coordinate system that avoids solving the problem in a moving domain where the discretized domain has to move according to the forcing motion. The measured

accelerations from the experiments are directly fed to the CFD code to minimize the uncertainties. The CFD results agree well with the experimental results for small forcing amplitude but at the expense of time and computational resources that make a parameter study almost impossible. However, an advantage is detailed flow information at the screen that is useful for calculation of viscous and pressure forces on the screen. The large forcing amplitude case $\varepsilon = 0.05$ at $h/l = 0.125$ is investigated only experimentally. Large spilling wave breakers and very strong liquid jet flows that trigger formations of three-dimensional flows and is believed to cause turbulence are observed in the experiments. As the CFD simulations are limited to two dimensions and laminar fluid flow, the above-mentioned phenomenon cannot be simulated.

1.4 Outline of the thesis

Chapter 2 explains the experimental setup and measurements, determining sources of uncertainties. The experimental results are analyzed and categorized for different depths separately. Chapter 3 is dedicated to finite water depth and chapter 4 to shallow water depth. Chapter 6 begins by giving a short introduction to CFD and the Volume of Fluid free-surface capturing method. The ability of the used code InterFoam (a part of OpenFOAM) in capturing the free-surface nonlinearities is tested first in a clean tank and then applied in the screen-equipped tank for the shallow water depth $h/l = 0.12$ by validating the numerical results with experimental results. Chapter 6 concludes the investigation and gives suggestions for future works. Appendix section is dedicated to article on multi-modal method starting with the quasi-linear multimodal and its modifications, i.e. QL0, QL1 and QL2. The last article in the Appendix section is dedicated to non-linear adaptive modal method and its modification for sloshing in the screen-equipped tank.

1.5 Contributions of the thesis

The contributions from the thesis can be summarized as the following:

A. Experiments:

- Extensive experimental work conducted in this thesis produced new results regarding the resonant sloshing due to harmonic excitation in a rectangular tank with a screen supported in the middle section of the tank. The novelty was considering screens with $0.45 < Sn < 0.96$ that has not been studied in the past or studied very rarely in the literature. A wide range of forcing frequency $\sigma_1^* < \sigma < \sigma_3^*$, different forcing amplitudes and water depths have been examined. The new experimental results can be used as reference results for validation and development of new theoretical methods.
- Time domain and Fourier analysis of the experimental results reveals the influence of higher harmonics of forcing frequency up to the third harmonic in finite water depth and fifth harmonic in shallow water depth, for sufficiently large forcing amplitudes. The nonlinear effect of the screen, quadratic pressure loss, on the sloshing can be observed as new peak points in the experiments. These new peak points, first time reported in this thesis, are due to secondary resonance that are influenced by the screen in such a way that they occur even for relatively small forcing amplitudes; in fact the screen largely affects the anti-symmetric (odd) modes relative to its almost negligible effect on symmetric modes (even). This fact causes more energy being transferred to the even modes.

- The experimental results were used as reference for validation and modification of the quasi-linear multi-modal method (Faltinsen and Timokha 2009) to account for nonlinear effects of the slat screens (quasi-linear modal method) with low and high solidity ratios. Modifications of the Quasi-Linear modal method for linear dominant free-surface effects and nonlinear adaptive modal method for nonlinear dominant effects were developed and used in finite water depth. The modified quasi-linear theory can provide very good results as long as the non-linearity of the free surface does not play an important role. The non-linear approach is examined against experiments for $\varepsilon \leq 0.01$ and the results are in a good agreement with the experiments. *Note*, investigations regarding validation and development of modal method, i.e. quasi- and non-linear modal method, are published as independent articles that are attached in the Appendix section. The author of this thesis has co-authored those articles through experimental analysis.

B. Numerical calculations

- An open-source CFD package called OpenFOAM was used for performing numerical simulations. OpenFOAM uses finite volume discretization. InterFoam solver from OpenFOAM package which couples Navier-Stokes equation and Volume Of Fluid (VOF) free surface capturing method was examined against experiments for $\varepsilon = 0.01$ and $h/l = 0.12$, i.e. in shallow water condition. The comparisons confirmed that the applied numerical method was able to capture the free-surface nonlinearities such as secondary resonance of sloshing modes and amplification of wave responses oscillating with sub-harmonics of the forcing frequency, in steady-state conditions. The laminar flow model used in the numerical calculations is not applicable for larger forcing amplitudes when turbulence and impact pressures on the walls and the screen become important. Numerical simulations showed that for a screen problem, relatively coarse elements distributed in the screen slots and near the screen zone could provide acceptable results. The number of numerical cells inside the gap can be as low as 6.

2 Experimental setup and uncertainties

2.1 Introduction

Experiments are carried out to identify sloshing resonant frequencies and responses in a rectangular tank with screen as a function of important physical parameters including forcing amplitude and frequency, water depth and the screen's solidity ratio. In this chapter, first the experimental setup is explained. Next, the accuracy of the experimental measurement is considered. Uncertainties that can affect the accuracy of the experimental results and the desired experimental conditions are determined and their effect on the measurements is estimated. The latter is important as the experimental results will be used later for validation studies.

2.2 Experimental setup and equipments

Forced lateral harmonic motion of a rectangular tank is considered. The screen is in the middle of the tank as shown in Figure **2-1**. The inner tank dimensions are $1\,m \times 0.1\,m \times 0.98\,m$ ($l \times b \times H$). The tank roof is open to the ambient air in order to achieve atmospheric air pressure on the free surface of the water. The excitation direction is along the tank length (l). The tank is mounted on a sloshing rig located at the Marine Technology Centre in Trondheim, Norway. The rig shakes the tank by reading from the input positions. Irregular tank excitations can also be fed to the rig. Inside the tank, two resistant wave probes consisting of two thin wires measure the wave elevations. The wave probes are placed $1\,cm$ away from the vertical walls at the tank ends and midways between the two vertical lateral walls parallel with the tank excitation direction (Figure **2-1**) in order to avoid the effect of thin local wave run-ups on the walls. The wave elevations are measured within a minimum accuracy of one millimeter. Instantaneous tank positions and accelerations are measured and checked with the desired input values.

The tank breadth b should be sufficiently small in order to achieve a global two-dimensional flow and avoid three-dimensional flow. For instance, a prismatic tank with a nearly square base and no interior structures may develop important nonlinear three-dimensional flow such as swirling, diagonal waves and chaos for lateral excitation along a tank wall (Faltinsen & Timokha, Sloshing, 2009). On the other hand b should be wide enough so that the thickness of the boundary layer on the walls relative to b becomes negligible. As a measure of the viscous boundary layer thickness a period of 1.83 seconds is considered. It follows by Froude scaling and a ratio between the full scale length and the model length (l_p/l_m) equal to 30 that a model scale period of 1.83 seconds corresponds to a full scale period of 10 seconds. Using linear boundary layer theory for harmonically oscillating laminar flow, the geometric 99% boundary layer thickness is approximately estimated as 0.0035 m. Assuming this thickness of boundary layer on the vertical walls, $b = 10$ cm is sufficient to have 99.3 per cent of the tank breadth out of the boundary layers. There occur meniscus (surface tension) effects at the intersection between the tank walls, screen and the free surface leading to three-dimensional waves with very small wave heights and lengths relative to the gravity waves. Bond number which represents the ratio between inertia and surface tension

forces measures the importance of surface tension. Bond number is defined as $\rho_l g L^2 / T_s$. ρ_l, g, L and T_s are density of the liquid, gravitational acceleration, a characteristic length (here the tank length in the direction of excitation) and surface tension, respectively. Surface tension is negligible if Bond number is smaller than $\sim 10^4$ (Faltinsen & Timokha, Sloshing, 2009). Assuming $L = 1$ m and fresh water in the tank, i.e. $T_s = 0.074$ N/s, Bond number is equal to 1.32×10^5. Therefore, the meniscus effects are believed to be negligible in this study.

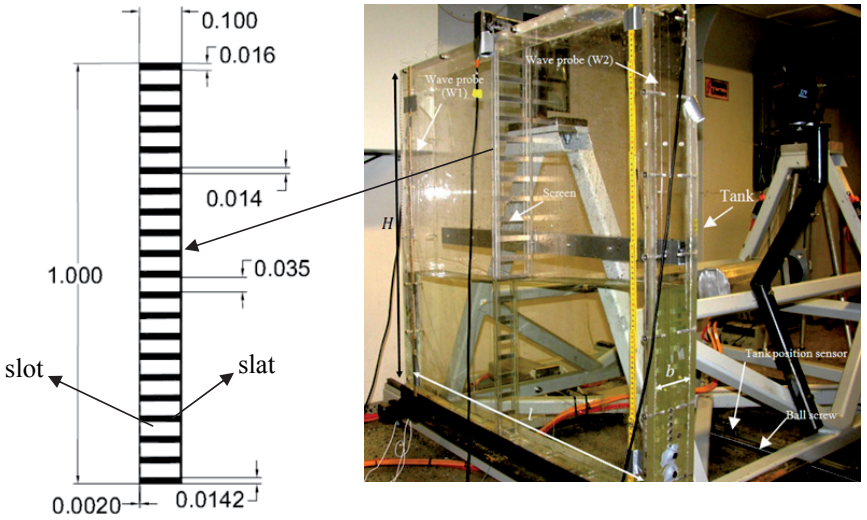

Figure 2-1. Left: Slat screen composed of rectangular slats (solid parts) and slots (openings). Dimensions are in meters. Right: Experimental setup and the tank with the screen in its middle section mounted on the sloshing rig.

2.3 Geometry of the screen openings

For the sake of two-dimensional flow in the screen zone, the screen openings are horizontal rectangles with constant height along the tank breadth (b) (Figure 2-1). Such a screen is called slat screen where slats are the rectangular solid parts. The openings are called slots. Screens are identified by their solidity ratio $Sn = A_s/A_t$. A_s is the submerged (under the mean free surface) solid area of the screen and A_t is the total area of the screen including the slots. To achieve a desired solidity ratio, Sn, fine or coarse slat/slot arrangements may be used. A fine arrangement is composed of small height slats/slots. The liquid flow through a screen with finer slat/slot arrangement produces less severe local free-surface effects such as free-surface fragmentation and local three-dimensional behavior at the screen. This matters when experimental results are used to validate results of a theoretical model for which the performance is sensitive to local free-surface effects at the screen. In addition, screens with finer arrangements cause smaller scale vortices shedding from their sharp-edged openings leading to wakes regularized in a short distance from the screen. Wakes of large scale vortices generated behind a screen with a coarse arrangement take a longer distance downstream the screen to diffuse their irregular flow motion. One should note that a fine arrangement in deep water can be coarse in shallow water, i.e. less number of slat/slots in shallow water. In

the experiments, the finest arrangement is achieved by having smallest possible slot heights. Assuming a fixed slot height for all screens, the solidity ratio can be increased only by increasing the slat height.

The slat screens here are made of aluminum plates with rectangular cutouts (slots). The smallest possible height of the slots is a technical limitation forced by the milling machine provided by Marintek (place where the experiments were conducted). The experiments were performed first with a set of screens whose geometrical dimensions are shown in the left side of Figure 2-2. At the first stages of the current study the focus was on achieving a desired solidity ratio and the geometry of the screen was not a priory consideration. Water-jet cutting tool was used for drilling the rectangular slots in the plates. After running experiments in finite water depth of $h/l = 0.4$, the results for the non-dimensional forcing amplitude of $\varepsilon = 0.01$ showed unequal wave elevations on the opposite vertical end walls. These differences were more noticeable for larger wave responses which were not necessarily around resonant frequencies. A closer look showed that the slot heights were not exactly equal on the opposite sides of the screen. This causes two solidity ratios, with a slight difference, on each sides that leads to different responses on the opposite tank sides. To solve this problem another set of screens were manufactured by an accurate milling machine. For the second set of the screens a constant slot height of 3 mm on both sides of the screen could be achieved. Although the slot height was not fixed for the first set of screen it was kept fixed for all screens in the second set. The geometrical dimensions of the first and second sets of screens are shown in Figure 2-2 (not all the solidity ratios are shown for the second set of screens). However, it will be shown later that nonlinearity can cause two distinct steady-state responses on the opposite tank sides at resonance even though the slot height along the tank length is constant.

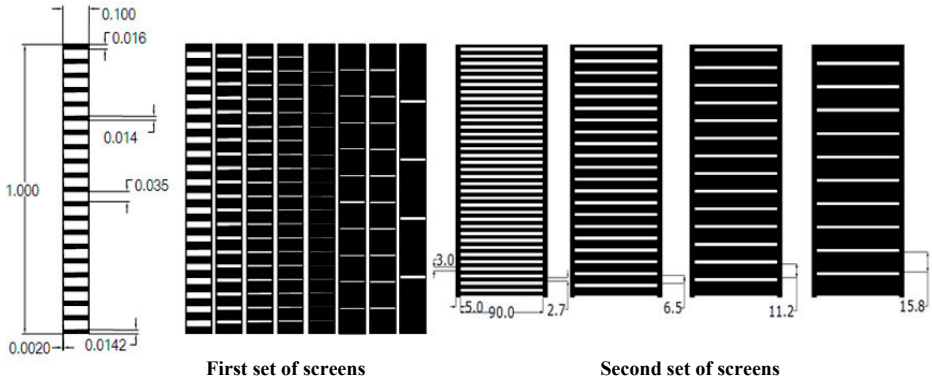

Figure 2-2. Geometrical details of the two screen sets. Left: The first set of screens (dimensions are in meters), Right: The second set of screens (dimensions are in millimeters) of screens. White parts present the slots. Not all the screens are shown for the second set.

Figure 2-2 shows that the distribution of slats/slots is more uniform over the height of the screen for lower solidity ratios. For a same solidity ratio, this uniformity is more obvious for the second set of the screens for which the number of openings is more than the first set. When the slot heights are fixed the solidity ratios is increased only by increasing the solid content of the screen.

2.4 Tank excitation motion

Harmonic tank excitation is considered in this study. The harmonic motion $\eta_2 = \eta_{2_a}\cos(\sigma t)$ covers forcing frequencies σ in the range $\sigma_1^*(1-\Delta_1) < \sigma < \sigma_3^*(1+\Delta_3)$ where Δ_1 and Δ_3 are small frequency intervals extending the frequency range. Here σ_1^* and σ_3^* are the first and the third natural frequency of sloshing in the clean tank. Because the focus is on the maximum steady-state wave elevation at the vertical tank end walls, the excitation should last for sufficient number of periods until waves with steady-state amplitude appear. How many forcing periods are required to reach steady-state waves depends on energy dissipation due to breaking waves, boundary layer flow and flow separation at the screen and is thereby a function of forcing motion, water depth, solidity ratio, transient free-surface behavior and screen's geometrical properties. Depending on the strength of the transient effects the tank is excited between 150 to 400 forcing periods to ensure that steady-state waves will appear. It is preferred to have at least 30 periods of steady-state waves. The maximum steady-state elevation is computed by taking average among the appeared steady-state waves. These steady-state waves are also used for performing FFT (Fast Fourier Transform) analysis to compute amplitude of the primary and higher harmonics of the forcing motion. The non-dimensional maximum steady-state elevations ζ_{max}/η_{2_a} and amplitude of the harmonics of the forcing are plotted against non-dimensional forcing frequency σ/σ_1^* to track the presence of the resonance areas. The plot shown in Figure 2-3 presents ζ_{max}/η_{2_a} against σ/σ_1^*.

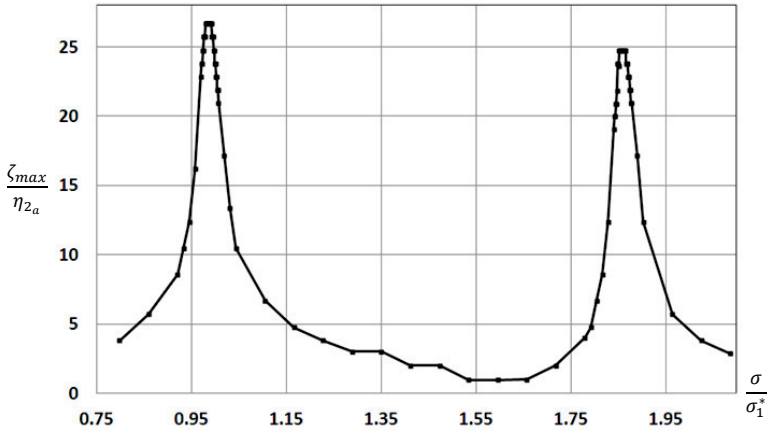

Figure 2-3. Non-dimensional maximum steady-state response ζ_{max}/η_{2_a} versus non-dimensional forcing frequency σ/σ_1^*. $h/l = 0.4, \varepsilon = 0.001, Sn = 0.4725$. η_{2_a}: forcing amplitude in sway.

In order to produce maximum responses in the experiments an important consideration is that the steady-state solution around resonance may belong to different solution branches due to nonlinear free-surface effects. Which steady-state solution is obtained depends on the transient time history. The possible theoretical solution branches at resonant for $h/l > 0.3368$ ((Faltinsen & Timokha, Sloshing, 2009), chapter 8) are shown on the right side of Figure 2-4. The presented theoretical response assumes one dominant mode. However, more than one dominant mode may be present. For instance at the theoretical critical depth $h/l = 0.3368$ as well as in shallow water

more than one dominant mode causes a more complex system of solution branches. Due to the soft-spring behavior for $h/l > 0.3368$ maximum steady-state response takes place at a frequency smaller than the natural frequency of sloshing. The solution branch associated with the maximum steady-state response is chosen by stepping down the forcing frequency from $\sigma > \sigma_{A_1}$ (see Figure 2-4) to $\sigma < \sigma_{A_1}$. In this way, the steady-state response passes the point A_1 and increases up to the maximum value A_{max} and then jumps down from A_2 to A_3. By stepping up the forcing frequency from $\sigma < \sigma_{A_3}$ to $\sigma > \sigma_{A_1}$ another solution branch is obtained; the response curve passes A_3 and increases up to the turning point T at which the solution jumps up to A_1. Further increase of the forcing frequency larger than corresponding frequency for A_1 causes lower responses. This phenomenon is called hysteresis and is observed in the experiments. The curve between T and A_1 in Figure 2-4 is an unstable solution branch and does not appear in the results. In order to obtain the maximum steady-state responses in the experiments, the forcing frequency always steps down for $h/l > 0.3368$ ... . In the experiments, after reaching steady-state waves at a forcing frequency σ, the frequency is lowered slightly by $\Delta\sigma$ (stepping down the frequency) and the tank is harmonically excited with the new frequency $\sigma - \Delta\sigma$ until steady-state waves are appeared. This process is repeated to cover the desired frequency range $\sigma_1^*(1-\Delta_1) < \sigma < \sigma_3^*(1+\Delta_3)$ from the highest frequency to the lowest. $\Delta\sigma$ is taken smaller around resonance frequencies to identify the maximum response and its corresponding frequency within sufficient accurately.

A hard spring behavior is expected for a clean tank when $h/l < 0.3368$. Unlike the soft spring behavior, the maximum response belongs to a frequency larger than the natural frequency for a hard-spring behavior. Hard-spring behavior is illustrated on the left side of Figure 2-4. To follow the branch with the maximum response the forcing frequency σ is raised by $\Delta\sigma$ after reaching each steady-state regime. It is noted that for small water depths, for instance $h/l < 0.24$, a "finger" type response may occur where many modes become dominant due to the secondary resonance (Faltinsen and Timokha 2002). As a result many resonant peaks can appear near the first resonant peak with comparable amplifications.

An important note is that the jump in the steady-state solution, i.e. from A_2 to A_3 (for both $h/l < 0.3368$ and $h/l > 0.3368$) occurs if damping is sufficiently small. For instance in a clean tank where the boundary layer and meniscus effects are the damping source in absence of wave breaking, a soft- or hard-spring phenomena happens even for forcing amplitudes as small as $\varepsilon = 0.001$. The large damping caused by the cross flow through the screens removes the jump of the steady-state response at sloshing resonant frequencies (Faltinsen & Timokha, Sloshing, 2009). Moreover, when large damping exists in the system, the frequency corresponding to the maximum resonant peak is less drifted away from the natural frequency of sloshing. Figure 3-3 shows the steady-state responses obtained in a clean tank and a tank equipped with a screen of solidity ratio $Sn = 0.4725$ for $h/l = 0.4$ and $\varepsilon = 0.001$. In the same figure, the resonant responses at $\sigma/\sigma_1^* = 1$ and $\sigma/\sigma_1^* = \sigma_3^*/\sigma_1^* = 1.8775$ for the clean tank depicts soft-spring jump for which the peaks occur at frequencies smaller than the natural frequencies while the same peaks in the screen-equipped tank does not experience a jump and occur at slightly larger frequencies.

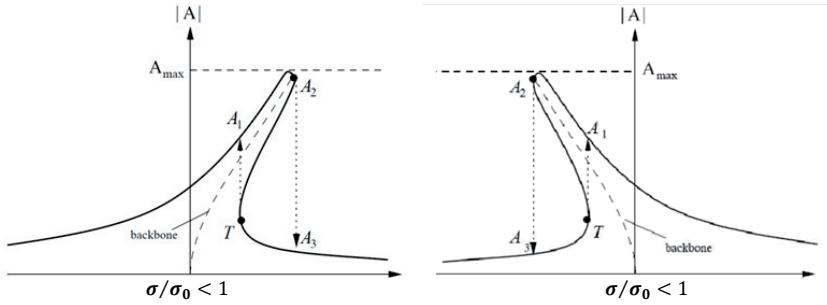

Figure 2-4. Steady-state solutions branches for depths smaller and larger than the critical depth $h/l = 0.3368$ according to Moisiev type theory with one dominant mode. Left: Hard-spring behavior for $.24 < h/l < 0.3368$, (Right) Soft-spring behavior for $h/l > 0.3368$.

A note here is that high solidity ratios will cause isolated sloshing on the two sides of the screen and as a results the ratio $h/(l/2)$ should be considered as a depth criteria, i.e. while the h/l value suggests a hard-spring sloshing response, $h/(l/2)$ can be larger than the critical depth. Therefore in such a condition, both stepping up and down the forcing frequency should possibly be considered to account for the maximum responses.

2.5 Experimental uncertainties

Experimental results are used as a reference for validating theoretical and numerical calculations. Experimental errors due to measurement or the setup always exist. These biases should be known and if possible quantified. For instance, the linear position sensor measures the instantaneous tank position within accuracy of 0.01 mm, i.e. 1% of the lowest forcing amplitude of 0.001 m in this study. This bias is considered negligible.

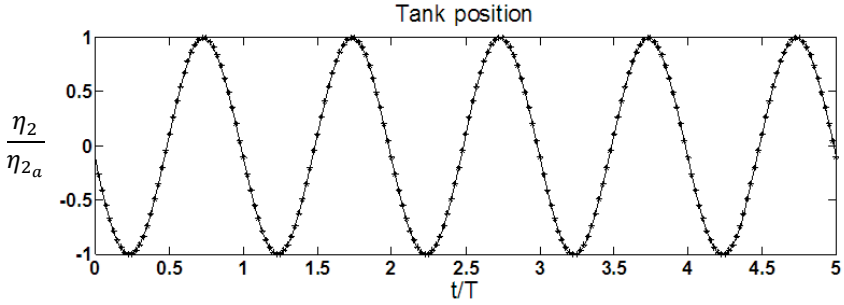

Figure 2-5. Comparison between desired (continuous line) and measured (dots) tank positions.

The instantaneous tank positions are input values to the system. The tank is forced to move based on the desired input positions fed every $\Delta t = 0.02\ s$ (the input sampling rate is 50Hz) into the sloshing rig's actuator. The input signal follows a linear ramp at start to avoid large accelerations. The quality of the measured tank positions is shown in Figure 2-5 to compare with the desired positions. According to Figure 2-5, the measured and desired tank positions are very similar in terms of amplitude and frequency of the motion. It should be noted that the quality of the input position is also perfect for the largest tested forcing amplitude.

Theoretically, the forcing motion is harmonic, i.e. position, velocity and acceleration must be purely harmonic. Figure 2-6 shows the measured acceleration signal that obviously contains high frequency components. These frequencies are generated because the rig only follows the instantaneous positions and not the accelerations. In other words, when the rig pushes the tank to move from its current position to the next, a large velocity change may be needed during a very short period of time to pave the distance. These unwanted high frequency accelerations may excite higher modes of sloshing if their energy content is large enough. In the bottom part of Figure 2-6 non-dimensional amplitude of the frequency components of the acceleration signal is plotted. The vertical red lines mark the non-dimensional frequency of the first 28 natural frequencies of sloshing in clean tank (when no screen is mounted). The largest peak corresponds to the applied forcing frequency σ. There are very small amplitude accelerations seen for frequencies larger than the third natural frequency (vertical line S_3 in Figure 2-6). These accelerations may cause very small amplitude waves. However, the experimental results did not show appearance of waves due to unwanted high frequency accelerations.

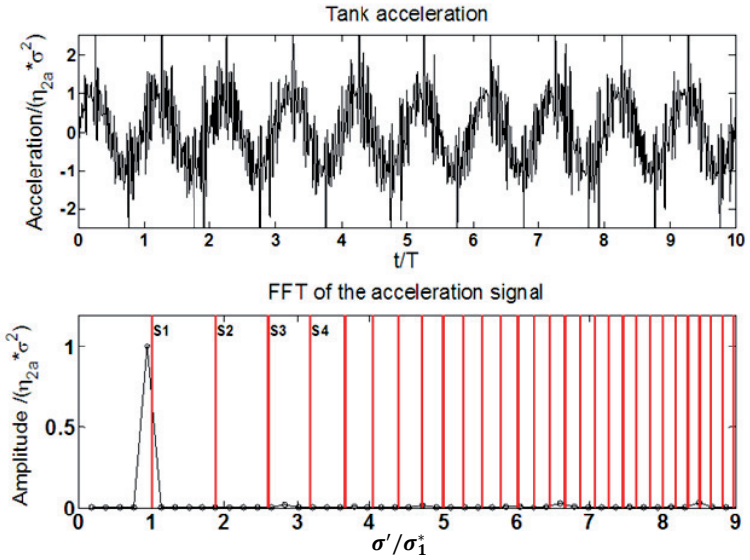

Figure 2-6. Top: Measured tank accelerations in time, Bottom: Amplitude of the frequency contents of the acceleration signal. σ' is the frequency content of the acceleration signal calculated by FFT. σ and η_{2_a} are forcing frequency and amplitude.

The wave probes made of two thin wires measure the free surface elevations relative to the undisturbed mean water level. The electrical resistance caused by the water column between the two wires is related to the free surface level by means of a multiplying factor α_C. α_C has the dimension of $\frac{meters}{Volts}$, i.e. $\alpha_C * V$ (V is the voltage read by the sensor) gives the wave elevation. To calculate α_C at least 5 still-water levels covering the maximum and minimum wave elevations are taken and the corresponding voltages are measured. Having the water levels (relative to the tank bottom) and the voltages, a line is fitted through the points as shown in the left part of Figure 2-7. As the

figure shows the relation between the measured voltages and corresponding water levels is very linear. The steepness of this relation, i.e. α_C, is equal to 1.5949 $\frac{meters}{Volts}$ in the left part of figure 7.

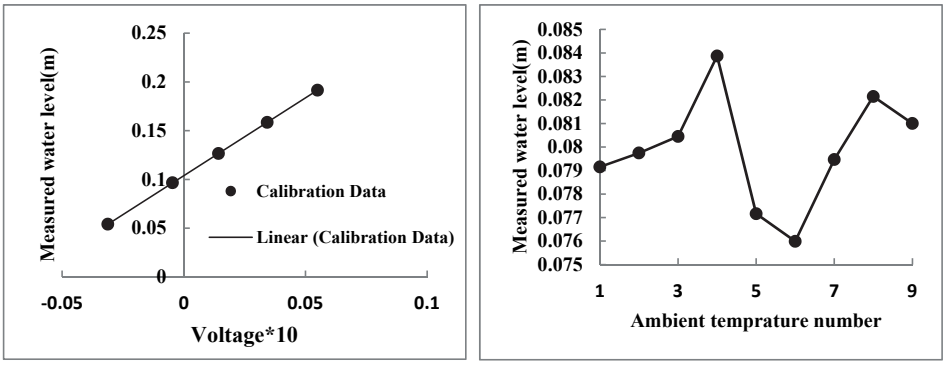

Figure 2-7. Calibration of wave probes, Left: wave elevation (m) versus voltage (V*10), Right: measured wave elevation (m) for a fixed voltage change ΔV, the horizontal axis represents numbers for different ambient temperatures, these numbers are only used for naming.

The electrical resistance of water is also a function of temperature which means α_C changes with temperature. To illustrate this, the measured wave heights are plotted on the right side of Figure 2-7 for a fixed voltage change, i.e. $\Delta V = constant$ at nine different ambient temperatures. The plot shows that wave probes measure different wave elevations in different ambient temperatures. Therefore if the temperature changes during the time, a new α_C has to be determined for new measurements.

Change in the ambient temperature may matter during test runs if the duration of each run is too long. In practice a test run might be conducted for a frequency range of $0.4\,Hz \leq f \leq 1.45\,Hz$. If the frequency range is divided to frequencies with $\Delta f = 0.01\,Hz$ difference where each frequency should excite the tank for 150 cycles, a single run will take 17100 seconds (4 hours and 45 minutes). Now, if the temperature continuously changes during this long run, the effect is that the zero level or the level of the water at rest reported by the wave will vary. This causes an inaccuracy in the measured value of the wave elevations. Keeping the tank at rest but measuring the water level for a long time showed that the wave probes measure up to 1 mm change in the mean water level. This value should be considered as a bias.

2.5.1 Experimental bias due to presence of the screen supports

The screen is fixed in the middle of the tank using two vertical strips (see Figure 2-8) attached to the opposite lateral walls. These vertical supports may impose unwanted local three-dimensional flow and hydrodynamic damping effects. The screen supports may add the following experimental biases:

a. 10% local contraction of the flow at the middle section that locally increases the flow rate through the screen openings. This increased flow rate is more pronounced for low solidity ratios ($Sn \leq 0.5$) that may lead to larger screen-induced damping.
b. Generation of unwanted damping due to flow separation at the sharp edges of the strip supports which may matter for low solidity ratios ($Sn \leq 0.5$).

c. Local three-dimensional effect by obstructing the flow in the tank middle.

Figure 2-8 shows a top view of the tank, screen and its supports. It is assumed that the flow is affected only at the screen openings where the support edges are exposed to the flow in the tank middle. In the following the magnitude of damping imposed by the supports is estimated by means of experiments and theoretical methods.

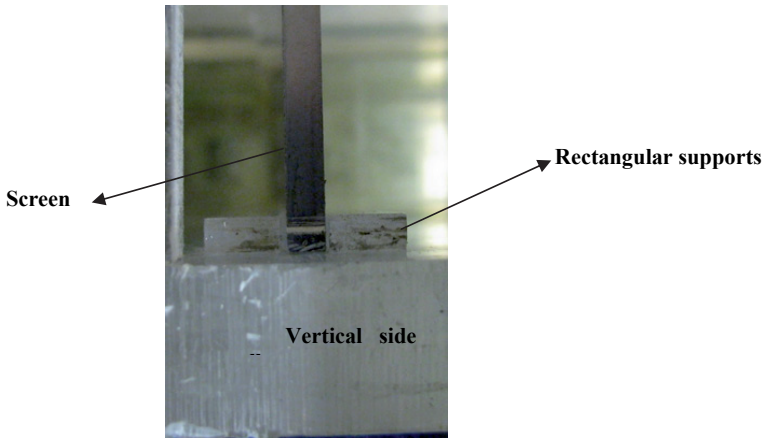

Figure 2-8. Top view of the tank, screen and rectangular supports fixed on the side wall.

2.5.2 Estimation of damping caused by the screen supports

2.5.2.1 Using free decay test

a) Keulegan's theory

In experiments the decay of wave amplitudes in free oscillations were used to examine the damping level at the highest natural period of sloshing. Wave breaking was avoided during the decay test. The tank without a mounted screen is excited for some periods at its lowest natural frequency and then the excitation is stopped. The water inside the tank is at rest before starting the excitation. During the excitation wave elevations at the vertical wall are growing until the tank motion is stopped. The amplitudes of these waves are seen in the left panel of Figure 2-9. They increase from 0 to a maximum value during the excitation. The decaying amplitudes appear right after stopping the tank excitation. Using the decaying amplitudes, the damping coefficient ξ or equivalently modulus of decay $\alpha = 2\pi\xi$ for the first mode of sloshing is calculated. Considering only the dissipation in the boundary layer as the damping source and assuming laminar flow, the amplitudes of the waves are expected to decay exponentially such that in a semi-log plot the amplitude ratio $\frac{a}{a_0}$ varies linearly against number of periods, i.e. $\frac{a}{a_0} = exp\left(-\frac{\alpha t}{T}\right)$ (Keulegan, 1959). a_0 is the initial amplitude and a is the decaying amplitude during the decay process. T is the highest natural period of sloshing (also the period of decaying waves) in the tank and α is the average value of modulus of decay. As an example a/a_0 is plotted versus t/T and shown on the right side of Figure 2-9. Maxima (h_{max}) and minima (h_{min}) of the standing waves on the opposite

sides of the tank are used to calculate the wave amplitude, i.e. $a = \frac{1}{2}(h_{max} - h_{min})$. An example of decaying amplitudes is shown on the left side of Figure 2-9 for $h = 0.833\ m$ and $\eta_{2a_0} = 0.00465\ m$. η_{2a_0} is the amplitude of excitation in meters during the excitation. α is calculated by taking an average value between 50 values of α calculated for 50 periods of decaying amplitudes.

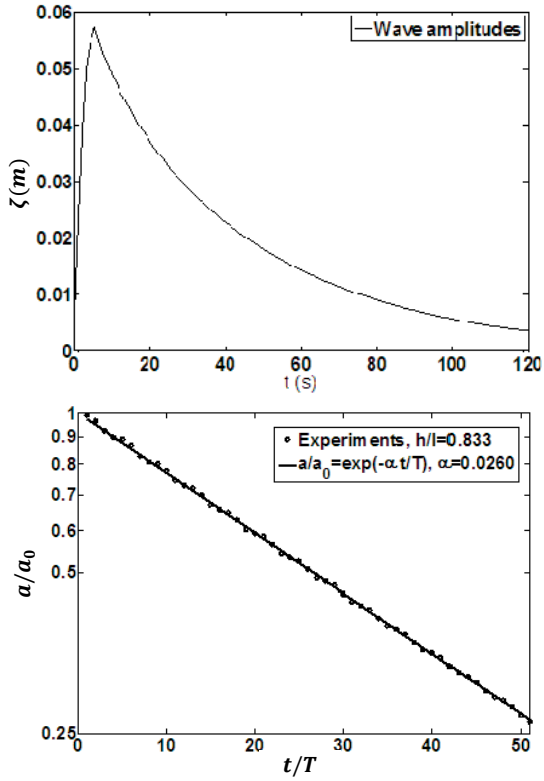

Figure 2-9. Calculation of modulus of decay. $h = 0.833\ m$, $T = 1.2516\ s$ and $\eta_{2a_0} = 0.00465\ m$. η_{2a_0} is the amplitude of excitation in meters during the excitation. Top: the decay of wave amplitude $a = \frac{1}{2}(h_{max} - h_{min})$, Bottom: Semi-log plot of the amplitude ratio a/a_0 versus number of decay periods t/T; the t/T values are discrete. t_T is the total time and t is the time during the decay.

The result presented in Figure 2-9 for free decay test of wave for $h = 0.833$ m and $\eta_{2a_0} = 0.00465$ m give $\alpha = 0.0260$. The results of a decay test in the same tank but without bracings and for the same experimental condition have given $\alpha = 0.0261$ (Abrahamsen, 2011) that shows negligible contribution of the bracings to the global damping. Keulegans' theory (1959) which considers viscous dissipation due to boundary layer at the tank bottom and four vertical walls gives $\alpha = 0.0208$ which is smaller than the experimental values. Experimental decay tests for $h/l = 0.4$ and $h/l = 0.12$ give $\alpha = 0.0290$ and 0.0427 respectively. The corresponding theoretical values $h/l = 0.4$ and $h/l = 0.12$ are $\alpha = 0.0218$ and 0.0338 respectively. Both theory and experiments give larger modulus of damping for smaller depths. The damping

coefficients ξ is related to the modulus of decay by the relation $\xi = \alpha/2\pi$ that gives ξ =0.0041, 0.0023 and 0.0068 for $h/l = 0.833$,0.4 and 0.12, respectively.

Keulegan (1959), relates the discrepancy between calculated α using theory and experiments to surface tension. Another reason for the discrepancy might be due to extra dissipation in turbulent boundary layers. The critical Reynolds number for transition from laminar to turbulent flow on a flat plate is $Re_{critical} = 5 \times 10^5$. This value is 20 times larger than the maximum Reynolds number $Re = \frac{\sigma A^2}{\nu} = 2.4 \times 10^4$ in the above decay tests (A and σ are the amplitude of the oscillating flow just outside the boundary layer and frequency of the oscillations). Therefore turbulence does not contribute to the amount of damping causing the decay.

b) Quadratic damping model

Damping due to the flow separation from the sharp edges of bluff bodies is significantly larger than viscous damping of boundary layers. In an oscillatory flow, the damping effects of a bluff body may be modeled as a quadratic damping term in the equation of wave motion. Here the rectangle supports are assumed as a quadratic damping source in a free oscillation wave model (Faltinsen, 1989):

$$\ddot{x} + p_1\dot{x} + p_2|\dot{x}|\dot{x} + p_3 x = 0 \tag{2.1}$$

where the term proportional to p_2 on the left hand side is responsible for the quadratic damping source. The term p_1 describes a linear damping effect caused by, for instance, laminar boundary layer on the vertical walls. x is the decaying amplitude of the wave elevations. The damping coefficients p_1 and p_2 are assumed to be constant with respect to the amplitude of the wave. They are determined by plotting the left hand side of relation $\frac{2}{T_m}\log\left(\frac{x_{n-1}}{x_{n+1}}\right) = p_1 + \frac{16}{3}\frac{x_n}{T_m}p_2$ against $\frac{16}{3}\frac{x_n}{T_m}$. x_n is the amplitude of the motion for period n and there is a half-period $T_m/2$ difference between x_n and x_{n+1}. A plot based on what is explained above is given in Figure 2-10. A solid line is fitted through the points by a least square method which estimates $p_1 = 0.04585$ and $p_2 = 0.01859$. If p_1 is redefined as $p_1 = 2\xi\sigma$ where $\xi = \alpha/2\pi$ and σ and ξ are the first natural frequency and damping coefficient of the first mode of sloshing, then $\alpha = 0.0264$ for $h/l = 0.833$ which is almost equal to $\alpha = 0.0261$ obtained from the Keulegan's method expressing the decay of the wave amplitude as $\frac{a}{a0} = exp\left(-\frac{\alpha t}{T}\right)$. The estimated value for p_2 is not reliable as it is equal to the slope of the line fitted through a highly scattered data set shown in Figure 2-10. It is noted here that the above way of modeling for quadratic damping is difficult to use when the Keulegan Carpenter number $KC = U_m T/D$ is experiencing a significant change during the decay (Faltinsen 1989). KC number relates the distance traveled by a flow particles oscillating with velocity amplitude of U_m about the rectangular supports of characteristic width D. T is the period of flow oscillations. Here D is equal to two width of a single support normal to the flow direction. In fact one can assume that the flow around the wall and the support attached to it is symmetric about the wall. This means that the flow around a vertical rectangular strip attached to a wall is similar to the flow around a rectangle with a width twice the width of a single support in an infinite flow. $U_m = \frac{\sigma A}{kh}$ is the depth-average value of the linear component of the velocity which is only dependent on the amplitude A of the decaying waves at the wall. Using the first 15 decaying amplitudes it

gives $7.8 < KC < 12.6$ which shows 20% decrease in KC number during the decay. On the other hand, the drag coefficient, which is directly related to the viscous dissipation, of a sharp edged square section (a single support in infinite fluid) is KC number dependent for $KC \approx 10$. This can be seen in Figure 2-12. This means that the quadratic damping model (2.1) is not applicable due to relatively large changes in the instantaneous value of drag coefficient.

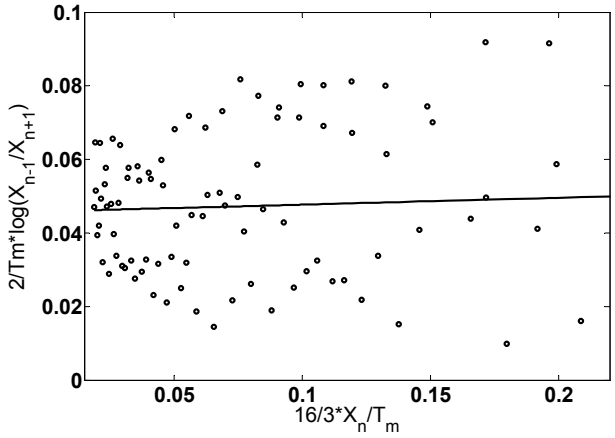

Figure 2-10. Estimation of damping in the clean tank by fitting the data of decaying wave amplitudes to a quadratic damping model. The fitted line through the data is used to estimate linear p_1 and quadratic p_2 damping coefficients defined by $\frac{2}{T_m}\log\left(\frac{X_{n-1}}{X_{n+1}}\right) = p_1 + \frac{16}{3}\frac{X_n}{T_m}p_2$. $h/l = 0.833, \varepsilon = 0.00465$.

2.5.2.2 Estimation of damping due to the screen supports using empirical drag coefficients

The unwanted damping due to the screen supports can be estimated by relating the average work done by the drag force applied on them to the rate of dissipation of potential and kinetic energy in sloshing waves during one period of oscillation. The rectangles experience a depth dependent ambient oscillatory flow. Only the effect of the first mode of sloshing is considered in the calculations because it causes the largest flow rate in the tank middle relative to the higher modes. Here the calculations are done for *shallow water* condition for which the flow is almost uniform in the middle of the tank.

As shown in Figure 2-11, two sets of rectangles of height l_b in a tandem arrangement with one l_b distance are mounted on each vertical wall parallel to the flow direction. Assuming that the flow around the rectangles is symmetric about the wall attached to the supports, a double-body configuration is considered (Figure 2-11). This gives two squares in tandem in cross flow of an infinite periodic flow. Now two limit cases are considered for the analysis; case (1) : In the extreme case from a damping point of view, two separate squares without hydrodynamic interaction can be considered where both squares experience the same inflow ambient velocity, case (2): The free space of length l_b between the squares is assumed to be a dead zone and a rectangle of length $5l_b$ and width $2l_b$ (aspect ratio=2.5) replaces the two squares. Case 1 is relevant for very low KC numbers while case 2 is relevant for large KC numbers.

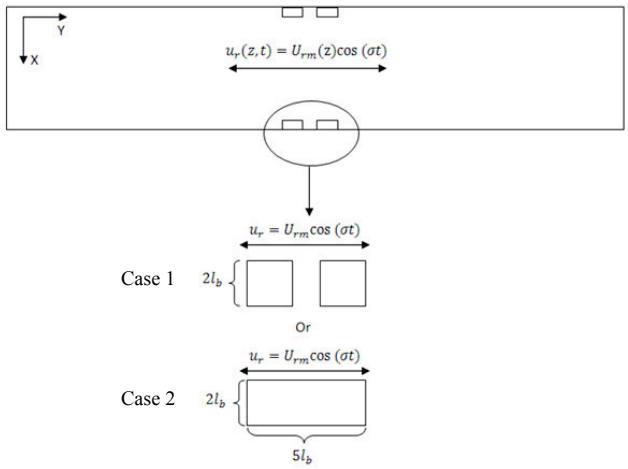

Figure 2-11. Double body assumption and two limit cases assumed in the investigation.

The average work done by the drag force in one period of oscillation applied on the supports with width of l_b (in X direction) elongated between 0 and h in the vertical direction (Z) reads:

$$D = \int_{-h}^{0} 1/T \int_{0}^{T} \frac{\rho}{2} C_d l_b |u_r| u_r u_r dt \; dz \tag{2.2}$$

$u_r = u_{rm}\cos(\sigma t)$ is the relative horizontal Z-dependent ambient velocity at $Y = 0$ (tank middle). ρ is the liquid density and T is the oscillation period. The drag coefficients C_d for bluff bodies subject to an infinite oscillatory flow are dependent on Keulegan-Carpenter number KC defined as $KC = \overline{u_{rm}} T/D$. For the current investigation, $= 2\pi/\sigma_1^*$, $D = 2l_b$. $\overline{u_{rm}} = \frac{\sigma_1^* A}{kh}$ is the depth-averaged horizontal velocity. A is the amplitude of the wave at the vertical wall, $k = \pi/l$ and h is the still water depth. Calculations are done for steady-state condition in presence of the screen for $\sigma = \sigma_1^*$. The hydrodynamic interaction between the screen and the supports and the effect of the screen on the first mode of clean-tank sloshing is neglected. For $h/l = 0.12$ and $\varepsilon = \eta_{2_a}/l = 0.01, Sn = 0.4725$ and $\sigma/\sigma_1^* = 0.9998$ $KC = 39.6$. The drag coefficient of a sharp edge cylinder (square) in a planar oscillatory flow has been experimentally measured first by Tanaka, et al. (1982) and by Bearman, et al. (1984b) (Figure 2-12). Figure 2-12 shows that for KCs larger than 40 the drag coefficient does not change (increase) significantly and becomes independent of KC with more increase in KC (Bearman et al., 1984b). The KC independent drag coefficient $C_d = 1.9$ for a squared rectangle is a little smaller than its steady value $C_d = 2.2$ in non-oscillating uniform flow with $Re > 10^4$ (Blevins 2000). Here the corresponding Reynolds number for the flow past the screen supports is equal to 2.1×10^4, i.e. $\beta = \frac{Re}{KC} = 530.05$. To be on the safe side the steady flow value of C_d which is a little larger than the periodic value is used in the calculations. For case 1, two separated rectangles, $C_d = 2.2$ is used. For case 2 of the current investigation, a continues rectangle with aspect ratio of $\frac{5}{2} = 2.5$, Blevins (2000) suggests steady-state drag coefficient $C_d = 1.4$.

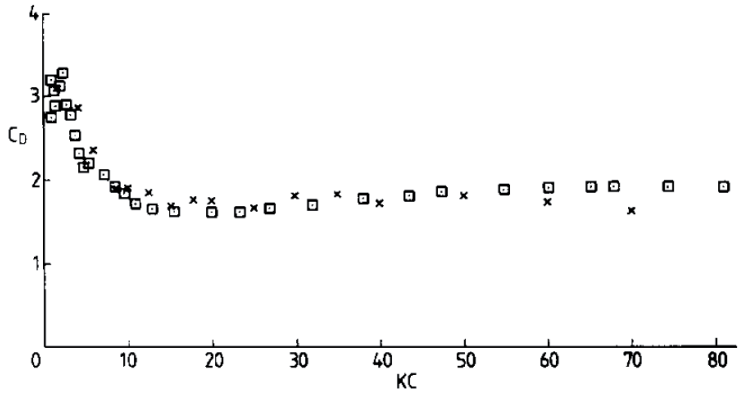

Figure 2-12. Cd of a sharp-edged cylinder (square) versus KC number. 'x', Tanaka et al, (1983); square, Bearman, et al., (1984).

The method proposed in section 6.5.1 of Faltinsen and Timokha (2009) for calculation of hydrodynamic damping caused by small height internal structures mounted on the tank walls (baffles) is applied to estimate modulus of damping α for the first mode of sloshing.

The linear potential theory for standing waves gives the horizontal velocity at the *tank middle* $u_r = u_{rm}(z)\cos(\sigma t)$. u_{rm} is the amplitude of the velocity and a function of vertical coordinates (Z), that is $u_{rm}(z) = \frac{\sigma A \cosh(k(z+h))}{\sinh(kh)}$. When calculating the integral expression in (2.2) the following sub-integrals are encountered:

$$\int_{-h}^{0} \cosh(k(z+h))^3 \mathrm{dz} = \frac{\sinh(\mathrm{kh})\,(\sinh^2(kh)+3)}{3\mathrm{k}}$$

$$\frac{1}{T}\int_0^T \cos^2(\sigma t)|\cos(\sigma t)|dt = \frac{4}{3\pi}$$

Therefore equation (2.2) reads:

$$D = \int_{-h}^{0}\frac{1}{T}\int_0^T \frac{\rho}{2} C_d l_b |u_r| u_r u_r dt\ dz = \frac{\rho}{2}\, C_d l_b \left(\frac{\sigma A}{\sinh(kh)}\right)^3 \frac{4}{3\pi}\frac{\sinh(\mathrm{kh})(\sinh^2(kh)+3)}{3\mathrm{k}}.$$

The rate of dissipation of energy of the waves $\dot{E}$ is related to the summation of kinematic and potential energy in the standing wave E and the time-averaged work done by the rectangles D using the relation $\dot{E} = -D = -\sigma E\alpha/\pi$. $E = \frac{1}{4}\rho g A^2 lb$ is the summation of potential and kinetic energy of an standing wave oscillating with amplitude A and wavelength of $2l$ in a tank with horizontal extents of l and b. The damping modulus can now be evaluated from $\alpha = \frac{\pi D}{\sigma E} = \frac{\pi D}{\sigma \frac{1}{4}\rho g A^2 lb}$. This relation shows the linear dependence of α on the wave amplitude A for a fixed forcing frequency. Calculations are done for $k = \pi/l$ (first mode) and $h = 0.12\ m, l = 1\ m, b = 0.1\ m$ and $l_b = 0.005\ m$. For case 1 with four separated rectangles D(the averaged work done by the drag force) should be multiplied by 4 to account for 4 rectangles (2 rectangles on each wall). The same calculation is also done for case 2. The damping modulus is plotted as a function of non-dimensional wave amplitude in Figure 2-13. For

comparison, the modulus of decay for boundary layer is also presented in Figure 2-13. The horizontal curve for the boundary layer is plotted using Keulegan's theory for laminar oscillatory flow which is fixed a value for all wave amplitudes. The figure shows that the dissipation in the boundary layer on the bounding vertical walls is the largest source of damping for $A/l \leq 0.0215$. For $A/l > 0.0215$ the separated rectangles (case 1) exceed the boundary layer damping but the continuous rectangle (case 2) does not, demonstrating the smallness of the damping due to the screen supports.

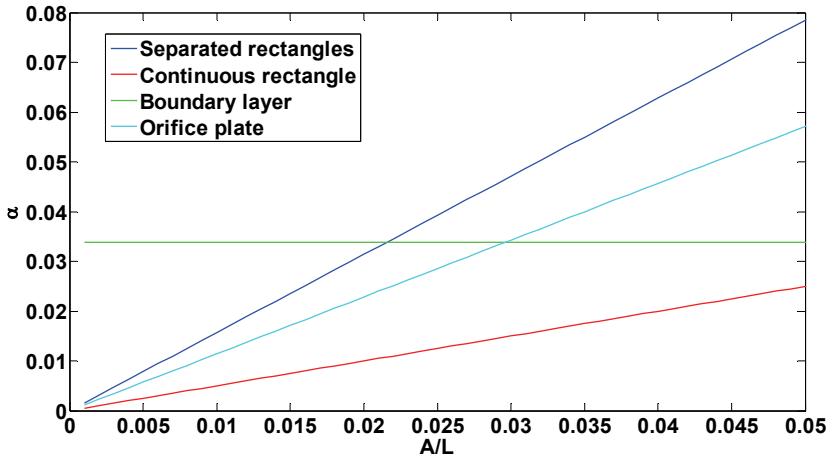

Figure 2-13. Calculated modulus of decay α of the lowest sloshing mode for different damping sources as a function of non-dimensional wave amplitude A/l for $h/l = 0.12$ in presence of a screen with $Sn = 0.4725$.

The damping effect due to the supports matters when it is comparable to the screen-caused damping. A same procedure can be followed for estimating the screen-caused damping assuming that the first mode of sloshing remains unchanged. Baines and Peterson (1951) suggest an empirical value for the pressure loss K and the drag coefficient of a screen in a steady uniform flow,

$$K = \left(\frac{1}{C_c(1-Sn)} - 1\right)^2, \; C_c = 0.405\exp(-\pi Sn) + 0.595, \; C_d = K/Sn.$$

Cc is a discharge coefficient dependent on the shape of the openings. The pressure loss K is defined as

$$\Delta p = K\frac{\rho}{2}|u|u \tag{2.3}$$

where u is the velocity of the ambient flow crossing the screen. For $Sn = 0.4725$ the pressure loss is equal to $K = 3.0986$.

D for a screen can calculated using the definition of pressure loss. The force on a screen element dz is equal to $df = \Delta p \times bdz$. Therefore,

$$\begin{aligned} D &= \int_{-h}^{0}\frac{1}{T}\int_{0}^{T}\frac{\rho}{2}K|u_r|u_r u_r dt \; Bdz \\ &= \frac{\rho}{2}Kb\left(\frac{\sigma A}{\sinh(kh)}\right)^3\frac{4}{3\pi}\frac{\sinh(\mathrm{kh})\,(\sinh^2(kh)+3)}{3\mathrm{k}}. \end{aligned} \tag{2.4}$$

Calculation shows that the screen-induced modulus of damping α is 13.35 and 42 times larger than those calculated for respectively for separated rectangles in case 1 and a rectangle in case 2. Neglecting the effect of boundary layer, α for case 1 and case 2 contributes up to 7% and 2.3% of the total damping including the effect of a screen with solidity ratio of 0.4725. The damping values computed for the screen supports are calculated based on the length of the bracings exposed to the flow passing through the screen openings. By increasing the solidity ratio, the parts of the supports exposed to the cross flow decreases. This means that the damping imposed by the supports becomes negligible for large solidity ratios.

Considering the contraction of the flow in the tank middle one relevant case is the flow through an orifice plate. The pressure loss due to a sharp-edge orifice plate in an axisymmetric flow in a pipe is given in engineering books (for instance Blevins (2000)). However, the flow in a circular cylinder pipe is confined from expansion in the direction normal to the fluid flow unlike the flow in a sloshing tank that can deform at the free surface zone due to local pressures. In addition, the behavior of vortex shedding from an orifice plate in a circular pipe is different than the vertical supports in the present rectangular tank. Pressure loss values for 2D cross section of a pipe including the orifice plate together with the main dimensions are given in Figure 2-14. The K (pressure loss) values are given for steady-state flow and Reynolds number $Re_n = \frac{U_m D}{\nu}$ is $\geq 10^4$. In the present case for $D = 0.1\ m$, $\nu = 10^{-6}$ the amplitude of the relative flow velocity should be larger than $0.1\ m/s$ which is not far from the maximum horizontal velocity observed in the experiments for $Sn \leq 0.5$ (for the first mode). For $d/D = 0.9$ the pressure loss is $K = 0.32$ according to the table in Figure 2-14. The modulus of decay α for orifice plate is plotted in Figure 2-13.

According to results in Figure 2-13, the estimated value for α assuming an orifice model is the second largest after the separated rectangles. The continuous rectangles, the most relevant case, produce the smallest damping.

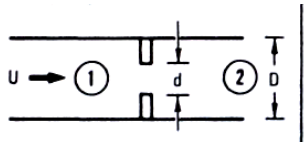

d/D	0.20	0.25	0.30	0.35	0.40	0.45	0.50
K	1600.	620.	300.	155.	87.5	49.	30.83

d/D	0.55	0.60	0.65	0.70	0.75	0.80	0.85	0.90
K	19.	12.	7.3	4.7	2.7	1.5	0.76	0.32

Figure 2-14. Empirical pressure loss values *K* for an orifice plate in a pipe with a circular section. Data is taken from Blevins (2000). *U* is the uniform ambient velocity. *D* and *d* are the inner diameter of the pipe and contracted diameter inside the orifice.

The experimental and theoretical estimation of modulus of damping α of the screen supports gives maximum 7% contribution in the total damping considering different bluff body models. One should remember that: Estimations are made for a tank equipped with a screen of solidity ratio $Sn = 0.4725$ in shallow water because the supports will cause larger damping when the flow is more uniform in the tank middle. In addition, the solidity ratio in the calculations is smaller than 0.5 which makes more than 50% of the length of the supports being exposed to the cross flow at the screen. Calculations are made within linear wave theory and small wave amplitudes. Wave amplitudes are kept small in free decay tests to avoid wave breaking which is an unknown damping source. However, the effect of the supports becomes less important

unknown damping source. However, the effect of the supports becomes less important for large solidity ratios due to less inflow through the screen openings, which is more relevant for the cases investigated in this thesis.

One should also note that the thickness of the boundary layer is comparable to the height of the screen supports. For laminar boundary layer flow the geometric 0.99% boundary layer thickness can be estimated by $\delta_{0.99} = 4.6\sqrt{2\nu/\sigma}$, where ν and σ are the kinematic viscosity and frequency of flow oscillation. For $h/l = 0.833, 0.4$ and $0.12\ m$ the corresponding boundary layer thickness is 2.8, 2.9 and 3.6 mm. This means that cross flow into the middle section of the tank is less affected by the presence of screen supports which accordingly reduces the unwanted damping caused by the supports.

3 Analysis of experimental results in finite water depth

Presenting and analysis of the experimental results will be the material of the current and next chapter. Experimental results are also used to validate results calculated by theoretical and numerical methods. The theoretical models (Appendix) which are extensions of the potential flow theory are based on assumptions such as two-dimensional flow, linearity of the free surface in case of linear models and degree of non-linearity of the free-surface for non-linear models. The numerical calculations presented in chapter 5 also assume laminar, incompressible two-dimensional flow model. The analysis of experimental results can help determining experimental conditions where the required assumptions by the theoretical and numerical models are satisfied.

Considering pure experimental analysis the effect of screen on the sloshing modes and frequencies due to its presence in the middle of the tank is also studied.

In this chapter the experimental results are categorized based on water depth and forcing amplitude. New findings are reported and classified based on experimental conditions.

The experiments are categorized in Table 3-1 based on the variation of non-dimensional physical parameters:

a. Non-dimensional water depth: h/l
b. Non-dimensional forcing amplitude: $\varepsilon = \eta_{2_a}/l$
c. Solidity ratio: Sn

Table 3-1. Variation of physical parameters in the experiments.

h/l	ε	Sn (First set)	Sn (Second set)
0.4 (finite depth)	0.001, 0.01	0.296-0.9592	.4725-0.9512
0.35 (finite depth)	0.03	-	0.4729-0.9529
0.12 (shallow depth)	0.01	0.3612-1.0000	0.4725-0.9625
0.125 (shallow depth)	0.05	-	0.4752-0.9640

As listed in Table 3-1, the experiments are carried out in non-dimensional finite depths: $h/l = 0.4$, $h/l = 0.35$ and shallow depths: $h/l = 0.12$ and $h/l = 0.125$. Very small and small forcing amplitudes including $\varepsilon = 0.001$ and $\varepsilon = 0.01$ and relatively large amplitudes $\varepsilon = 0.03$ and $\varepsilon = 0.05$ are tested in different depths. Small forcing amplitudes are relevant for sloshing in Tuned Liquid Dampers (TLDs) used for example as vibration control devices in tall buildings. Larger forcing amplitudes are more relevant for marine applications. The analysis starts with experiments in finite water depth $h/l = 0.4$ and small forcing amplitudes. Analysis of the results obtained in shallow water will be carried out in the next chapter. This is for the sake of better readability of the thesis.

3.1 Water depth ratio h/l=0.4, forcing amplitude ratio ε = 0.001

Very small forcing amplitude of $\varepsilon = 0.001$ is chosen to avoid strong free surface nonlinearities as well as any kind of special free-surface effects such as wave breaking and thin wave run-ups on the vertical walls or on the screen. Such small forcing amplitude is useful when reference results are needed for validation of linear free-surface based theoretical methods. For the current forcing amplitude experimental measurements for two sets of screens are studied. The geometry of the two screen sets are shown in Figure 2-2. The solidity ratios for $h/l = 0.4$ are:

First set : 0.296, 0.498 , 0.696 , 0.797 , 0.847 , 0.896 , 0.9225, 0.944 , 0.9592.

Second set: - , 0.4725, 0.6825, 0.7863, 0.8388, 0.8913, 0.9138, 0.9363, 0.9513.

The solidity ratios are almost the same for both sets except for $Sn = 0.296$ from the first set that does not have a counterpart in the second set. The forcing frequencies are in the range of $0.8\sigma_1^* \leq \sigma \leq 2.1\sigma_1^*$. The soft-spring behavior of steady-state wave responses for $h/l > 0.3368$ should be considered by stepping down the forcing frequency after reaching each steady-state regime to account for the maximum possible responses. Figure 3-1 and Figure 3-2 present the non-dimensional maximum steady-state response ζ_{max}/η_{2_a} (top panel in the figures) and its first Fourier harmonic ζ_{1st}/η_{2_a} (bottom panels in the figures) as a function of σ/σ_1^* for the first and the second sets of the screens. The results for the first set of screens shown on the two upper panels and for the second set on the lower panels. The measured steady-state responses (ζ_{max}/η_{2_a}) are only shown for one side of the tank.

The results in Figure 3-1 and Figure 3-2 are very similar for both sets of screens demonstrating the importance of solidity ratio rather than the geometrical details of the screens (excluding $Sn = 0.296$ from the first set of screens that does not have a similar counterpart in the second set of screens). Considering the presented results in Figure 3-1 and Figure 3-2 some noteworthy conclusions can be made. Due to very similar results for both sets of screens, only the results obtained for the second set of screens are used for detailed discussion.

For solidity ratios $0.45 \leq Sn \leq 0.85$, the steady-state responses in Figure 3-2 show two clear resonance peaks associated with the two lowest anti-symmetric (odd) modes in the clean tank. The peaks remain close to $\sigma/\sigma_1^* \approx 1$ and $\sigma/\sigma_1^* \approx 1.878$, i.e., they occur in a neighborhood of the first and the third natural sloshing frequencies in the clean tank. Furthermore, the maximum non-dimensional wave elevations in the considered frequency range becomes smaller with increasing Sn. The reason is that increasing Sn between ≈ 0.5 and and ≈ 0.85 increases the global damping in the mechanical system.

Results for $Sn = 0.8913$ and 0.9138, show that further increase of the solidity ratio leads to an increase of the global damping at $\sigma/\sigma_1^* \approx 1$, but the experimental steady-state resonance response at the second resonance peak (associated with the second anti-symmetric mode $\sigma/\sigma_1^* \approx 1.878$) remains almost the same. Furthermore, this second resonance peak drifts to the left of $\sigma/\sigma_1^* \approx 1.878$, i.e., from 1.87 to 1.75.

Changing the solidity ratio to 0.9363 leads to vanishing of the first resonance peak and shifting the second resonance peak to $\sigma/\sigma_1^* = 1.6$. The largest tested solidity ratio 0.9513 drifts the latter peak more toward smaller forcing frequencies at $\sigma/\sigma_1^* =$

1.54 which is larger than $\sigma_2^*/\sigma_1^* = 1.5238$, i.e. the second natural frequeny of the clean tank or the lowest natural frequency of a compartmented tank. This means that the cross-flow through the screen still matters and the non-linear soft-spring behavior effect is not dominant to push the resonant peak to take place at a forcing frequency smaller than $\sigma_2^*/\sigma_1^* = 1.5238$. When $Sn \to 1$, the limit case of watertight wall is reached where the wall divides the tank into two equal-length isolated compartments. When $= 1$, boundary layer is the only source of damping if no wave breaking is present. This means very small forcing amplitude can trigger non-linear effects and the lowest resonant response of a compartment can occur at $\sigma/\sigma_1^* < \sigma_2^*/\sigma_1^* = 1.5238$.

Comparing the steady-state response curves for all screen, the lowest maximum response in the tested frequency range occurs for $Sn = Sn_{min} = 0.8913$. The peak point response for this solidity ratio belongs to a frequency smaller than $\sigma_3^*/\sigma_1^* = 1.878$.

Figure 3-2 shows that the magnitude of the peak responses at $\sigma/\sigma_1^* = 1$ and $\sigma_3^*/\sigma_1^* = 1.878$ are closely comparable for a given solidity ratio in the range $0.45 \leq Sn \leq 0.85$. The latter fact is implicitly a consequence of the fact that the screen causes a larger damping of flow oscillations associated with the first mode than with that of the third mode. To demonstrate this fact, Figure 3-3 compared the maximum responses measured in a clean tank and also in a tank equipped with a screen of $Sn = 0.4725$. Considering the clean tank, the peak response at σ_1^* is almost 1.7 times larger than the one at σ_3^* while the screen with $Sn = 0.4725$ damps the peaks at σ_1^* and σ_3^* down to almost the same value. The reason is that the average flow rate through the screen, which directly related to damping, is larger for the first mode relative to that of the third mode. For the third mode, the screen is only effective in the free surface zone because of faster exponential decay of the horizontal velocity in the tank middle toward the tank bottom.

One may notice the step-wise behavior of the responses for very large solidity ratios, for instance $Sn = 0.944$ and $Sn = 0.9552$ in the upper plots of Figure 3-1 and Figure 3-2. The reason is the accuracy of the wave gauges which is 1 mm, i.e. $(measurement\ error)/\eta_{2_a} = 1$. The latter means differences within 1 mm cannot be measured. Therefore if changing the forcing frequency changes the responses less than the measurement error, a constant or step-wise response curve appears.

Figure 3-2 also shows that the maximum steady-state responses and their corresponding amplitude of the first Fourier harmonic are almost the same for large values of solidity ratios. This means that the non-linearity of the free surface is reduced due to presence of screen-caused damping. In a clean tank where wave breaking does not occur and the only source of damping is the boundary layer attached to the tank walls, free-surface non-linearities matter more. For instance, for $\varepsilon = 0.001$ and $h/l = 0.4$ non-linearities cause larger responses relative to responses in a screen-equipped tank at primary resonance frequencies, i.e. $\sigma/\sigma_1^* \approx 1$ and $\sigma/\sigma_1^* \approx \sigma_3^*/\sigma_1^* = 1.878$ accompanied with jumps in the steady-state amplitudes. Figure 3-3 shows a clear steady-state jump in the responses measured in the clean tank at $\sigma_3^*/\sigma_1^* = 1.878$. The jump at $\sigma/\sigma_1^* \approx 1$ is not clearly seen due to lack of sufficient number of forcing frequencies around the resonant frequency. In contrast, in a screen-equipped tank the screen-caused damping decreases the level of free-surface nonlinearity and removes the steady-state jumps at both peak responses (see Figure 3-3).

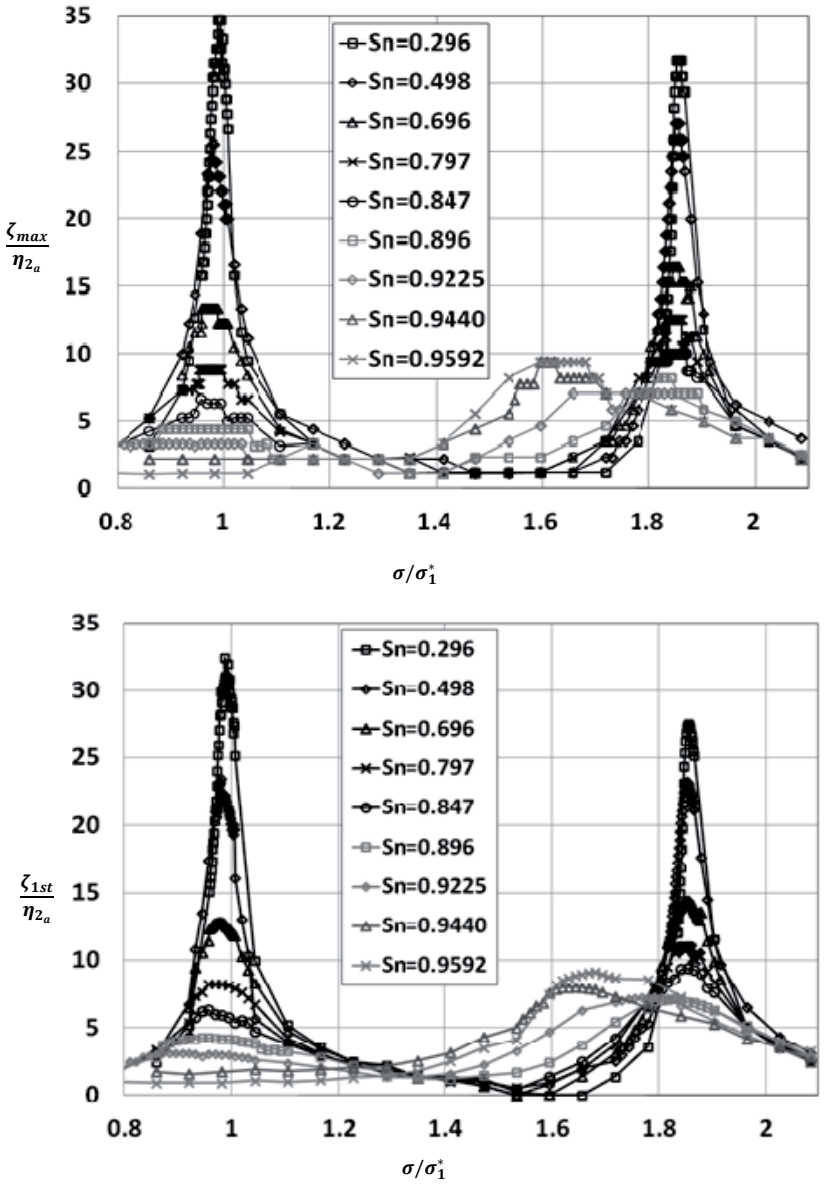

Figure 3-1. Non-dimensional maximum steady-state response ζ_{max}/η_{2_a}(top panel) and its amplitude of the first Fourier harmonic ζ_{1st}/η_{2_a} (bottom panel) versus σ/σ_1^* for all solidity ratios Sn. The results belong to the first set of screens. $h/l = 0.4$, $\varepsilon = 0.001$.

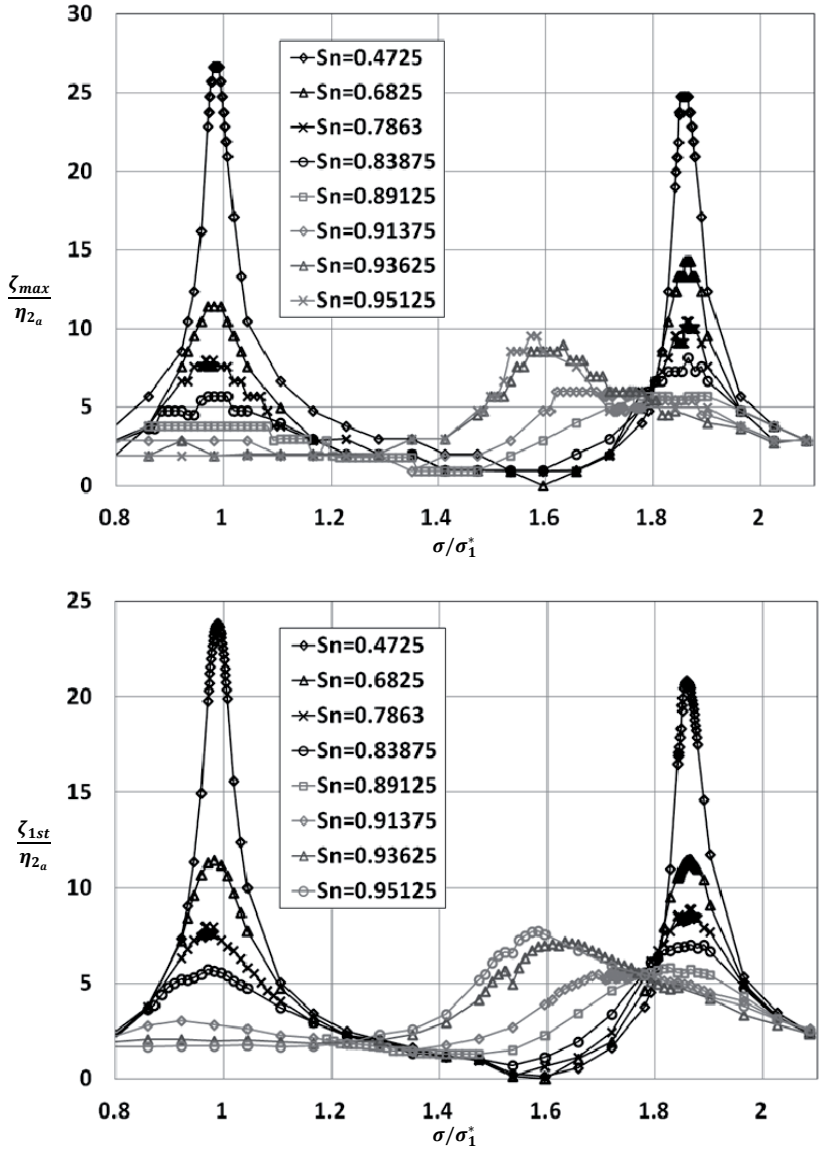

Figure 3-2. Non-dimensional maximum steady-state response ζ_{max}/η_{2_a}(top panel) and its amplitude of the first Fourier harmonic ζ_{1st}/η_{2_a} (bottom panel) versus σ/σ_1^* for all solidity ratios. The results belong to the second set of screens. $h/l = 0.4$, $\varepsilon = 0.001$.

3.2 Water depth ratio h/l=0.4, forcing amplitude ratio ε = 0.01

Increasing the forcing amplitude to $\eta_{2_a}/l = 0.01$ leads to a set of specific free surface phenomena documented by means of photographs in Figure 3-4 to Figure **3-9**. These phenomena are mainly observed in the frequency range $1.25 \leq \sigma/\sigma_1^* \leq 1.78$ and for the screen with the smallest tested solidity ratio $Sn = 0.4725$ in the range $0.92 \leq$

$\sigma/\sigma_1^* \leq 1.04$. The solidity ratios of the tested screens are $Sn = 0.4725$, 0.6825, 0.7863, 0.8388, 0.8913, 0.9138, 0.9363, and 0.9513.

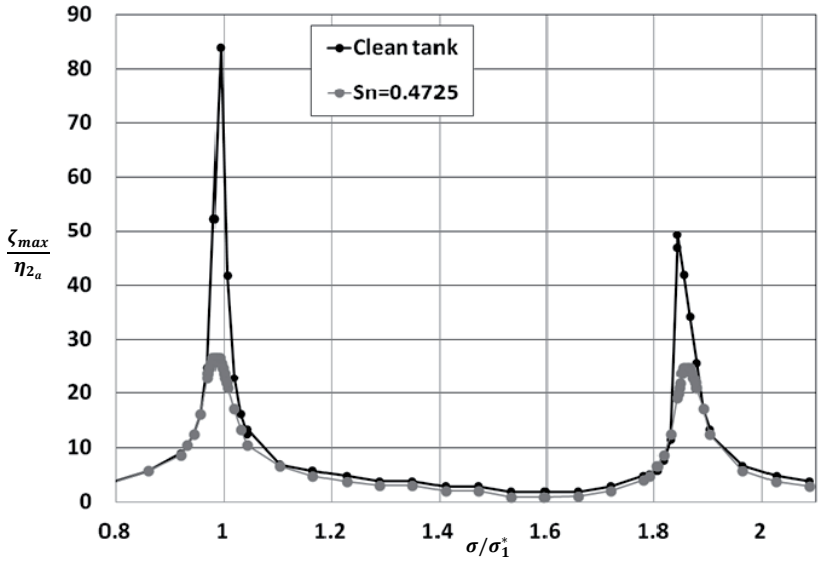

Figure 3-3. Non-dimensional maximum steady-state response ζ_{max}/η_{2_a} versus σ/σ_1^* in a clean tank and in a tank equipped with a screen with Sn = 0.4725. $h/l = 0.4$, $\varepsilon = 0.001$.

3.2.1 Special free-surface effects

Wave breaking (basically of spilling type) happens for all the tested solidity ratios with $Sn \leq 0.9$ (except $Sn = 0.4725$) in the frequency range of $1.25 \leq \sigma/\sigma_1^* \leq 1.78$. It is most severe for lower solidity ratios. Figure 3-4 exhibits the corresponding photograph for the screen a with $Sn = 0.4725$ at $\sigma/\sigma_1^* = 1.71$. The wave breaking occurs periodically in the left and right compartments as a consequence of collision between cross-flow through the screen and going toward the vertical wall and an incoming wave in the corresponding compartment. For the lowest solidity ratio $Sn = 0.4725$, a local wave breaking is also observed for $\sigma/\sigma_1^* = 0.98$ which is seen in Figure 3-5. The latter disappears for other screens with higher solidity ratios.

For $0.6825 \leq Sn \leq 0.9$, *three-dimensional* wave motions are established in the frequency range $1.66 \leq \sigma/\sigma_1^* \leq 1.73$. Figure 3-6 displays the corresponding photograph for $Sn = 0.6825$ and $\sigma/\sigma_1^* = 1.72$. Two vertical arrows at the end walls depict different wave elevations in the vertical plane normal to the direction of motion. These three-dimensional waves are accompanied by a local wave breaking. The video recordings show that the wavelength of the standing wave oscillating normal to the forcing direction (Figure 3-6) is almost equal to $2b$ (b is the width of the tank normal to the direction of motion). This wave almost oscillates two times during each forcing period i.e. $2\sigma/\sigma_1^* = 3.44$, which is very close to the frequency of the lowest sloshing mode of the tank in the lateral direction with $h/l = 0.4/0.1 = 4$ ($\frac{\sigma_{1_{lateral}}}{\sigma_1^*} = 3.4295$).

The wavelength of capillary waves dominated by surface tension is smaller than few centimeters ($\lambda < 0.05$ m). This wavelength is 4 times smaller than 20cm ($2b$) which is the wavelength of the oscillating way in the lateral direction. Therefore surface tension cannot be a reason for appearance of three-dimensional waves. One reason might be the three-dimensional local effects at the screen migrating toward the end tank-walls that might excite the lowest lateral sloshing mode.

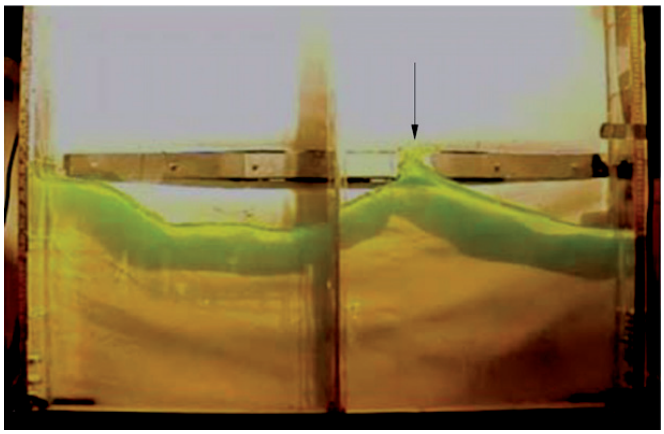

Figure 3-4. Typical wave breaking indicated with arrow; occurring for all the tested solidity ratios $Sn \leq 0.9$ in the range of $1.25 \leq \sigma/\sigma_1^* \leq 1.78$ for the model tests with $h/l = 0.4$ and $\eta_{2_a}/l = 0.01$. The photo is for a screen with $Sn = 0.4725$ and the forcing frequency $\sigma/\sigma_1^* = 1.71$.

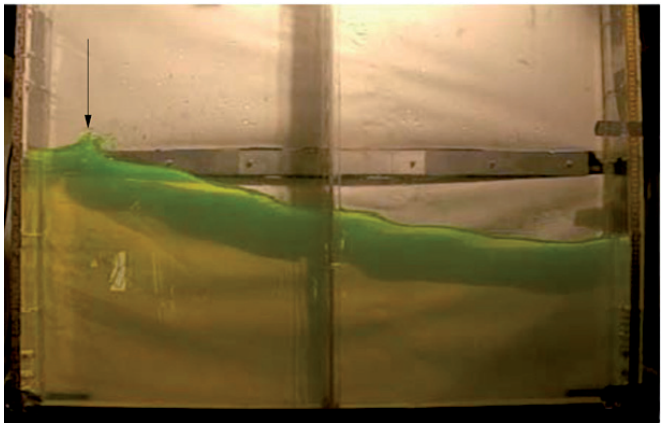

Figure 3-5. Local wave breaking indicated by arrow; occurring for $= 0.4725$, $h/l = 0.4$, and $\eta_{2_a}/l = 0.01$, $\sigma/\sigma_1^* = 0.98$.

The photo in Figure 3-7 illustrates steep waves generated in the tank due to the amplification of the higher harmonics of the forcing established in the visual observations for solidity ratios 0.6825, 0.7863, 0.8388. The latter fact indicates nonlinear amplification of higher harmonics through secondary resonance of higher modes when the necessary condition $n\sigma = \sigma_n^*$ is valid and the forcing amplitude is

sufficiently large. (Faltinsen and Timokha, Sloshing, 2009, chapter 8). For the case shown in Figure 3-7, the condition $4\sigma = \sigma_4^*$ is valid. It is noted that the secondary resonance, which is a non-linear phenomenon, was not observed for $\varepsilon = 0.001$ due to very small forcing amplitude.

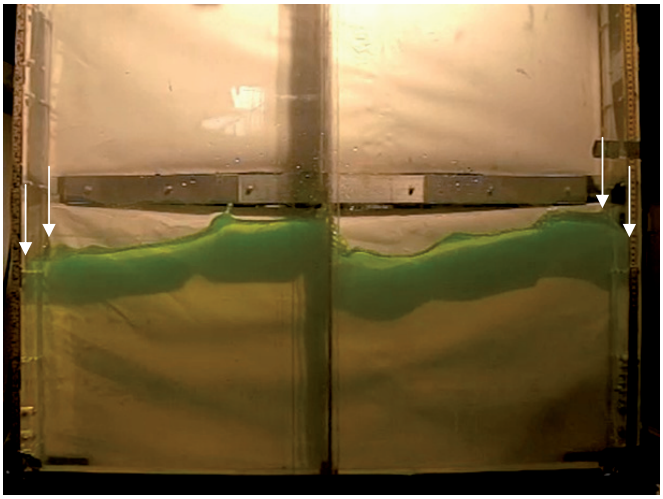

Figure 3-6. Typical three-dimensional perturbations of the free surface occurring for $0.7 \le Sn \le 0.9$ and $1.66 \le \sigma/\sigma_1^* \le 1.73$; $h/l = 0.4$, $\eta_{2_a}/l = 0.01$. The photo is for $Sn = 0.6825$ and $\sigma/\sigma_1^* = 1.72$.

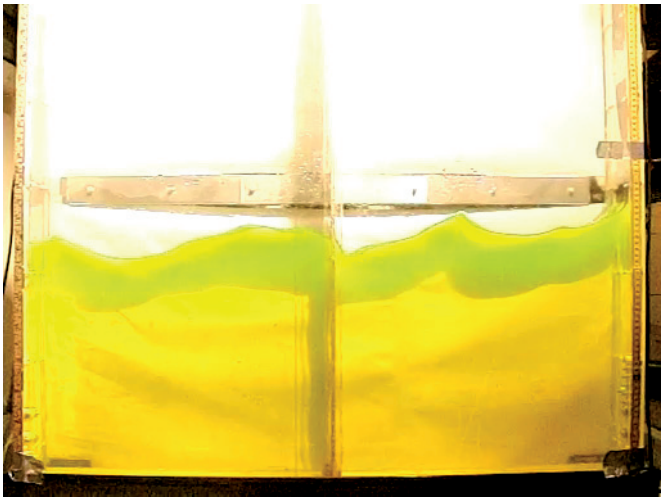

Figure 3-7. Snapshot of a video recording of a steep wave with the double superharmonics elevations at the walls. $h/l = 0.4$, $\varepsilon = 0.01$, $Sn = 0.7863$, $\sigma/\sigma_1^* = 1.2888$.

Liquid jets through the screen openings over the free surface with subsequent fallout on the opposite free surface are seen for $\varepsilon = 0.01$. They get stronger by increasing the solidity ratio between 0.8913 and 0.9513 in a frequency range around

$\sigma/\sigma_1^* = 1.524$. Figure 3-8 shows the liquid jets for $Sn = 0.8913$ and $\sigma/\sigma_1^* = 1.48$. The jets that travel the longest distance from the screen due to very large horizontal flow velocity at the screen openings and finally hit the underlying free-surface are seen for the largest solidity ratio and around $\sigma/\sigma_1^* = \sigma_2^*/\sigma_1^* = 1.524$, i.e. the lowest natural frequency of one compartment.

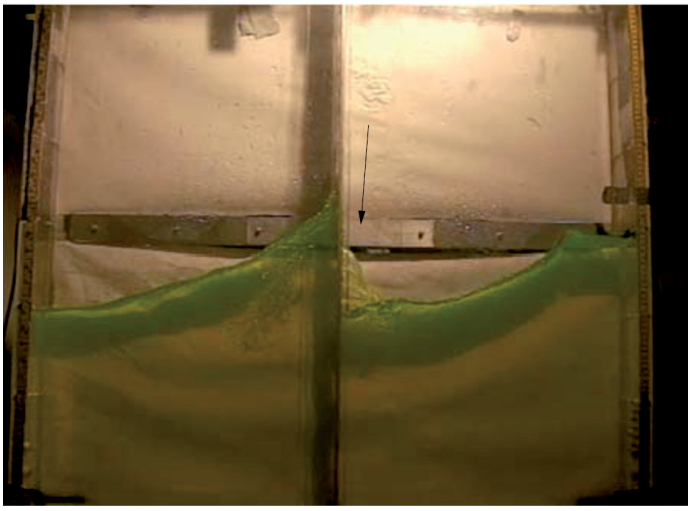

Figure 3-8. Photo of the liquid jet through the screen for $Sn = 0.8913$ and $\sigma/\sigma_1^* = 1.48$. $h/l = 0.4$, $\varepsilon = 0.01$.

Run-up with a detachment of a liquid portion along the screen happened for the solidity ratios $0.9 \leq Sn$. Figure **3-9** shows the corresponding snapshot.

The above-mentioned phenomena cause strong flow perturbations. Strong perturbations affect the steadiness of the response waves leading to waves oscillating with a mean steady-state maximum elevation superposed with transient deviations. The frequency ranges accompanied with relatively strong transient effects are categorized in Table 3-2. The non-dimensional standard deviation std/η_{2_a} of the maximum steady-state elevations is used to identify the unsteadiness of the responses. One can also compare the reported std/η_{2_a} values with corresponding ζ_{max}/η_{2_a} to get better understanding about magnitude of the unsteady effects. The steady-state response curves that include ζ_{max}/η_{2_a} for $h/l = 0.4$, $\varepsilon = 0.01$ and all solidity ratios will be presented in the next section. However, the frequency ranges reported in Table 3-2 report frequencies with $std/\eta_{2_a} \geq 0.1$. This limit, i.e. $std/\eta_{2_a} = 0.1$ is the accuracy of the measurements. The unsteady effects are generally seen in $1.28 \leq \sigma/\sigma_1^* \leq 1.9$. $Sn = 0.6825$ gives the lowest level of unsteady behavior in the total tested frequency range. Increasing the solidity ratio to $Sn \geq 0.7863$ amplifies the maximum value of std/η_{2_a} and also lowers the upper frequency limit associated with the unsteady effects to $\sigma/\sigma_1^* = 1.7$. For the two largest solidity ratios $Sn = 0.9363$ and 0.9513, the non-dimensional standard deviation is larger than the non-dimensional forcing amplitude, i.e. std/η_{2_a} is larger than 1.

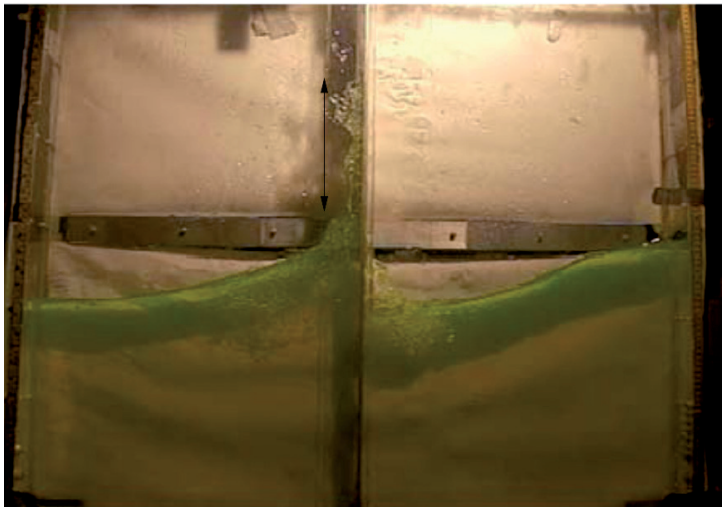

Figure 3-9. The photograph and video recording of the run-up at the screen occurring for $0.9 \leq Sn.\ h/l = 0.4, \varepsilon = 0.01$.

Table 3-2. Non-dimensional standard deviation std/η_{2_a} of the reported steady-state values about the mean value categorized for different screens. $(std/\eta_{2_a})_{max}$ is the maximum value of the non-dimensional standard deviation. The last column on the right presents the non-dimensional frequency σ/σ_1^* when $(std/\eta_{2_a})_{max}$ occurs.

Screen	Frequency range (σ/σ_1^*)	Special free-surface phenomena	$(\mathrm{std}/\eta_{2_a})_{\max}$	Frequency σ/σ_1^* for $(std/\eta_{2_a})_{max}$
0.4725	1.7-1.9	Local wave breaking	0.9	1.73
0.6825	1.63-1.8	Three-dimensional flow	0.2	1.64 and 1.69
0.7863	1.63-1.8	Three-dimensional flow	0.45	1.67
0.8388	1.3-1.7	Liquid-to-gas jet flows	0.561	1.31
0.8913	1.28-1.7	Liquid-to-gas jet flows	0.6	1.46
0.9138	1.28-1.8	Run-up on the screen and liquid detachment, Liquid-to-gas jet flows	0.73	1.46
0.9363	1.3-1.7	Run-up on the screen and liquid detachment, Liquid-to-gas jet flows	2.1	1.42
0.9513	1.35-1.65	Run-up on the screen and liquid detachment, Liquid-to-gas jet flows	3.5	1.36

The above-mentioned phenomena are accompanied by very steep free-surface profiles (run-ups), fragmented free-surfaces (liquid detachment and liquid-to-gas jet flows) and overturning flows (wave breaking) that cannot be handled by theoretical methods such as the linear and nonlinear multi-modal methods. These methods assume a one-to-one relationship between free-surface elevation and horizontal coordinates of the tank. In addition multimodal method is not able to capture fragmentation of the free-surface. Computational Fluid Dynamics (CFD) may provide better predictions because of their ability in handling free-surface with over-turned profiles. For instance, the Volume of Fluid (VOF), a CFD method used for capturing interfaces between two fluids, for instance water and air, can capture over-turning free-surface flows, free-surface fragmentation which is caused by cross-flow through the screen in the free-

surface zone. As it will be shown in chapter 5 it can successfully simulate flow through the screen as long as free-surface fragmentations are not massive.

3.2.2 Steady-state response curves of free-surface amplitude

Non-dimensional maximum steady-state responses ζ_{max}/η_{2_a}as a function of forcing frequency σ/σ_1^* are presented in Figure 3-10 to Figure 3-13 for all solidity ratios. Increasing the forcing amplitude to $\varepsilon = 0.01$ causes unequal steady-state responses at the end wall on the opposite sides of the screen at some of the resonant frequencies. To exhibit this fact Figure 3-10 to Figure 3-13 include responses in both compartments. The amplitudes of the first, second and the third Fourier harmonics of the response are also plotted to identify their contribution to the total response.

Comparing the results presented in Figures Figure 3-10 to Figure 3-13 for $\varepsilon = 0.01$ and the results in Figure 3-1 and Figure 3-2 for $\varepsilon = 0.001$ show that increasing the forcing amplitude leads to stronger nonlinear effects. The nonlinearities cause:

a. Additional resonance peaks occurring at frequencies apart from natural sloshing frequencies in the clean tank (σ_k^*),
b. A nonlinear soft-spring type behavior around $\sigma/\sigma_1^* = \sigma_3^*/\sigma_1^*$ for the lowest solidity ratio, $Sn = 0.4725$, and around $\sigma/\sigma_1^* = \sigma_2^*/\sigma_1^*$ for the largest solidity ratios.

The upper panel of Figure 3-10 presents the responses for $Sn = 0.4725$. Comparing these results with the results obtained for the same solidity ratio and $\varepsilon = 0.001$, (see Figure 3-2) shows a much clearer soft-spring response at $\sigma/\sigma_1^* = \sigma_3^*/\sigma_1^*$ for $\varepsilon = 0.01$. The experimental resonance peak at the first natural frequency σ_1^* remains in these figures of a linear character for both forcing amplitudes. In fact lower cross-flow through the screen by the 3rd natural mode associated with stronger exponential decay to the bottom leads to a lower screen-caused damping. The latter causes strong enough free-surface non-linearity which for the tested liquid depth implies a non-linear soft-spring type response. The vanishing of the first resonance peak occurs for $Sn = 0.7863$ while the lower forcing amplitude, $\varepsilon = 0.001$, detected this to vanish only for solidity ratios larger than $Sn = 0.9363$. As Sn increases, the natural sloshing frequency decreases from σ_3^* to σ_2^* and the results show a soft-spring type response curves at σ_2^* for $Sn \geq 0.8388$. For smaller forcing amplitude (Figure 3-2) this kind of discrepancies was detected only for the maximum tested solidity ratio, $Sn = 0.9513$.

Figure 3-10 to Figure 3-13 also show that the sum of the first, second and third harmonics contributions gives approximately the actual wave elevation for almost all the experimental data and, therefore, relates the appearance of the additional peaks to amplification of second (2σ) and third harmonic (3σ) components. The amplification of the third harmonic component is smaller than the second harmonic for all solidity ratios. For some cases the magnitude of the maximum steady-state wave elevation ζ_{max} is even *smaller* than the amplitude of the primary harmonic. The reason is amplification of higher harmonics combined with a linear harmonic with a special phase difference leading to standing waves with maximum absolute values smaller than their minimum absolute value in one period of the tank oscillation. An example of such a wave response is presented in Figure **3-14** for $Sn = 0.6825$ at $\sigma/\sigma_1^* = 1.0679$.

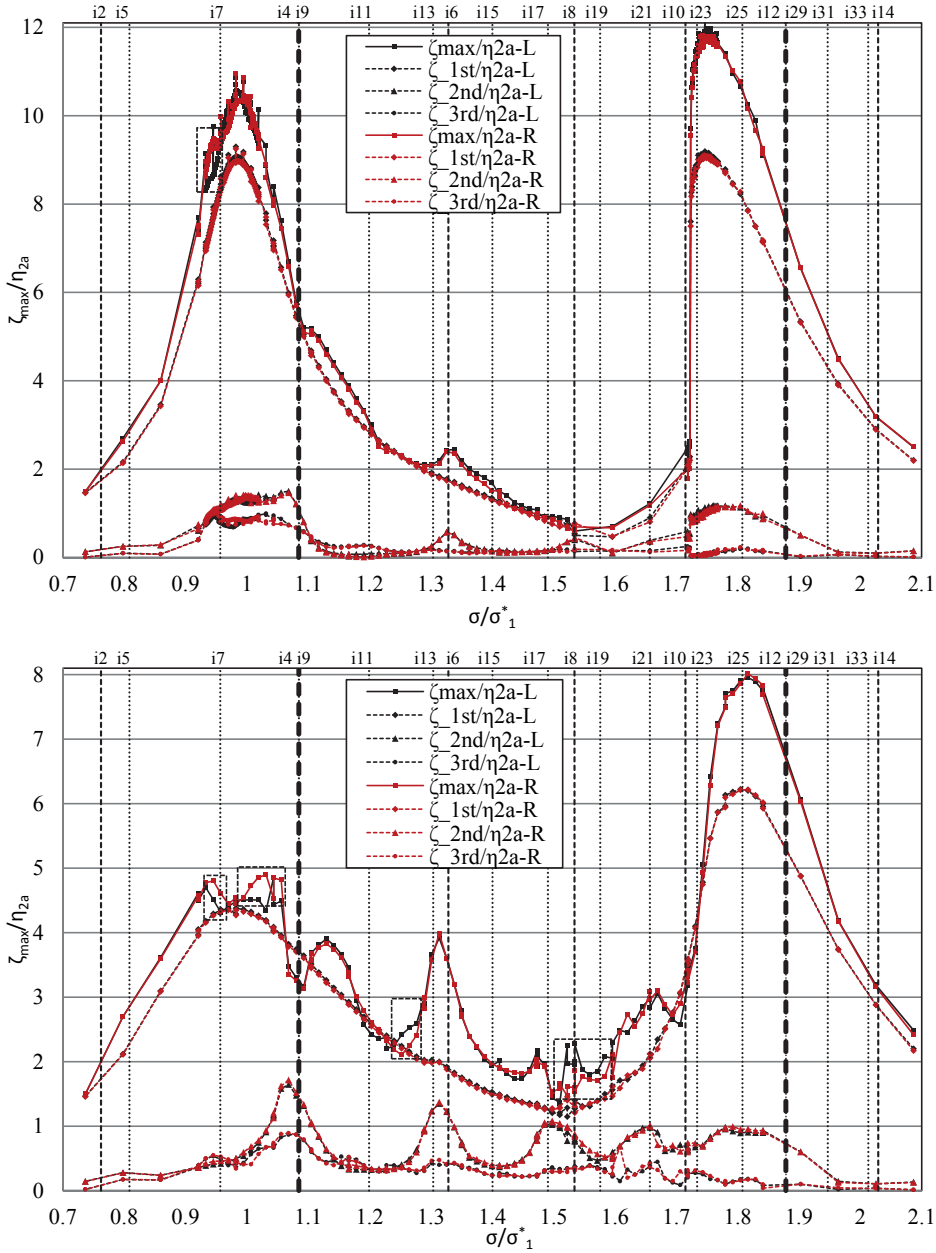

Figure 3-10. Non-dimensional maximum steady-state response ζ_{max}/η_{2_a} and the amplitude of the first three Fourier harmonics of the response ζ_{1st}/η_{2_a}, ζ_{2nd}/η_{2_a}, ζ_{3rd}/η_{2_a} versus σ/σ_1^*. $h/l = 0.4, \varepsilon = 0.01$. The letters 'L' and 'R' distinguish the two sides of the tank. Top panel: $Sn = 0.4725$, bottom panel: $Sn = 0.6825$. The vertical dashed i_{2k} and dotted lines i_{2k+1} mark the frequencies where secondary resonance of higher modes may occur. The rectangle mark unequal responses on the two sides of the screen occurring close to resonance areas.

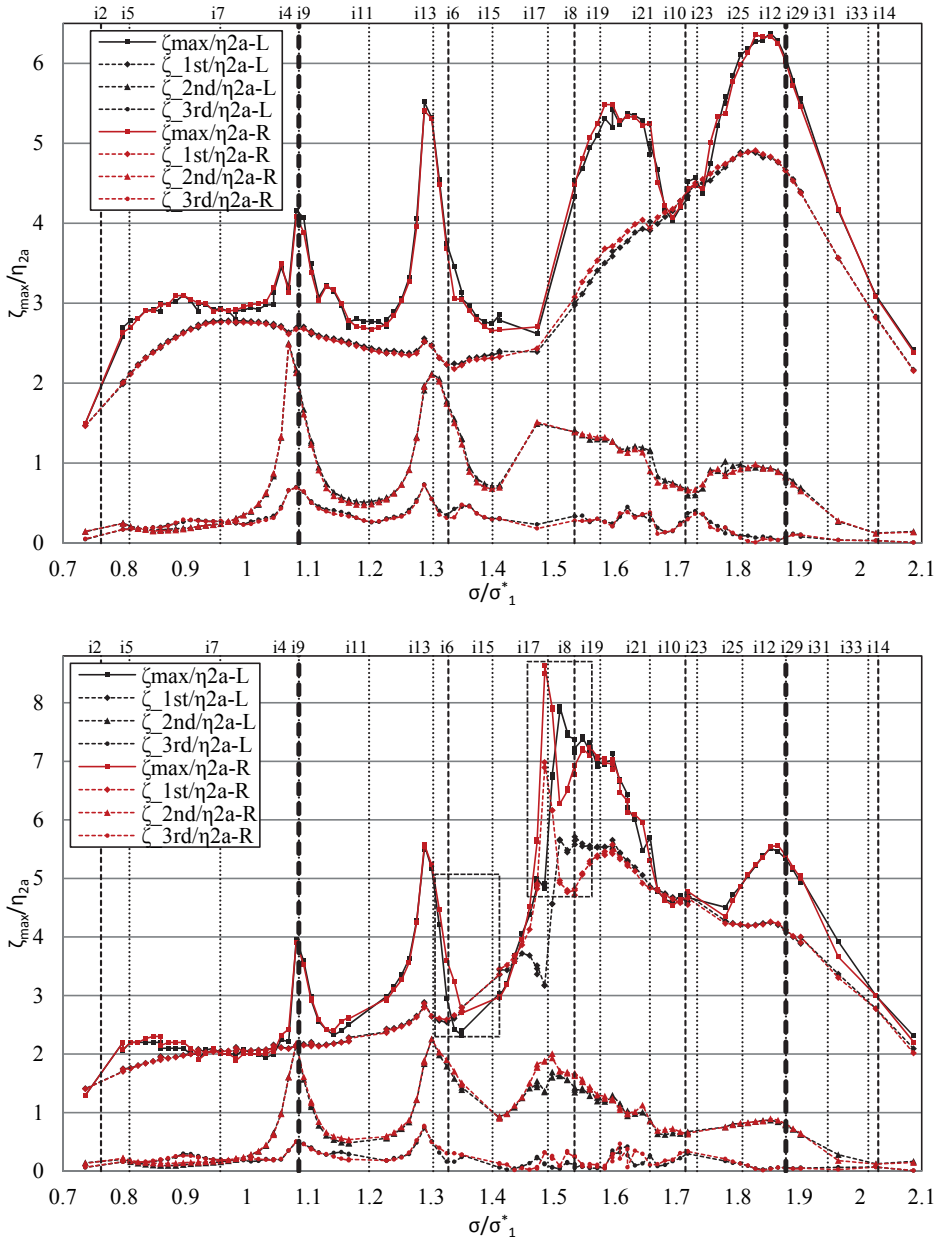

Figure 3-11. Top panel: $Sn = 0.7863$, bottom panel: $Sn = 0.8388$. Explanation is given in the caption of Figure 3-10. $h/l = 0.4, \varepsilon = 0.01$.

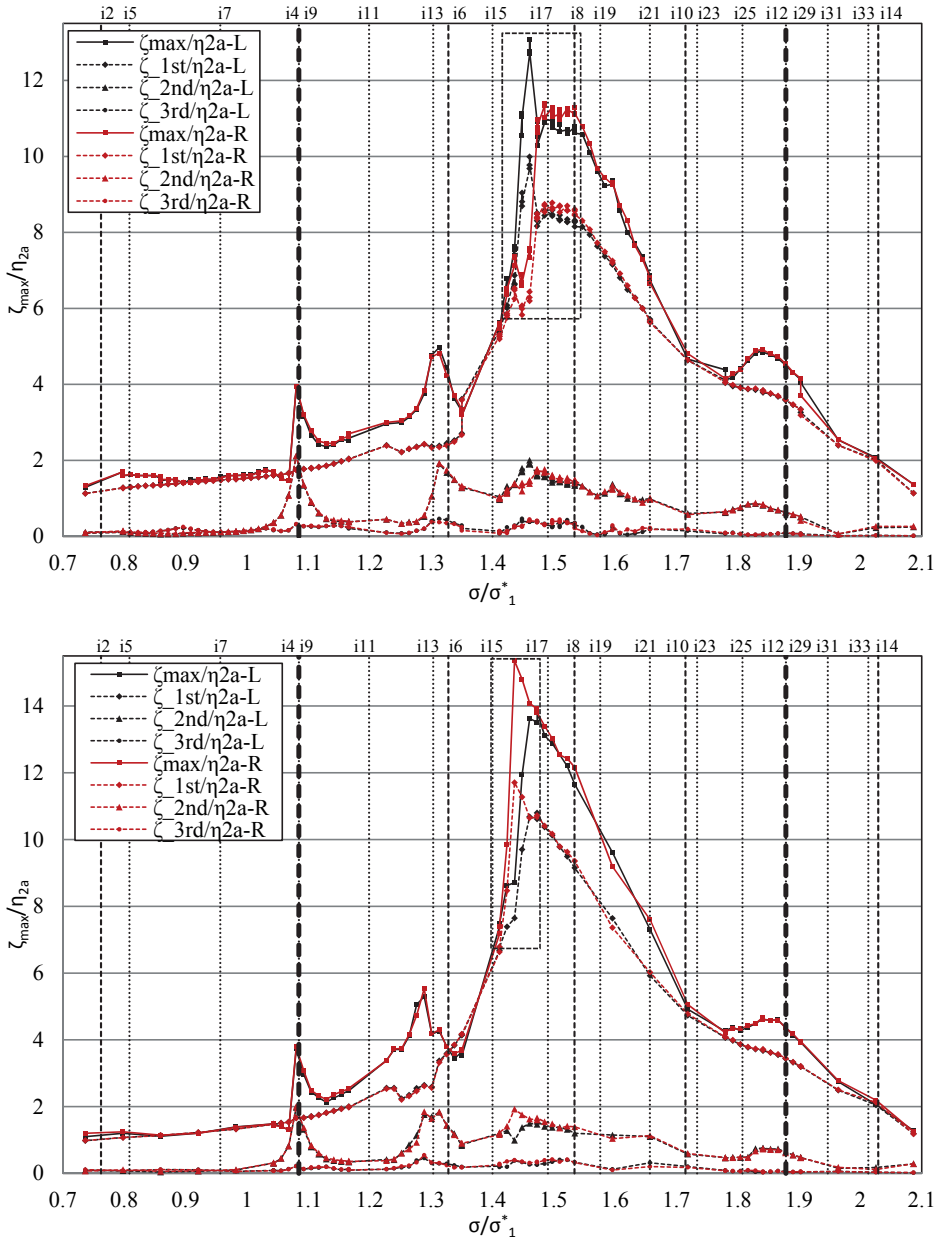

Figure 3-12. Top panel: $Sn = 0.8913$, bottom panel: $Sn = 0.9138$. Explanation is given in the caption of Figure 3-10. $h/l = 0.4, \varepsilon = 0.01$

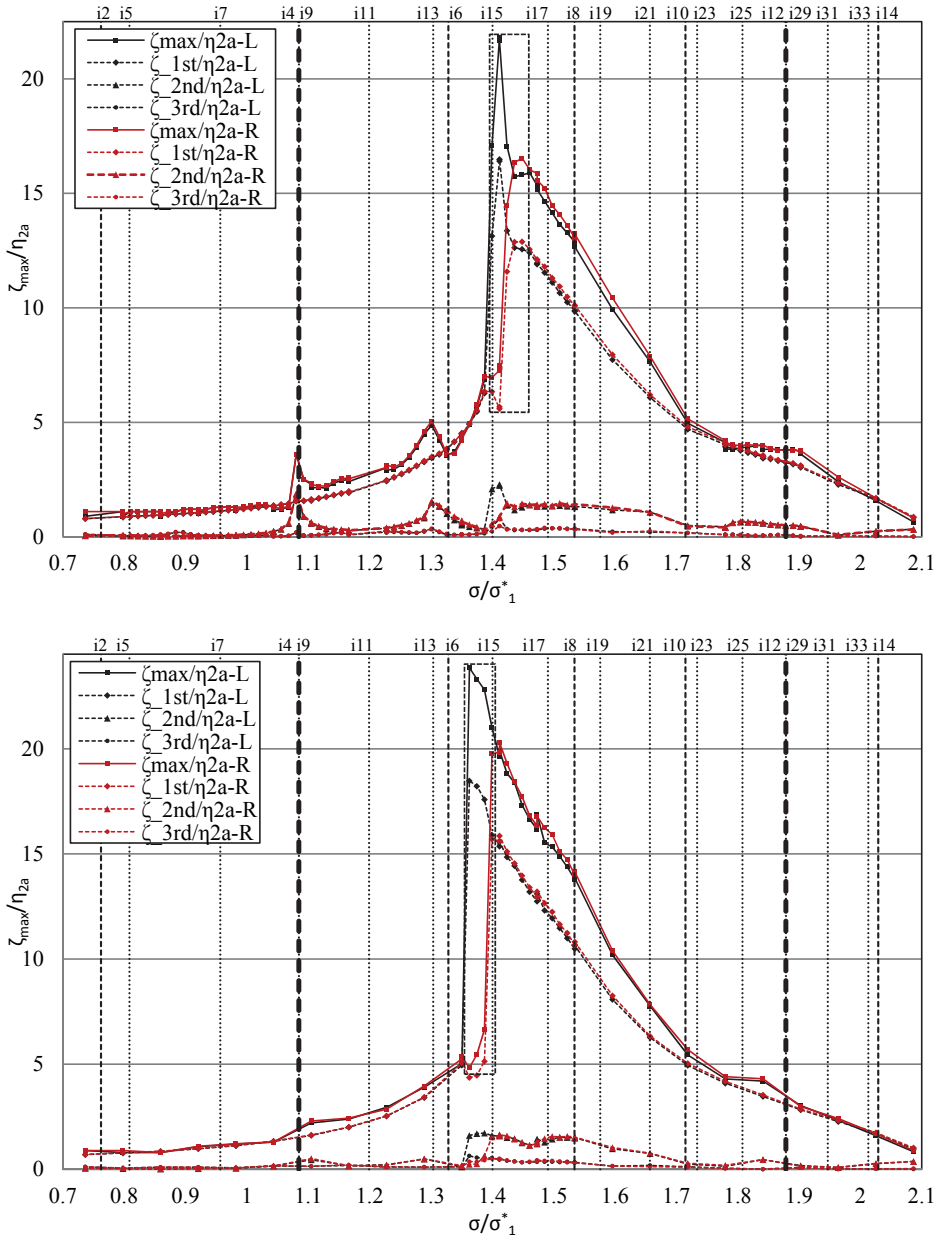

Figure 3-13. Top panel: $Sn = 0.9363$, bottom panel: $Sn = 0.9513$. The explanation is given in the caption of Figure 3-10. $h/l = 0.4$, $\varepsilon = 0.01$.

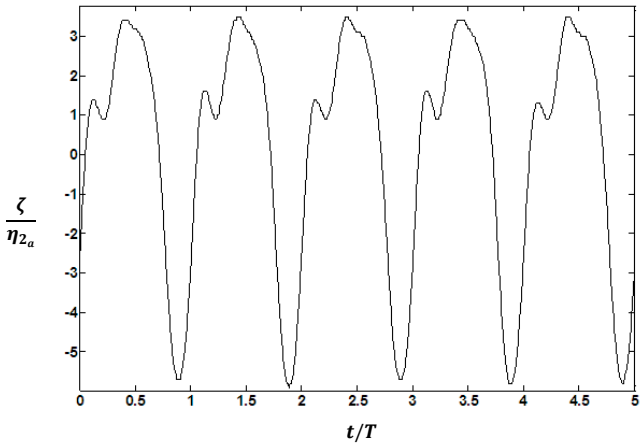

Figure 3-14. Wave elevations response with absolute minimum values larger than the absolute maximum values. Non-dimensional wave elevation ζ/η_{2_a} versus non-dimensional time t/T at 1 cm distance from the wall for $h/l = 0.4, \varepsilon = 0.01, Sn = 0.6825, \sigma/\sigma_1^* = 1.0679$. T: forced oscillation period.

3.2.3 Secondary resonance

The higher harmonics in the measured resonant wave elevations contribute up to 35% to the total response. The large amplification of the higher harmonics, i.e. 2σ, 3σ , at some certain frequencies is due to the amplification of higher modes of sloshing. This phenomenon which is called secondary resonance is mathematically possible if $n\sigma = \sigma_n^*$ in a *clean* tank excited with harmonic lateral motion of frequency σ (Faltinsen and Timokha 2009). The latter condition is necessary but not sufficient for secondary resonance. Large enough forcing amplitude is also needed to amplify higher harmonics that in return excite the higher modes of sloshing.

The schematic response curves representing the maximum steady-state wave elevation A versus forcing frequency σ/σ_1^* for $h/l > 0.3368$ ... due to lateral harmonic excitation are presented in Figure 3-15. The dashed line presents the results of linear sloshing theory that cannot predict secondary resonance of higher modes and gives a very large response at $\sigma/\sigma_1^* = 1$. The response of the linear system at $\sigma/\sigma_1^* = 1$ is infinite if no viscous damping is present. The solid bold lines display stable nonlinear steady-state regimes. A hysteresis effect at $\sigma/\sigma_1^* = 1$ is possible and denoted by the points T, T_1, T_2, and T_3. The points i_2 and i_3 mark the most important secondary resonance points occurring as the forcing frequency satisfies the conditions $2\sigma = \sigma_2^*$ (amplification of the second mode) or $3\sigma = \sigma_3^*$ (amplification of the third mode), respectively. A hysteresis effect at i_2 and i_3 is also possible when damping is small and the forcing amplitude is relatively large.

The present experimental results for the screen-equipped tank show the extension of the secondary resonance to frequencies satisfying the conditions $2\sigma = \sigma_{2k}^*$ and $3\sigma = \sigma_{2k+1}^*, k = 1,2,3, \ldots$. The occurrence of secondary resonance is indicated with vertical dashed and dotted lines, respectively named i_{2k} and i_{2k+1} in Figure 3-10 to Figure 3-13. i_{2k} and i_{2k+1} correspond to forcing frequencies where secondary resonance may occur due to $2\sigma = \sigma_{2k}^*$ (in non-dimensional form $i_{2k} = \frac{\sigma}{\sigma_1^*} = \frac{\sigma_{2k}^*}{2\sigma_1^*}$) and

$3\sigma = \sigma_{2k+1}^*$ (in non-dimensional form $i_{2k+1} = \frac{\sigma}{\sigma_1^*} = \frac{\sigma_{2k+1}^*}{3\sigma_1^*}$) , respectively. The non-dimensional forcing frequencies marked by i_{2k} and i_{2k+1} are listed in Table 3-3. Nondimensional frequencies corresponding to i_{16}, i_{18}, $i_{20}$and i_{22} are not listed since they are not in the tested forcing frequency range.

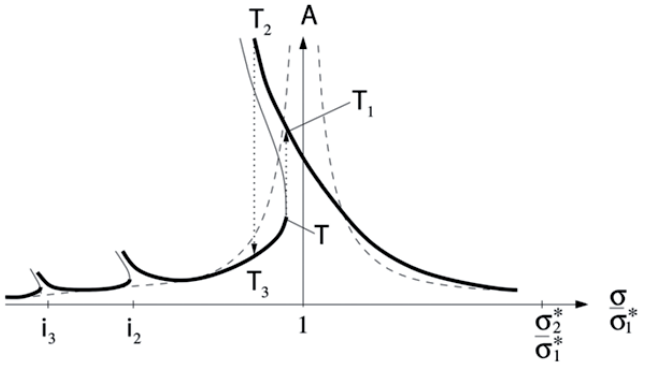

Figure 3-15. Soft-spring behavior and effect of secondary resonance for $h/l > 0.3368$.

Table 3-3. Non-dimensional frequencies corresponding to secondary resonance at $2\sigma = \sigma_{2k}^*$and $3\sigma = \sigma_{2k+1}^*$.

i_{2k}	i_2	i_4	i_6	i_8	i_{10}	i_{12}	i_{14}	i_{16}	i_{18}	i_{20}	i_{22}
$\frac{\sigma_{2k}^*}{2\sigma_1^*}$	0.762	1.085	1.328	1.534	1.715	1.879	2.029	-	-	-	-
i_{2k+1}	i_3	i_5	i_7	i_9	i_{11}	i_{13}	i_{15}	i_{17}	i_{19}	i_{21}	i_{23}
$\frac{\sigma_{2k+1}^*}{3\sigma_1^*}$	0.626	0.808	0.956	1.085	1.199	1.303	1.4	1.491	1.576	1.657	1.734

It should be noted that marking lines i_{2k} and i_{2k+1} are defined assuming that the presence of screen does not change both linear symmetric and anti-symmetric modes of sloshing. This assumption is exact for symmetric modes which do not cause a cross-flow through the screen mounted in the tank middle. Anti-symmetric modes and frequencies are affected by the screen because they cause a large horizontal cross flow at the tank middle. The natural odd modes and frequencies can be assumed preserved for low solidity ratios (roughly speaking $Sn \leq 0.5$). Faltinsen and Timokha (2011) showed that the screen reduces the odd natural frequencies in the clean tank to lower values. This means that the corresponding frequencies marked by i_{2k+1} vertical lines in Figure 3-10 to Figure 3-13 are larger than the real values especially for large solidity ratios.

Considering the results in Figure 3-10 to Figure 3-13, the behavior of the secondary resonance of the symmetric and anti-symmetric modes can be determined by following the curves of amplitudes of the second and third harmonics.

Starting with the secondary resonance of the symmetric modes, the amplitude of the second harmonic component shows peak responses at i_4, i_6 and i_8 for $Sn = 0.4725$ (top panel in Figure 3-10). The predicted frequencies by i_{2k} for the secondary resonance agree very well with the experimental results. Increasing the solidity ratio to $Sn = 0.6825$ amplifies the amplitude of the peak points and drifts them to emerge at lower

frequencies relative to the ones predicted by i_{2k} indicators (soft-spring effect) (bottom panel in Figure 3-10). For $Sn = 0.7863$ the peak points at i_4, i_6 and i_8 continue growing (see top panel in Figure 3-11). A clear steady-state jump can be seen for the peak points at i_4 and i_6. The peak point at i_8 is not very clear due to the lack of experimental information. A small drift in the frequency of the resonant peaks is present for this solidity ratio. The next solidity ratio $Sn = 0.8388$ does not change the amplitude of the second harmonics at i_4 and i_6 but the amplitude at i_8 is now increased (see bottom panel in Figure 3-11). The peak point at i_8 is more drifted to lower frequencies. The steady-state jump at i_4 and i_6 is clear for the maximum steady-state values but not for the amplitude of the second harmonic. Further increase of the solidity ratio removes the jump at i_6 and the peak resonance at i_8 (see Figures 2-26 and 2-27). For the largest solidity ratio, i.e. screen h with $Sn = 0.9513$ the information is not sufficient about i_4 and i_6.

Continuing with secondary resonance of the anti-symmetric modes, the amplitude of the third harmonic component shows peak responses at i_7, i_9 , i_{13}, i_{21} and i_{23}. The responses at these peak points are much lower than those of the second harmonic. The peak point at i_7 is only clear for $Sn = 0.4725$ and hardly recognizable for $Sn = 0.6825$. By further increase of the solidity ratio the latter peak response at i_7 disappears. For screen b a new peak is clearly seen at i_9 and other new peak points start growing at i_{13}, i_{21} and i_{23}. Clearer peaks are seen for $Sn = 0.7863$ and 0.8388. For $Sn \geq 0.8913$ almost no peak is present for the amplitude of the third harmonic.

In Figure 3-10 to Figure 3-13 i_4 and i_9 have almost the same frequency implying that a double amplification may be expected. This double amplification appears as two close narrow peaks for $Sn = 0.7866$. i_{12} and i_{29} mark almost a same forcing frequency but they do not cause a double amplification for any of the screens. However, the secondary resonance is less strong for frequencies around σ_3^* and not visible for very large solidity ratios.

In general the secondary resonance due to amplification of the symmetric modes, i.e. 2σ harmonics is clearer in Figure 3-10 to Figure 3-13. This is mainly because of the larger amplification of the second harmonic component relative to the third harmonic. Also transfer of energy to higher harmonics through free-surface nonlinearity requires large forcing amplitudes. Furthermore, the symmetric modes are not affected by the screen. This means that the same-order of forcing of symmetric and anti-symmetric modes should give a larger response of the symmetric modes. This is a novelty for the screen-equipped tanks relative to the corresponding clean tanks for which amplification of higher modes due to the secondary resonance requires, normally, larger forcing amplitude.

3.2.4 Unequal steady-state sloshing responses on the two sides of the screen

Two different steady-state responses on the opposite sides of the tank have been observed for almost all solidity ratios except for $Sn = 0.7863$. The latter phenomenon occurs at some of the resonant frequencies including frequencies associated with secondary resonance. The left snap shot from the experiments in Figure 3-16 shows two unequal responses on the opposite sides of the tank. The experimental conditions are $\varepsilon = 0.01, h/l = 0.4, Sn = 0.94, \sigma/\sigma_2^* = 0.9264$.

Frequencies corresponding to these unequal responses are marked by rectangles in Figure 3-10 to Figure 3-13. As mentioned above, for $Sn = 0.7863$ no unequal responses has been observed.

Table 3-4. Non-dimensional frequency ranges associated with unequal steady-state wave responses on the opposite sides of the tank.

Sn	0.4725	0.6825	0.8388	0.8913	0.9138
$(i = \frac{\sigma}{\sigma_1^*})$	$0.93 < i < 0.96$	$0.93 < i < 0.97$ $0.99 < i < 1.06$ $1.24 < i < 1.29$ $1.5 < i < 1.56$	$1.3 < i < 1.42$ $1.46 < i < 1.58$	$1.44 < i < 1.55$	$1.41 < i < 1.47$
Sn	0.9363	0.9513			
$(i = \frac{\sigma}{\sigma_1^*})$	$1.39 < i < 1.46$	$1.38 < i < 1.46$			

Repeating the tests for the largest solidity ratio $Sn = 0.9513$ at the frequency range mentioned in Table 3-4 confirms the repeatability of the unequal responses. Moreover, the unequal responses may switch between the compartments from one test to another. Different responses are more pronounced around $\sigma/\sigma_1^* = \sigma_2^*/\sigma_1^*$ for $Sn \geq 0.8913$ when cross-flow through the screen is reduced. This reduced cross flow also reduces the damping. For these conditions a soft-spring response behavior around $\sigma/\sigma_1^* = \sigma_1^{**}/\sigma_1^*$ accompanied with a jump is expected. For these conditions the compartments on the sides of high solidity ratio screens are at resonance. As shown in Figure **3-12** and Figure 3-13 for $0.8388 \leq Sn \leq 0.9513$ different responses occur for σ_1^{**}/σ_1^* when the soft-spring jump of the steady-state responses takes place. The exact frequency of the resonance, i.e. the forcing frequency associated with maximum response is damping dependent. Figure **3-12** and Figure 3-13 show that the frequency associated with the jump decreases with increasing the solidity ratio for $\sigma/\sigma_1^* = \sigma_1^{**}/\sigma_1^*$. The latter is because of the decreased damping.

The occurrence of unequal responses close to $\sigma/\sigma_1^* = \sigma_1^{**}/\sigma_1^*$ may be explained as follows. The main reason for unequal responses in the two compartments is that multiple solutions exist for the sloshing amplitudes in the two compartments. These solutions are indicated in the right panel of Figure 3-16 by black and red curves. The idea is that the damping in the two compartments on the two sides of the screen is slightly different. Therefore each side has a different solution. Here one of the solutions is shown in red. It is assumed that the solutions are very similar and they are only different near the maximum response. Figure 3-16 presents the possible solution branches for steady-state sloshing versus non-dimensional forcing frequency close to resonance due to harmonic excitation. The plot shows the so-called soft-spring behavior for sloshing in finite water depth (Faltinsen & Timokha, Sloshing, 2009). Part of the black curve between A_2 and the turning point T is unstable. The maximum steady-state wave responses occur when the forcing frequency decreases continuously from frequencies larger than the expected natural frequency ($\sigma/\sigma_0 = 1$) to frequencies smaller than that. Considering the black curve, for decreasing frequencies, the solution has a maximum at A_{max}(B_{max} on the red curve) and then it drops from A_2(B_2 on the red curve) to $A_3(B_3)$. In case of smaller damping, the solution near the maximum response possibly follows the red curve. The black curve can be considered as the solution for the compartment with slightly larger damping. The latter means by decreasing the forcing

frequency, the solution represented by the black curve jumps from A_2 to A_3 while the solution in the other compartment still oscillates with a larger amplitude B_0. Sloshing scenarios corresponding to amplitudes A_3 and B_0 are marked in the left panel of Figure 3-16. The reason for different damping content in the two compartments might be related to transient effects near the screen.

According to results presented in Figure 3-10 to Figure 3-13, unequal responses close to lowest sloshing natural frequency of a compartment, i.e. $\sigma = \sigma_1^{**}$, occurs when the solidity ratio is very large, i.e. $Sn \geq 0.9$, and therefore the screen causes lower inflow/outflow through its perforations leading to lower damping values. However, for larger forcing amplitudes, unequal responses around $\sigma/\sigma_1^* = \sigma_1^{**}/\sigma_1^*$ can occur for smaller solidity ratios. As it will be shown later, for $h/l = 0.35$ and $\varepsilon = 0.03$, unequal responses around $\sigma/\sigma_1^* = \sigma_1^{**}/\sigma_1^*$ occur for $Sn \geq 0.8414$.

The explanation given above for unequal responses due to multiple solutions for sloshing on the two sides of the screen might be extended to secondary resonance as well especially when the secondary resonance occurs near i_{2k} frequencies in Figure 3-10 to Figure 3-13. Around these frequencies, the higher even modes that do not cause cross flow through the screen may be excited. The latter means the screen-caused damping is small and the scenario explained in Figure 3-16 may be applicable to those cases where the unequal responses are seen near i_{2k} frequencies.

Unequal responses can also occur when the forcing amplitude is small and sloshing wave responses are large such that real steady-state waves do not appear. Due to this fact the experimental measurements show unequal responses on the two sides of the tank. For $h/l = 0.35$ and $\varepsilon = 0.03$ strong unsteady effects due to wave breaking and liquid-to-gas jet flows through the screen slats hitting the underlying free-surface, cause small differences in the wave elevations measured on the two sides of the screen. These kinds of unequal responses are not marked in Figure 3-10 to Figure 3-13.

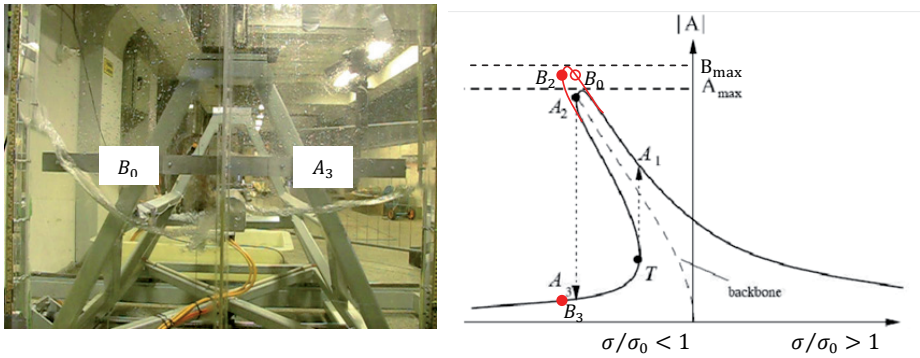

Figure 3-16. Two different curves of solutions for amplitude of steady-state sloshing in the compartments in the two sides of the tank. Left panel shows experimental results and the right panel shows corresponding theoretical solutions. Points marked by A and B are amplitudes of two different solutions. σ_0 is the natural frequency of a compartment. The larger response in the left compartment is corresponding to amplitude B_0 and the smaller response in the right compartment to amplitude A_3. Experiments were performed for $\varepsilon = 0.01, h/l = 0.4, Sn = 0.94, \sigma/\sigma_2^* = 0.9264$.

It is noted that the lowest maximum response in the tested frequency range belongs to $Sn = 0.7863$ which is smaller than $Sn = 0.8913$ that causes the lowest

maximum response for $\varepsilon = \frac{\eta_{2a}}{l} = 0.001$. This fact is predicted by the quasi-linear modal theory presented by Faltinsen and Timokha (2009) expressing that increasing the forcing amplitude reduces the solidity ratio associated with lowest maximum responses. However, the latter conclusion is based on a linear free-surface theory.

3.3 Water depth ratio h/l=0.35, forcing amplitude ε=0.03

$h/l = 0.35$ is close to the critical depth $(h/l)_{critical} = 0.3368\ldots$ where the change from soft- to hard-spring (if the depth is lowered from $h/l > (h/l)_{critical}$ to $h/l < (h/l)_{critical}$) or hard- to soft-spring (if the depth is raised from $h/l < (h/l)_{critical}$ to $h/l > (h/l)_{critical}$) response behavior for steady-state resonant sloshing in a clean tank occurs according to potential flow theory when the forcing amplitude is asymptotically small. However, increasing the forcing amplitude decreases the critical depth (Faltinsen and Timokha 2009). The latter definition of critical depth is a consequence of a non-linear multimodal theory with the lowest natural mode as the dominant mode and forcing frequency in the vicinity of the lowest natural frequency. Experiments performed by Colagrossi et al. (2003), for $h/l = 0.35, \varepsilon = 0.03$ show the non-linear amplification of sub-harmonics at the tested periods $T/T_1 = 1.03$ and 0.87. In the current study and in the presence of the screens no sub-harmonic amplification is observed for the above-mentioned forcing periods.

For $h/l = 0.35$ the solidity ratios are slightly different than for $h/l = 0.4$. The solidity ratios are 0.4729, 0.6871, 0.7900, 0.8414, 0.8929, 0.9143, 0.9357 and 0.9529.

3.3.1 Special free-surface effects

Increasing the forcing amplitude to $\varepsilon = 0.03$ makes the previously described free-surface phenomena for $\varepsilon = 0.01$ much more severe. Along with very strong wave breaking and run-up, overturning waves and formation of gas pockets at the left and right tank walls are observed. A representative snapshot of overturning waves is given in the left side of Figure 3-17. The right side of the figure demonstrates the formation of gas pockets that only occurs for $Sn = 0.4729$ and for $0.949 \leq \sigma/\sigma_1^* \leq 1.0121$.

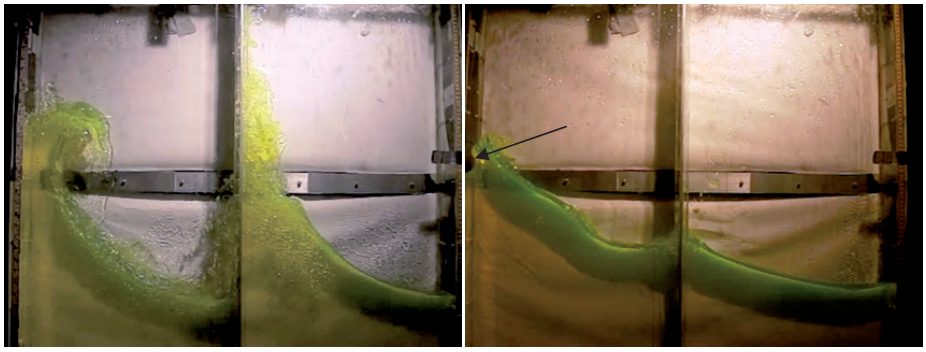

Figure 3-17. Left: overturning wave at the vertical wall, $Sn = 0.9143$, $\sigma/\sigma_1^* = 1.328$. Right: formation of gas pocket on the vertical wall, $Sn = 0.4729$, $\sigma/\sigma_1^* = 0.96$. Experimental condition: $h/l = 0.35, \eta_{2_a}/l = 0.03$.

Wave breaking can take place at the vertical wall as an overturning wave shown in Figure 3-17 (left). It can also happen in the screen region. This wave breaking hits the screen with jet flows spilling from the wave crest (Figure 3-18, Left). The wave may

break in the middle part of a compartment similar to the one shown in Figure 3-4. For the lowest solidity ratio, $Sn = 0.4729$, wave breaking occurs almost everywhere for all tested forcing frequencies. Increasing the solidity ratio moves the wave-breakings to the frequency range $\sigma_2^*/\sigma_1^* \leq \sigma/\sigma_1^* \leq \sigma_3^*/\sigma_1^*$. For instance, very large overturning waves are seen for $Sn \geq 0.8414$ when $\sigma/\sigma_1^* \approx \sigma_2^*/\sigma_1^*$. As a matter of fact, for $Sn \geq 0.8414$ the compartmentation of the main tank is reached and resonant sloshing takes place in both compartments for $\sigma/\sigma_1^* \approx \sigma_2^*/\sigma_1^*$ accompanied with large wave breakings and run-ups.

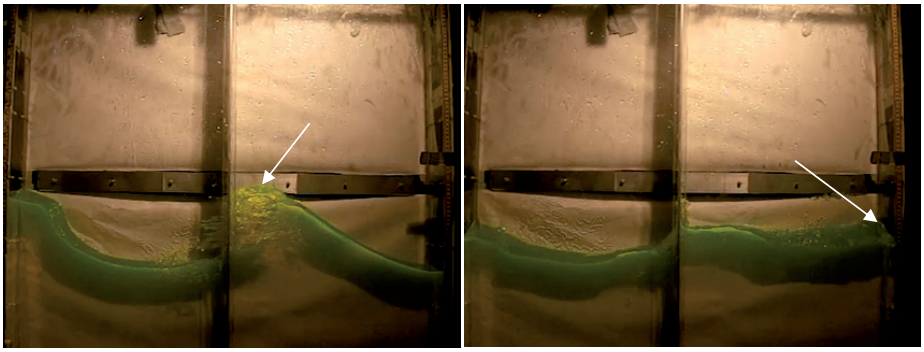

Figure 3-18. Left:Wave breaking in the screen zone with an spilling jet hitting the screen $Sn = 0.4729$, $\sigma/\sigma_1^* = 1.71$, Right: Three dimensional flow $Sn = 0.4729$, $\sigma/\sigma_1^* = 1.1134$. $h/l = 0.35$, $\eta_{2_a}/l = 0.03$.

Videos demonstrate oscillating flow motions perpendicular to the forcing direction. These three-dimensional flows are accompanied with local wave breakings at the vertical end walls and in the screen zone. An example of three-dimensional flow is illustrated on the right side of Figure **3-18**. The intersection line between the free-surface and the vertical end wall is clearly not perpendicular to the side walls. The 3D flows appear in specific frequency ranges for each solidity ratio. Table 3-5 lists the solidity ratios and corresponding frequency ranges associated with three-dimensional flow.

Table 3-5 shows that smaller solidity ratios cause wider frequency ranges associated with three-dimensional flow. For larger solidity ratios, the three-dimensionality is more focused around the primary resonant frequency of a compartment, i.e. σ_2^* where very large wave breakings and run-ups on the wall and screen are present.

For large solidity ratios, i.e. Sn ≥ 0.8414 (Figure 3-17, left panel), wave run-ups on the screen followed by separation of liquid fragments in the air above the free surface is present for $\varepsilon = 0.03, h/l = 0.35$. The same phenomena with much smaller intensity was shown in Figure **3-9** for $\varepsilon = 0.01, h/l = 0.4$. The large fragments of liquid eventually fall down and hit the underlying free surface. This creates large air-liquid mixture in the screen zone forced to go back and forth through the screen by flow oscillations. This complex three-dimensional flow composed of two phase's air and water which is also turbulent is a challenging problem for all the state of the art numerical methods. Cases accompanied with liquid or free-surface fragmentations are only experimentally discussed in this thesis using visual aids.

Table 3-5. Observed three-dimensional flow for $\varepsilon = 0.03, h/l = 0.35$.

Sn	Three-dimensional flow
0.4729	$1.7079 \leq \frac{\sigma}{\sigma_1^*} \leq 1.9609$, $1.3410 \leq \frac{\sigma}{\sigma_1^*} \leq 1.4043$, $1.025 \leq \frac{\sigma}{\sigma_1^*} \leq 0.139$
0.6871	$1.6447 \leq \frac{\sigma}{\sigma_1^*} \leq 1.9609$, $1.227 \leq \frac{\sigma}{\sigma_1^*} \leq 1.544$, $1.088 \leq \frac{\sigma}{\sigma_1^*} \leq 1.139$
0.7900	$1.531 \leq \frac{\sigma}{\sigma_1^*} \leq 1.885$, $1.353 \leq \frac{\sigma}{\sigma_1^*} \leq 1.43$
0.8414	$1.468 \leq \frac{\sigma}{\sigma_1^*} \leq 1.87$
0.8929	$1.328 \leq \frac{\sigma}{\sigma_1^*} \leq 1.860$
0.9143	$1.278 \leq \frac{\sigma}{\sigma_1^*} \leq 1.834$
0.9357	$1.253 \leq \frac{\sigma}{\sigma_1^*} \leq 1.822$
0.9529	$1.24 \leq \frac{\sigma}{\sigma_1^*} \leq 1.822$

3.3.2 Steady-state response curves of free-surface amplitude and secondary resonance

The steady-state responses were shown in Figure 3-19 to Figure 3-26 for solidity ratios: 0.4729, 0.6871, 0.7900, 0.8414, 0.8929, 0.9143, 0.9357 and 0.9529. The upper panels in Figure 3-19 to Figure 3-26 represent the non-dimensional standard deviation std/η_{2_a} of the corresponding maximum steady-state free-surface amplitudes shown in the lower panels. Large $std/\eta_{2_a}$are due to the specific free-surface phenomena described in the previous sub-section. In general the maximum steady-state wave elevations are expected to be almost equal to the summation of the amplitudes of the harmonics of the response. The results show that this is almost valid for all forcing frequencies with negligible corresponding std/η_{2_a}values. One should note that the maximum steady-state elevations shown in Figure 3-19 to Figure 3-26 are the average between maximum wave elevations for a certain number of forcing periods. This average value includes the effect of transient waves as well. The effect of transient waves is not seen in the curves plotted for the amplitude of the first three harmonics. Therefore one can see that the summation of the amplitudes of the harmonics of the forcing frequency is not so close to the average of the maximum wave elevations. 300 oscillations per each forcing periods has been used to ensure that steady-state waves appear for all forcing frequencies. Here after std/η_{2_a} values are presented whenever these values are comparable to the non-dimensional forcing amplitude, $\varepsilon = \eta_{2_a}/l$.

For the lower forcing amplitude, $\varepsilon = 0.01$, the peak points on the curve of amplitudes of the second and third harmonics of the wave elevations were used as a guidance for indicating the occurrence of secondary resonance. Generally, when secondary resonance occurs, the corresponding higher harmonics depict larger responses relative to those of the first harmonic.

Similar to the results presented for $\varepsilon = 0.01, \mathrm{h/l} = 0.4$, vertical dashed ($\mathrm{i_{2k}}$) and dotted ($\mathrm{i_{2k+1}}$) marking lines in Figure 3-19 to Figure 3-26 indicate frequencies that the secondary resonance of higher sloshing modes may occur due to the fact that, 2σ and 3σ is equal to an even and odd harmonic, respectively. Considering the secondary resonance of even modes, clear peaks can be detected at i_2 and i_4 for all solidity ratios.

Due to the soft-spring effect the latter peaks occur on the left side of i_2 and i_4. However, the lack of information does not reveal them for $Sn = 0.4729$. The amplitude of the second harmonics contains a peak between i_{11} and i_6 for solidity ratios up to 0.9143. The peak is closer to i_6 for $Sn = 0.4729$ and drifts towards i_{11} as the solidity ratio increases. Most of the resonant peaks seen for frequencies larger than i_4 do not match the i_{2k} lines for all of the screens. This shows that the secondary resonance in case of the larger forcing amplitude, $\varepsilon = 0.03$, is of a more complicated nature specially for frequencies larger than i_4. A reason is the complex flow behavior in the screen zone that can change the modes and their interaction with other modes.

Regarding the secondary resonance of odd modes, the amplitude of the third harmonic show peaks around i_7 and i_{11} for $Sn = 0.4729$. i_7 is very close to the first natural frequency and amplification of the response near i_7 might be related to the resonance of the first mode. For $Sn = 0.6871$, the amplitude of the third and second harmonics are almost the same. The third harmonic shows peak responses around i_5, i_7 and i_9. For $Sn = 0.7900$, the amplitude of the third harmonic at i_5, i_7 and i_9 drops to small values. For $Sn = 0.8414, 0.8929, 0.9143$ the amplitude of the third harmonic becomes very small. However, a small peak is still visible at i_{11} for $Sn = 0.8414$.

Different steady-state wave elevations at the opposite tank side are visible for $\varepsilon = 0.03$. The different responses marked by rectangles in the above figures (very small differences due to unsteady effects are ignored) occur at resonant areas. In fact, the presence of the screen causes the global sloshing to have multiple solutions. Because the geometrical dimensions of the tank and the screen are symmetric with respect to the tank middle, the differences should switch from one side of the tank to another by repeating the experiments. In other words, initial conditions determine which solution branch is followed in each side of the tank. The differences are seen for all solidity ratios. For $Sn =$ 0.8414, 0.8929, 0.9143, 0.9357 and 0.9529 the responses are clearly different for frequencies around σ_2^*/σ_1^*. For these screens, the compartmentation is almost reached and due to the soft-spring behavior the maximum response occurs on the left side of σ_2^*/σ_1^* on the horizontal axis. Here, the compartmentation means that the screen causes almost two isolated responses in the two sides of the tank equally divided by the screen. To account for this kind of multi-branching one should consider all the details of the complex flow at the screen zone. Liquid-to-gas jet flows, wave breaking, liquid fragmentation of the water on the screen and wave breaking on the screen are present for the current forcing amplitude. Numerical based methods such as CFD might be able to predict multiple solutions if they are forced to capture sufficient flow details in the screen zone.

For $\varepsilon = 0.03, h/l = 0.35$ the lowest maximum response in the tested frequency range belongs to $Sn = 0.7900$. However, the highest maximum response for $Sn =$ 0.6871 is only 5% larger than that of $Sn = 0.7900$. The latter screen with $Sn =$ 0.7900 caused the minimum response for $\varepsilon = 0.01, h/l = 0.4$. For $\varepsilon = 0.001, h/l =$ 0.4 the minimum response occurred for a larger solidity ratio, that is $Sn = 0.8913$. Therefore one expects a solidity ratio lower than 0.79 associated with the lowest minimum response for $\varepsilon = 0.03, h/l = 0.35$. Unfortunately there is no screen with $0.6871 < Sn < 0.7900$ among the tested solidity ratios to support the above-mentioned expectation.

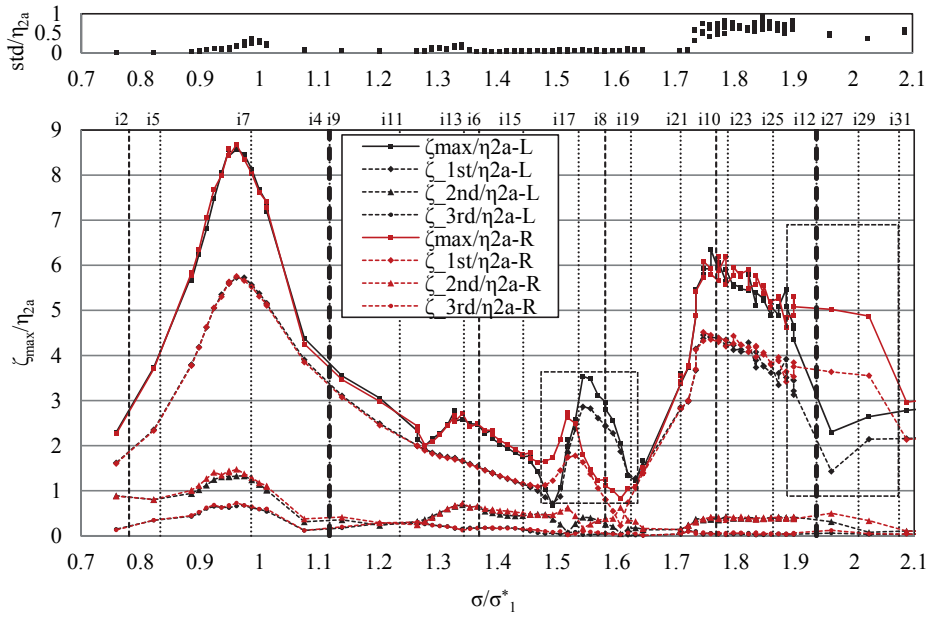

Figure 3-19. Top panel: non-dimensional standard deviation std/η_{2_a} of the maximum steady-state response ζ_{max}/η_{2_a} versus σ/σ_1^*. Bottom panel: Non-dimensional maximum steady-state response ζ_{max}/η_{2_a} and the amplitude of the first three Fourier harmonics of the response ζ_{1st}/η_{2_a}, ζ_{2nd}/η_{2_a}, ζ_{3rd}/η_{2_a} versus σ/σ_1^*. $h/l = 0.35$, $\varepsilon = 0.03$, $Sn = 0.4729$. The letters 'L', for Left, and 'R', for Right, are used to distinguish the results measured on the two sides of the tank. The vertical dashed i_{2k} and dotted i_{2k+1} lines mark the frequencies where secondary resonance of higher modes may occur. The rectangles mark regions with different results on the left and right tank sides.

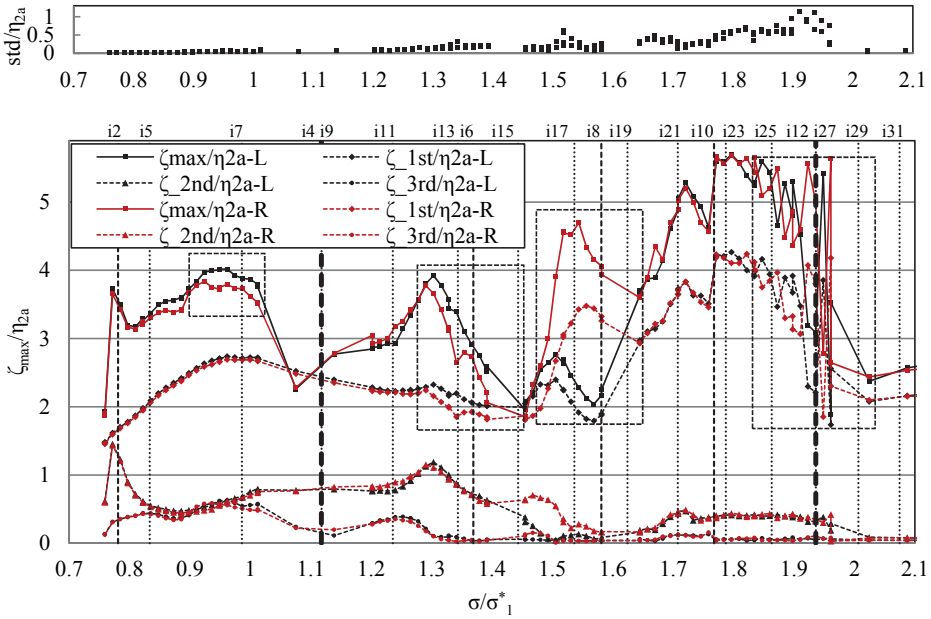

Figure 3-20. $Sn = 0.6871$, explanation is given in the caption of Figure 3-19. $h/l = 0.35$, $\varepsilon = 0.03$.

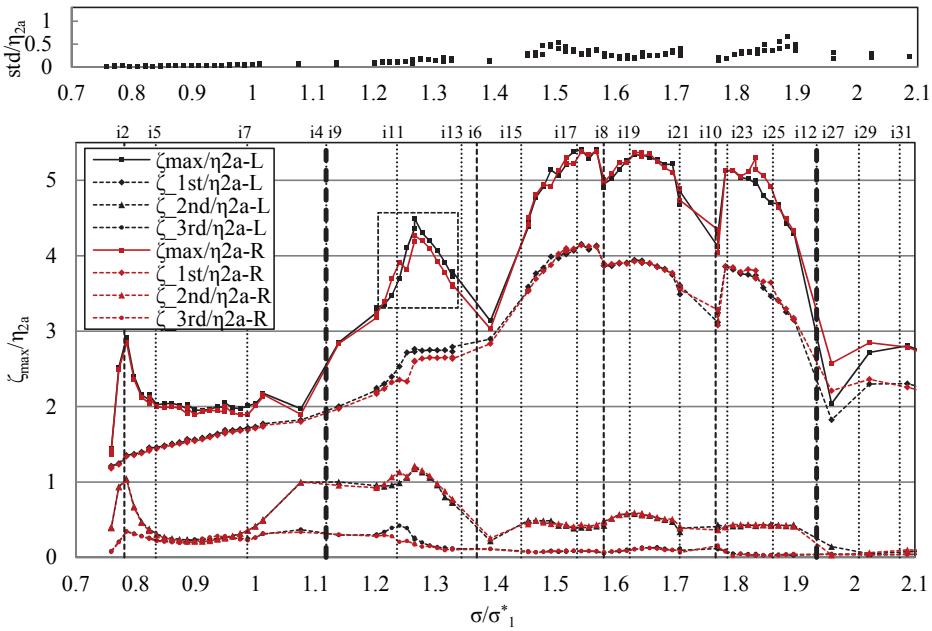

Figure 3-21. $Sn = 0.7900$, explanation is given in the caption of Figure 3-19. $h/l = 0.35$, $\varepsilon = 0.03$.

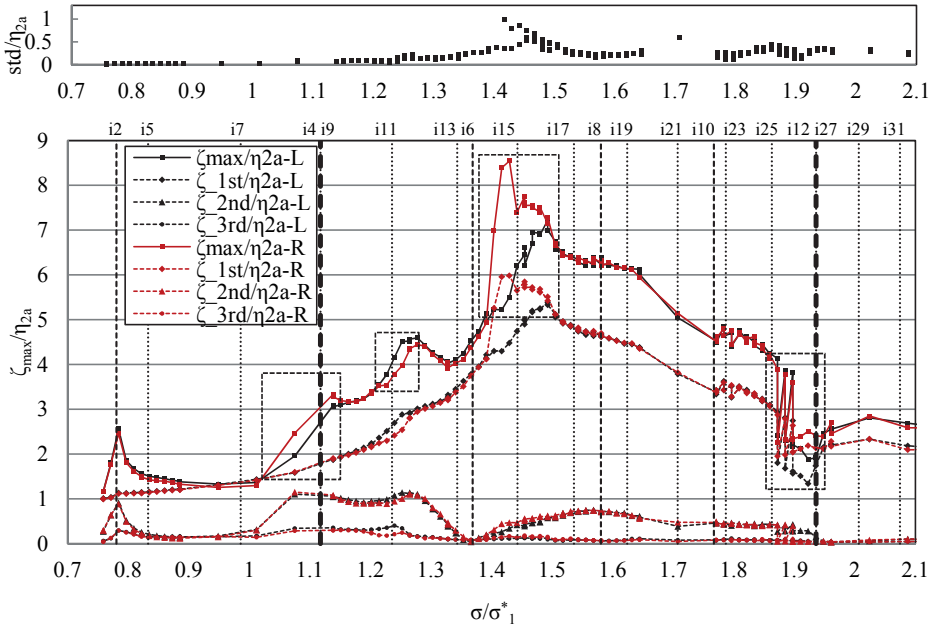

Figure 3-22. $Sn = 0.8414$, explanation is given in the caption of Figure 3-19. $h/l = 0.35$, $\varepsilon = 0.03$.

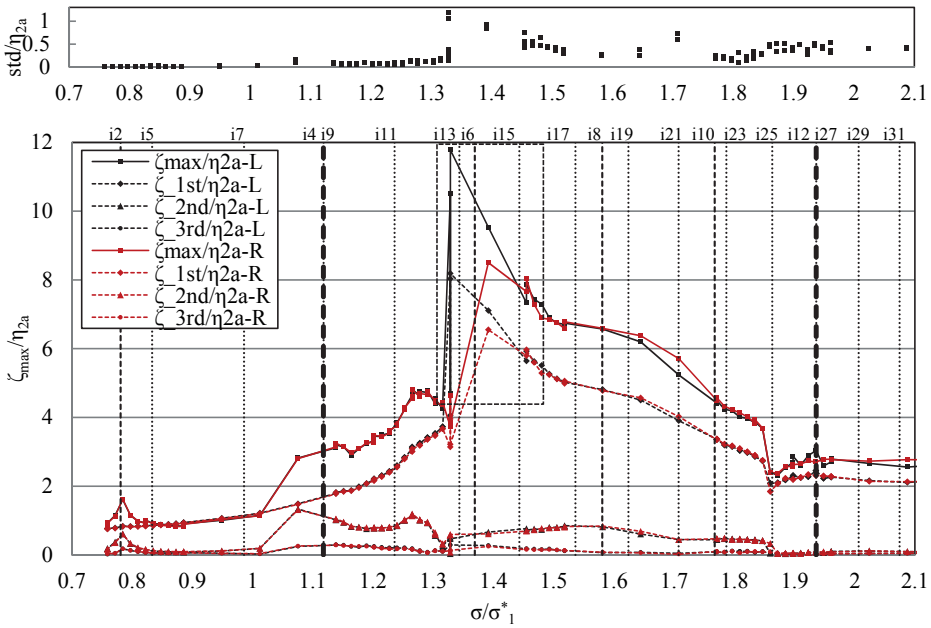

Figure 3-23. $Sn = 0.8929$, explanation is given in the caption of Figure 3-19. $h/l = 0.35$, $\varepsilon = 0.03$.

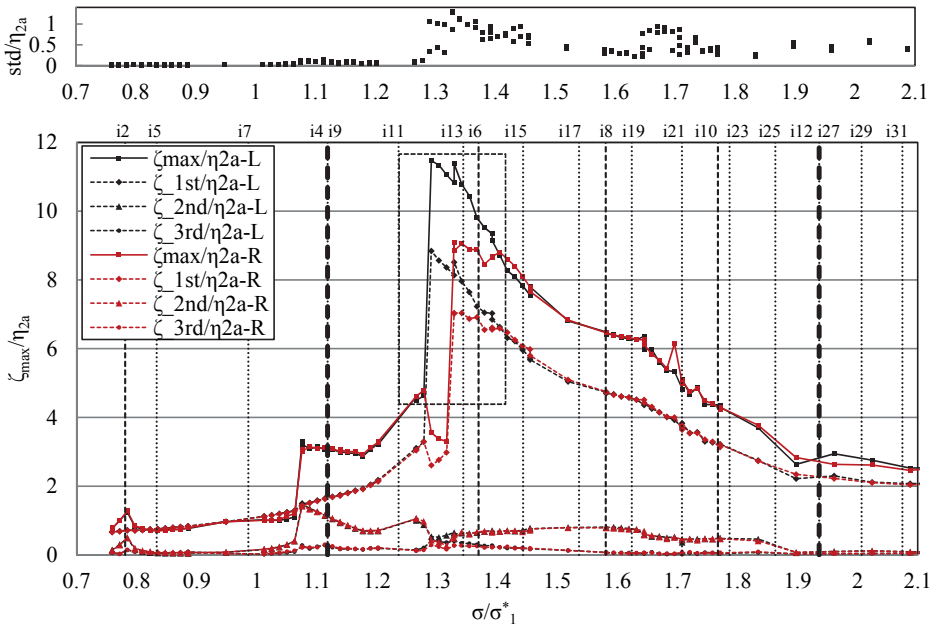

Figure 3-24. $Sn = 0.9143$, explanation is given in the caption of Figure 3-19. $h/l = 0.35$, $\varepsilon = 0.03$.

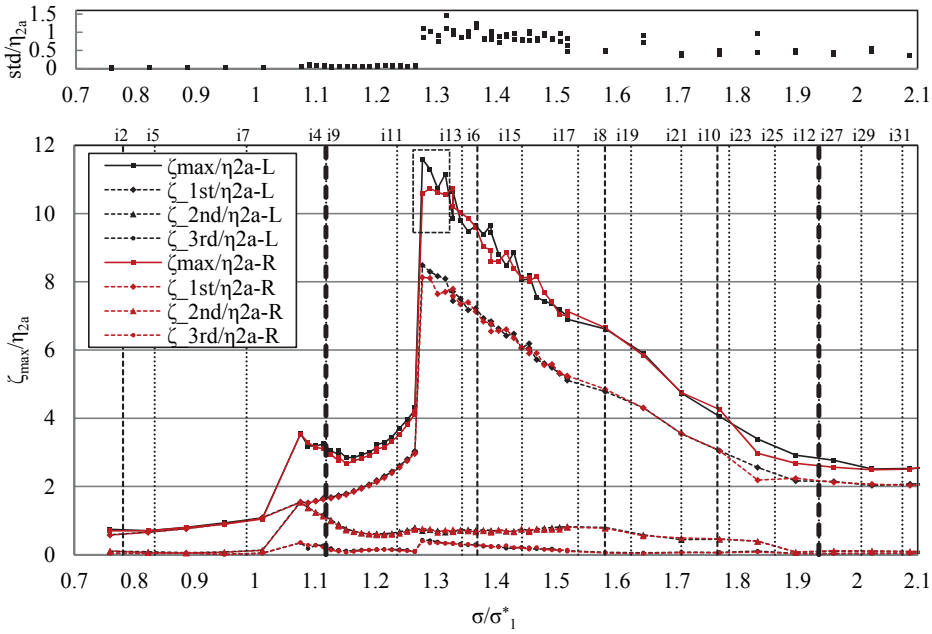

Figure 3-25. $Sn = 0.9357$, **explanation is given in the caption of Figure 3-19.** $h/l = 0.35,\ \varepsilon = 0.03$.

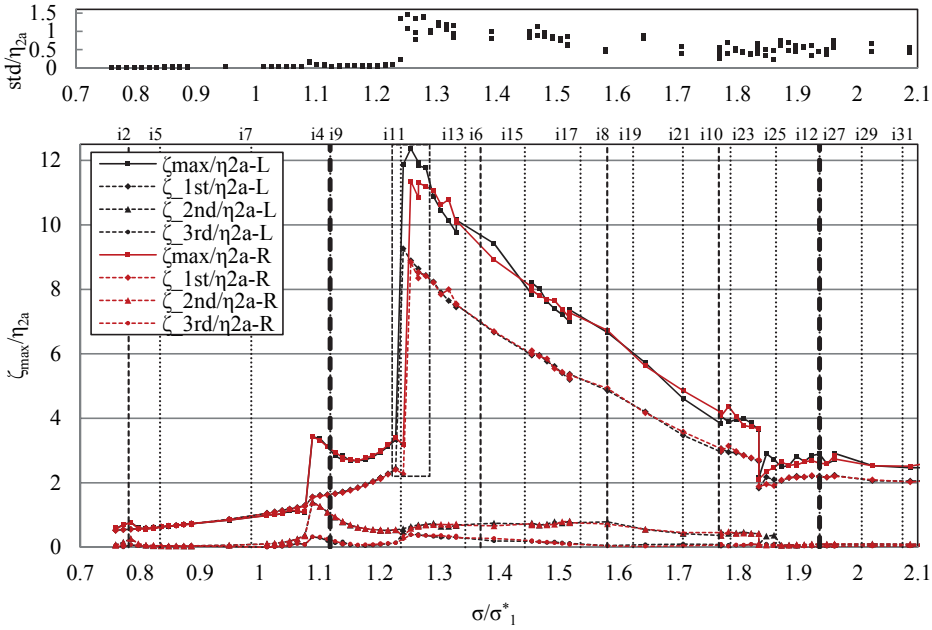

Figure 3-26. $Sn = 0.9529$, **explanation is given in the caption of Figure 3-19.** $h/l = 0.35,\ \varepsilon = 0.03$.

3.4 Closure

Steady-state sloshing wave responses in a screen-equipped tank in finite depths were experimentally investigated. When the water depth-to-tank length ratio $h/l = 0.4$, the smallest non-dimensional forcing amplitude $\varepsilon = 0.001$ causes sloshing wave responses with a linear character for almost all tested screens and forcing frequencies. As a result, a linear free-surface based mathematical model that incorporates the effect of the screen must be able to provide results comparable with experiments (Faltinsen et al., 2011c). Running the tests for two sets of screens with different geometrical details but with almost the same solidity ratios reveals that the results are much more dependent on the solidity ratio rather than the geometrical details of the screens. Experimental results in the same depth but with a ten times larger forcing amplitude, $\varepsilon = 0.01$, show that the nonlinear free-surface effects become important at primary resonant frequencies. In addition to that, is the strong amplification of the higher harmonics of the forcing frequency due to the secondary resonance of sloshing modes. Steady-state jump of the wave responses at the primary resonant clean-tank sloshing frequency (lowest solidity ratio) and at the primary resonant sloshing in a compartment (very large solidity ratios) are examples of non-linear free-surface effects occurring for $\varepsilon = 0.01$. Moreover, larger forcing amplitude causes special free-surface effects such as wave breaking, run-up on the screen and the wall and liquid-to-gas jet flows caused by the flow motion through the screen openings in the middle of the tank which are impacting the underlying free-surface on the other side of the screen. These effects are seen for very large solidity ratios ($Sn > 0.9$). Large solidity ratio screens highly change the clean-tank sloshing such that no resonant response appears at the lowest natural clean-tank sloshing frequency σ_1^* for solidity ratios larger than 0.9. In fact a high solidity ratio screen transforms the sloshing in the clean tank into isolated sloshing in two compartments on the two sides of the screen. As a result the resonant frequencies and modes change drastically (compartmentation). Which solidity ratio isolates the sloshing in the two compartments is a function of forcing amplitude for a given depth, i.e. for larger forcing amplitudes the compartmentation occurs for a smaller solidity ratio. Performing the experiments in a depth close to the nominal critical depth $h/l = 0.35$ and for $\varepsilon = 0.03$ amplified the non-linear effects accompanied with violent free-surface effects such as formation of very thick run-ups on the vertical walls for $Sn \geq 0.9$. In addition the compartmentation occurs for a smaller solidity ratio due to the larger forcing amplitude.

4 Analysis of experimental results in shallow water depth

Sloshing in shallow-intermediate water depth is accompanied with stronger nonlinear free-surface effects for a same level of forcing motion relative to finite water depth. Very small amplitude sloshing with $Sn < 0.5$ in shallow water is of interest for TLD applications. Testing larger solidity ratios can provide more information about the transition of sloshing in shallow water to sloshing in intermediate depths due to increase in the solidity ratio. On the other hand, larger amplitude sloshing in shallow depths can impose severe slamming pressures on the vertical tank walls. Large solidity ratios strongly affect the large amplitude sloshing as discussed in the following text. The analysis starts with small forcing amplitude $\varepsilon = 0.001$.

4.1 Water depth ratio h/l=0.12, forcing amplitude ratio ε=0.01

For $h/l = 0.12$ the solidity ratios are 0.4725, 0.6875, 0.7875, 0.8375, 0.8875, 0.9125 and 0.9375.

To begin, video recordings are examined for special free-surface effects such as wave breaking, three-dimensional waves and free-surface fragmentations. In addition, the time series of the measured wave responses are studied for special amplification of nonlinear effects such as sub-harmonic amplifications of the forcing motion. Frequencies associated with special free-surface effects and nonlinear amplifications are documented. This information is useful for assessing and developing theoretical and numerical methods when assumptions related to free-surface conditions should be taken.

4.1.1 Special free-surface effects

For $Sn = 0.4725$, the available recorded videos show small wave breaking appearing for $2.4330 \leq \sigma/\sigma_1^* \leq 2.5273$. The wave breaking becomes larger as the frequency increases in the above-mentioned range. In addition, three-dimensional waves are seen at $\sigma/\sigma_1^* = 2.527$. A clear oscillating motion relevant for excitation of the lowest sloshing mode in the lateral direction, i.e. perpendicular to direction of forcing, cannot be recognized for this frequency. Videos are not available for $\sigma/\sigma_1^* > 2.5273$ and the author cannot accurately predict how far in the frequency range the wave breaking and three-dimensional flows are present. However, the non-dimensional standard-deviation of the maximum steady-state wave elevations is clearly larger for $2.45 \leq \sigma/\sigma_1^* \leq 2.71$ among other frequencies which might be due to the presence of transient effects such as wave breaking and irregular three-dimensional motions. This frequency range contains the third natural frequency $\sigma/\sigma_1^* = 2.5999$ where resonant sloshing is also expected. Figure 4-1 demonstrates a typical wave breaking seen at frequency $\sigma/\sigma_1^* = 2.5273$. Wave run-ups are not present for this screen neither on the wall nor on the screen.

The time series of the measured data show strong amplification of many super harmonics for $Sn = 0.4725$ in the resonant area around the first natural frequency. This is a property of shallow water sloshing at resonance due to secondary reason. One

reason is associated with fact that the nth natural frequency σ_n^* is almost equal to $n\sigma_1^*$ when $h/l \to 0$. In addition is the amplification of "extra" harmonics which are sub and super-harmonics of the forcing frequency. These "extra" harmonics are seen for $2.4708 \leq \sigma/\sigma_1^* \leq 2.5273$ and $2.6028 \leq \sigma/\sigma_1^* \leq 2.7348$. For the last two tested forcing frequencies in the above-mentioned range, i.e. $\sigma/\sigma_1^* = 2.716$ and 2.7348, the frequencies of the extra sub- and super harmonics of the forcing frequency are equal to $k\sigma$ where k =1/3, 2/3, 4/3, 5/3. Figure 4-2 shows the time history of wave elevations and its frequency content for 10 periods of forcing frequency $\sigma/\sigma_1^* = 2.7348$. The figure shows that due to strong amplification of sub-harmonics, the two adjacent maximum elevations are three forcing periods apart in the time history.

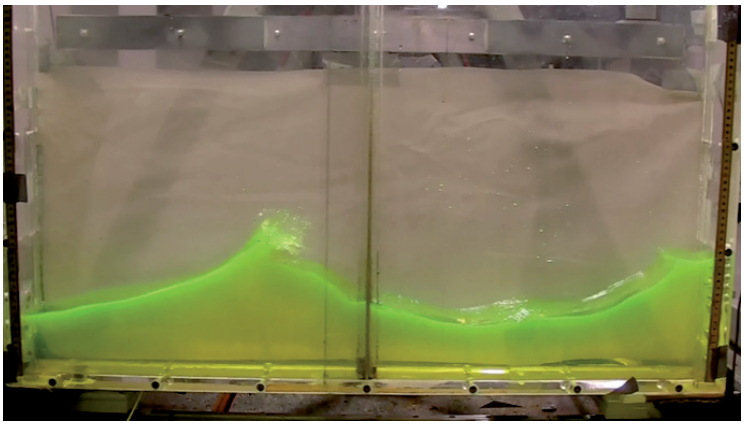

Figure 4-1. Typical wave breaking at $\frac{\sigma}{\sigma_1^*} = 2.5273$. $\frac{h}{l} = 0.12, \varepsilon = 0.01, Sn = 0.4725$.

For forcing frequencies in the range $2.6405 \leq \sigma/\sigma_1^* < 2.6971$ "extra" harmonics cause waves with a steady beating period. This effect is also called modulation. Figure 4-3 shows the time history of wave elevations and the frequency content for frequency $\sigma/\sigma_1^* = 2.6971$. The modulation can be seen in the wave elevations shown in the top panel of Figure 4-3. The Fast Fourier Transform analysis of the time history presented in the lower panel of Figure 4-3 shows amplification of a new set of "extra" harmonics that contains more frequency components than the case shown in Figure 4-2. A group of the frequencies in the new set of "extra" harmonics are numbered in the bottom panel of Figure 4-3. These new excited frequencies, numbered from 1 to 8 consist of four couples. Each of these couples can cause a steady beating effect in the time history of the wave elevations. Combination of the beating responses and the response due to the forcing frequency gives the complex time history shown in the upper panel of Figure 4-3. How energy transfers from the forcing motion to these extra harmonics is of a nonlinear nature. How nonlinearity works has been tried to be understood by Ezersky et al. (2009) who experimentally observed steady-state modulated waves in a very long wave flume equipped with a piston wavemaker at one end and closed with a vertical wall at the other end of the flume that reflects the waves and causes standing waves after a sufficient period of time. In their case h/l is equal to 0.0103 which is an extreme shallow depth. For this depth excitation of one mode can lead to excitation of many modes. They have observed a same kind of modulation due to amplification of extra harmonics. They qualitatively relate the occurrence of extra

harmonics to the energy leakage to lower frequencies by a three-wave resonance interpretation. As they say "in a 3-oscillator system with quadratic nonlinearity, lower frequencies may effectively get energy from the high frequency oscillator"

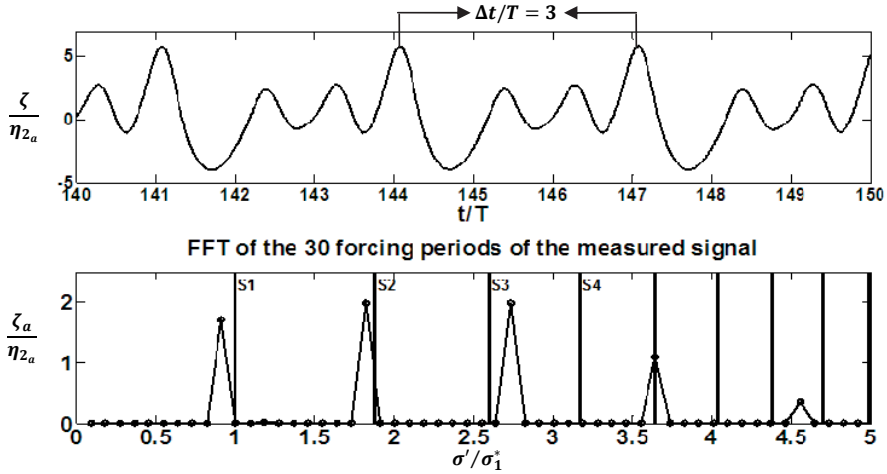

Figure 4-2. Amplification of sub-harmonics of the forcing frequency. top panel: Non-dimensional wave elevation at the vertical wall, Bottom panel: Non-dimensional amplitude of the frequency components in frequency domain. The vertical lines, $S_1, S_2, \ldots$ in the lower panel identify the linear natural sloshing frequencies in the clean tank. σ' is the frequency content of the measured signal calculated by FFT. $h/l = 0.12, \varepsilon = 0.01, Sn = 0.4725, \sigma/\sigma_1^* = 2.7348$.

Table 4-1. Extra harmonics' multipliers for $2.6405 \leq \sigma/\sigma_1^* \leq 2.6971$. Frequencies corresponding to K_1 to K_8 are numbered in Figure 4-3. k_i is the ratio between the frequency of the corresponding extra harmonic and the forcing frequency.

σ/σ_1^*	k_1	k_2	k_3	k_4	k_5	k_6	k_7	k_8
2.6405	0.31	0.39	-	0.69	1.31	1.39	1.61	1.69
2.6594	0.31	0.38	0.62	0.69	1.31	1.38	1.62	1.69
2.6781	0.32	0.37	0.63	0.68	1.32	1.37	1.63	1.68
2.6971	0.32	0.36	0.64	0.68	1.32	1.36	1.64	1.68

The new set of "extra" harmonics contains frequencies with special multiples of the forcing frequency that cannot be identified by fractions constructed by dividing two integer numbers. For instance for frequency $\sigma/\sigma_1^* = 2.7348$, the case with no wave modulation, the multipliers were $k = i/m$ where $i = 1,2,4,5$ and $m = 3$ resulting in $k = 0.3333, 0.6667, 1.3333, 1.6667$. However, for the new harmonics no clear integer i and m can be found. To clarify this, the extra harmonics marked by numbers 1,2,…,8 in the bottom panel of Figure 4-3 and the ratio between their corresponding frequency and frequency of the main harmonic, i.e. k, is calculated. The multipliers marked in Figure 4-3 are also recalculated for other forcing frequencies associated with presence of new set of extra harmonics and presented in Table 4-1. The k values are almost fixed for all the listed forcing frequencies in the table. The extra sub harmonics $k_1\sigma, \ldots k_4\sigma$ and their corresponding $k_5\sigma, \ldots k_8\sigma$ super harmonics, respectively, are one forcing frequency apart, i.e. $k_4 - k_1 = 1$, $k_5 - k_2 = 1$. This fact is well-known in fluid mechanics that a sum or a difference frequency of two excited frequencies may also be

excited. In other words the sub-harmonics are the reason for presence of the super-harmonics and vice versa.

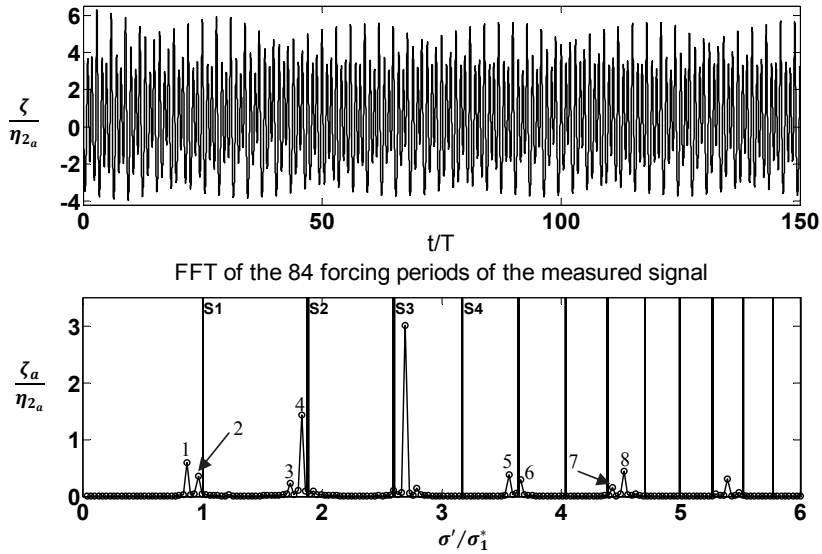

Figure 4-3. Modulated waves. Explanation is given in the caption of Figure 4-2. $h/l = 0.12, \varepsilon = 0.01$, $Sn = 0.4725$, $\sigma/\sigma_1^* = 2.6971$.

For frequencies $2.4708 \leq \sigma/\sigma_1^* \leq 2.5273$ another set of extra harmonics are present with k =0.7619, 1.2381 and 1.7619. The video recordings show wave breakings for the above frequency range.

Increasing the solidity ratio to $Sn = 0.6875$, reduces the intensity of the wave breaking. The wave breakings occur for frequencies around σ_3^*, i.e. for $2.4708 \leq \sigma/\sigma_1^* \leq 2.5651$, and also in a new frequency range $2.3576 \leq \sigma/\sigma_1^* \leq 2.4142$. This new frequency range is accompanied with the secondary resonance of the 8th mode of sloshing that is a reason for occurrence of steep wave profiles. Three-dimensional waves are not visible in the available videos for the current screen.

"Extra" harmonics of the forcing frequency and modulated waves are present in a wider frequency range for $Sn = 0.6875$, that is $2.5273 \leq \sigma/\sigma_1^* \leq 2.7348$. Figure 4-4 presents the wave responses at frequency $\sigma/\sigma_1^* = 2.716$ for $Sn = 0.4725$ and $Sn = 0.6875$. The figure shows occurrence of modulation only for $Sn = 0.6875$. Due to this modulation, larger maximum wave elevations occur for $Sn = 0.6875$ as shown in Figure 4-4. This fact shows the effect of solidity ratio on the resonant frequencies and modes that can cause new nonlinear interaction between the forcing frequency, its harmonics and the new sloshing modes. It is noted that only the odd modes and frequencies (σ_{2n-1}^*, $n = 1,2,3, ...$) are modified by the screen. The bottom part of Figure 4-4 compares the frequency content of the measured signals for $Sn = 0.6875$ and $Sn = 0.4725$. The presence of extra harmonics for $Sn = 0.6875$ describes the beating behavior of the measured signals. The mechanism of modulation is qualitatively described for $Sn = 0.4725$. For $Sn = 0.6875$ the modulated waves appear for more frequencies than those for $Sn = 0.4725$.

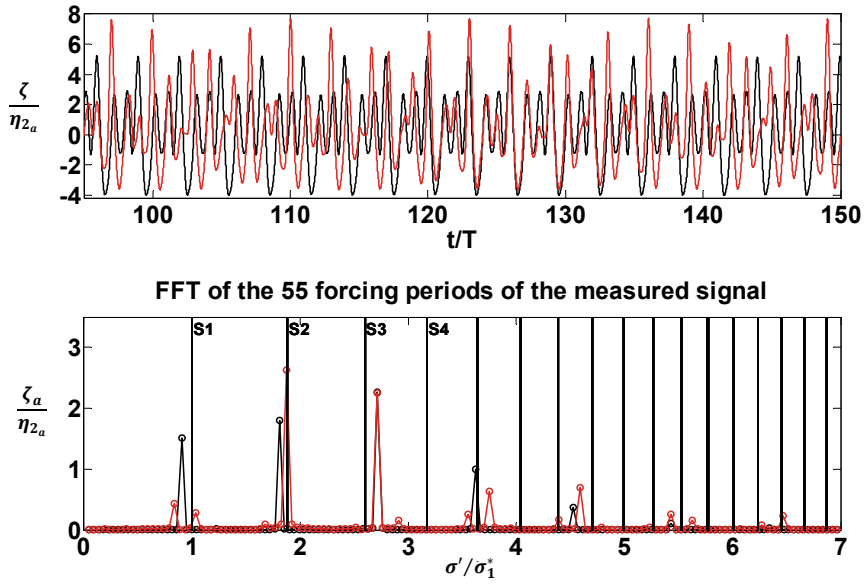

Figure 4-4. Extra harmonic amplification for $h/l = 0.12, \varepsilon = 0.01$, $\sigma/\sigma_1^* = 2.716$, red line: Sn=0.6875, black line: Sn=0.4725. Top panel: Non-dimensional wave elevation ζ/η_{2_a} versus time divided by forcing period T. Bottom panel: Non-dimensional amplitude ζ_a/η_{2_a} of frequency components of the wave elevation. σ' is the frequency content of the measured signal calculated by FFT.

Looking into the time history of the wave elevations an interesting phenomenon happens for $Sn = 0.6875$ and $\sigma/\sigma_1^* = 1.9992$ shown in Figure 4-5. Many forcing periods are needed to reach a steady-state wave regime. Taking the Fast Fourier Transform of the time series in two time windows for $30 \leq t/T \leq 70$, i.e. before reaching steady-state responses (Figure 4-5, left window on the top panel) and then for $110 \leq t/T \leq 140$, i.e. after reaching steady-state responses (Figure 4-5, right window on the top panel), reveals that only the amplitude of the second harmonic is increased by increasing the number of forcing periods while the amplitude of the main harmonic stays almost unchanged. In fact this amplification is connected to the secondary resonance of mode number 6. Due to this amplification the response becomes two times larger during almost 150 forcing periods as seen in the top panel of Figure 4-5. This particular case can be a good example to check the ability of a CFD code in capturing the free-surface nonlinearity which is interconnected with the amount of damping caused by the screen.

By increasing the solidity ratio to $Sn = 0.7875$, small wave breakings occur in a narrow frequency range $2.3387 \leq \sigma/\sigma_1^* \leq 2.3765$. As shown in Figure 4-6, the free surface becomes steep with a very small spilling breaker marked by a circle. The available videos also show developing three-dimensional flow in the tank for $\sigma/\sigma_1^* = 2.5273$. Considering Figure 4-5, a similar kind of response taking large number of oscillations to get steady-state is also present for $Sn = 0.7875$ at a slightly smaller forcing frequency $\sigma/\sigma_1^* = 1.9804$. In addition to the mentioned special free-surface effects, the "extra" harmonic amplification of the forcing frequency is present for

$Sn = 0.7875$ and $2.5651 \leq \sigma/\sigma_1^* \leq 2.7348$ with very small amplitudes relative to those ones measured for lower solidity ratios.

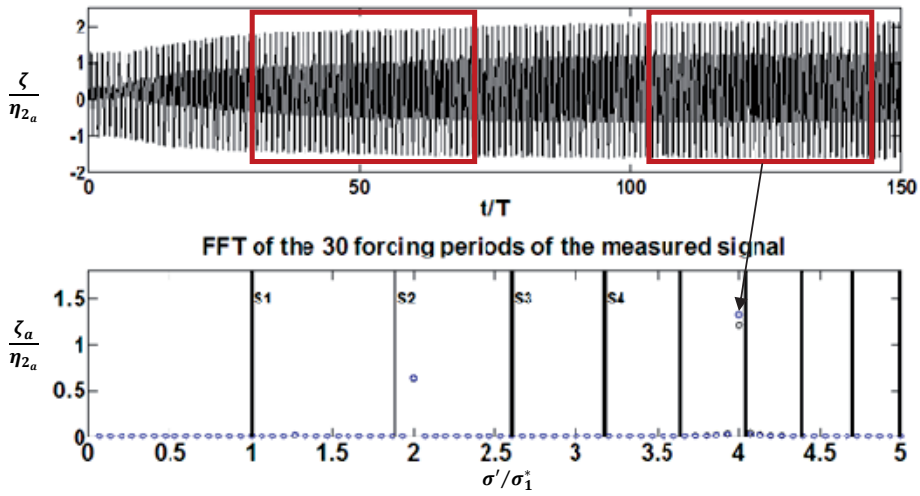

Figure 4-5. $h/l = 0.12, \varepsilon = 0.01, Sn = 0.6875, \sigma/\sigma_1^* = 1.9992$. Top panel: Non-dimensional wave elevation at the vertical wall versus time divided by forcing period T. Bottom panel: Non-dimensional amplitude of the frequency components in frequency domain for $30 \leq t/T \leq 70$ (Black) and $110 \leq t/T \leq 140$ (Blue). σ' is the frequency content of the measured signal calculated by FFT.

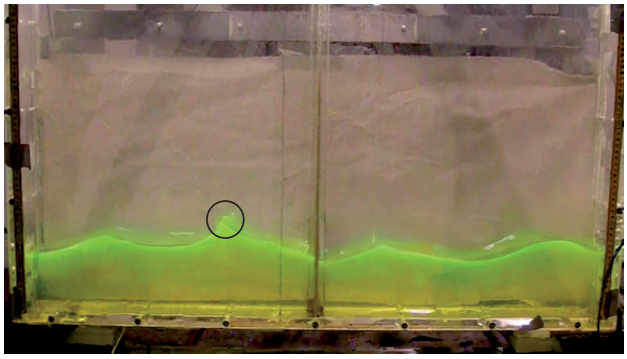

Figure 4-6. Weak wave breaking for $h/l = 0.12, \varepsilon = 0.01, Sn = 0.7875, \sigma/\sigma_1^* = 2.3387$.

For $Sn = 0.8375$ wave breaking is shifted to lower forcing frequencies. The wave breaking is also accompanied by thick wave run-ups on the screen. The wave breakings are seen for $1.9615 \leq \sigma/\sigma_1^* \leq 2.0181$. Examples of wave breaking and run-ups in the above-mentioned frequency range are shown in Figure 4-7. Very small wave breakings are seen for $\sigma/\sigma_1^* = 2.3576$ and 2.3765, as well. Three-dimensional waves are also present for $\sigma/\sigma_1^* = 2.5839$ and 2.6028 ($Sn = 0.8375$).

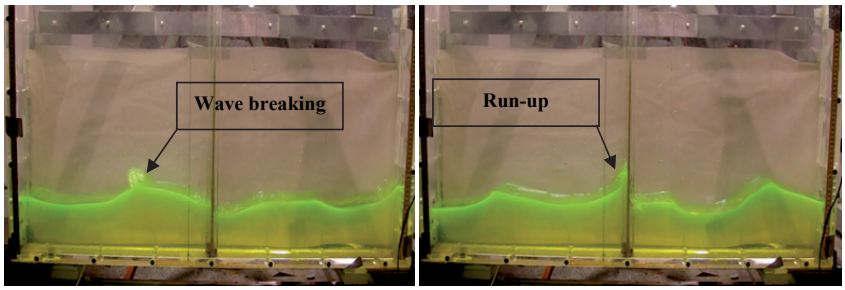

Figure 4-7. Left: wave breaking, Right: run-up along the screen. $\frac{h}{l} = 0.12, \varepsilon = 0.01, Sn = 0.8375, \sigma/\sigma_1^* = 1.9992$.

Searching in the time history of the response elevations for special free surface effects, strong secondary resonance of the 4th mode of sloshing together with the amplification of many super-harmonics are seen for $1.9615 \leq \sigma/\sigma_1^* \leq 2.0181$. This frequency range is the same as the one mentioned above where wave breaking and run-ups are also detected. Sub-harmonic amplification is not noticed for this solidity ratio. However, the "extra" super harmonics are still visible but with a small amplitude for $2.5839 \leq \sigma/\sigma_1^* \leq 2.6405$.

Videos taken for $Sn = 0.8875$ clearly show that for forcing frequencies around σ_2^* the response waves on the two side of the screen are almost isolated and in fact the main tank is divided into two equal compartments. The latter division of the main tank is called comparmentation in this thesis. Although the two wave responses behave almost independent, the liquid-to-gas jet flows that are generated by the cross flow through the screen and fall on the underlying free surface on the other side of the screen are clearly affecting the flow at the screen zone by generating liquid-gas mixture in the screen zone and imposing extra hydrodynamic damping. In addition, the jet flows hitting the underlying free surface can affect the symmetric modes and increase the nonlinear behavior. For $Sn = 0.8875$ the largest waves occur around σ_2^* (or σ_1^{**} , the lowest natural mode of a compartment with a half length of the main tank) demonstrating that flow motion through the screen is reduced for this solidity ratio. These large responses occurring for $1.9238 \leq \sigma/\sigma_1^* \leq 2.0558$ are accompanied with wave breaking and run-ups on the vertical wall. Very small wave breaking is also present at $\sigma/\sigma_1^* = 2.3387$ which is due to the large responses arising from the secondary resonance of 8th mode of sloshing in the clean tank. Considering the time history of the response wave elevations, small-amplified extra harmonics are seen for frequencies $1.9992 \leq \sigma/\sigma_1^* \leq 2.0558$ that are also accompanied with wave breaking. Small extra harmonic amplification is detected only for $\sigma/\sigma_1^* = 1.9615$.

$Sn = 0.9125$ and $Sn = 0.9375$ cause larger flow responses around $\sigma_1^{**} = \sigma_2^*$ leading to larger wave breaking, run-ups and liquid-to-gas jet flows in the screen zone. The frequency ranges associated with the above mentioned special free-surface effects are $1.9049 \leq \sigma/\sigma_1^* \leq 2.0558$ and $1.8672 \leq \sigma/\sigma_1^* \leq 2.0558$ for $Sn = 0.9125$ and $Sn = 0.9375$, respectively. In addition, irregular three-dimensional behavior is seen around the largest wave responses that might be due to the propagating disturbances caused by the wave breaking and liquid-to-gas jet impacts on the underlying free-surface at the screen zone. Away from σ_2^*, a tiny wave breaking is seen for $\sigma/\sigma_1^* =$

2.3387 for $Sn = 0.9125$. This is the same kind of wave breaking which was observed at the same frequency for $Sn = 0.8875$ due to secondary resonance of the 8th mode.

At $\sigma/\sigma_1^* = 1.867$ two different steady-state solutions in the two compartments are clear in the video recordings. Free-surface fragmentation is seen in form of free falling portions of water detached from the large run-ups on the screen. This phenomenon occurs for large solidity ratios and sufficiently large forcing amplitudes according to previous results measured for $h/l = 0.4$ and $\varepsilon = 0.01$ and $h/l = 0.35$ and $\varepsilon = 0.03$ (see Figure 3-9). Amplification of extra harmonics of forcing frequency is not detected for $Sn = 0.9125$ and $Sn = 0.9375$; increasing the solidity ratio to very large values, $Sn \to 1$, weakens and finally removes the amplification of the extra harmonic components.

Table 4-2 summarizes forcing frequencies associated with special free-surface effects and amplification of "extra" harmonics for all tested solidity ratios. This information is based on the available videos and measurements.

Table 4-2. Special free-surface effects and their corresponding forcing frequency observed for $h/l = 0.12$ and $\varepsilon = 0.01$. Frequency ranges are denoted by a dash (-) between the minimum and maximum values of the range.

Solidity ratio (Sn)	0.4725	0.6875	0.7875	0.8375	0.8875	0.9125	0.9375
Wave breaking ($\frac{\sigma}{\sigma_1^*}$)	2.433-2.527	2.471-2.565 2.358-2.414	2.339-2.377	1.962-2.018 2.358	1.928-2.056 2.339	1.905-2.056 2.339	1.867-2.056
Run-up($\frac{\sigma}{\sigma_1^*}$)	NA	NA	NA	1.962-2.018	1.928-2.056	1.905-2.056	1.867-2.056
Extra-harmonics ($\frac{\sigma}{\sigma_1^*}$)	2.603-2.735	2.527-2.735	2.565-2.735	1.962-2.018 2.584-2.641	1.999-2.056 1.962	NA	NA
Three-dimensional flow ($\frac{\sigma}{\sigma_1^*}$)	2.5273	NA	2.5273	2.584-2.603	NA	NA	NA

4.1.2 Steady-state response curves of free-surface amplitude and secondary resonance

The steady-state maximum wave elevations for $0.75 \leq \sigma/\sigma_1^* \leq 2.7$ are shown in Figure 4-8 to Figure 4-14. The figures also include the amplitudes of the 1st, 2nd and 3rd harmonics of the response computed by FFT (Fast Fourier Transform). The vertical dashed and dotted lines are used to mark i_{2k} and i_{2k+1} frequencies associated with the secondary resonance of even and odd modes, respectively (See page 37 for the definition of i_{2k} and i_{2k+1}). Whenever the amplification of extra harmonics causes steady (regular) beating periods ζ_{max}/η_{2_a} is calculated by finding the maximum wave elevations for each beating periods and taking the average between them. For irregular beating waves, it is difficult to determine fixed beating periods and therefore ζ_{max}/η_{2_a} is taken as the average of sufficient number of maximum elevations. The non-dimensional standard deviation of the maximum steady-state values std/η_{2_a} due to

transient effects triggered by special free-surface effects are very small and are not presented in Figure 4-8 to Figure 4-14.

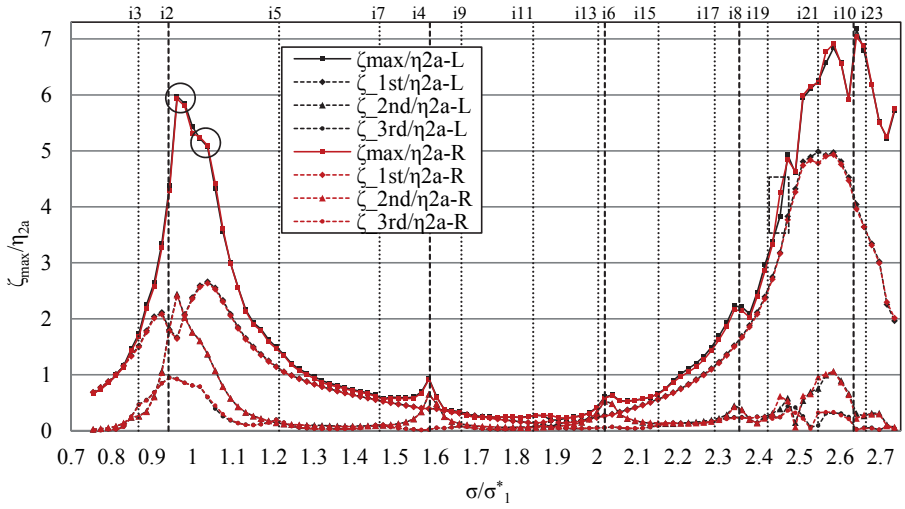

Figure 4-8. Non-dimensional maximum steady-state response ζ_{max}/η_{2_a} and the amplitude of the first three Fourier harmonics of the response ζ_{1st}/η_{2_a}, ζ_{2nd}/η_{2_a}, ζ_{3rd}/η_{2_a} versus σ/σ_1^*. $h/l = 0.12$, $\varepsilon = 0.01$, $Sn = 0.4729$. The letters 'L', for Left, and 'R', for Right, are used to distinguish between the measured results on the two sides of the tank. The vertical dashed i_{2k} and dotted i_{2k+1} lines mark the frequencies where secondary resonance of higher modes is expected. The rectangles mark regions with different results on left and right tank sides. The two circles (only $Sn = 0.4725$) mark the "double" peak resonant at $\sigma/\sigma_1^* = 1$.

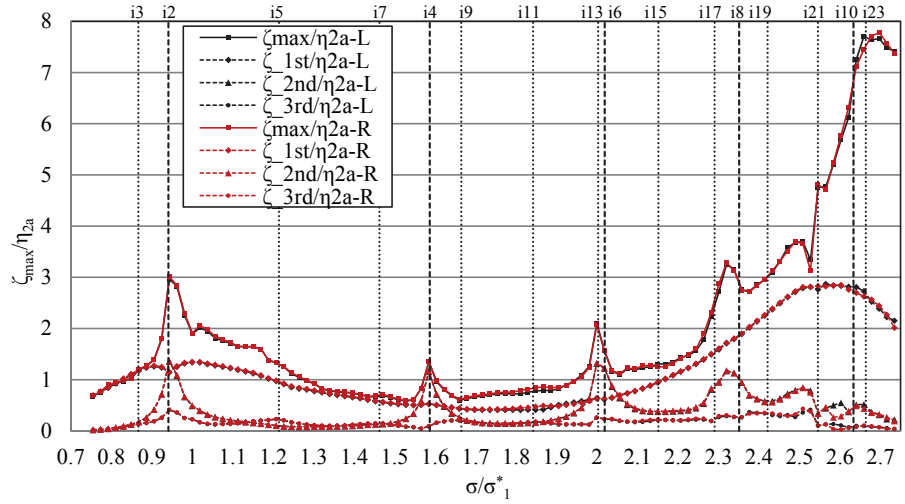

Figure 4-9. $h/l = 0.12$, $\varepsilon = 0.01$, $Sn = 0.6875$. Explanation is given in the caption of Figure 4-8.

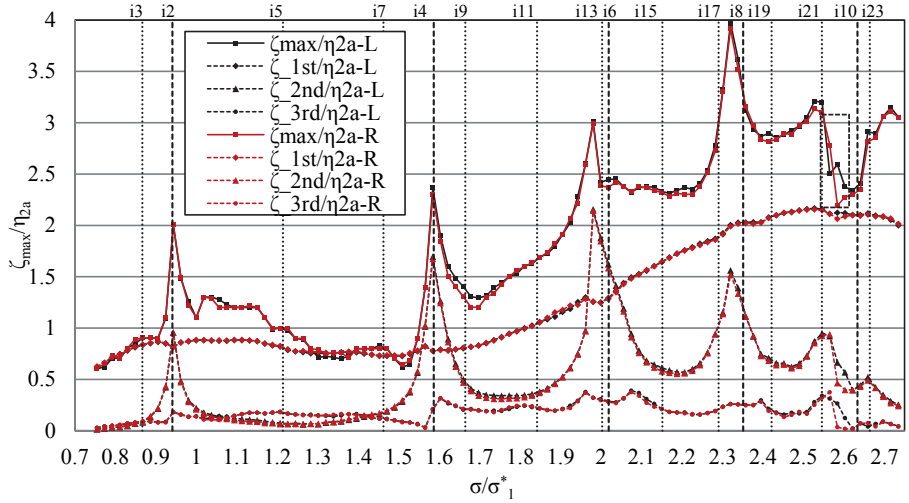

Figure 4-10. $h/l = 0.12, \varepsilon = 0.01,\ Sn = 0.7875$. Explanation is given in the caption of Figure 4-8.

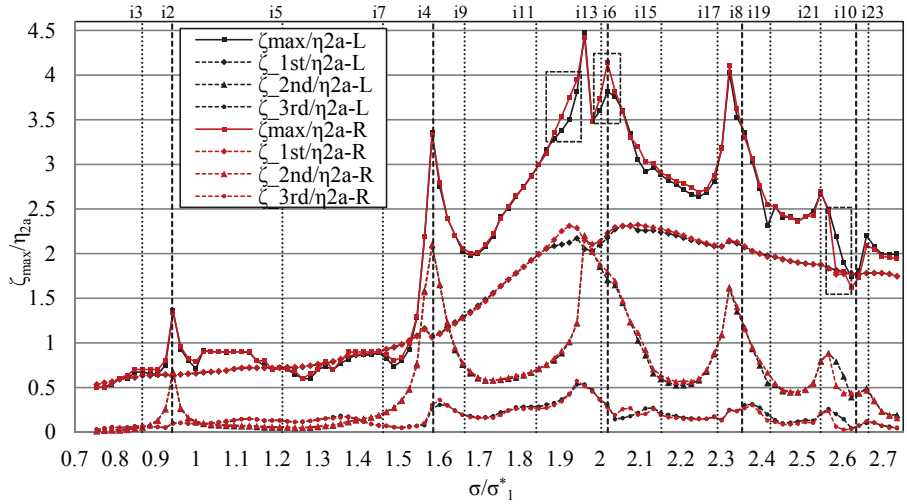

Figure 4-11. $h/l = 0.12,\ \varepsilon = 0.01, Sn = 0.8375$. Explanation is given in the caption of Figure 4-8.

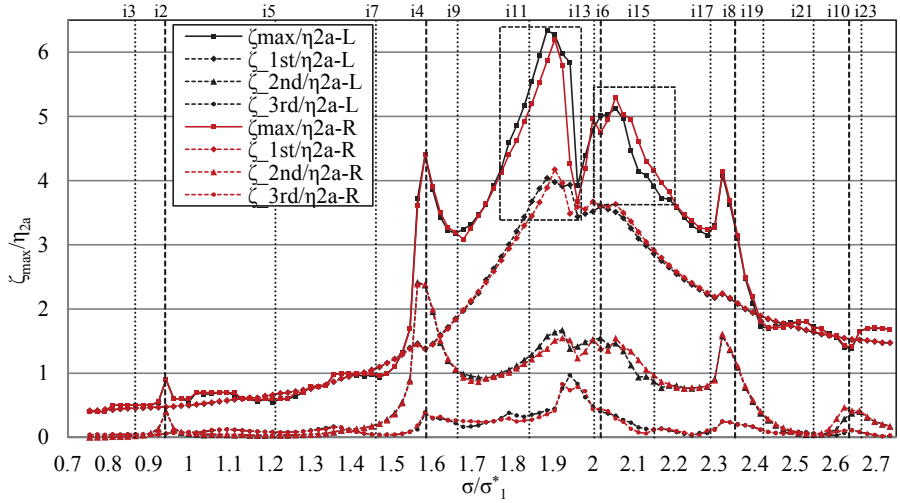

Figure 4-12. $h/l = 0.12$, $\varepsilon = 0.01$, $Sn = 0.8875$. Explanation is given in the caption of Figure 4-8.

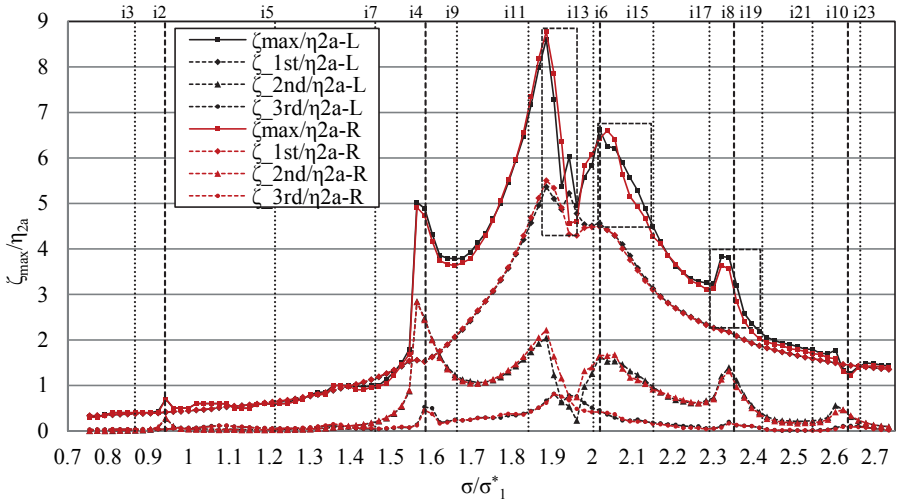

Figure 4-13. $h/l = 0.12$, $\varepsilon = 0.01$, $Sn = 0.9125$. Explanation is given in the caption of Figure 4-8.

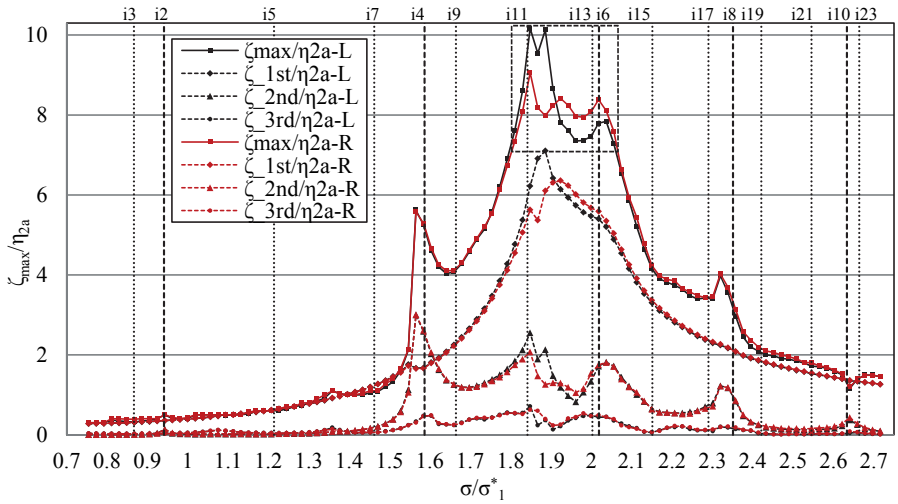

Figure 4-14. h/l = 0.12, ε = 0.01, screen (f) with $Sn = 0.9375$. Explanation is given in the caption of Figure 4-8.

The measured results for with $Sn = 0.4725$ in Figure 4-8 show strong amplification of higher harmonics of the forcing for $\sigma/\sigma_1^* \approx 1$. For the sake of clear graphs, only the amplitudes of the first three harmonics of the forcing are presented in Figure 4-8 to Figure 4-14. According to the results, increasing the solidity ratio reduces the strength of the higher harmonics in general and specially for σ around σ_1^*.

Figure 4-8 also shows two wide band resonant areas for $\sigma/\sigma_1^* \approx 1$ and $\sigma/\sigma_1^* = \sigma/\sigma_3^* \approx 2.5999$. These resonant areas are getting weaker by increasing the solidity ratio such that for $Sn = 0.8375$, 0.8875, 0.9125 and 0.9375 no resonant response is present around the first and the third natural frequency of sloshing in the clan tank. Instead a new peak emerges around $\sigma/\sigma_1^* = \sigma_2^{**}/\sigma_1^* = 1.8817$ demonstrating that the compartmentation of the main tank is reached for $Sn = 0.8375$. This fact can be realized by following the changes experienced by the steady-state amplitude of the first harmonic due to the increase in the solidity ratio.

Figure 4-8 shows a double peak behavior for ζ_{max}/η_{2_a}, marked by circles, around $\sigma/\sigma_1^* = 1$. In fact the secondary resonance of the second mode of sloshing at i_2 together with the primary resonance at $\sigma/\sigma_1^* \cong 1$ cause two response peaks closely apart in the frequency domain. The double peak behavior is clearer for the amplitude of the primary harmonic. Considering the amplitude of the second harmonics, a resonant peak is present at the right side of i_2, at $\sigma/\sigma_1^* = 0.9619$. This resonant peak has got larger amplitude than that of the primary harmonic. The reason is that the first mode experiences larger damping than the second mode which does not cause a flow through the screen. This fact together with secondary resonance of the second mode leads to a larger response peak for the amplitude of the second harmonic at $\sigma/\sigma_1^* = 0.9619$. Increasing the solidity ratio reduces both resonant responses at i_2 and $\sigma/\sigma_1^* \approx 1$.

Considering the secondary resonance, the i_{2k} marker lines in Figure 4-8 to Figure 4-14 give good predictions on the occurrence of resonance due to secondary resonance

at even natural frequencies, i.e. i_2 to i_8. The figures also show that the predicted frequencies for secondary resonance marked by i_{2k} lines are more accurate for smaller frequencies. The response curves do not reveal resonant behavior at i_{2k+1} frequencies for any of the screens. This is related to the forcing amplitude which is not large enough to excite higher order nonlinearities. Very small peaks at i_3 and i_5 is present for $Sn = 0.4725$ and $Sn = 0.6875$. Other peaks seen for the amplitude of the third harmonic do not fall on the i_{2k+1} frequencies. A reason might be due to the fact that the odd modes are altered by the presence of the screen (Faltinsen and Timokha, 2011) and therefore the i_{2k+1} frequencies must be different.

Different steady-state responses in the compartments for some of the forcing frequencies are present and marked by rectangles in Figure 4-11 to Figure 4-14. Those differences that are in the same order as the measurement error are not marked in the figures. The differences are larger for larger solidity ratios and for forcing frequencies around $\sigma/\sigma_1^* = \sigma_1^{**}/\sigma_1^* = 1.9992$. In general, large responses, low level of damping imposed by the screen and large transient effects at the screen zone can cause different solution branches at resonance in each compartment.

As mentioned earlier in the chapter, to account for the maximum response for $\frac{h}{l} < 0.3368\ldots$ the frequency range should be swept by stepping up the forcing frequency. Due to the hard-spring behavior, by stepping up the forcing frequency the maximum steady-state response reaches a maximum point at a frequency larger than the corresponding natural frequency and then jumps down to a lower value. Such a response is shown on the left side of Figure 2-4 where the solution branch containing A_1-A_2-A_3, respectively, causes the maximum possible response. However, the jump is only seen if the global damping is very small. For small depths $0.12 < h/l < 0.24$ Faltinsen and Timokha (2001) show that many modes can be excited and cause multiple peak behavior close to the main resonance. Following Faltinsen and Timokha (2001), the double peak behavior in Figure 4-8 at i_2 and σ/σ_1^* is due to the multiple mode amplification.

Considering the main resonant peaks at $\sigma_i^*, i = 1,3$, no steady-state jumps occur for $Sn = 0.4725, 0.6875, 0.7875$ due to the large screen-induced damping. For $Sn = 0.8375, 0.8875, 0.9125\ and\ 0.9375$, responses show a wide band resonant area around i_{11} and i_{13} growing in magnitude as the solidity ratio increases. This is mainly due to resonance at the lowest resonant frequency of a compartment, σ_1^{**} and secondary resonance at i_6 which visually create a double-pick response curve. By increasing the solidity ratio between $Sn = 0.8375$ and $Sn = 0.9375$ the peak at i_6 stays almost fixed in the frequency domain while the peak closer to σ_2^* drifts towards σ_2^*. Near σ_2^* a clear hard-spring type of jump can be seen for $Sn = 0.8875, 0.9125$ and 0.9375, i.e. the steady-state response jumps down to lower values by increasing the forcing frequency. One should also consider that the resonance area around σ_2^* (Figure 4-11 to Figure 4-14) contains different responses in the two compartments due to multi-branch steady-state responses.

It's worth noting that increasing the solidity ratio from 0.4725 to 0.9375 changes the effective depth for sloshing from $h/l = 0.12$ in the main tank to $h/l = 0.24$ in one compartment depending. Assuming the validity of multimodal theory with one dominant mode, the hard-spring effect should be still valid for $h/l = 0.24$ which means

the response curves at the main resonance of a compartment, σ_1^{**} should, follow a hard spring effect as one can clearly see in Figure 4-13 for $Sn = 0.9125$.

The steady-state jumps are also expected around peaks associated with the secondary resonance especially at i_{2k} frequencies. For instance a jump can be seen at i_2 for $Sn = 0.4725$. By increasing the solidity ratio steady-state jumps can be seen for almost all resonant peaks at i_{2k}. The interesting phenomenon is that these jumps are not of hard-spring kind, i.e. they jump up from lower values to higher values due to increase in the forcing frequency. This kind of jump occurs for soft-spring behavior which was shown on the right side of Figure 2-4 where the accepted solution branch follows the curve through A_3-T-A_1, respectively. In fact hard- or soft-spring behavior has only been studied for sloshing in clean tanks. Experiments by Chester and Bones (1968) show only hard-spring behavior for primary and secondary resonance in shallow water. In fact, the screen can change the modes and internal energy exchange between them (Timokha, personal communication). The latter phenomena needs dedicated theoretical study to find out how the depth criteria should be defined for switching between soft- and hard-spring behavior in case of secondary resonance.

The maximum response among all solidity ratios and in the total frequency range is the lowest for $Sn = 0.7875$. The same screen with $Sn = 0.7863$ in $h/l = 0.4$ (solidity ratio is depth dependent) caused the lowest maximum response for $\varepsilon = 0.01$. In addition, the maximum response for the above mentioned screen for both depth ratios $h/l = 0.4$ and $h/l = 0.12$ occurs at frequencies near the third natural frequency of sloshing in clean tank. The latter similarities show the importance of the forcing amplitude prior to water depth.

4.2 Water depth ratio h/l=0.125, forcing amplitude ratio ε=0.05

The sloshing phenomena studied in the previous sections are mostly resonant standing waves. These waves do not cause strong impact pressures on the vertical walls and the screen because the free-surface profile never progress toward the walls with a steep profile. Sufficiently large forcing amplitudes can cause very steep sloshing waves in shallow water travelling back and forth in the tank. In the following experiments shallow-liquid sloshing in a screen-equipped tank due to relatively large forcing amplitudes is considered. For these experiments $h/l = 0.125$, $\varepsilon = 0.05$ and 5 screens with solidity ratios 0.4752, 0.6760, 0.7960, 0.8440, 0.8920 are chosen. For this depth the first three non-dimensional natural frequencies in the clean tank are $\sigma/\sigma_1^* = 1, 1.8735, 2.5764$.

Figure 4-15 presents different wave systems observed for $h/l = 0.125$ in experiments performed by Lugni *et al.,* (reported in (Faltinsen & Timokha, Sloshing, 2009)) in a *clean tank* of same dimensions used in the current study. Depending on the forcing frequency, the wave systems are standing waves (wave system A), progressive non-breaking waves that are traveling back and forth in the tank (wave system B), progressive waves traveling back and forth in the tank and, eventually breaking near the vertical walls (wave system C) and Hydraulic jumps traveling back and forth in the tank (wave system D) presented by (●), (■) and (♦) and (▲) in Figure 4-15, respectively. The theory of Verhagen & van Wijngaarden (1965) predicts the hydraulic jump for combinations of η_{2_a}/l and T/T_1 located above the curve in Figure 4-15. T and T_1 are

the forcing and the highest natural periods. According to experimental results for $h/l = 0.125$, $\varepsilon = 0.05$ in Figure 4-15 the wave system is hydraulic jump for $0.85 < \sigma/\sigma_1^* < 1.25$. Hydraulic jump can cause a large slamming force if it hits a vertical walls with vertical free-surface at a large horizontal velocity. Experimental results by Lugni *et al.,* (reported in (Faltinsen & Timokha, Sloshing, 2009)) report large slamming loads when $\eta_{2_a}/l = 0.05$ and $h/l = 0.125$ when a hydraulic jump is present. How screens with different solidity ratios affect the hydraulic jump in particular and the free surface in general is discussed in the following text using video recordings and measured wave elevation.

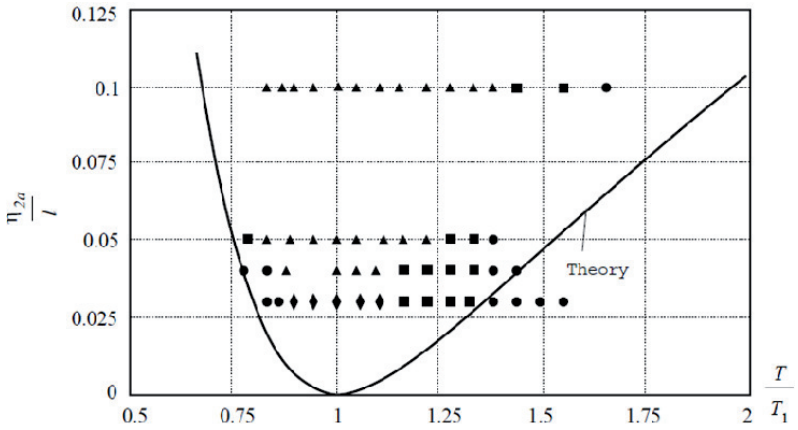

Figure 4-15. Occurrence of different wave systems as a function of forcing period T/T_1 and η_{2_a}/l for $h/l = 0.125$. (▲) identify the occurrence of hydraulic jump wave system. Solid line: Theory by Verhagen & van Wijngaarden (1965) predicting the occurrence of hydraulic jump in the convex part of the curve. Wave system corresponding to(●), (■) and (♦) are defined in the text. The plot is taken from Faltinsen and Timokha 2001.

4.2.1 Analysis of the results using experimental measurements and visual observations

The analysis starts with $Sn = 0.4752$. The recorded videos are available for $0.9258 \le \sigma/\sigma_1^* \le 1.2035$ and $1.4812 \le \sigma/\sigma_1^* \le 2.685$ including the first three lowest natural frequencies: $\sigma_1^*/\sigma_1^* = 1, \sigma_2^*/\sigma_1^* = 1.8735, \sigma_3^*/\sigma_1^* = 2.5764$.

Videos taken for frequencies around $\sigma/\sigma_1^* = 1$ show that the wave profile is strongly affected by the screen such that no hydraulic jump is present for $0.85 < \sigma/\sigma_1^* < 1.25$. The screen reduces the height of the waves and turns them to small-height steep progressive waves moving toward the tank walls. These waves are observed for frequencies $0.9258 \le \sigma/\sigma_1^* \le 1.2035$ that according to the presented results for the clean tank in Figure 4-15 are steep progressive waves and hydraulic jumps. An example of the free surface profile is illustrated in Figure 4-16 by means of snapshots taken every 1/20 of the forcing period for $\sigma/\sigma_1^* = 1.1294$. It is noted that the evolution of the free surface shown in Figure 4-16 is a representative example for $0.9258 \le \sigma/\sigma_1^* \le 1.2035$. The first snap shot at $t = 0$ shows a column of water piled up on the left side of the screen propagating toward the right side. Once the free surface

of the flow touches the screen, a small part of it runs up on the screen slats or is reflected back and the other part, major part, goes through the screen slots (T/20 in Figure 4-16). On the right side of the screen, a propagating wave is formed which is traveling toward the tank wall (2T/20, same figure). The free surface at the front of the propagating wave becomes sharp and then overturns. The overturning free surface traps a gas-pocket on the wall (The gas pocket is highlighted with a circle in Figure 4-17). A similar gas pocket was observed for $h/l = 0.35, \varepsilon = 0.03$, $Sn = 0.4729$ (right side of Figure 3-17) where the forcing amplitude is relatively large and the solidity ratio is the smallest. One should also note that the mentioned gas pocket becomes more visible as the forcing frequency increases in the frequency range $0.9258 \leq \frac{\sigma}{\sigma_1^*} \leq 1.2035$. The wave breaking on the wall together with formation of gas pockets generates a strong vertical up-going jet on the wall together with free surface fragments splashing on the lateral walls and the underlying free surface. Although these transient effects decrease the steadiness of the sloshing waves especially at the wall, the global profile of the free surface seems to be repeatable during half a forcing period (see t=0 and t=T/2 snapshots in Figure 4-16). The standard deviation of the maximum wave elevations measured at the vertical walls is used later on to provide a (local) scale for the steadiness of the sloshing waves.

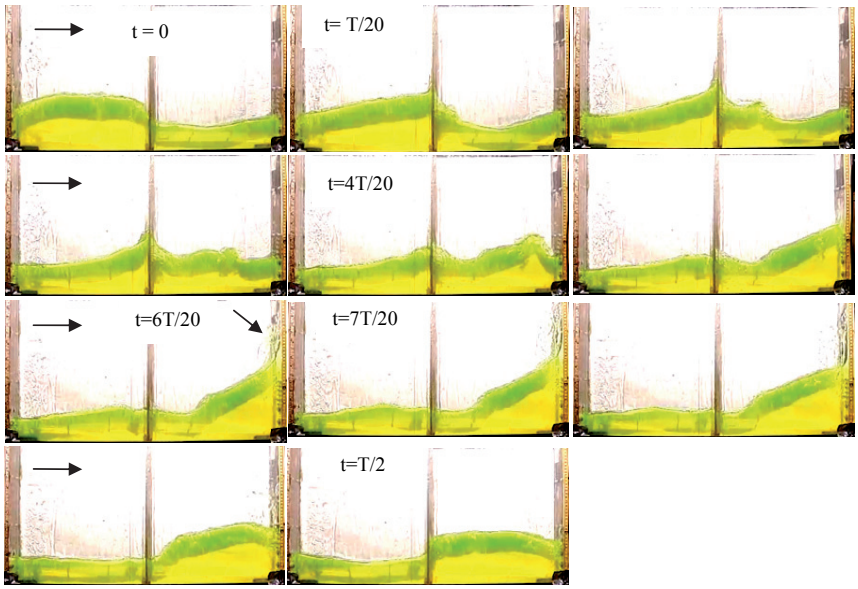

Figure 4-16. Profile of the free-surface at every 1/20 of the forcing period for $h/l = 0.125, \varepsilon = 0.05$, $Sn = 0.4725, \sigma/\sigma_1^* = 1.1294$.

The steepness of the free surface of a progressive wave and its approach velocity before touching the vertical wall is important from a hydrodynamic loading point of view. An example is the situation shown in Figure 4-17 where the free surface of the liquid

impacts the wall. Due to the impact an upward high velocity jet on the wall accompanied with liquid fragments takes place. This kind of liquid impact is expected to impose large slamming pressures. Unfortunately pressure has not been measured which makes it impossible to provide precise values for pressures occurring on the walls. Having this lack of information, it is tried to use the available videos to provide rough estimates on occurrence of high pressures on the vertical walls as a function of forcing frequencies.

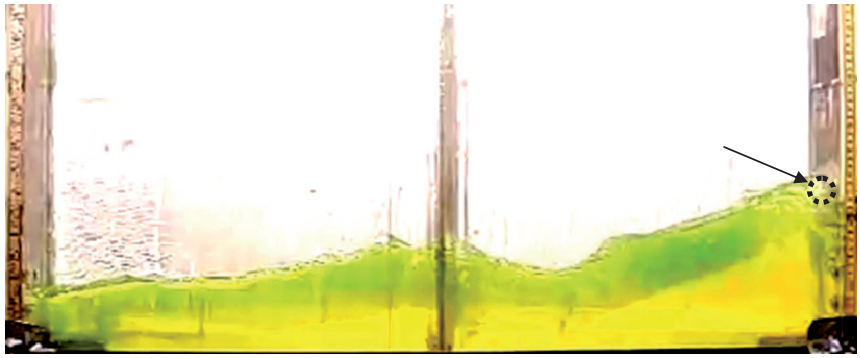

Figure 4-17. Formation of gas pockets on the vertical wall (marked by a circle). $\boldsymbol{h/l = 0.125, \varepsilon = 0.05, Sn = 0.4752, \frac{\sigma}{\sigma_1^*} = 1.1294}$**.**

For $Sn = 0.4752$ videos show formation of steep wave profiles progressing toward the vertical walls for frequencies around $\sigma/\sigma_1^* = 1$. To perform a visual investigation, the frequency interval $0.9258 \leq \sigma/\sigma_1^* \leq 1.2035$ is divided into 4 sub intervals and the shape of the free surface before and after hitting the wall is illustrated in Figure 4-18 for $\sigma/\sigma_1^* = 0.9258, 1.0183, 1.1109, 1.2035$. Each row belongs to one of the forcing frequencies mentioned above and from the top to the bottom the frequency increases. Each row contains snap shots taken every 1/60 seconds showing the advance in time from left to right. The first and the last two snap shots from the left in each row show the free surface before and after touching the vertical wall on the right tank side. For the frequencies shown in Figure 4-18 a high velocity jet is formed on the vertical wall after the free surface touches the wall. Such a jet is shown on the last snap shot of each row in Figure 4-18. Large pressure gradient on the wall must be present to form a liquid jet. The pressure gradient is caused by a phenomenon called wave focusing occurring due to the converging crest and trough of a progressing wave at a solid boundary (here the vertical wall). Wave focusing and the subsequent highly accelerated jet create a phenomena called flip-through that causes large impact pressures at the wall. This phenomenon is explained in detail by means of theory and experiments in a review paper by Peregrine (2003). More in-detail analysis of the flip-through phenomena based on experimental observations and measurements has been conducted by Lugni *et al.*, (2006).

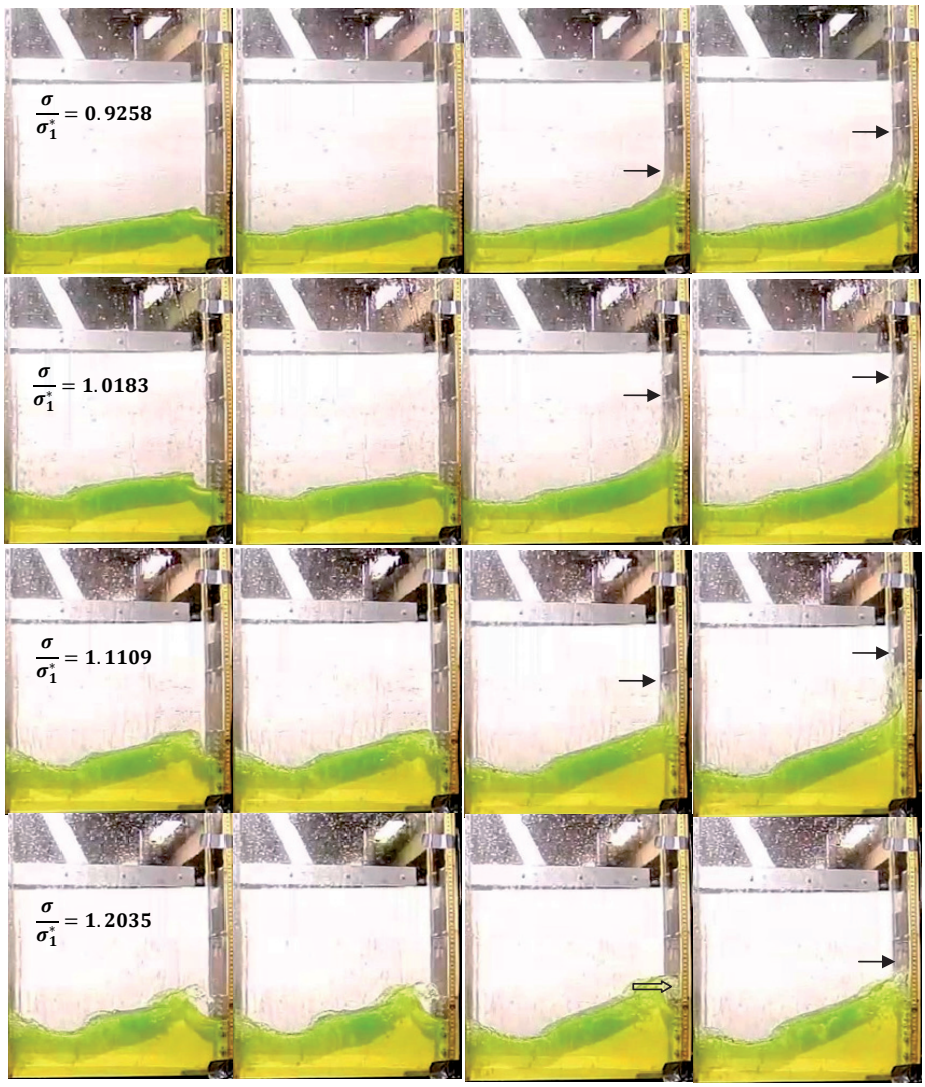

Figure 4-18. Evolution of the free surface at the vertical wall. From top to the bottom, each row belongs to one frequency. Each row has four snap shots. Snapshots are taken for one compartment. The right side of the snapshots corresponds to the tank vertical wall and the left side to the screen. The non-dimensional forcing frequencies are displayed on the first snap shot in each row. From left to right the time difference between two snap shots is T/60. The bold arrows marks the liquid height pumped up by the jet. The hollow arrow marks the liquid pushed down by a downward jet. $\boldsymbol{h/l = 0.125, \varepsilon = 0.05,\ Sn = 0.4752}$.

Considering the first row in Figure 4-18 for $\sigma/\sigma_1^* = 0.9258$, the free surface is steep in the first and the second snap shot before hitting the vertical wall. Right after the hit, a thin jet forms quickly on the wall due to the convergence of the crest and trough of the wave. The height of the water pumped up by the jet is marked by an arrow in Figure 4-18 at 1/60 and 2/60 seconds after the hit. This height qualitatively shows how strong the jet is and indirectly the magnitude of the gradient of the pressure on the wall.

Increasing the forcing frequency to $\sigma/\sigma_1^* = 1.0183$ (second row in the same figure) makes the free surface steeper before impacting the wall and creating a stronger jet with a thicker horizontal cross-section. For the third row, $\sigma/\sigma_1^* = 1.1109$, the crest of the free surface turns over and hits the trough while advancing toward the wall. A relatively small gas pocket between the water and the wall forms during the focusing of the wave and subsequently a thick three-dimensional jet is generated on the wall that is accompanied with liquid fragments thrown vertically and horizontally inside the tank. The last row, $\sigma/\sigma_1^* = 1.2035$, shows a thin wave breaker hitting the vertical wall before the wave focusing occurs. Once the horizontal jet of the wave breaker hits the wall a downward jet (marked by a hollow arrow) appears that collides with the running-up of the wave trough on the wall and reduces the strength of the wave focusing effect and therefore the acceleration of the up-going jet. Due to the occurrence of the wave breaking with a large breaker, a large gas pocket is trapped between the water and the wall. This gas pocket is the same as the one shown in Figure 4-17. The top side of the gas pocket is supported by a thin layer of water that cannot yield high pressures to maintain the gas pocket (see the last row in Figure 4-18). As a result, the thin layer of water breaks down into many liquid fragments splashing all over the tank walls and the underlying free surface. The latter fragmentation makes the flow locally three-dimensional at the end walls.

Occurrence of flip-through and formation of the wave breaking on the vertical walls accompanied with a gas pocket can cause large impact forces on the walls (Peregrine 2003). The flip-through occurs in a very short period of time. If a gas pocket is trapped between the liquid and the wall it may start oscillating due to the impact and compressibility of the air which is probably the case for $\sigma/\sigma_1^* = 1.1109$ shown on the third row of snap shots in Figure 4-18. The frequency of the gas pocket oscillations is much higher than the forcing frequency, for instance 600Hz. Therefore, video recordings and pressure measurements should be taken with a very high sampling rate to capture the flow figure and pressure fluctuation. For the flip-through problem, at least 1000 video frames per a second are needed to capture the evolution of the free surface during wave focusing and jet formation (Lugni, personal communication, 2012). Pressure measurements should be taken with an average rate of 10 kHz sampling rate. The videos were taken with a rate of 300 frames per a second which is hardly enough to perform a complete study on the evolution of the flow and the free surface during a flip-through. Based on the available videos flip-through and wave breaking accompanied with impact events are roughly seen for $0.9258 \leq \sigma/\sigma_1^* \leq 1.2035$.

4.2.2 Application of pressure impulse theory

The lack of direct pressure measurement on the vertical walls makes it difficult to evaluate pressures due to impact events. Here the pressure impulse theory developed by Peregrine and his coworkers (1992-1995) for liquid impact problems on solid walls is used to provide a rough estimate of impact pressures on the vertical walls. Cooker and Peregrine (1995) studied the problem of a steep wave profile impacting a vertical wall. The schematic of the problem is shown in Figure 4-19. Instead of working with the impact pressure p, its integration during the impact period, i.e. pressure impulse P, is used,

$$P = \int_{t_b}^{t_a} p dt. \tag{2.5}$$

t_b and t_a are the time instants before and after the impact. In this way $\Delta t = t_b - t_a$, which in practice is very difficult to determine, does not appear in the final formulation or pressure impulse P. The schematic of a typical impact event and its ideal translation in mathematical representation are shown in Figure 4-19. The velocity of the impacting surface U_0 is assumed to be vertically uniform. H stands for the total height of the wave profile just before the impact, μH is the fraction of H impacting the wall surface, b is a chosen length of the liquid with constant depth H where an atmospheric free-surface condition applies and ρ is the density of the liquid. One should note that this theory does not account for impacts accompanied with a trapped air pocket between the wave crest and the wall. Wood, Peregrine, & Bruce (2000) have modified the pressure impulse theory to account for air-trapped impact problems. They have reported satisfactory agreemens with small-scale experiments that have performed on a caisson breakwater with an impermeable berm. Computations that are made here are for non air-trapped cases.

The solution of the boundary value problem presented in Figure 4-19 is (Cooker and Peregrine 1995):

$$P(x,y) = \rho H \sum_{n=1}^{\infty} a_n \sin(\lambda_n y/H) \frac{\sinh[\lambda_n (b-x)/H]}{\cosh(\lambda_n y/H)} \ . \tag{2.6}$$

(2.6) is applied on a surface bounded in $-H \le y \le 0$ and $0 \le x \le b$. The summation constants are determined as $\lambda_n = (n - 1/2)\pi$ and $a_n = 2U_0 \frac{\cos(\mu\lambda_n)-1}{{\lambda_n}^2}$. The summation needs to be truncated over a finite number of terms. Here up to 200 terms, i.e. $n = 1$ to $n = 200$ are sufficient. Small μH values need more terms included in the summation to construct a smooth curve for the pressure impulse.

Applying pressure impulse theory needs good estimates of μ and b. Lugni, et al., (2006) showed a good agreement between the results computed by the pressure impulse theory and their experimental measurements. However, they also note the difficulty of estimating b and μ. As they comment, the computed results using (2.6) are less sensitive to value of U_0. To find an estimate for pressure and pressure impulse, similar calculation are done here for $\sigma/\sigma_1^* = 1.0183$ for which the free surface evolution before and after the impulse is shown in the second row of snap shots in Figure 4-18. For this case $U_0 = 1.7467 \frac{m}{s}$, $\mu = 0.0864$ and $b = 0.0415\ m$ are estimated from the video recordings. The quality of the video shots gives 0.002 m of accuracy for geometrical lengths. U_0 is calculated by dividing the travelled distance $\Delta x = 0.0524\ m$ of the free-surface front toward the wall by $\delta t = 9 \times \frac{1}{300}\ s = 0.03\ s$. 300 video frames are taken per a second meaning $\frac{1}{300} s$ accuracy of the computed δt. $U_0 = 1.7467\ m/s$ is the average value taken between the minimum and maximum estimated values.

The sensitivity of pressure impulse P to the geometrical parameters μ and b is shown in Figure 4-20. The middle plot contains estimated values of $\mu_e = 0.0864$ and $b = 0.2346H$. For the sensitivity study, two other values for μ are tested, one smaller and one larger than the estimated value, i.e. $\mu_e/2$ and $2\mu_e$. Moreover, b is varying

between 0 and H to consider the influence of b on the pressure impulse. The plots in Figure 4-20 show that both larger values of μ and b increase the maximum pressure impulse. However, the maximum pressure impulse P becomes less sensitive to b as $b \to H$.

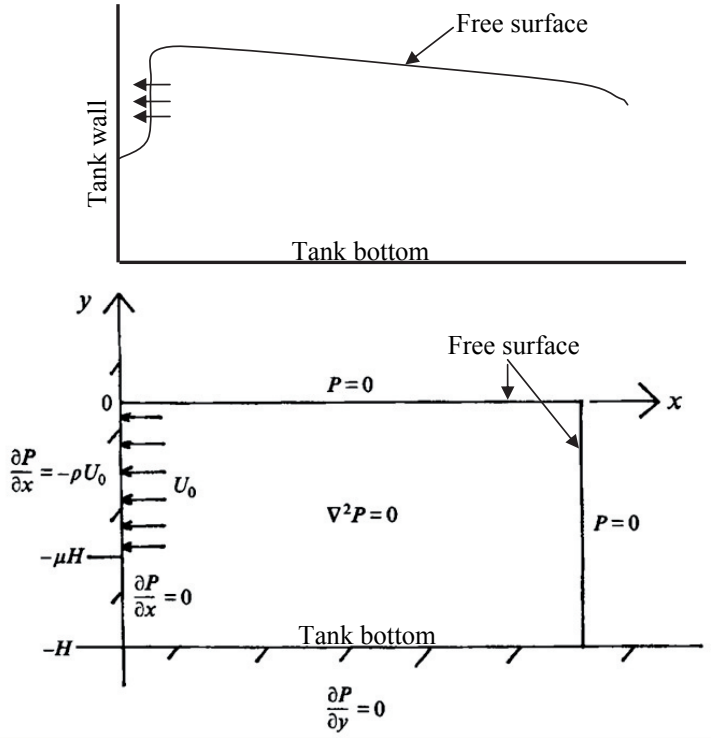

Figure 4-19. Boundary conditions for pressure impulse *P* for idealized impact of a wave front on a vertical wall (Cooker and Peregrine 1995)

In an impact pressure analysis, the maximum pressures are of more interest. One can calculate the maximum impact pressure assuming that the impact pressure increases linearly to a maximum pressure and then decreases linearly to zero during the impact period. This assumption gives $p_{max} = 2P/\Delta t$. Assuming $\Delta t = 0.001\ s$, suggested by Peregrine for laboratory scale experiments, and taking the maximum pressure impulses presented in Figure 4-20, the maximum pressures are calculated and listed in Table 4-5. The non-dimensional pressure range is $1.37 < p_{max}/\rho g L < 6.1$. The minimum and maximum pressures are calculated for minimum and maximum vales of μ and b. The non-dimensional values are comparable to the values measured by Abramson et al., (1974) (Faltinsen & Timokha, Sloshing, 2009) in a clean prismatic tank where $h/l = 0.4$ and $\varepsilon = 0.1$. The maximum pressure in the current study is almost two times the maximum pressure measured by Abramson et al., (1974) (Faltinsen & Timokha, Sloshing, 2009). It is therefore necessary to conduct an experimental investigation to measure the pressures on the vertical walls. The estimations made above were obtained for $Sn = 0.4725$. Larger solidity ratios strongly affect the sloshing resonance at the

lowest natural mode and remove the impact events on the vertical wall. This will be shown later in the text. However, due to large magnitude of the forcing amplitude, larger solidity ratios should be tested for presence of high pressures on the vertical walls that may occur for other forcing frequency ranges.

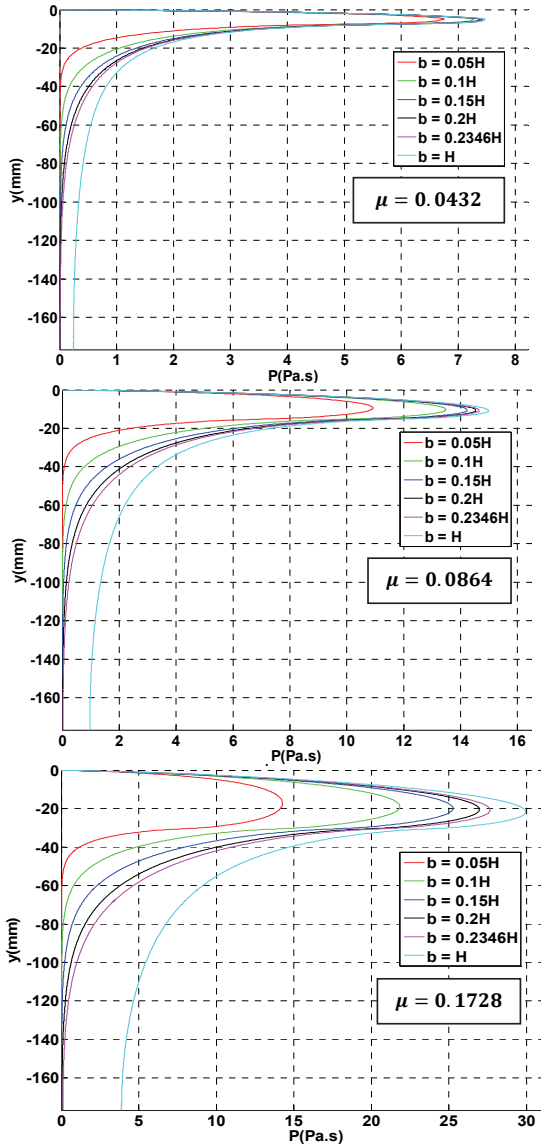

Figure 4-20. Sensitivity of the pressure impulse on estimated values of μ and b (see Figure 4-19 for definition of μ and b).

Table 4-3. Maximum pressures (kPa) calculated for maximum pressure impulse value P in Figure 4-20 using $p_{max}(kPa) = 2P/\Delta t$. $\Delta t = 0.001\ s$. $\mu_e = 0.0864$ is the estimated value.

b/H	0.05	0.1	0.15	0.2	0.2346	1
p_{max} , $\mu = \mu_e/2$	13.5	14.5	14.8	14.8	14.9	15.0
p_{max} , $\mu_e = 0.086$	21.9	27.0	28.5	29.1	29.3	30
p_{max} , $\mu = 2\mu_e$	28.6	43.7	50.5	53.9	55.4	59.9

Considering other violent free surface effects, wave breaking occurs for many forcing frequencies at variable horizontal distances relative to the tank wall and with variable intensity depending on the forcing frequency. For instance it can take place at the wall as shown in the last row of snapshots in Figure 4-18. Increasing the forcing frequency in the frequency range $1.4812 \leq \sigma/\sigma_1^* \leq 2.6847$, i.e. away from the lowest natural frequency of sloshing in the clean tank, reduces the progressive behavior of generated waves and moves the wave breaking from the tank wall toward the tank middle. Figure 4-21 shows an example of wave breaking for $1.4812 \leq \sigma/\sigma_1^* \leq 1.5738$ taking place far away from the vertical wall. This wave breaking does not splashes liquid fragments either on the wall or on the screen.

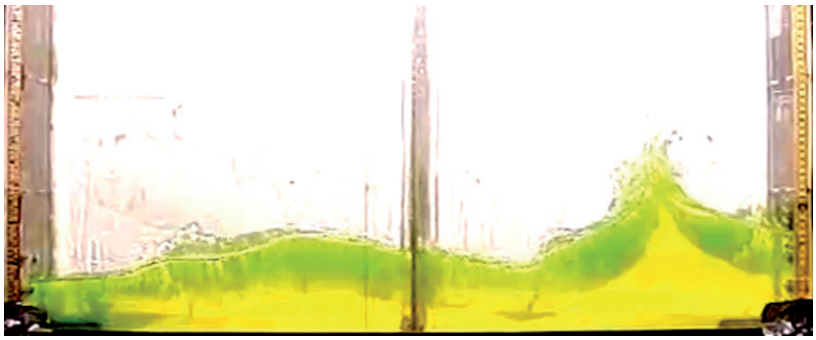

Figure 4-21. Typical wave breaking seen for $1.4812 \leq \sigma/\sigma_1^* \leq 1.5738$, $h/l = 0.125, \varepsilon = 0.05$, $Sn = 0.4752$.

As stated above the wave breaking occurs near the tank middle if the forcing frequency increases from values around σ_1^* to larger values around σ_2^* and σ_3^*, i.e. forcing frequencies belong to $1.4812 \leq \sigma/\sigma_1^* \leq 2.6847$. The solidity ratio is equal to 0.4752. In the mentioned frequency range, wave breaking may cause local impact forces not on the wall but on the *screen* caused by the liquid fragments hitting the screen. Such a wave breaking for instance occurs for $1.9441 \leq \sigma/\sigma_1^* \leq 2.444$. How the wave breaking causes impact on the screen is shown in Figure 4-22 for $\sigma/\sigma_1^* = 2.2403$ using 7 snap shots taken with almost 1/15 seconds time difference. The time increases from left to right and from top to the bottom as marked with ascending numbers. On snap shot (1) in Figure 4-22 and in the left compartment, two opposite-travelling free surface flows are marked by two opposing arrows. A progressive column of water with a flat horizontal free surface which is started forming near the vertical wall collides with the flow coming from the other side of the screen leading to wave breaking (snap shot (2)). This wave breaking reduces the kinetic energy of the progressive water column which is

moving toward the tank middle. As the breaking occurs, a very thick jet with large liquid fragments forms (snap shots (2),(3),(4)) at the wave breaker and hits the screen. Right after this, the progressive, lowered-height and reduced-energy water column goes through the screen with a high velocity (marked with an arrow on snap shot (5)) and causes two post impact effects: *a)* generation of liquid-to-gas jet flows hitting the underlying free surface on the opposite side of the screen (snap shots (6) and (7)) and *b)* thick liquid run-ups on the screen ending up with liquid fragments splashing around in the corresponding tank compartment (snap shot (7), liquid fragments are marked by an arrow). The reduced-energy water column that turns to a thick progressive layer of water may cause impact pressures on the screen if it hits the screen with a vertical flat free surface and large enough approach velocity. The pressure impulse theory might be applied here if the screen assumed to be a solid wall. The latter would give overestimated values for the maximum pressures.

For $Sn = 0.4752$ and for larger forcing frequencies, $2.4625 \leq \sigma/\sigma_1^* \leq 2.6847$, the waves are more of a standing type resembling the free surface profile of the third mode of sloshing in a clean tank. Even though the wave breaking occurs close to the screen, the flow at the breaker does not hit the screen. In addition the post impact effects such as large liquid-to-gas jet flows and run-up on the screen and liquid fragmentation are not present.

As long as the waves are mainly of propagating type, $1.4812 \leq \sigma/\sigma_1^* \leq 2.444$, the run-up on the screens is still strongly seen even though the free surface front is not close to vertical.

Another phenomenon which is visible in the video recording for $Sn = 0.4752$ is the occurrence of three-dimensional flow for $1.4812 \leq \sigma/\sigma_1^* \leq 1.7404$ and $2.3329 \leq \sigma/\sigma_1^* \leq 2.684$. When the flow is strongly three-dimensional (the second frequency range in the previous sentence) it almost *swirls* in the tank and causes local wave breakings and run-ups on the vertical tank walls and corners (corner between the vertical end walls and lateral walls). The latter effect that are related to the resonance at σ_3^* produces strong violent flows ($2.3329 \leq \sigma/\sigma_1^* \leq 2.684$). Figure 4-23 shows the three-dimensional behavior of the free surface by marking the free surface on the opposite lateral walls using two pointing arrows. The fragmentation of the free surface and liquid splashes due to the swirling of the liquid in the tank is also visible in the tank corner on the right side of Figure 4-23. This kind of motion is similar to swirling occurring in nearly square-based tanks due to harmonic horizontal excitation (Faltinsen and Timokha 2009) that increase the hydrodynamic pressure forces on the lateral (parallel to excitation direction) tank wall.

Following the discussions made above based on the *visual observations* local high pressure loads might be present on the wall and also on the screen depending on the forcing frequency and solidity ratio. These frequencies with rough estimates are reported in Table 4-5.

The time history of the wave elevations is now considered. Large amplification of super harmonic wave components of the forcing frequency especially around σ_1^* is present in the time history of the wave elevations measured at 1 cm distance from the vertical walls for $Sn = 0.4752$. The bottom panel of Figure 4-24 shows amplification of up to 8 super harmonics.

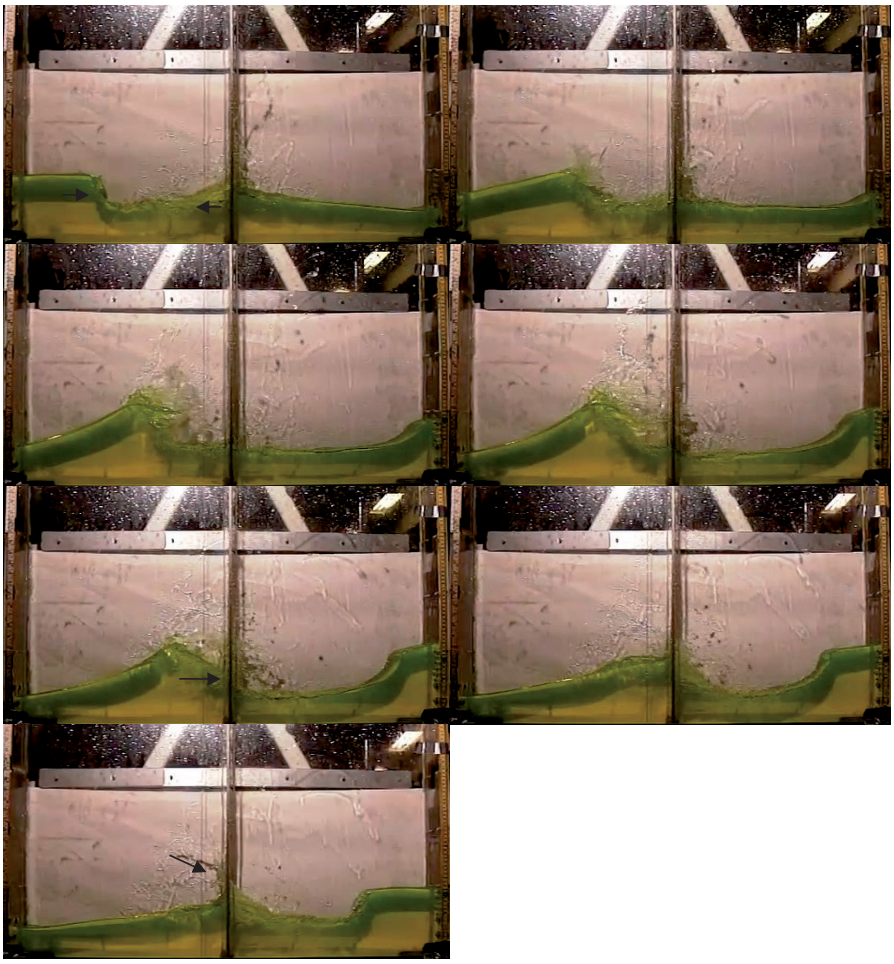

Figure 4-22. Formation of wave breaking at $\mathbf{h/l = 0.125, \varepsilon = 0.05, Sn = 0.4752, \sigma/\sigma_1^* = 2.2403}$. The evolution of the free surface before and after the wave breaking. The increase in time is marked by ascending number on the snap shots.

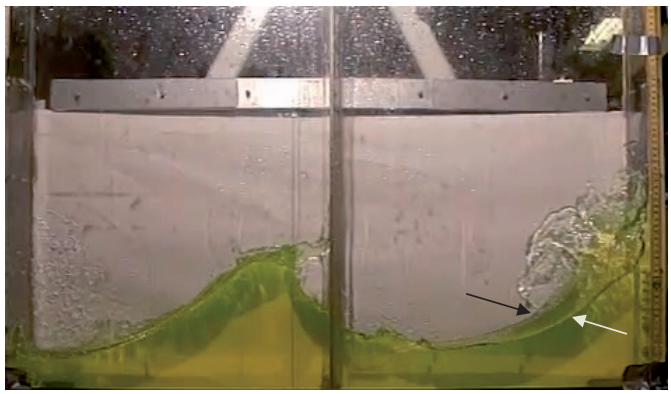

Figure 4-23. Three-dimensional flow. $\mathbf{h/l = 0.125, \varepsilon = 0.05, Sn = 0.4752, \sigma/\sigma_1^* = 2.5736}$.

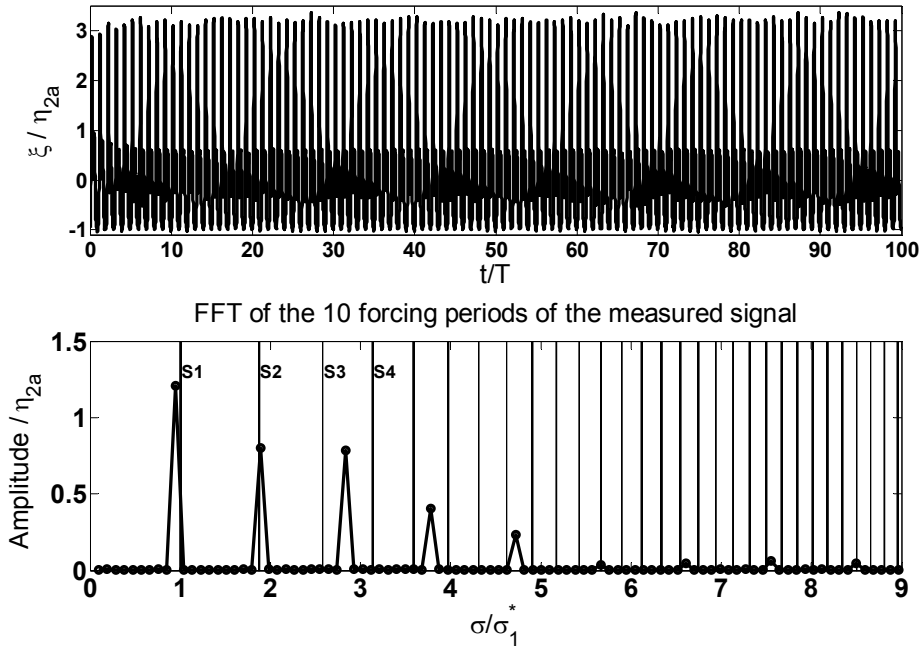

Figure 4-24. Strong amplification of higher harmonics for $\mathbf{h/l = 0.125, \varepsilon = 0.05, Sn = 0.4752, \sigma/\sigma_1^* = 0.9443}$. Top panel: Non-dimensional wave elevation at the vertical wall, bottom panel: Non-dimensional amplitude of the frequency components in frequency domain.

In addition to amplification of main super harmonics of the forcing frequency, "extra" harmonics are also amplified for the current depth $h/l = 0.125$ and forcing amplitude $\varepsilon = 0.05$ and frequencies $2.5921 \leq \sigma/\sigma_1^* \leq 2.6847$. The word "extra" means that the harmonics are not the main integer multiple bound harmonics of the forcing frequency. Figure 4-25 shows the time history and the frequency content of measured wave elevations for $Sn = 0.4752, \sigma/\sigma_1^* = 2.6847$. The top panel of the figure shows a beating behavior of the measured responses. The bottom panel of the same figure demonstrates amplification of the "extra" harmonics marked with integer

numbers. One may remind that for $\varepsilon = 0.01, h/l = 0.12$ and $Sn = 0.4725$ a same frequency range was associated with "extra" harmonic amplifications and wave modulation. This fact shows the prior importance of water depth for appearance of the "extra" harmonics prior to the forcing amplitude. However for the current case with a larger forcing amplitude $\varepsilon = 0.05$, the wave elevations are affected by transient effects such as large wave breaking. Wave breaking can smear the beating effect with irregular behavior. For the current case, $\varepsilon = 0.05, \frac{h}{l} = 0.125, Sn = 0.4752$, increasing the forcing frequency for frequencies $2.5921 \leq \sigma/\sigma_1^* \leq 2.6847$ makes the beating periods a little more regular which is probably related to weaker wave breaking.

To calculate the value of the multipliers, the extra harmonics are marked by numbers 1 to 5 in the bottom panel of Figure 4-25 and the ratio k_i of their corresponding frequency relative to frequency of the main harmonic (forcing frequency) is calculated. These k_i values are calculated for the range of frequencies associated with extra harmonics and are listed in Table 4-4. The calculations show almost equal values for k_i for all forcing frequencies. The dash (-) in the table means no clear peak is found for the corresponding k_i. For the current screen and for frequencies $2.5921 \leq \sigma/\sigma_1^* \leq 2.6847$ the multipliers $k_1 - k_5$ are equal to 0.36, 0.64, 1.28, 1.36, 1.64. These values are slightly different than k_i values reported in Table 4-1 for $Sn = 0.4725$, $h/l = 0.12$ and $\varepsilon = 0.01$.

Table 4-4. Multipliers k_i related to "extra" harmonics marked in Figure 4-25 for $h/l = 0.125, \varepsilon = 0.05$, $Sn = 0.4752$. k_i are the ratio between the frequency of the "extra" harmonics and the forcing frequency.

σ/σ_1^*	k_1	k_2	k_3	k_4	k_5
2.5921	0.3600	0.6400	-	-	1.6400
2.6291	0.3600	0.6400	-	1.3600	1.6400
2.6477	0.3600	0.6400	1.300	1.3600	1.6400
2.6662	0.3600	0.6400	1.2800	1.3600	1.6400
2.6847	0.36	0.6401	1.2802	1.3599	1.6401

Increasing the solidity ratio to $Sn = 0.676$ leads to much weaker progressive waves around $\sigma/\sigma_1^* = 1$. The result is formation of very small wave run-ups and breakings on and at the vicinity of the vertical walls for $0.9258 \leq \sigma/\sigma_1^* \leq 1.2035$. The only special event is occurrence of a weak wave focusing accompanied with a small gas pocket and a very thin run-up on the vertical wall at $\sigma/\sigma_1^* = 0.9443$. This gas pocket did not appear for $Sn = 0.4752$ at $\sigma/\sigma_1^* = 0.9443$ and is a new event for $Sn = 0.676$. Another new event for $Sn = 0.676$ is the presence of three-dimensional flow for a new frequency range $1.1294 \leq \sigma/\sigma_1^* \leq 1.2035$. For $2.1478 \leq \sigma/\sigma_1^* \leq 2.6847$ strong three-dimensional flow accompanied with large wave breakings exist. The three-dimensional flow causes a rotary (swirling) motion in the tank compartments that can increase the hydrodynamic pressure on the vertical lateral walls. Visual observations show that when the flow velocity is large the three-dimensional rotary motion can causes impacts on the lateral walls with an irregular behavior. In addition to three-dimensional flow, run-ups on the screen with variable intensity are seen for wide range of frequencies belong to $0.926 \leq \sigma/\sigma_1^* \leq 2.551$. This frequency range almost covers the total tested forcing frequency range. Strong run-ups on the screen leading to generation of large liquid fragments splashing on the underlying free surface, lateral walls and on the screen are seen for $1.185 \leq \sigma/\sigma_1^* \leq 1.2035$ and $1.4812 \leq \sigma/\sigma_1^* \leq$

2.481. These effects are usually seen in the current study whenever a high velocity liquid with a steep free surface hits the screen. The video recordings show that high-velocity steep profiles hitting the screen are the most energetic for $1.481 \leq \sigma/\sigma_1^* \leq 1.4997$ and $1.7404 \leq \sigma/\sigma_1^* \leq 2.444$. Tracking the energetic free-surface flows in the video recordings, two major effects may cause impact pressures on the screen: *1)*

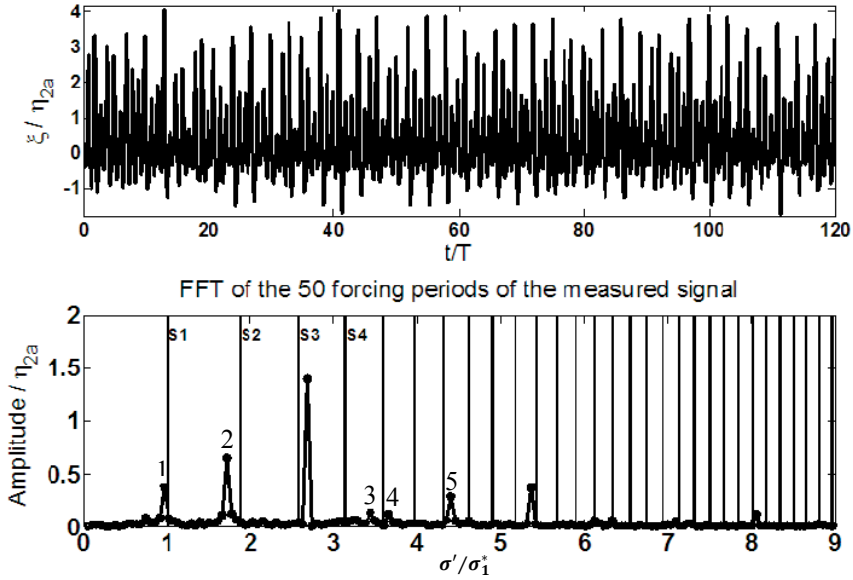

Figure 4-25. Sub- and special super-harmonic amplification marked by numbers. Top: Time history of wave elevations, bottom: Frequency content of the measured elevations. $h/l = 0.125$, $\varepsilon = 0.05$, $Sn = 0.4752$, $\sigma/\sigma_1^* = 2.6847$. σ' is the frequency content of the measured signal calculated by FFT.

Splashing of the liquid fragments on the screen due to wave breaking and *2)* being hit by a high velocity liquid flow with a perpendicular free surface which can be more severe than the first effect. For $Sn = 0.676$ the above-mentioned effects are stronger than those occurring for $Sn = 0.4752$ for almost the same frequency range. Figure 4-26 shows large liquid fragments and horizontally long-travelling liquid-to-gas jet flows that are the post effects of a high velocity flow with a very steep profile hitting the screen. It should be noted that the case shown in Figure 4-22 and Figure 4-26 are not presenting the phenomena for a same forcing frequency but they are presenting the most severe behavior observed for $Sn = 0.4725$ and $Sn = 0.4725$. Similar violent flows at the screen region might also be present for $1.2035 < \sigma/\sigma_1^* < 1.481$ but no video recording is available for those frequencies.

Considering the wave run-ups on the vertical walls, very thin and small scale jets/run-ups are seen around for $0.9258 \leq \sigma/\sigma_1^* \leq 0.9628$ due to very localized focusing of an overturning wave. Small wave breaking very close to the vertical walls is also present. The scenario shown in Figure 4-18 is almost seen here but with very smaller intensity and in a much narrower frequency range ($0.9258 \leq \sigma/\sigma_1^* \leq 0.9628$). However, the small progressive waves cause thicker run-ups for $1.0183 \leq \sigma/\sigma_1^* \leq 1.2035$. In addition, secondary resonance of higher modes increases the responses

causing thin run-ups on the vertical wall as well. For instance, the secondary resonance of the 6th mode of sloshing (clean tank) causes wave run-ups on the wall for $1.833 \leq \sigma/\sigma_1^* \leq 1.87$. Very thick run-ups can also appear. An example is given in the left side of Figure 4-22, snap shot 1, where the free-surface of the run-up is flat and horizontal.

For $Sn = 0.676$ wave breakings with different intensities are seen for all forcing frequencies except a narrow forcing frequency around σ_1^*, that is $1.0368 \leq \sigma/\sigma_1^* \leq 1.1109$. The latter shows the strong effect of the screen on the flow field near the lowest natural frequency of the clean tank.

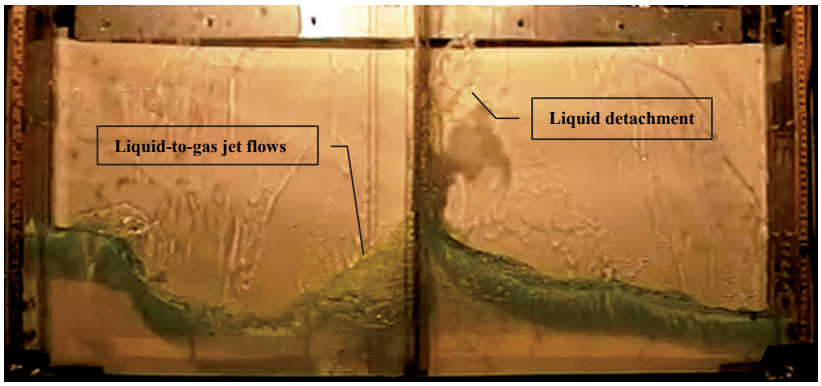

Figure 4-26. Liquid detachment on the screen and large liquid-to-gas jet flows. $h/l = 0.125, \varepsilon = 0.05$, $Sn = 0.6760, \sigma/\sigma_1^*$=1.7404.

Time series of the response elevations measured for $Sn = 0.676$ contain larger amplification of "extra" harmonics for $2.5921 \leq \sigma/\sigma_1^* \leq 2.6847$ with smaller amplifications compared to the results measured for $Sn = 0.4752$. The multipliers of the above-mentioned harmonics corresponding to numbered peaks in Figure 4-25 are the same as the ones found for $Sn = 0.4752$. In addition, for $Sn = 0.676$ a new frequency range $2.2218 \leq \sigma/\sigma_1^* \leq 2.3884$ associated with amplification of "extra" harmonics appears. An example is shown in Figure 4-27 for $\sigma/\sigma_1^* = 2.3144$. The bottom part of the figure shows two sub harmonics and three super harmonics marked with numbers 1-5. Corresponding to these numbers are new values of for $k_1 - k_5$, which are 0.2692, 0.7308, 1.2692, 1.4615, 1.7308 respectively.

Appearance of different set of multipliers for two different frequency ranges is a new behavior observed for $Sn = 0.676$ at $h/l = 0.125$ and with forcing amplitude $\varepsilon = 0.05$ and it might be related to the large forcing amplitude and strong influence of the special free surface effects such as the ones shown in Figure 4-26.

Increasing the solidity ratio to 0.7960 causes more reduction in the magnitude of wave responses around the lowest natural frequency of the clean tank. Except for very small wave breakings happening for $1.1479 \leq \sigma/\sigma_1^* \leq 1.2035$, non of the special free surface effects mentioned before are present for $0.9258 \leq \sigma/\sigma_1^* \leq 1.2035$. The video recordings are not available for $1.2220 \leq \sigma/\sigma_1^* \leq 1.4627$ but the available videos for $1.4812 \leq \frac{\sigma}{\sigma_1^*} \leq 2.6847$ which includes σ_2^* and σ_3^*, show the presence of wave breaking, three-dimensional flow, very large run-ups on the screen ending up with liquid fragmentation and large scale fragments of liquid caused by free surface impact on the

screen which are splashing on the screen and on the underlying free surface. These effects which were also observed for $Sn = 0.676$ are seen with more amplification for the current screen implying that intensity of the impacts has been increased. These impacts are roughly observed for $1.4812 \leq \sigma/\sigma_1^* \leq 1.5368$ and $1.6478 \leq \sigma/\sigma_1^* \leq 2.3144$. The second frequency range covers σ_2^* implying that the lowest natural frequency of the compartments is excited. For the current screen with $Sn = 0.7960$, an example with very severe post impact effects is shown in Figure 4-28 for $\sigma/\sigma_1^* = 2.0181$. As shown in Figure 4-28, a high-velocity liquid with an almost vertical flat free surface (marked by an arrow and a short black vertical line on the left panel in the figure) is hitting the screen. On the right side of Figure 4-28, the post effects resulting from the impact is also shown. The distance traveled by the liquid at the tip of a liquid-to-gas jet flow on the right side of Figure 4-28 and the large fragments of liquid generated and splashed opposite to the direction of the impacting liquid on the screen qualitatively depict the strength of the impact evevnts on the screen. Again one can qualitatively make a comparison between intensity of the impact events on the three lowest solidity ratios by comparing the post impact effects shown in Figure 4-22, Figure 4-26 and Figure 4-28, respectively.

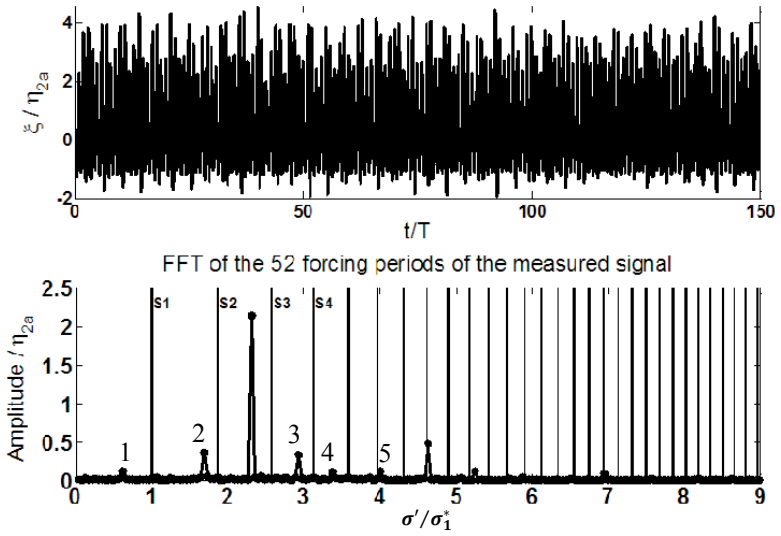

Figure 4-27. Sub- and special super-harmonic amplification marked by numbers. Top: Time history of wave elevations, bottom: Frequency content of the measured elevations. $\mathbf{h/l = 0.125, \varepsilon = 0.05, Sn = 0.676, \frac{\sigma}{\sigma_1'} = 2.3144}$. $\boldsymbol{\sigma'}$ is the frequency content of the measured signal calculated by FFT.

Thin run-ups on the walls are present for almost all forcing frequencies larger than 1.481 except $1.7774 \leq \sigma/\sigma_1^* \leq 1.833$.

The "extra" harmonics of the forcing frequency are weakly amplified for $2.0181 \leq \sigma/\sigma_1^* \leq 2.2959$ and $\sigma/\sigma_1^* = 2.444$ with multipliers $k = 1/2, 3/2$ which were not seen for $Sn = 0.4752$ and $Sn = 0.676$ for the mentioned frequency. The "extra" harmonics are also present for $2.6106 \leq \sigma/\sigma_1^* \leq 2.685$ with multipliers $k = 0.3462, 0.6538, 1.3462, 1.6538$. These values are slightly different than the ones

calculated for lower solidity ratios. These frequency ranges are also accompanied with large wave breaking, liquid fragmentation and three-dimensional flows. These effects can influence the nonlinear mechanism of energy exchange between the sloshing modes that are now strongly modified by the presence of the screen. For instance the liquid-to-gas jet flows hitting the underlying free surface two times in each period of oscillations enters a non-linear damping source into the system that will affect sloshing modes and their energy content.

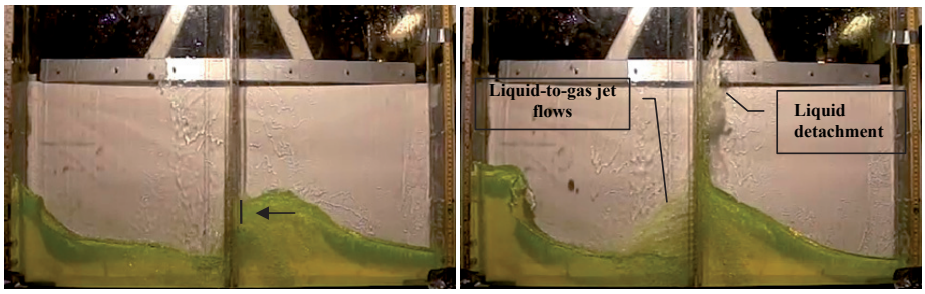

Figure 4-28. Slamming force on the screen by a high-velocity flow. Left: Before impact. Arrow shows the direction of the hitting liquid, Right: After impact. $\mathbf{h/l = 0.125, \varepsilon = 0.05, Sn = 0.7960, \frac{\sigma}{\sigma_1^*}}$=2.0181.

Video recordings for the next tested screen, $Sn = 0.844$, show quasi-steady responses around σ_1^*. For frequencies in the range $1.4812 \leq \sigma/\sigma_1^* \leq 2.685$, i.e. far from σ_1^* but including σ_2^* and σ_3^*, the flow is strongly three-dimensional and violent. One reason for presence of the three-dimensional flow is the strong spray of liquid fragments in the screen zone and another reason is high velocity liquid-to-gas jet flows originated from the flow crossing the screen crossing. Liquid impact events on the screen that are roughly seen for $1.4812 \leq \sigma/\sigma_1^* \leq 1.537$ and $1.629 \leq \sigma/\sigma_1^* \leq 2.314$ seem to be stronger for $Sn = 0.8440$. They occur in a slightly wider range for the current screen relative to the previously tested screens. Following the previous way of discussions, frequencies associated with liquid impacts on the screen are estimated based on the shape of the free surface before hitting the screen and strength of the post impact effects. Compartmentation of the clean tank and resonance at σ_1^{**}, the lowest natural frequency of a compartment, causes larger wave responses and increase the intensity of the liquid impact events on the screen. A *new* phenomena for the current screen is formation of steep wave profiles at the vertical walls due to the resonance around σ_1^{**}. The steep wave profiles can hit the wall due to the progressive nature (as seen in the videos) of the waves. The scenario of the impact events applied on the walls is similar to those presented in Figure 4-18 but with smaller intensity and less repeatability. The impact scenario includes wave breaking together with trapping a gas pocket on the vertical walls and formation of a vertical highly accelerated jet on the wall due to wave focusing An example of such event is shown in Figure 4-29 for $\sigma/\sigma_1^* = 2.1478$. Snap shots in Figure 4-29 taken before and after the impact respectively show the formation of the gas pocket (left snap shot) and the height of the liquid at the tip of the jet after the impact (right snap shot). This kind of impact on the wall can be roughly seen for frequencies $1.5553 \leq \sigma/\sigma_1^* \leq 1.7404$ and $1.9256 \leq \sigma/\sigma_1^* \leq 2.4255$. As expected the impacts seem to be larger around σ_1^{**}. Moreover, it should be noted that three-dimensional flow is always present near the vertical walls when the wave

responses are strong. The latter makes the impacts to be more irregular and localized. For instance they can occur at vertical corners between the end walls and lateral walls. The three-dimensional flow together with strong liquid fragmentation everywhere in the tank is present for frequencies between $\sigma_1^{**} = \sigma_2^*$ and σ_3^*.

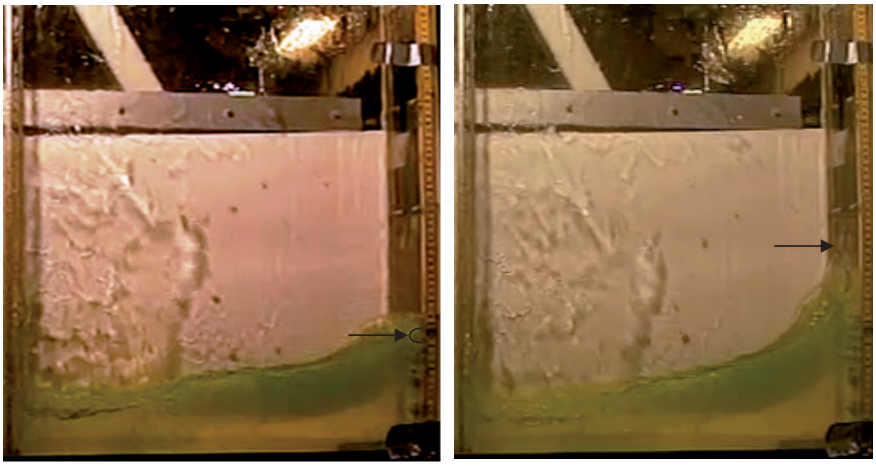

Figure 4-29. Liquid impact on the vertical wall, $\varepsilon = 0.05$, Sn = $0.844, \sigma/\sigma_1^*$=2.1478. Left: Formation of gas pocket marked by an arrow and a half circle. Right: Formation of the jet on the wall and the height of the liquid at the tip of the jet marked by a horizontal arrow.

The observed impact events on the screen and on the vertical walls that happen for forcing frequencies around $\sigma_2^* = \sigma_1^{**}$ brings up this conclusion that in case of large forcing amplitudes and small water depths (based on clean-tank length), even shifting up the lowest natural frequency of the clean tank using a large solidity ratio screen to that of a compartment may not potentially reduce the risk of large impact forces neither on the screen nor on the vertical walls. However, this conclusion needs more experimental support. Dynamic pressures due to the impact on the walls and the screen should be measured and analyzed to approve the occurrence of high pressures.

Looking into the time history of the wave elevations measured for $Sn = 0.844$ wave components oscillating with "extra" harmonics of the forcing frequency are present for $2.0181 \leq \sigma/\sigma_1^* \leq 2.129$ and $\sigma/\sigma_1^* = 2.444$ with multipliers $k = 1/2,3/2$ and also for $2.6106 \leq \sigma/\sigma_1^* \leq 2.685$ with multipliers $k = 0.3537, 0.6463, 1.3537, 1.6463$. The latter frequency range and the pattern of multiples are similar to those observed for for $Sn = 0.796$.

Increasing the solidity ratio to $Sn = 0.892$ turns the sloshing in the clean tank into a clearly compartmented sloshing such that the responses around σ_1^* are of a quasi-steady nature and no wave-like amplification appears. The available videos for $1.4812 \leq \sigma/\sigma_1^* \leq 2.685$ show very large responses around σ_2^*. These responses create impact events on the screen and also on the vertical walls. The impacts are accompanied with large three-dimensional flows which make them take place locally and at random places on the vertical walls and wall corners during each forcing period. The impact events on the screen and on the vertical walls can be seen for $1.4812 \leq \sigma/\sigma_1^* \leq 2.2774$ and $1.9071 \leq \sigma/\sigma_1^* \leq 2.2403$, respectively. It should be noted that the impact on the screen is probably much larger than on the walls because of the volume,

velocity and the vertical shape of the free surface hitting the screen. An example of an impact event on the screen is shown in Figure 4-28; this kind of impact with a large intensity never occurs on the vertical walls for any of the screens and forcing frequencies for the current depth and forcing amplitude.

Table 4-5. Special free-surface effects categorized by solidity ratio and non-dimensional forcing frequencies σ/σ_1^*. $h/l = 0.125, \varepsilon = 0.05$.

Solidity ratio / Special effect	0.4752	0.676	0.7960	0.8440	0.892
Local impact on the wall	0.926-1.204	-		1.926-2.426	1.907-2.240
Local impact on the screen	1.944-2.444	1.481-1.5 1.74-2.444	1.481-1.537 1.648-2.314	1.481-1.537 1.629-2.314	1.481-2.277
Wave breaking ($\frac{\sigma}{\sigma_1^*}$)	0.9258-2.685	2.148-2.685	1.148-1.204	1.4812-2.685	1.481-2.685
Run-up($\frac{\sigma}{\sigma_1^*}$) on screen	0.926-1.204 1.481-2.481	0.926-2.551	1.481-2.685	1.481-2.5	1.481-2.685
Run-up($\frac{\sigma}{\sigma_1^*}$) on wall	0.926-1.2035 2.351-2.685	1.018-1.204 1.833-1.87 2.148-2.685	1.481-1.778 1.833-2.685	1.481-2.685	1.481-2.685
Extra harmonics ($\frac{\sigma}{\sigma_1^*}$)	2.592-2.685	2.222-2.388 2.592-2.685	2.018-2.296 2.444 2.611-2.685	2.018-2.129 2.444 2.611-2.685	1.481-2.685
Wave modulation	2.592-2.685	2.222-2.388 2.592-2.685	2.611-2.685	2.611-2.685	1.481-2.685
Three-dimensional flow ($\frac{\sigma}{\sigma_1^*}$)	1.481-1.7404 2.333-2.685	1.129-1.204 1.481-1.889 2.148-2.685	1.4812-2.685	1.4812-2.685	1.481-2.685

For the current screen with $Sn = 0.892$, the time history of the wave elevations shows amplification of "extra" harmonics only for a narrow frequency range, i.e. $2.6291 \leq \sigma/\sigma_1^* \leq 2.685$. These harmonics oscillate with very small amplitudes relative to the amplitude of the main harmonic. The corresponding multipliers are $= 0.36, 0.64, 1.36, 1.64$.

To summarize the discussions and observations made based on the video recordings and the time history of the wave elevations measured at the vertical walls,

important phenomena and their corresponding forcing frequency ranges for each solidity ratio are listed in Table 4-5.

4.2.3 Steady-state response curves of free-surface amplitude

The steady-state response curves include the non-dimensional maximum steady-state wave elevations ζ_{max}/η_{2_a} and non-dimensional amplitude of their first, second and third Fourier harmonics, i.e. ζ_{1st}/η_{2_a}, ζ_{2nd}/η_{2_a} and ζ_{3rd}/η_{2_a}, respectively. The applied forcing frequencies cover the three lowest natural frequencies of sloshing in a clean tank. The curves are plotted for solidity ratios 0.4752, 0.676, 0.7960, 0.8440, 0.892 and shown in Figure 4-30 to Figure 4-34. The measurements were performed for both tank sides. Due to strong transient effects, clear steady-state waves do not appear for many of the forcing frequencies. This is demonstrated by presenting the corresponding η_{2_a} scaled standard-deviations std/η_{2_a} of ζ_{max} about its mean value as a function of σ/σ_1^* in the top panels of Figure 4-30 to Figure 4-34. The vertical dashed and dotted lines are corresponding to $i_{2k} = \sigma_{2k}^*/2\sigma_1^*, k = 1, 2, 3, \ldots$ and $i_{2k+1} = \sigma_{2k+1}^*/3\sigma_1^*, k = 1, 2, 3, \ldots$ non-dimensional frequencies where secondary resonance of higher modes (2nd and higher) is expected.

Starting with $Sn = 0.4752$, Figure 4-30 shows two major resonant peaks for σ_1^* and σ_3^* at $\sigma/\sigma_1^* = 1$ and $\sigma/\sigma_1^* = 2.5764$. The peak expected at σ_1^* occurs on the right side of $\sigma/\sigma_1^* = 1$ on the horizontal axis showing a hard-spring response behavior which is typically expected for sloshing in shallow depth. However the peak at σ_3^* takes place at a frequency smaller than $\sigma/\sigma_1^* = 2.5764$ that does not support hard-spring response behavior. These peak responses become smaller due to the increased damping and geometrical changes of the screen as the solidity ratio increases. This can be understood by following the sequence of the graphs presented in Figure 4-30 to Figure 4-34. One can focus on the amplitude of the primary Fourier harmonic, ζ_{1st}, to track the presence of the resonant peaks at $\sigma/\sigma_1^* = 1$ and $\sigma/\sigma_1^* = 2.5764$. Considering this argument, the curve representative for ζ_{1st}/η_{2_a} values plotted for $Sn = 0.676$ in Figure 4-31 shows almost no resonant amplification at $\sigma/\sigma_1^* = 1$. On the other hand, comparing the results for $Sn = 0.4752$ and $Sn = 0.676$ presented in Figure 4-30 and Figure 4-31 show that the peak response at $\sigma/\sigma_1^* = \sigma_3^*/\sigma_1^* = 2.5764$ is reduced by increasing the solidity ratio and moves further toward lower forcing frequencies. Moreover, the range of frequencies with larger responses is wider around σ_3^* for $Sn = 0.676$. For $Sn = 0.796$ the peak at σ_3^*/σ_1^* disappears and a wide band resonance frequency range containing σ_2^* appears in the middle part of the tested forcing frequency range implying that the compartmentation of the clean tank is reached. The latter resonance region and the corresponding peak move further toward σ_1^{**}/σ_1^* when the solidity ratio increases. Results for the largest solidity ratios, $Sn = 0.844$ and $Sn = 0.8875$ in Figure 4-34 show a strong resonance peak at σ_1^{**}/σ_1^* which demonstrates isolated responses in the compartments on the two sides of the screen.

Different responses on the two tank sides for a single forcing frequency are present and marked with rectangles in Figure 4-30 to Figure 4-34. The widest frequency range with different responses among all screens happens for Sn=0.4752. This frequency range $1.55 < \sigma/\sigma_1^* < 2.1$ includes strong amplification of the higher harmonics which is related to the secondary resonance of higher modes. One possible reason for having two different steady-state responses at resonance areas, as discussed

earlier in the chapter 3, is the difference in the amount of damping on each compartment due to transient effects during the time when forcing frequency changes to a larger (or smaller if frequency should be stepped down) value. Two compartments with different amount of damping will have maximum responses at frequencies with very small difference. The latter means that for a single forcing frequency two responses are possible for the two compartments.

Considering the upper panel in Figure 4-30 which presents the non-dimensional standard deviation of the measured responses for $Sn = 0.4752$, the largest unsteady effects appear for forcing frequencies around σ_3^*/σ_1^*. For these frequencies, the non-dimensional standard deviation std/η_{2_a} is as large as '1' which is equal to 40% of the unperturbed water depth. It should be noted here that frequencies in the range $2.5921 \leq \sigma/\sigma_1^* \leq 2.6847$, are associated with amplification of "extra" harmonics and irregular wave modulations. Whenever irregular modulations occur the standard deviations from the average value become larger. This must be remembered that the values used to plot ζ_{max}/η_{2_a} are computed by taking the average between the maximum wave-elevations for certain number of forcing periods (for instance 30 forcing periods). Examples of extra harmonics were shown in Figure 4-25 and Figure 4-27 where large deviations can be recognized around the mean value of the maximum elevations. The results show that increasing the solidity ratio reduces ζ_{max}/η_{2_a} around σ_1^* but expands the frequency range of large standard deviations of the maximum wave elevations. For instance, measured responses for $Sn = 0.892$ show relatively large ζ_{max}/η_{2_a} values for frequencies in $1.35 < \sigma/\sigma_1^* < 2.685$.

4.2.3.1 Secondary resonance

The resonant peak areas on the steady-state response curves are due to primary and also secondary resonance of the sloshing modes. In the following the resonant areas that are relevant for secondary resonance of sloshing modes are notified and discussed for each screen separately.

Sn=0.4752. Considering $Sn = 0.4752$, the results for ξ_{max}/η_{2_a} in Figure 4-30, shows a double peak behavior (marked by arrows) accompanied with steady-state jumps near $\sigma/\sigma_1^* = 1$. The peak on the left, marked by a hollow arrow, is due to secondary resonance of mode number 2 while the one on the right, marked by a bold arrow, is due to the primary resonance of mode number 1(first mode). The steady-state jumps at the two peaks are not of a hard-spring response behavior. One expects that for a hard-spring behavior occurring near the lowest natural frequency, the maximum possible resonant response occurs at a frequency larger than the natural frequency and by increasing the frequency the response jumps down to small value. Such a jump is shown on the left panel of Figure 2-4. One can also recognize jumps on the curves of amplitude of the first ξ_{1st}/η_{2_a} and the second ξ_{2nd}/η_{2_a} harmonic responses that are marked by hollow and bold arrows. These jumps are marked in accordance with the jumps seen on the ξ_{max}/η_{2_a} curve.

As the forcing frequency increases another resonant peak is seen in Figure 4-30 at i_4. The response curves of the measured waves in the two tank sides, i.e. "left" and "right", show a complex behavior between i_{11} and i_{15}, especially around $\sigma_2^*/\sigma_1^* =$

1.8735. On the "left" tank side a peak is clearly seen for $\left(\frac{\xi_{max}}{\eta_{2a}}\right)_L$ and $\left(\frac{\xi_{1st}}{\eta_{2a}}\right)_L$ at $\sigma/\sigma_1^* = 1.907$ just on the right side of $\sigma_2^*/\sigma_1^* = 1.8735$ on the horizontal axis. However, at the same forcing frequency, amplitude of the second harmonic component, $\left(\frac{\xi_{2nd}}{\eta_{2a}}\right)_L$, shows a hard-spring jump which is away from values marked by i_{2k} and i_{2k+1} giving predictions about the occurrence of the secondary resonance. For the "right" tank side, the maximum response $(\xi_{max}/\eta_{2_a})_R$ and its primary Fourier component $(\xi_{1st}/\eta_{2_a})_L$ shows a soft-spring response while the second harmonic component $(\xi_{2nd}/\eta_{2_a})_R$ follows a hard-spring response. The present complexity of responses shows the strong interaction of the sloshing modes in the compartments on the two sides of the screen at resonance. For larger frequencies, the curves of maximum responses ξ_{max}/η_{2_a}, primary harmonic ξ_{1st}/η_{2_a} and the second harmonic ξ_{2nd}/η_{2_a} components reveal soft-spring jumps at i_8 and i_{19}. In general, when secondary resonance occurs, the reason is the amplification of higher harmonics of the response, i.e. ξ_{2nd}/η_{2_a} and ξ_{3rd}/η_{2_a} or higher and not the main harmonic component ξ_{1st}/η_{2_a}. This means that the jumps seen at i_8 and i_{19} are not due to the secondary resonance. The reason can be realized from the video recording where formation of strong three-dimensional flow for $\sigma_2^*/\sigma_1^* \geq 2.3$ causes thick and strong run-ups on the wall. In other words, formation of these run-ups are the reason for the sudden increase of the responses at i_8 and i_{19}.

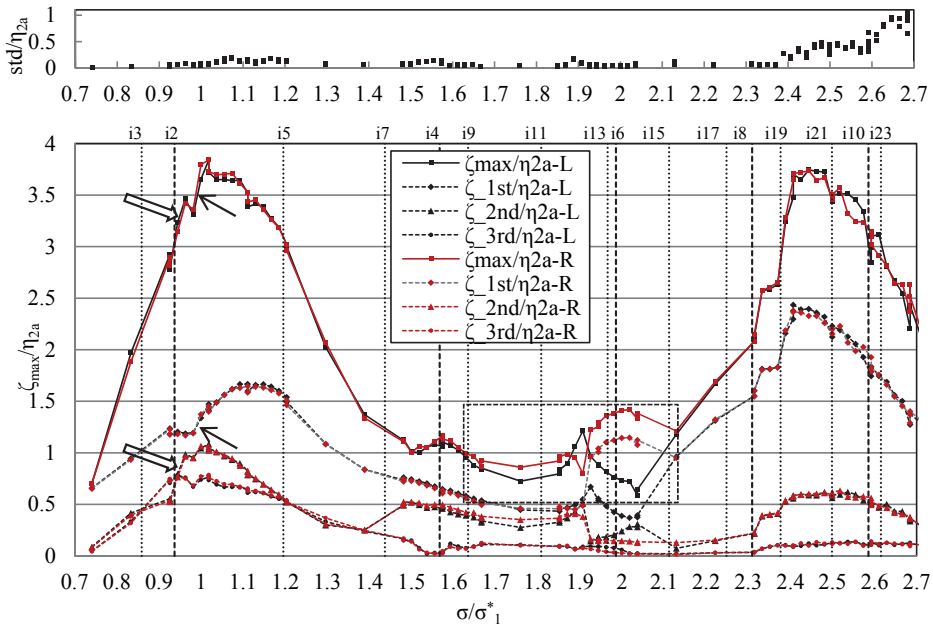

Figure 4-30. Top panel: non-dimensional standard deviation std/η_{2_a} of the maximum steady-state response ζ_{max}/η_{2_a} versus σ/σ_1^*. Bottom panel: Non-dimensional maximum steady-state response ζ_{max}/η_{2_a} and the amplitude of the first three Fourier harmonics of the response ζ_{1st}/η_{2_a}, ζ_{2nd}/η_{2_a}, ζ_{3rd}/η_{2_a} versus σ/σ_1^*. $h/l = 0.35$, $\varepsilon = 0.03$, $Sn = 0.4752$. The letters 'L', for Left, and 'R', for Right, are used to distinguish the results measured on two sides of the tank. The vertical dashed i_{2k} and dotted i_{2k+1} lines mark the frequencies where secondary resonance due to amplification of higher modes may occur. The rectangles mark regions with different results on left and right tank sides.

Sn=0.676. Considering the results shown in Figure 4-31 for $Sn = 0.6760$, the double peak behavior on the curve of ζ_{max}/η_{2_a}around σ_1^* is clearer comparing to the one seen for $Sn = 0.4752$. However the responses are smaller for the peak responses. Here, no jump is visible at the peaks. Also the reason for emerging the second peak on the right side of the double peak is the secondary resonance of mode number 5 at i_5. This peak follows the peak appearing on the curve for ξ_{3rd}/η_{2_a}close to i_5.

For $0.926 \leq \sigma/\sigma_1^* \leq 1.907$ the amplitude of the second harmonic component $\xi_{2nd}/\eta_{2_a}$is comparable to the amplitude of the first harmonic ξ_{1st}/η_{2_a}. The latter frequency range contains i_4 which surprisingly does not cause a resonant peak. A clear hard-spring jump exists close to σ_2^* between $\sigma/\sigma_1^* = 1.832$ and $\sigma/\sigma_1^* = 1.907$ which must be due to the secondary resonance of an even mode because the primary harmonic amplitude does not contain a jump or a peak at the above-mentioned frequency while the second harmonic component follows a jump. However, none of the dashed and dotted marking lines indicate a jump at σ_2^*. In addition, the time history of the wave elevations does not show amplification of higher even harmonics such as fourth harmonic. These facts show that the even modes and their corresponding frequencies may also be affected by the presence of the screen when the forcing amplitude is (relatively) large and the effects of transient flows in the screen zone strongly affect the sloshing modes. The ξ_{max}/η_{2_a}curve shows a jump between i_{18} and i_{11} in the "right" compartment which is due to formation of thick run-ups and three-dimensional flow. Due to the same reason, another jump is seen on the right side of the last marking line i_{23}.

Sn=0.796. Proceeding to a larger solidity ratio, $Sn = 0.796$, Figure 4-32 shows that the responses around $\sigma/\sigma_1^* = 1$ are weaker compared to results measured for lower solidity ratios. The double peak behavior is still present near $\sigma/\sigma_1^* = 1$. The left peak on the double peak moves more towards i_2 and the right peak moves toward lower frequencies as well. The third harmonic component ξ_{3rd}/η_{2_a} shows a small resonant peak close to i_5 which is located on the right side of the right peak (of the double peak) on the horizontal axis.

Strong amplification of the second harmonic component is present for $1.388 \leq \frac{\sigma}{\sigma_1^*} \leq 1.808$. However, the lack of sufficient data points makes it difficult to make an investigation in this frequency range.

The amplitude of the third harmonic ξ_{3rd}/η_{2_a}has a maximum at the left side of i_7 which might be related to the secondary resonance of mode number 7. The curve of maximum response $\xi_{max}/\eta_{2_a}$and the second harmonic ξ_{2nd}/η_{2_a}component show a drop at i_{11}. Looking at the time history of the wave elevations does not help to find a reason for this drop. Moving further to higher frequencies, the response curves for ξ_{max}/η_{2_a} and ξ_{1st}/η_{2_a} reveal a soft-spring jump at i_8 which is similar to the jump seen for Sn=0.4752 and Sn=0.676 at the same forcing frequency. The reason for this soft-spring jump as discussed before for Sn=0.4752 and Sn=0.676, is formation of three-dimensional flow with thick run-ups on the wall. A similar but stronger jump occurs around i_{21} and i_{11} which is also related to local three-dimensional effects.

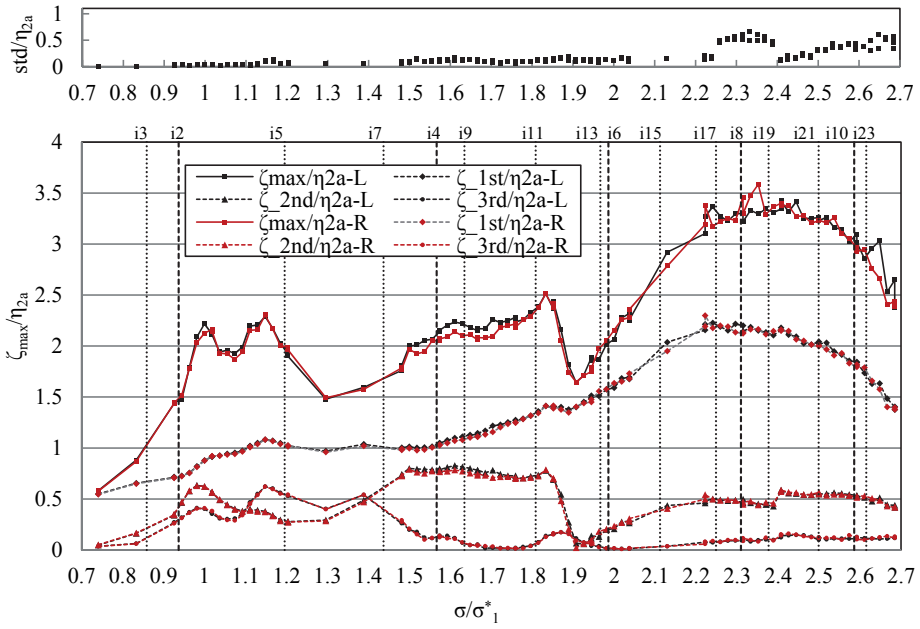

Figure 4-31. $Sn = 0.6760$. Explanation is given in caption of Figure 4-30.

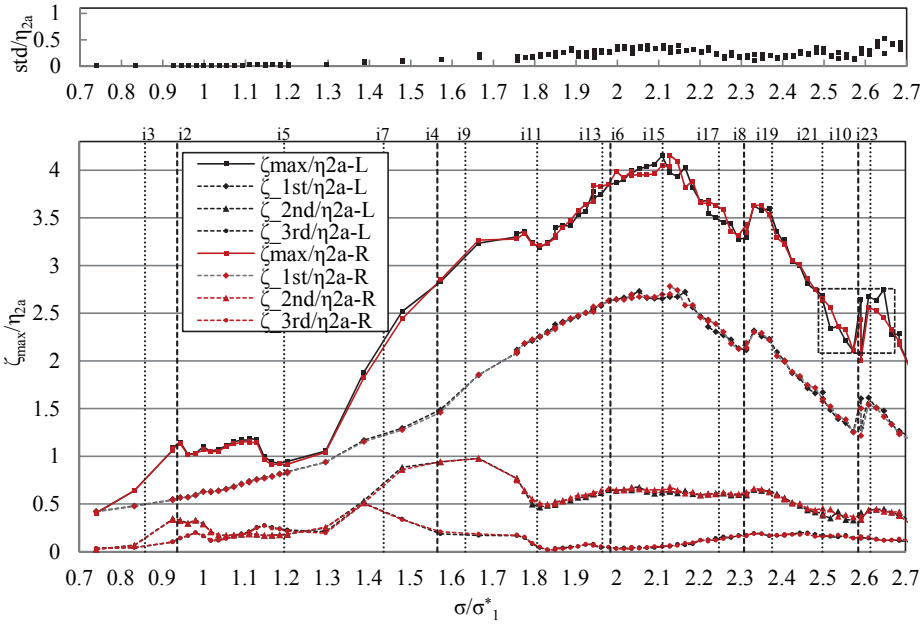

Figure 4-32. $Sn = 0.7960$. Explanation is given in caption of Figure 4-30.

Sn=0.844. The response curves plotted in Figure 4-33 for $Sn = 0.844$, shows reduced responses near σ_1^* . However, a double peak behavior is still visible. The peak at i_2 is clearly due to the secondary resonance of mode number 2. The time history of the wave elevations show that the peak on the right side of the double peak is due to the nonlinear amplifications of many higher harmonics of the forcing frequency. However it cannot be related to the secondary resonance of higher modes in the clean tank marked by i_{2k} and i_{2k+1}. For larger forcing frequencies, the amplitude of the third harmonic component ξ_{3rd}/η_{2_a} is largest at $\sigma/\sigma_1^* = 1.389$ which is just on the left side of i_7 on the horizontal axis. Further right on the frequency axis the secondary resonance of mode number 4 causes a resonant peak close to i_4 on both ξ_{max}/η_{2_a} and ξ_{2nd}/η_{2_a}.

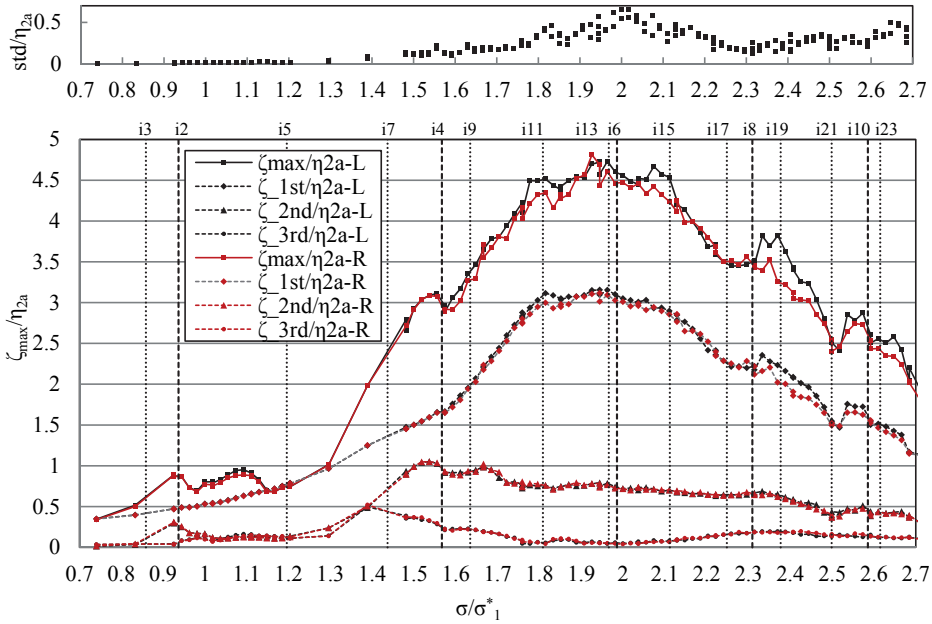

Figure 4-33. $Sn = 0.844$. Explanation is given in caption of Figure 4-30.

Sn=0.892. Figure 4-34 contains response curves measured for $Sn = 0.892$. Secondary resonance of mode number 2 causes a relatively small peak on the curve of maximum steady-state responses $\xi_{max}/\eta_{2_a}$and the second harmonic component ξ_{2nd}/η_{2_a} at i_2. Unfortunately the information is not enough around $\sigma/\sigma_1^* = 1$ to assess the presence of the double peak behavior observed for the previous screens with lower solidity ratios. Considering the curve of total wave amplitude response, ξ_{max}/η_{2_a}, 5 soft-spring jumps are marked by numbered arrows in Figure 4-34. The jumps numbered 1-4 are mostly due to the nonlinear amplification of higher harmonics. For instance the jump number 1 is at a frequency where the third harmonic component shows a local peak. The same can be said for jumps number 2-4 but in connection with the amplitude of the second harmonic component ξ_{2nd}/η_{2_a}. The jump number 5 is probably due to the resonance at σ_1^{**} which shows a soft-spring behavior. The other jumps seen on the curve for ξ_{max}/η_{2_a}on the right side of marking line i_{11} are mostly related to the local three-dimensional effects. Three-dimensional effects are accompanied with irregular

responses. The latter means that the repetition of the experiments may cause the mentioned jumps to occur at slightly different frequencies.

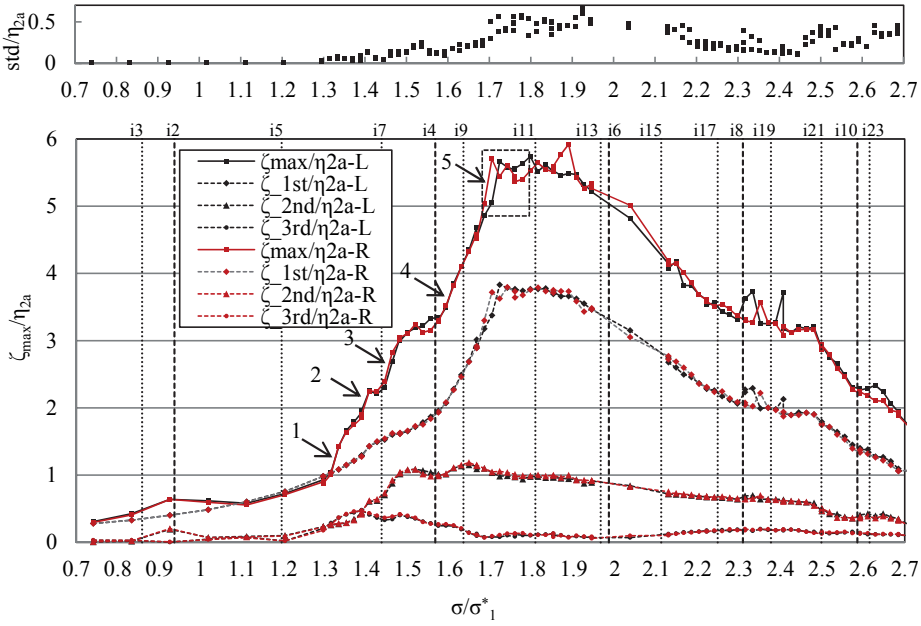

Figure 4-34. $Sn = 0.892$. **Explanation is given in caption of Figure 4-30.**

4.3 Closure

In shallow/intermediate depth, $h/l = 0.12$, the forcing amplitude $\varepsilon = 0.01$ is sufficient to trigger small-water-depth non-linear phenomena such as large nonlinear amplification of higher harmonics of the oscillation frequency. Secondary resonance is more pronounced in shallow water than in finite depth and causes clear extra resonance peaks in the total range of tested forcing frequencies especially when the solidity ratio is between 0.7 and 0.9. A new phenomenon is the appearance of "extra" harmonic components of the forcing frequency in the measured sloshing responses. Extra harmonics oscillate with $k\sigma$, where k is not an integer number. These harmonics are seen for frequencies around the third natural frequency of the clean tank and amplified through non-linear energy transfer to frequencies smaller than the forcing frequency. These extra harmonics can cause standing modulated waves with steady beating periods when they oscillate with frequencies close to the resonant sloshing frequencies. Increasing the solidity ratio of the screen changes both the frequency range associated with extra harmonics and the magnitude of maximum elevations of the steady-state wave system. Increasing the forcing amplitude to $\varepsilon = 0.05$ and conducting the experiments in a slightly larger water depth $h/l = 0.125$ lead to formation of very violent flows. Liquid impact on the vertical walls and on the screen, strong three-dimensional flows, very intense liquid fragmentation and highly accelerated liquid-to-gas jet flows in the screen zone are examples of the special, non-linear free-surface effects for this experimental condition. The impact events on the vertical walls are

visually and theoretically investigated. The theoretical investigation is based on Peregrine and coworkers' pressure impulse theory that needs spatial and temporal details of the impact event. Estimation of the pressure impulse on the vertical walls for $Sn = 0.4725$ and $\sigma/\sigma_1^* \approx 1$ predicts values comparable to the previous values taken by other investigators, for instance by Abramson et al., (1974) (Faltinsen & Timokha, Sloshing, 2009) for shallow water sloshing in a clean tank. This suggests a new set of experiments with direct pressure measurements on the walls that needs to be conducted in the future.

Investigating the video recordings the following observations and conclusions are made. The screen can reduce the risk of liquid impact on the vertical end wall only for the frequencies around the lowest natural frequency of the clean tank and for solidity ratios larger than 0.7. The impact on the walls appears for larger solidity ratios when a clearly isolated sloshing in the two compartments is present and the forcing frequency is near the lowest resonant frequency of a compartment. The impact events are also seen on the screen for the smallest and largest solidity ratios for forcing frequency ranges covering the second and the third natural frequencies of clean-tank sloshing. The impact on the screen increases for large solidity ratios. Considering the above observations one should be aware that installing a screen in the tank middle when the forcing amplitude is large and the water depth is small does not necessarily reduces the probability of occurrence of sever liquid impact events on the wall or on the screen for all combinations of solidity ratio and desired ranges of forcing frequencies in shallow liquid conditions.

5 Application of Computational Fluid Dynamics

5.1 Introduction

Computational Fluid Dynamics (CFD) based on the finite volume method is used in this chapter to test its ability in prediction of non-linear and non-violent free-surface effects in presence of a screen in the middle of the tank. The simulations are performed with laminar flow assumptions. Instantaneous evolution of the air/water interface, i.e. free surface, is captured by the Volume Of Fluid (VOF) method. The nature of the VOF method allows capturing local jet flows from liquid to air due to presence of free-surface piercing structures (here screen).

CFD simulations are used to provide information regarding flow details in the domain such as distribution of velocity and pressure around the screen and near the free surface. Hydrodynamic forces imposed on the screen (not measured in the experiments) due to liquid sloshing are estimated as well.

OpenFOAM which is an open source package is used for the numerical simulations. Before investigating the main problem, i.e. sloshing in presence of a screen, the code is verified and validated. In the verification stage (section 5.2), the governing equations used for formulating the problem are described and the methodology of the solution is explained. The validation stage (section 5.3) considers first sloshing in a clean tank with weakly nonlinear free-surface effects. Next a stronger non-linear case is tested. The results are validated against experimental results obtained in a rectangular tank. Effect of a bottom-mounted baffle in the tank middle on sloshing is tested for validation before running simulations in a screen-equipped tank.

The numerical simulations and the results in the screen-equipped tank are given in section 5.3.3.2. The results include simulations for two solidity ratios $Sn = 0.4725$ and $Sn = 0.7875$ in shallow water depth, $h/l = 0.12$ and small non-dimensional horizontal forcing amplitude $\varepsilon = \eta_{2_a}/l = 0.01$.

5.2 Method of solution of two-phase flow in OpenFOAM

OpenFOAM is an open source finite-volume based package that includes solvers for variety of different problems in fluid mechanics. The solver used here is called interFOAM which makes use of the Volume Of Fluid (VOF) method to capture the interface of two incompressible and immiscible fluids. It can work on static and moving grids[1].

5.2.1 Selection of coordinate system

The numerical computations may be performed in Earth-fixed (inertial) or tank-fixed (non-inertial) coordinate systems. Working with an Earth-fixed coordinate system requires a moving grid that should experience the excitation motion responsible for

[1]The network or the grid made of Control Volumes (CVs) distributed over a numerical domain

sloshing in the tank. This needs updating the grid coordinates at each time step and resolving the boundary conditions at new positions. In the second option, the calculations are carried out in a fixed numerical domain and the effect of tank motion is forced by applying a body force in the momentum equation. This option is used in the current study because of its simplicity and smaller computational time. Comparison between simulations using both options shows longer computational times for the moving-grid method increasing with the number of Control Volumes (CV) inside the grid.

The Navier-Stokes momentum equation for an incompressible fluid in a conservative form in a tank-fixed coordinate system is (Faltinsen & Timokha, Sloshing, 2009):

$$\frac{\partial \boldsymbol{u}}{\partial t} + \nabla.(\boldsymbol{uu}) = -\frac{\nabla p}{\rho} + \boldsymbol{g} + \nu\nabla^2\boldsymbol{u} - \boldsymbol{a}_o - (\boldsymbol{\omega} \times \boldsymbol{v}_o) - \boldsymbol{\omega} \times \boldsymbol{r} - 2(\boldsymbol{\omega} \times \boldsymbol{u}) \quad - \boldsymbol{\omega} \times (\boldsymbol{\omega} \times \boldsymbol{r}). \tag{5.1}$$

Here $\boldsymbol{u}$ is the velocity vector relative to the tank-fixed coordinate system. $\boldsymbol{a}_o$ and $\boldsymbol{v}_o$ are the tank's acceleration and velocity relative to an Earth-fixed coordinate system. $\boldsymbol{\omega}$ is the rotational velocity of the coordinate system about a point connected with vector $\boldsymbol{r}$ to its origin. The variables in (5.1) represented in bold-face are vectors. The sixth and seventh terms on the right hand side of the equation are Coriolis and centripetal accelerations. The time derivative $\frac{\partial \boldsymbol{u}}{\partial t}$ means time differentiation of $\boldsymbol{u}$ at a fixed point in the tank-fixed coordinate system. This time differentiation does not apply on the unit vectors of the tank-fixed coordinate system. All variables including gravitational acceleration are expressed with respect to the directions of the tank-fixed coordinate system. In the current study rotational motions are not considered leaving $\boldsymbol{a}_o$ as the only non-inertial acceleration term.

5.2.2 Governing equations of a two-phase flow

Air and water are two phases with large difference in density ρ and viscosity μ sharing an interface (so-called free surface) in the sloshing tank. Numerically, two main different approaches are used to resolve the free surface. One approach is to follow or *track* the free surface as a sharp boundary. In this approach, the CVs at the interface are deformed to satisfy: a) the so-called kinematic free-surface boundary condition, i.e. continuity of the normal velocity, and b) dynamic free-surface boundary condition, i.e. continuity of the normal and tangential stresses on the interface. Another method is to *capture* the interface or the free surface using a fixed grid that doesn't provide a completely sharp estimate of the free surface. This method is used in this study. Generally, both phases, gas/air or liquid/water, are included in the numerical domain and the interface between them is estimated using an indication function α. The indication function is normally a step function defined as,

$$\alpha = \begin{cases} 1, & liquid\ phase(water) \\ 0, & gas\ phase(air) \end{cases} \tag{5.2}$$

α is also called volume of phase fraction or Volume of Fluid (VOF) function. The location of the interface is where in the numerical domain α changes from 0 to 1 or vice versa. The quality of the captured interface is depending on the local grid size and orientation of the CV's surfaces at the interface. The VOF method is powerful as it can

handle discontinuous free surface profiles. The latter phenomena always occur in a sloshing tank equipped with a surface piercing screen.

A simulation starts by first marking the liquid and gas phases in the numerical domain as defined in (5.2). When the tank is excited the volume of fraction is transported by applying the transportation law (Ferziger and Peric 2002) for an incompressible fluid:

$$\frac{\partial \alpha}{\partial t} + \boldsymbol{u} \cdot \nabla \alpha = 0. \tag{5.3}$$

In general on a fixed grid the interface is not aligned with the CVs surfaces. This means CVs that are lying on the free surface should carry both values of $\alpha = 1$ and 0 which is numerically impossible. Instead a value of $0 \leq \alpha \leq 1$ is calculated for these CVs. In fact CVs with $0 \leq \alpha \leq 1$ construct the free surface. The minimum possible thickness of the interface is "one" CV normal to the interface. To achieve a thin interface, the convective term of equation (5.3), $\nabla.(\alpha \boldsymbol{u})$, should be discretized carefully. In the original VOF method (Hirt & Nichols 1981) the convective term $\nabla.(\alpha \vec{u})$ is discretized using donor-acceptor method which combines upwind and downwind flow information and the local slope of the free surface to achieve a thin/compressed interface. An important note is that the solution of (5.3) should be bounded between zero and one. Muzaferija and Peric (1998) suggest a simple scheme which takes care of boundedness of α and results in a thin and locally smooth free surface. According to them their scheme provides an interface usually with one to three CVs thickness across the interface. They have applied their method to simulate three-dimensional sloshing in a chamfered tank (Peric, Zorn, el Mokhtar, Schellin, & Kim, 2009). Their applied method is a modified derivation of the fundamental work of Ubbink (1997). In his method a local CFL number is defined based on the average flow flux passing through the CV faces in the free-surface zone in order to control the amount of phases leaving/entering a CV. The latter removes the generation of non-physical values $\alpha > 1 \; or \; \alpha < 0$ in the interface CVs. This CFL number is called *alphaCo* and defined as $alphaCo = \frac{1}{2}\frac{\sum_{i=1}^{6}|\phi_i^n|}{V_{CV_n}}\Delta t$ for each single control volume. The maximum *alphaCo* is used to determine the next time step of the solution.

In OpenFOAM, the boundedness of α and compression of the interface is achieved by means of introducing an artificial convective term to the left side of (5.3) (Rousche, 2002),

$$\frac{\partial \alpha}{\partial t} + \nabla \cdot (\alpha \boldsymbol{u}) + \nabla \cdot \left(\boldsymbol{u_r} \alpha (1-\alpha)\right) = 0 \tag{5.4}$$

$\nabla.(\boldsymbol{u_r}\alpha(1-\alpha))$ contains $\alpha(1-\alpha)$ making it effective only inside the interface. Therefore it does not significantly influence the solution outside the interface. $\boldsymbol{u_r}$ is a velocity field used for compression of the numerical free surface.

In a finite volume discretization, volume integrals are converted to surface integrals by applying Gauss theorem. For instance equation (5.4) is written in a finite volume format as,

$$\int_{\boldsymbol{V_{CV}}} \frac{\partial \alpha}{\partial t}\, dv + \int_{S_{CV}} \alpha \boldsymbol{u} \cdot \boldsymbol{dA} + \int_{S_{CV}} \alpha(1-\alpha)\boldsymbol{u_r} \cdot \boldsymbol{dA} = 0. \tag{5.5}$$

where calculation of convective integrals needs evaluation of $\boldsymbol{u}$, $\boldsymbol{u_r}$ and α at CV faces. V_{CV} and S_{CV} are the volume and surrounding area of a CV. How $\boldsymbol{u_r}$ is computed can be understood from the semi-discretized version of Equation (5.5) :

$$\int_{V_c} \frac{\partial \alpha}{\partial t}\, dv + \sum_{i=1}^{n} \boldsymbol{u}_{f_i} \cdot \boldsymbol{S}_{f_i}\, \alpha_{f_i} + \sum_{i=1}^{n} \boldsymbol{u}_{\boldsymbol{r}_{f_i}} \cdot \boldsymbol{S}_{f_i}\, \alpha_{f_i}\left(1-\alpha_{f_i}\right) = 0. \tag{5.6}$$

where

$$\boldsymbol{U}_{r_{f_i}} \cdot \boldsymbol{S}_{f_i} = \boldsymbol{n}_{f_i} \cdot \ \boldsymbol{S}_{f_i}\, min\left(max\left(\left|\frac{\phi_i}{|\boldsymbol{S}_{f_i}|}\right|\right), c_\alpha \left|\frac{\phi_i}{|\boldsymbol{S}_{f_i}|}\right|\right). \tag{5.7}$$

$\boldsymbol{n}_{if}$ and $\boldsymbol{S}_{f_i} = |\boldsymbol{S}_{f_i}|\boldsymbol{n}_{f_i}$ are the unit normal vectors of the interface on a CV face and CV face area vector. The subscript f means that the corresponding variable is calculated on a CV face. $\phi_i = \boldsymbol{u}_{f_i} \cdot \boldsymbol{S}_{f_i}$ is the flow flux at face i of CV_i.

Equation (5.6) is solved explicitly using the velocity field resulting from the solution of the momentum equation.

Velocity and pressure fields are found by solving the conservation of mass and momentum. The momentum equation should account for the sharp gradients of density ρ and viscosity μ at the vicinity of the free-surface due to phase change. In order to consider this fact in the numerical computations, the divergence of the laminar stress tensor $\boldsymbol{\tau}$ in equation (5.1) is reformulated as (Rousche, 2002):

$$\begin{aligned} \nabla \cdot \boldsymbol{\tau} &= \nabla \cdot \left(\mu\left(\nabla \mathbf{u} + (\nabla \mathbf{u})^{\mathrm{T}}\right)\right) \\ &= \nabla \cdot (\mu \nabla \mathbf{u}) + \ \nabla \cdot (\mu (\nabla \mathbf{u})^{T}) \\ &= \nabla \cdot (\mu \nabla \mathbf{u}) + \ (\nabla \mathbf{u}) \cdot \nabla \mu + \mu \nabla (\nabla \cdot \mathbf{u}) \\ &= \nabla \cdot (\mu \nabla \mathbf{u}) + (\nabla \vec{u}) \cdot \nabla \mu \end{aligned} \tag{5.8}$$

The superscript T means transpose. For the sake of simplicity of applying boundary conditions for the pressure, another modification is made to the pressure term by decoupling the pressure into hydrostatic and dynamic parts. The pressure is therefore,

$$p = p_{-\rho g h} + \rho \boldsymbol{g} \cdot \boldsymbol{x}. \tag{5.9}$$

$\boldsymbol{x}$ is the position vector and $p_{-\rho g h}$ is the dynamic pressure or pressure minus its hydrostatic part.

Applying the gradient operator ∇ on both sides of the above equation gives:

$$\nabla p = \nabla\left(p_{-\rho g h}\right) + \rho \boldsymbol{g} + \boldsymbol{g} \cdot \boldsymbol{x} \nabla \rho \tag{5.10}$$

Combining (5.1), (5.8), (5.10), the final form of the momentum equation reads:

$$\begin{aligned} \frac{\partial (\rho \boldsymbol{u})}{\partial t} + \nabla \cdot (\boldsymbol{u}\boldsymbol{u}) = -\nabla\left(p_{-\rho g h}\right) + \nabla \cdot (\mu \nabla \boldsymbol{u}) + (\nabla \boldsymbol{u}) \cdot \nabla \mu \\ -\boldsymbol{g} \cdot \boldsymbol{x} \nabla \rho - \boldsymbol{a}_o. \end{aligned} \tag{5.11}$$

$\boldsymbol{x}$ is the position vector of CV's center measured from the coordinates origin. Equation (5.11) is solved for both phases on either sides of the interface and for those cells constructing the interface. For solving the momentum equation the local density ρ

and dynamic viscosity μ are calculated based on the local value of α in liquid, gas and interface regions,

$$\rho = \rho_{liquid}\alpha + (1-\alpha)\rho_{gas} \tag{5.12}$$

$$\mu = \mu_{liquid}\alpha + (1-\alpha)\mu_{gas} \tag{5.13}$$

Equations (5.12) and (5.13) give an average value for ρ and μ in the interface region. This artificial layer appearing in the numerical solutions carries momentum and energy which is not present in reality. To reduce this artificial momentum sufficiently small CVs should be used in the interface zone. In addition the numerical discretization of equation (5.4) should result in a sharp and thin interface.

In the next section the method of solution of the coupled momentum and continuity and volume of fraction is described.

5.2.3 The solution algorithm

The general algorithm of the solution procedure of a VOF solver for a transient problem can be summarized as follows(OpenCFD, OpenFOAM Source Code):

1) Initialization of all variables.

   At start, all the variables such as $\boldsymbol{u}$, p, α, ρ and μ are initialized at cell centers. OpenFOAM solves the equations over a collocated grid, i.e. all variables are stored at CV centers. The advantage is handling complex geometries and less complex equation indexing.

2) Before time integration, the time step is set and the CFL number Co is calculated using the average fluxes passing the faces of each control volume. The CFL number is called *Co*urant number for a one-dimensional case. By definition the CFL number $Co = u_i \Delta t / \Delta x_i$ states number of control volumes a fluid particle passes through in one time step in direction i. u_i, Δx_i and Δt are the fluid velocity, cell edge length in direction i and solution time step, respectively. For an explicit solution algorithm the stability conditions imply $0 \leq Co \leq 1$. In this study, the time step is set automatically according to a maximum desired CFL number selected before run time. Another input parameter is the maximum CFL number in the cells located in interface region where $0 < \alpha < 1$ which is denoted in OpenFOAM by alphaCo. At the beginning of each time step of the solution new alphaCo and Co maximum values are calculated and the ratio between them and the input values is found. The minimum ratio between these two values and a factor of 1.2 is chosen as a multiplication factor which amplifies or reduces the current time step. The maximum multiplication factor for time step is chosen as default to be 1.2 in OpenFOAM to avoid unstable oscillations (OpenFOAM documentation).

3) The initial phase fraction and location of the free surface is set. Equation (5.6) is solved using the initial fluxes and velocities and free surface is transported to a new location. Having α for all cells, ρ and μ are calculated using (5.12) and (5.13). Obviously, zero initial velocities do not affect the value of volume of fractions.

4) The new distribution of ρ, α and μ is used to perform a momentum prediction and continue with the PISO[2] algorithm (Issa 1983). The solution of momentum equations in the predictor stage gives a velocity field u^*. The semi-descritized version of the momentum equation solved in the predictor stage is

$$Au_i^* + H'u_i^* = -\frac{\delta {p_{-\rho gh}}^n}{\delta x_i} + s_i. \tag{5.14}$$

A and H' are diagonal and off-diagonal elements of left hand side matrix of discretized coefficients. ${p_{-\rho gh}}^n$ stands for the modified pressure obtained for the previous time step or taken from the initial pressure values. A is not velocity dependent and is a result of temporal discretization but H' changes every time that the velocity field is corrected; it actually comes from the contribution of neighbor cells in implicit discretization of convective, $\nabla \cdot (\boldsymbol{uu})$, and diffusive, $\nabla \cdot (\mu \nabla \boldsymbol{u})$, terms for current prediction or correction and also explicit discretization of the term $(\nabla \boldsymbol{u}) \cdot \nabla \mu$. s_i or the source term includes the effect of the terms $-\boldsymbol{g} \cdot \boldsymbol{x} \nabla \rho - \boldsymbol{a}_o$ from the previous time step or iteration. Obviously the predicted velocities u_i^* do not satisfy the continuity equation.

5) The predicted values for velocity should be corrected. In the first corrector step, a new velocity and pressure field u^{**} and p^{**} are found by enforcing the continuity. The new equation is,

$$Au_i^{**} = -\frac{\delta {p_{-\rho gh}}^{**}}{\delta x_i} + s_i - H'u_i{}^* \tag{5.15}$$

or

$$u_i^{**} = -A^{-1}\frac{\delta {p_{-\rho gh}}^{**}}{\delta x_i} + A^{-1}H'u^* + A^{-1}s_i. \tag{5.16}$$

u_i^{**} is assumed mass conservative, therefore applying divergence on the above equation leads to a Poisson equation for the corrected pressure ${p_{-\rho gh}}^{**}$,

$$\frac{\delta}{\delta x_i}\left(A^{-1}\frac{\delta {p_{-\rho gh}}^{**}}{\delta x_i}\right) = \frac{\delta}{\delta x_i}(A^{-1}H'u^* + A^{-1}s_i) \tag{5.17}$$

Now if the gradient of the pressure is computed in the cell centers and then interpolated to cell faces, applying the continuity divergence operator on these gradients will lead to decoupling of velocity and pressures on alternate cell centers. The remedy is to apply the so-called Rhie-Chow interpolation. This method implies that the gradients are calculated directly on the cell faces using cell center pressures. This method removes the oscillating pressure filed but introduces an inconsistency in calculation of pressure gradient in momentum and Poisson pressure equation. This scheme does not conserve energy and may cause instability problems. The error introduced to the system by this scheme is of the same order as the basic descritization error (Ferziger and Peric 2001). In brief the Rhie-Chow interpolation used in OpenFoam follows these steps for the pressure corrector step(OpenCFD, OpenFOAM Source Code):

[2] Pressure-Implicit Splitting of Operators

1. First a pressure independent velocity $u_0 = \frac{H}{A}$ is calculated at cell centers. H is equal to the right-hand side of (5.14) minus the product of the off-diagonal terms and predicted velocity, i.e. $H = s_i - H' u_i{}^*$.
2. u_0 is interpolated to cell faces to compute a flux $\phi_{u_0} = \boldsymbol{u_0} \cdot \boldsymbol{S_f}$. $\boldsymbol{S_f}$ is the area vector of a cell face.
3. An updated flux ϕ_0 is computed by subtracting the surface normal gradient of the density to ϕ_{u_0}: $\phi_0 = \phi_{u_0} + (-|\boldsymbol{g} \cdot h_f| \nabla_{nf} \rho) A^{-1} \cdot \boldsymbol{S_f}$
4. Equation (5.17) is solved for corrected pressure $p_{-\rho g h}{}^{**}$. The Rhie-Chow interpolation is applied on the descretization of the Laplacian of the modified pressure i.e. $p_{-\rho g h}{}^{**}$.
5. The computed pressures at the cell centers are then interpolated to the faces of each control volume to correct the flux ϕ_0. The updated flux is computed from $\phi_1 = \phi_0 - \left(A^{-1} \nabla p_{-\rho g h} \right)_f \cdot \boldsymbol{S_f}$. Here the effect of pressure is subtracted from the face fluxes.
6. The last step is to update the velocities at cell centers by applying the following correction: $u^{**} = u_0 + u_{correction}$. Where $u_{correction} = recon(A(\phi_1 - \phi_{u_0}))$ is the difference between the reconstructed velocities in the cell centers due to the fluxes ϕ_1 and ϕ_{u_0} at cell faces

This completes one corrector step. The error analysis by Issa (1986) shows that at least two pressure-velocity corrections are necessary to obtain a solution with an error smaller than the basic descritization error. Therefore the corrector step (step 5)) is repeated at least one more time.

6) If simulation time is not reached the next step of solution is started from step 2).

5.2.4 Selection of linear solvers

OpenFOAM uses iterative solvers for solving linear implicit and explicit equations with symmetric and asymmetric matrices. These solvers use smoothers or/and pre-conditioners to achieve faster convergence. Preconditioners reduce the number of iterations by increasing the propagation speed of information in the numerical grid. For a linear equation system $Ax = b$, in which A is the resultant matrix of discretization coefficients, x the unknown and b the known vector on the right-hand side, a preconditioner finds an M matrix such that its multiplication with the equation system results in a matrix system which is computationally cheaper. For a *left* preconditioner the modified equation is $M^{-1}Ax = M^{-1}b$. Within every preconditioner a smoother may be used for performing the iterations. In case of using a multigrid solver/pre-conditioner smoothers are essential for iterations (Behrens, 2009).

Solution of the linear implicit equation for velocity in the predictor stage is performed by an iterative solver known by OpenFOAM as smoothSolver which uses a Gauss-Seidel smoother for iterations. The Gauss-Seidel smoother is applicable for system of equations having matrices with non-zero diagonal elements. However, the convergence is only guaranteed if the matrix is diagonally dominant or symmetric and positive definite.

Before solving the pressure Poisson equation (equation (5.17)) in corrector step, an improvement is applied on the pressure field by a Preconditioned Conjugate Gradient

solver (PCG) which is applied on LDU[3] matrices. The preconditioner is GAMG which is the short form for Geometric Agglomerated Algebraic Multigrid or Generalized Geometric-Algebraic Multi-grid as mentioned in the OpenFOAM manual. GAMG is a multigrid solver that finds quick solutions first for a coarsened grid and uses those solutions for solving the finer grids. The coarse grid solution smoothes out the high frequency errors. Coarsening the grid can be done geometrically (geometric multigrid) on the grid or algebraically by decomposing the matrix to sub-matrices. The smoother used with the GAMG solver/preconditioner is DIC Gauss-Seidel applicable for symmetric matrices. This smoother first applies a simplified Diagonal-based Interpolated Cholesky (DIC) smoother which may introduce some large-local errors. This issue is removed by applying a Gauss-Seidel smoother.

After pre-correction of the pressure equation matrices, the first pressure correction equation is solved by a GAMG solver using a DIC smoother.

The final pressure correction equations is solved by a PCG solver using a GAMG geometric-multigrid solver using a DIC Gauss-Seidel smoother. Table 5-1summarizes the solvers, preconditioners and smoothers used in one time step of solution.

Table 5-1 Selection of solvers, preconditioners and smoothers for each step of solution in the PISO algorithm

Solution stage	Solver	Preconditioner	Smoother
Predictor	smoothSolver	-	Gauss-Seidel
Corrector (pre-correction)	PCG	GAMG	DICGauss-Seidel
Corrector(first)	GAMG	-	DIC
Corrector(final)	PCG	GAMG	DICGauss-Seidel

Once the velocity and pressure fields are updated, equation (5.6) is solved using the known velocities. The solver is called MULES which stands for Multidimensional Universal Limiter with Explicit Solution (OpenCFD, OpenFOAM Documentation). As OpenFOAM documentation says " it solves a convective-only transport equation using an explicit universal multi-dimensional limiter". Limiters are used to control the solution by taking into account the local sharp gradients α in the interface region.

5.3 Simulation of sloshing

The code is validated against experimental results for sloshing in a clean and a screen-equipped tank. Small amplitude transient sloshing in a clean tank is first tested. Next, the non-linearity of the free surface is raised by increasing the forcing amplitude. Before validating the code for sloshing in the tank equipped with a screen, sloshing in a tank with a bottom-mounted baffle is considered. In a baffled tank, the vortex shedding due to flow separation at the sharp edge of the baffle generates larger hydrodynamic damping relative to the viscous damping in the boundary layer attached to the tank walls. The density of the distributed CVs near the sharp edges of the baffle must be sufficient to capture the details of the velocity and pressure fields.

[3] A symmetric matrix factorized into its elements on the diagonal (D), above the diagonal (U) (upper triangle) and below the diagonal (L) (lower triangle).

5.3.1 Clean tank

5.3.1.1 Weak free-surface nonlinearities

The experimental results used for validation were obtained in a rectangular tank with inner dimensions Length x Breadth x Height = 1 m x 0.1 m x 0.98 m filled with water up to 0.833 m depth ($h/l = 0.833$). The tank is excited along its longest length following a harmonic oscillation $\eta_2 = \eta_{2_a}(1 - \cos(\sigma t))$ where $\eta_{2_a} = 0.00465\ m$ and $\sigma = 6.075$ rad/s ($\sigma/\sigma_1^* = 1.1$).

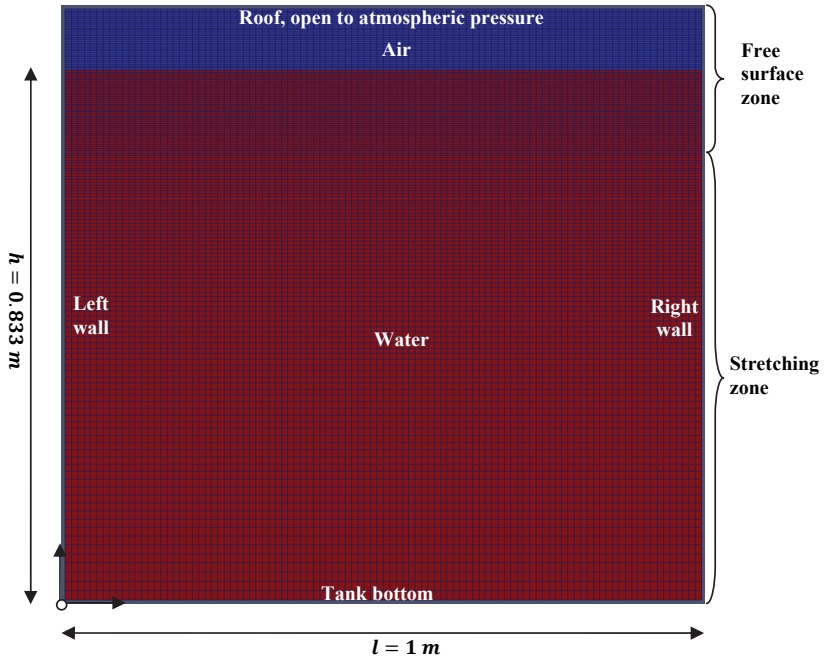

Figure 5-1. Computational domain for validation in a clean tank. The red and blue areas represent water and air phases, respectively. The total height of the domain is 0.93 m. The free-surface zone contains uniform grid distribution in both horizontal and vertical directions. For the stretching zone the grid is non-uniform in the vertical direction with a growth factor of 1.0164 toward the bottom.

Numerical simulations are conducted in a two-dimensional rectangular domain with the same dimensions as the inner dimensions of the tank used in the experiments except for the height that is lower in the numerical domain to reduce the computational time. 100 CVs are distributed evenly in the direction of motion. The latter means 200, 100 and 67 elements per wavelength for the first, second and the third lowest natural modes, respectively. In the vertical direction, the CVs are distributed in two zones. In the free-surface zone (see Figure 5-1) 60 CVs are uniformly distributed. This zone covers maximum and minimum wave elevations. The height of each CV is 3 mm. The convergence study showed that the smaller height elements do not significantly increase the accuracy of the results. In the lower part of the domain, between the free-surface zone and the tank bottom, the height of the CVs is increased smoothly toward the tank

bottom (stretching zone in Figure 5-1) such that the ratio between the height of the last and the first CV is 5. The latter means a growth factor[4] of 1.0164. Information regarding the numerical domain, its dimensions, phase fractions and domain boundaries are presented in Figure 5-1.

The boundary layer is not resolved in the numerical simulations. The main reason is that effect of lateral walls cannot be included in a two-dimensional simulation. The contribution of lateral walls in the damping caused by the boundary layer on all surrounding walls is as large as 70%. Therefore resolving the boundary layer only on the end side walls and the tank bottom will not result in the total boundary layer damping.

5.3.1.2 Selection of boundary conditions

Boundary conditions for velocity $\boldsymbol{u}$, pressure p^* and volume of phase fraction α are introduced in Table 5-2. The names or expression mentioned in the table are known expressions for boundary conditions in OpenFOAM (see (OpenCFD, OpenFOAM Documentation)).

For velocity $\boldsymbol{u}$, non-zero tangential values are allowed on the left, right and bottom walls. The latter means that the gradient of the tangential velocities are not zero along the walls. This condition known to OpenFOAM as "Slip", also applies the zero normal relative velocity on the walls. On the roof "pressurInletOutletVelocity" BC expresses that *air* phase is free to enter or exit the domain. The latter means the roof is open to atmospheric pressure (see Figure 5-2). This boundary condition applies zero normal gradients on all velocity components if the normal velocity is outgoing. If calculations require an inflow from the outside of the numerical domain, a fixed value, here zero, condition is applied to the tangential velocity component and the normal velocity will be calculated. In reality the tangential inflow velocity is not zero. However due to the very small ratio between the density of air and water the vertical flow enforcement of the light phase does not have a significant influence on the flow of the heavy phase.

For the modified pressure $p^* = p - \rho\vec{g}.\vec{x}$, "Buoyant Pressure" BC means that normal gradient of p^* on the walls should be calculated by taking into account the value of the density gradients at the boundaries. This can be seen from the modified momentum equation (Equation (5.11)). For instance for a rigid wall with zero velocity boundary condition, Equation (5.11) gives $\nabla p^* = -g.x\nabla\rho + \cdots$ that needs evaluation of $\nabla\rho$ on the vertical walls. The pressure boundary condition on the roof called "total pressure", applies a fixed-value on p^* calculated from specified total pressure $p_0 = 0$ and local velocity $\boldsymbol{u}$. For this condition the relation between local and total pressure is $p_0 = p + \frac{1}{2}\rho|\boldsymbol{u}|^2$ where $p^* = p - \rho\vec{g}.\vec{x}$.

On rigid boundaries, α is forced to have zero normal gradients to neglect the effect of surface tension. On the roof, "inletOutlet" condition expresses zero normal gradients for out flow and zero fixed-value for inflow.

[4] Ratio between the edge of two adjacent CVs

Table 5-2. Boundary conditions for the dependent variables on the domain boundaries. Condition names are known to OpenFOAM. Explanations are given in the text.

Variable	Boundary conditions on left, right and bottom walls	Boundary conditions on the roof
$\boldsymbol{u}$	Slip	pressurInletOutletVelocity
p^*	Buoyant Pressure	Total Pressure
α	Zero normal gradient	inletOutlet

5.3.1.3 Selection of numerical discretization schemes

Finite Volume methods make use of Gauss theorem for transforming the volume integrals into surface integrals. As a result the variables should be quantified on CV faces (see Equation (5.5)). This is done by interpolation of the nodal variable values in CV centers to their surrounding faces. The interpolation methods are selected for each term of the governing equations depending on their physical importance. Several temporal and spatial discretizations schemes are provided by OpenFOAM. For the temporal discretization, i.e. time integration, the implicit Euler schemes is used throughout this study. This scheme is first order accurate in time and needs very small time steps to provide satisfactory results. The author's experience is that the higher order methods such as second order backward integration and Crank-Nicholson cause instability problems. Considering the spatial terms in appearing in the momentum, Poisson and phase fraction equations, Table 5-3 lists the selected interpolation schemes for the corresponding terms enforced in the simulations.

Table 5-3. Selected discretization schemes for various terms of the applied governing equations.

Equation	Term	Scheme	Explanation
Momentum	$\frac{\partial(\rho \boldsymbol{u})}{\partial t}, \frac{\partial \alpha}{\partial t}$	Euler	First order implicit
Momentum	$\nabla \cdot (\boldsymbol{uu})$	Upwind (clean tank)	Upwind interpolation
Momentum	$\nabla \boldsymbol{u}$	Linear	Linear interpolation
Momentum	$\nabla \cdot (\boldsymbol{uu})$	Blended, $b = 0.5$ (screen)	Combined upwind and linear interpolation
Momentum	$\nabla(p^*), \nabla\rho, \nabla\boldsymbol{\mu}$,	Corrected	
Phase fraction	$\nabla \cdot (\alpha \boldsymbol{u})$	Van Leer	Van Leer limiter
Phase fraction	$\nabla \cdot \left(\boldsymbol{U_r}\alpha(1-\alpha)\right)$	Van Leer	Van Leer limiter
Poisson	Laplacian	Corrected	

The author has extensively investigated the combination of many of the available schemes in OpenFOAM. The selection of schemes listed in Table 5-2 is taken because of stability reasons and physical behavior.

5.3.1.4 Comparison between experimental and numerical results

The numerical results computed in the domain shown in Figure 5-1 are presented in Figure 5-2 together with the experimental results measured at 0.005 m distance from the vertical end walls (black line). The absolute value of the maximum and minimum responses in experiments is slightly different demonstrating the weak influence of nonlinearity of the free surface.

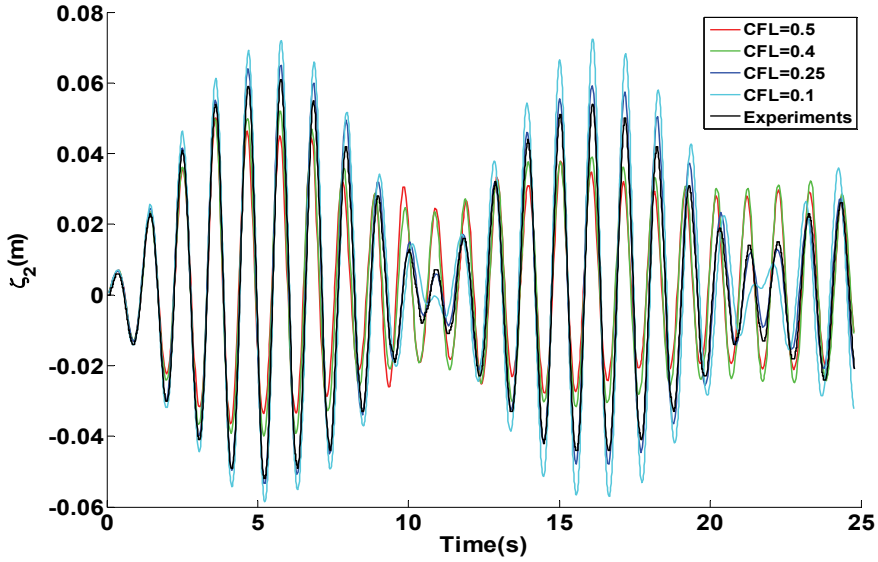

Figure 5-2. Comparison between numerical and experimental results and effect of CFL number (time step size) on the numerical results. The results present wave elevations at 5 mm distance from the vertical walls. The input parameters are h/l=0.833, $\varepsilon = 0.00465$, $\sigma/\sigma_1^* = 1.1$.

Combination of the response due to the forcing at $\sigma/\sigma_1^* = 1.1$ and transient effects oscillating with the lowest natural frequency an small damping leads to a beating behavior of the response waves. Figure 5-2 shows that the numerical simulations with CFL=0.25 and 0.1 provide a very good estimate of the beating periods. This shows that InterFOAM solver can capture a very good estimate of the lowest natural frequency of sloshing for sufficiently small time steps. Another fact is that the amplitude of the waves decreases in the experiments due to hydrodynamic damping in the boundary layers at the bottom and vertical surrounding walls. The results for the first three CFL numbers show decay in the maximum wave elevations. The decay becomes weaker for the smaller CFL values and the smallest CFL produces non-decaying wave elevations that are larger than the wave elevations measured in experiments. As a matter of fact the only source of damping in the computations is numerical diffusion which is reduced by decreasing the time step (or decreasing the CFL number) leading to increase of the maximum wave elevations for both beating periods. The results with CFL=0.25 shows the best prediction of the experimental results in terms of both wave elevations and beating periods among the other numerical curves. This is because the amount of damping due to numerical diffusion is almost the same as viscous diffusion due to boundary layer flow in the experiments. This will be more explained later by conducting a free decay test of sloshing waves. Even though the results for CFL=0.1 are accompanied with almost no damping, they are less similar to experimental results than the results for CFL=0.25.

To compare the damping level in numerical simulations with experiments, the results of free decay of sloshing waves are used. The results are shown in Figure 5-3. The wave elevations obtained for CFL=0.5 and 0.4 are accompanied with large numerical damping and decaying quickly during the time while the values presented for CFL=0.1 shows almost no decay. The results for CFL= 0.25 is the most similar to the

experiments. For this case, the numerical diffusion that causes artificial damping introduces almost the same amount of global damping as the boundary layer attached to the tank walls generates in the experiments (the effect of viscous bulk damping is believed to be negligible (Faltinsen & Timokha, Sloshing, 2009). The close similarity between the numerical results obtained for CFL=0.25 and results of experiments for forced-transient oscillation (Figure 5-1) and free decay oscillations (Figure 5-3) demonstrate the effect of global damping on the transient sloshing. However to achieve negligible numerical diffusion the CFL should be as small as 0.1 which is considered a very small value.

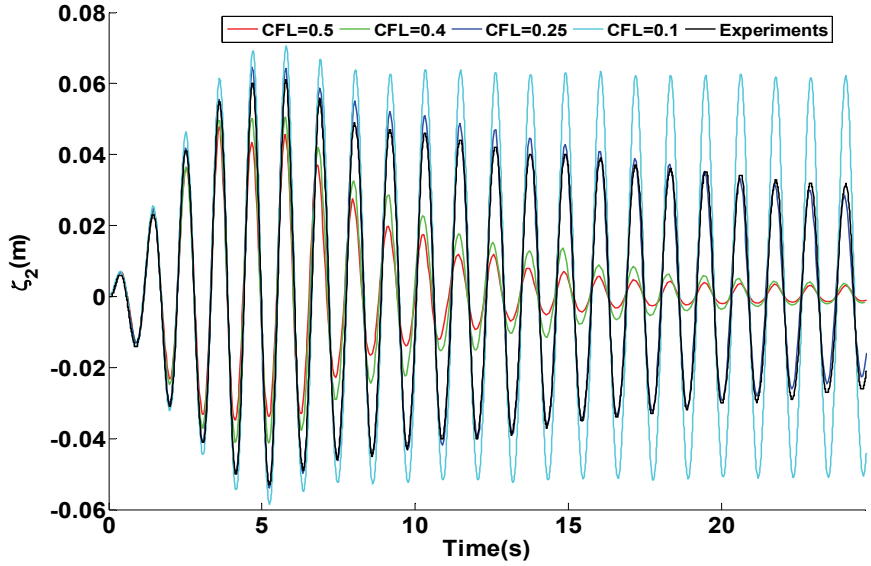

Figure 5-3. Free decay of sloshing waves at 5 mm distance from the vertical end wall. Comparison between the results of numerical calculations and experiments. $h/l = 0.833$, $\varepsilon = 0.00465$. Forcing frequency during excitation $\sigma/\sigma_1^* = 1.1$. The forcing motion stops at t=7.4 seconds.

Numerical experiments show that the descretization of the convective term $\nabla.(\boldsymbol{uu})$ of the momentum equation strongly affects the amount of numerical diffusion. The results shown in Figure 5-2 and Figure 5-3 are obtained by applying upwind scheme for discretization of the convective term. Although this scheme is numerically very diffusive, the results show that sufficiently small time steps can remarkably reduce the diffusive damping. Other higher order schemes such as linear central interpolation or second order upwind interpolations (both second order accurate on uniform grids) show less diffusive behavior. Numerical experiments show that these higher-order schemes can generate negative diffusive damping, i.e. during a decay test maximum elevations begin to increase instead of decreasing. Applying an upwind discretization does not show negative diffusion even for CFL=0.05. In fact there is a trade-off between precision, computational time and physical behavior of the numerical schemes. Here upwind scheme with small time steps is preferred. One also should note that the upwind scheme is very simple to implement unlike the other higher order schemes. This

property reduces the computational time. Moreover, an upwind scheme is non-conditionally stable (Ferziger & Peric, 2002).

5.3.1.5 Strong free-surface nonlinearities

To test out the performance of the code for simulation of sloshing with strong free surface nonlinearity, the forcing amplitude is raised to $\varepsilon = 0.01$. The depth ratio is now $h/l = 0.4$. The wave elevations are measured at 1 cm distance from the vertical walls. Strong nonlinearity causes amplification of more than one dominant mode leading to appearance of waves with maximum absolute elevations clearly larger than absolute minimums. Experiments show that excitation at $\sigma/\sigma_1^* = 1$ in a clean tank generates very large waves with wave-amplitude to forcing-amplitude ratio of $\frac{\zeta_a}{\eta_{2a}} > 60$ accompanied with roof impact and large wave overturning ending up with breaking. To avoid these effects the forcing frequency is taken sufficiently far from the resonance, i.e. $\sigma = 4.6068\, rad/s$ ($\sigma/\sigma_1^* = 0.9$).

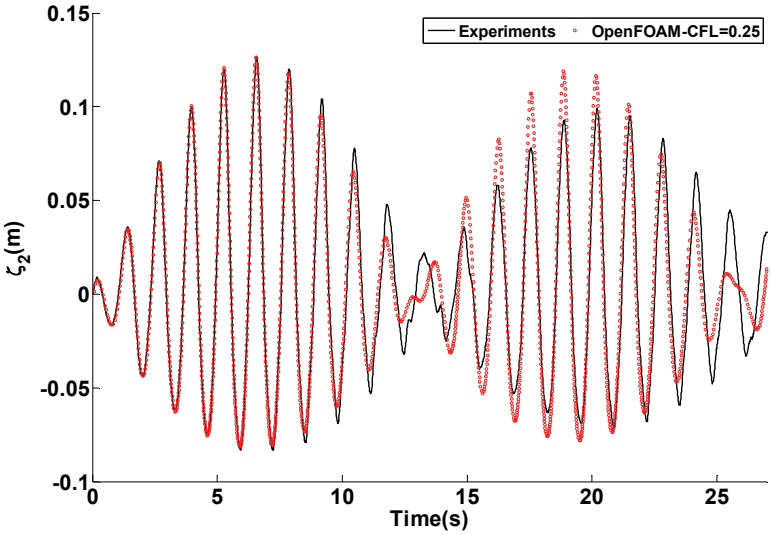

Figure 5-4. Wave elevations at 0.01 m distance from the vertical walls. The input parameters are $h/l = 0.4$, $\varepsilon = 0.01$, $\sigma/\sigma_1^* = 0.9$.

In the numerical domain, the grid is uniformly distributed in the vertical direction in the free-surface zone and it stretches up outside the free surface zone toward the tank bottom. In the horizontal direction, the grid is uniform everywhere. The tested CFL number is equal to 0.25. The numerical and experimental results are presented in Figure 5-4. Since the artificial numerical damping is smaller than the viscous damping in the boundary layer at the tank bottom and vertical surrounding walls, the transient effects are not dying out as fast as in the experiments. This is clear for the second beating period where experimental results show smaller responses. The beating period is underestimated by the numerical simulations and the numerical wave elevations are more similar to experiments in the beginning of the first beating period. These

differences can be related to unequal amount of damping in numerical and experimental results.

5.3.2 Baffled tank

Transient small amplitude sloshing in a baffled tank is considered. No experimental result is available for comparison. The numerical results will be compared with numerical computations by Liu and Lin (2008). They have applied spaced-averaged Navier-Stokes (momentum) equations that accounts for turbulence by means of Large Eddie Simulation (LES). They have also used the Volume Of Fluid (VOF) method for capturing the free surface. The baffle is in the tank middle and its tip is sufficiently far away from the free surface to avoid piercing it during sloshing. The main dimensions are $l = 1\,m$, $h = 0.5\,m$, baffle height $h_b = 0.375\,m$ ($h_b/h = 0.75$). The tank motion follows a harmonic excitation of $\eta_2 = \eta_{2_a}\sin(\sigma t)$ where $\eta_{2_a} = 0.002\,m$ and $\sigma = 5.29\,rad/s$ ($\sigma/\sigma_1^* = 0.995$). Figure 5-5 shows a good agreement between the computed wave elevations by Liu and Lin (2008) and OpenFOAM in the current study. The minor difference in the beginning of the simulations is due to different starting accelerations in the two numerical simulations.

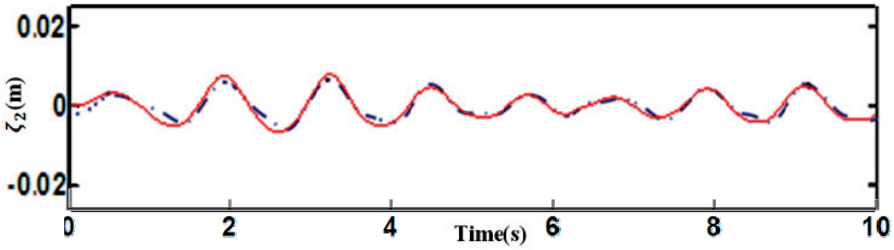

Figure 5-5. Wave elevation at the vertical wall in a tank with a vertically mounted baffle on the bottom. Solid line: OpenFOAM, dashed-dotted line: Liu and Lin 2008. $h_b/h = 0.75$, $\varepsilon = 0.002$, $h/l = 0.5$, $l = 0.5$ m.

Liquid sloshing causes the flow to separate from the sharp edges of the baffle and to generate vortices. The simulations show that at each half a period of oscillation, one vortex is shed and convected away from the tip of the baffle. 4 vortices shedding during two periods of oscillations are made visible in Figure 5-6. These vortices are convected with the flow to the free surface zone and interact with the free surface. However, no deformation is visible in the simulations at the free surface due to influence of the vortices. In Figure 5-6, the velocity vector is plotted on top of the vorticity field. The velocity vectors are of the same size and do not represent the magnitude of the velocity.

The vortex shedding increases the global damping and reduces the time needed to reach steady-state waves. Liu and Lin (2008) have used turbulence modeling that cause faster diffusion of vortices and they have not refined their grid around the baffle. In the current study, small sized CVs are used near the baffle and close to the tip. This is seen from the larger density of the velocity vectors near the baffle in Figure 5-6.

Analogous to a screen, one can define a solidity ratio $Sn = 0.75$ for a submerged baffle with $h_b/h = 0.75$. The experimental results in chapter 2 for $h/l = 0.4$, $\varepsilon = 0.001$ showed that the non-dimensional steady-state responses are highly reduced for

$Sn > 0.7$. The main reason is the flow obstruction by the screen in the tank middle which drastically changes the flow field inside the tank. This scenario is present in Figure 5-6 where due to flow obstruction by the baffle, the sloshing is almost isolated in the two sides of the baffle. In case of a clean tank, the maximum relative horizontal velocity occurs in the tank middle where the vertical velocity is almost zero. The latter situation is almost present for both compartments on the two sides of the baffle.

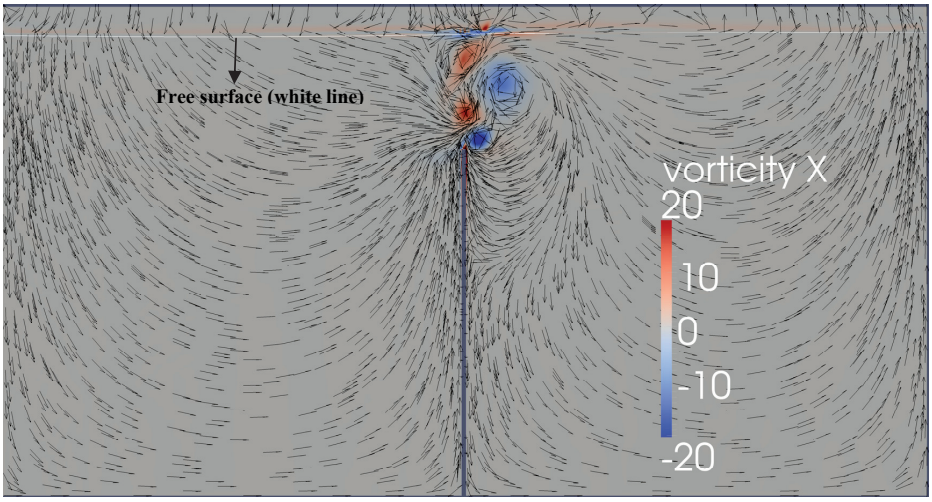

Figure 5-6. Velocity vectors plotted on top of vorticity field which is quantified by color scale at $t = 5.6$ seconds. The dimension of computed vorticity field is $1/(seconds)$. In order to produce a streamline-like picture, the length of the velocity vectors is kept the same everywhere and is not representing the velocity magnitude. X direction is normal to the plane.

5.3.3 Sloshing in a screen-equipped tank

InterFOAM solver was shown capable of modeling small amplitude sloshing in presence of an internal damping device, i.e. baffle in the previous section. The final test case, the main case in this chapter, is sloshing due to larger forcing amplitude $\varepsilon = 0.01$ and in presence of a slat screen which generates relatively larger damping than a vertical bottom-mounted baffle, for a fixed underwater solidity ratio. The simulation uses a two-dimensional representation of the model. Therefore, three-dimensional effects including the effect of the screen supports, wave breaking and turbulence cannot be included in the simulations. As discussed in chapter 2 the supports may matter if the solidity ratio is smaller than $Sn <\cong 0.5$.

A slat screen is in fact a combination of small-height horizontal baffles evenly distributed over the depth. The flow separation from the sharp edges of the slats causes vortex shedding. The vertical distance between the edges of two consecutive slats is 3mm. For the smallest solidity ratio $Sn = 0.4725$, the ratio between the height of the slot h_{so} and height of the slat h_{sa} is $\frac{h_{so}}{h_{sa}} = \frac{3}{2.7}$. According to Faltinsen and Timokha (2009), this ratio should be at least larger than two in order to neglect the interaction between the downstream flows behind two consecutive slats. Two solidity ratios will be studied here. For them, the ratio h_{so}/h_{sa} is smaller than two, meaning that the separated

vortices from the slats are so close that their interaction matters. The important note is that the total effect of the flow separation from all slat edges that applies a pressure drop in the tank middle should be correctly captured by numerical computations. There are local free-surface effects in the screen-zone such as wave breaking, liquid-to-gas jet flows and run-ups on the screen that affect the results especially for large solidity ratios when the forcing frequency is around the second natural sloshing frequency σ_2^* of the clean tank (see chapter 3, for instance Figure 3-8 and Figure 3-9). The experimental cases accompanied with the above-mentioned effects are not used for validations here. That is why only the experimental results for $Sn = 0.4725$ and $Sn = 0.7875$ are selected for validating the CFD result since they do not show strong influence of special free-surface effects. These strong free-surface effects while can be handled by the VOF method are computationally very expensive to simulate.

The screen imposes abrupt changes on the flow field in the middle of the tank. The size of the CV edges at the vicinity of the screen should be sufficiently small to capture the large gradients of flow velocities and pressure. For a fixed forcing frequency and amplitude, the dynamics and kinematics of the flow at the screen change with increasing the solidity ratio between 0 and 1.

5.3.3.1 Convergence studies

In a CFD study, a set of significantly different domain discretizations should be tested to achieve convergence for every single combination of forcing frequency σ and amplitude η_{2_a} and solidity ratio Sn. Therefore one expects a huge number of preliminary simulations (convergence studies). To reduce the number of preliminary simulations, one can take only a case associated with the largest horizontal velocity at the screen slots, i.e. lowest mode resonance and postulate that a converged solution for this case would cause a converged solution for the rest of the frequencies for a single solidity ratio. According to the experimental measurements for $h/l = 0.12$ and $\varepsilon = 0.01$ and $Sn = 0.4725$, the largest steady-state response occurs for $\sigma/\sigma_1^* = 0.9619$. The latter combination of parameters is chosen for performing a convergence study which will provide information about distribution of CVs in the numerical domain used for further simulations. However using a single grid for all computational cases is not very efficient because unnecessary large grids may be applied for less severe cases.

The screen divides the tank into two identical compartments. In each one a structured grid with non-uniform distribution in the horizontal direction is used. The grid distribution is uniform in the vertical direction. To account for large flow changes specially near the screen and also near the end walls the grid has to be refined at those areas. The length of the horizontal edges of the CVs are therefore increased from the screen toward the middle part of the compartment and then decreased toward the vertical end walls. The stretching pattern is controlled by two fixed stretching parameters r_1 and r_2, length of each compartment and total number of CVs. The stretching parameter $r > 1$, is the ratio between the length of horizontal edges of two neighbor CVs i.e. $r = e_{i+1}/e_i$. r_1 stretches up the edges from the wall and r_2 from the screen's vertical edge toward the tank middle. The smallest edge length belongs to CVs attached to the screen and those ones inside the slots. The largest horizontal edge is in the middle part of the tank where the two stretching areas share their largest edge. The distribution of the horizontal edges on one side of the screen and along the tank bottom

is shown in Figure 5-7. In Figure 5-7 the horizontal and vertical axis present the position of the midpoints of the horizontal edges m_i from the end wall and the length of the edges a_i, respectively.

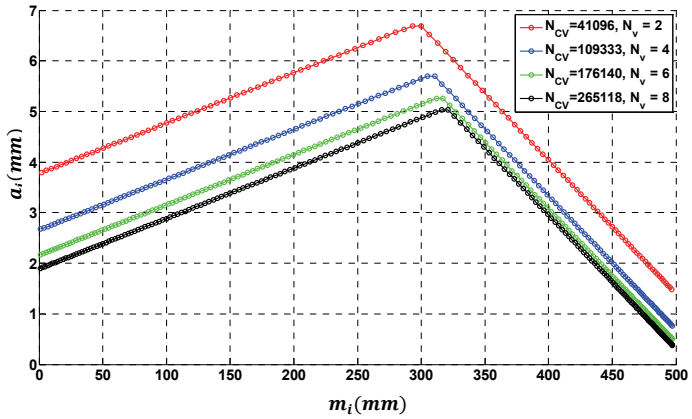

Figure 5-7. Variation of the CVs' horizontal edge length a_i between the wall and the screen as a function of the midpoint coordinates of the horizontal CV edges m_i on the tank bottom. Zero horizontal coordinate corresponds to the vertical wall. N_{CV} and N_v are total number of CVs in the whole domain and number of vertical CVs in a slot, respectively.

The boundary conditions applied on the surrounding walls and the roof are given in Table 5-2. No-slip conditions is enforced for the velocity on the screen.

Table 5-4. Properties of the grid distributions used in the convergence study. N: number of longitudinal CVs in one compartment. N_v: number of vertical CVs inside the slot. $r_1 = a_{i+1}/a_i$: Stretching factor near the wall. $r_2 = a_{i+1}/a_i$: stretching factor near the screen.a_{min1}: Size of the smallest CV edge adjacent to the wall. a_{min2}: size of the smallest CV edge adjacent to the screen. $a_{i_{max}}$: size of the longest longitudinal CV edge. a_v:size of the vertical edge of a CV inside the slot. $\frac{a_{i_{max}}}{a_v}$: Maximum aspect ratio. N_{total}: total number of CVs in the numerical domain.

N	N_v	r_1	$a_{min1}(mm)$	r_2	$a_{min2}(mm)$	$a_{i_{max}}(mm)$	$\frac{a_{i_{max}}}{a_v}$	N_{total}
116	2	1.01	3.7955	1.0268	1.4822	6.6925	3.8	41096
154	4	1.01	2.6730	1.0268	0.7630	5.6942	7.6	109333
180	6	1.01	2.1710	1.0268	0.5001	5.2634	10.5	176140
198	8	1.01	1.8990	1.0269	0.3771	5.0352	13.4	265118

Number of vertical CVs in the slots determines the size of the vertical edge of the elements because the grid is uniform in the vertical direction. In addition the CVs attached to the screen are forced to have a square shape, i.e. four equal lengths, in order to achieve the same accuracy for vertical and horizontal gradients of flow pressure and velocities. More information about the properties of the applied grid in the convergence study is given in Table 5-4. The height of the total fluid domain including both water and air is 0.23 cm to avoid excessive number of CVs. This height is also sufficiently high to avoid wave responses reaching the tank roof in the numerical domain.

Steady-state waves in numerical calculations and experiments are compared in Figure 5-8. The numerical results in the top panel of Figure 5-8 are *not* showing a

significant difference for 2, 4, 6 and 8 vertical CVs inside the slots although the largest grid size is 6 times greater than the smallest. This means either the fineness of elements is not very crucial for the current case or much smaller CVs should be used to capture very fine details. Considering the maximum steady-state wave elevation ζ_{max}, the over estimation by the numerical results is $\frac{\left|\zeta_{max(num)}-\zeta_{max(exp)}\right|}{\zeta_{max(exp)}} \cong 10\%$. Because both absolute minimum and maximum elevations in the numerical results are larger than the experimental results it cannot be out ruled that much smaller CVs are needed. However, the latter increases the computational time up to many hours making the numerical simulations impractical.

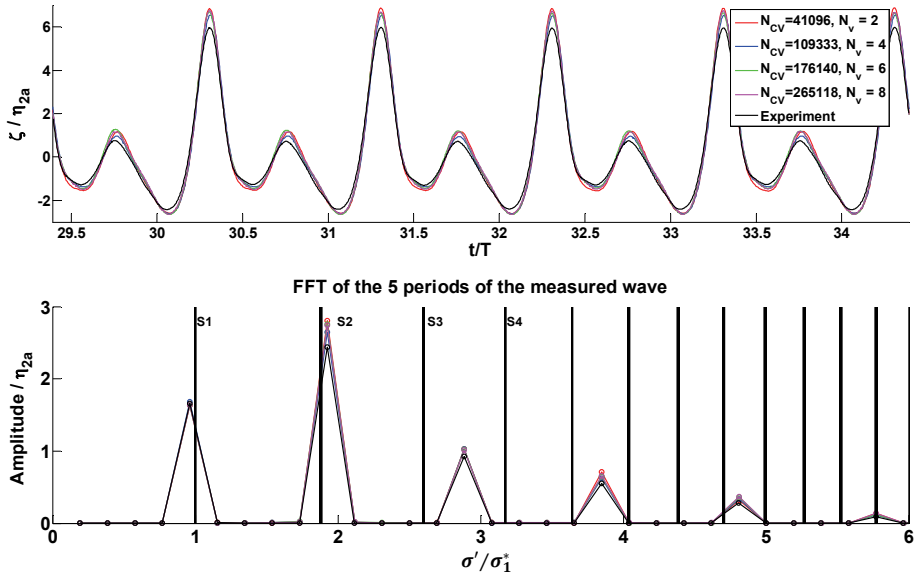

Figure 5-8. Comparison between the results of a grid convergence study and experiments. Top panel: Non-dimensional wave elevation at 1 cm from the vertical wall, Bottom panel: Non-dimensional amplitude of the frequency components in frequency domain. $h/l = 0.12$, $\varepsilon = 0.01$, $Sn = 0.4725$, $\sigma/\sigma_1^* = 0.9619$. The vertical lines, $S_1, S_2, \ldots$ in the bottom panel identify the linear natural sloshing frequencies in the clean tank. σ' is the frequency content of the measured signal calculated by FFT.

The bottom panel of Figure 5-8 presents the amplitude of the steady-state wave components. Except for the forcing component σ ($\sigma/\sigma_1^* = 0.9619$), the amplitude of the other frequency components 2σ, 3σ, … are over estimated by the numerical results. However, the amplitude of all components was predicted with the same trend as in the experiments. The amplitude of the 2σ-component is the largest among all harmonics of the forcing in both the numerical and experimental results due to secondary resonance of mode number 2 of sloshing in the clean tank. This fact demonstrates the capability of InterFOAM in capturing strong free-surface non-linearities.

Asymptotically speaking, the even modes do not cause cross flow through the screen and they are damped only by dissipation in the boundary layer attached to the wall. In the simulations, the boundary layer is not resolved which leads to overestimated values for 2σ and its harmonics $4\sigma, 6\sigma$. Attempts to resolve the boundary layer on the

bottom and vertical walls did not show significant changes in the results. In fact 70% of the boundary layer damping are generated on the vertical lateral walls that are not accounted for in the present two-dimensional simulation.

One should remember that in the simulations the flow is assumed to be two-dimensional and laminar everywhere. In addition the extra hydrodynamic damping effects of the screen supports are neglected. Estimations in chapter 2 showed that 2.3% to 7% extra damping might be introduced at the first resonance frequency by the presence of the screen supports when $Sn = 0.4725$.

All simulations were run in parallel by dividing the numerical domain into sub-domains with equal number of CVs. In general the computational time is very lengthy for the current study even with parallel computation. The main burden here is to reach steady-state regimes which may take many forcing periods to be established. This is depending on the forcing frequency and amplitude and also amount of damping (solidity ratio).

5.3.3.2 Numerical results and analysis for Sn=0.4725 and 0.7875

8 screens with $0.4725 \leq Sn < 0.9375$ were experimentally tested. Due to long computational time only two screens with $Sn = 0.4725$ and $Sn = 0.7875$ are selected for validation study. For the selected screens, the special free-surface effects such as wave breaking and strong wave run-ups on the walls are small and negligible.

a. $Sn = 0.4725$

Starting with $Sn = 0.4725$, a rough estimate is produced by applying the coarsest grid that has only 2 vertical CVs in a screen slot. Small number of CVs in the slot means coarser grids adjacent to the screen as well. The results of the computations are compared with experiments in Figure 5-9. The numerical results are not satisfactory at primary resonant areas, i.e. the first and the third natural frequencies of clean tank sloshing. The differences are largest for the second resonant area around $\frac{\sigma}{\sigma_1^*} \approx 2.5999$, i.e. at the third natural frequency of sloshing in clean tank. Away from resonance, a fairly good agreement exists between numerical and experimental results. Figure 5-9 shows that the coarse grid can capture secondary resonance of even modes 2, 4 and 6 at i_2, i_4 and i_6. The peak at i_8 in experiments is not captured by the coarse grid. Applying a finer grid which has 6 vertical cells inside the gap reduces the maximum error for wave responses at $\frac{\sigma}{\sigma_1^*} \approx 1$ from 50% to about 20% and significantly improve the results around $\frac{\sigma}{\sigma_1^*} \approx \frac{\sigma_3^*}{\sigma_1^*}$. At $\frac{\sigma}{\sigma_1^*} = 2.5839$ numerical simulations fail to capture the experimental results. The time series of wave elevations for this case is shown (Figure 5-14) and discussed in the next sub-section. Refining the grid to have more than 6 CVs in the slots may reduce the error but at the expense of time. It should be reminded that the unwanted added damping due to screen supports could not be included in the current two-dimensional simulations.

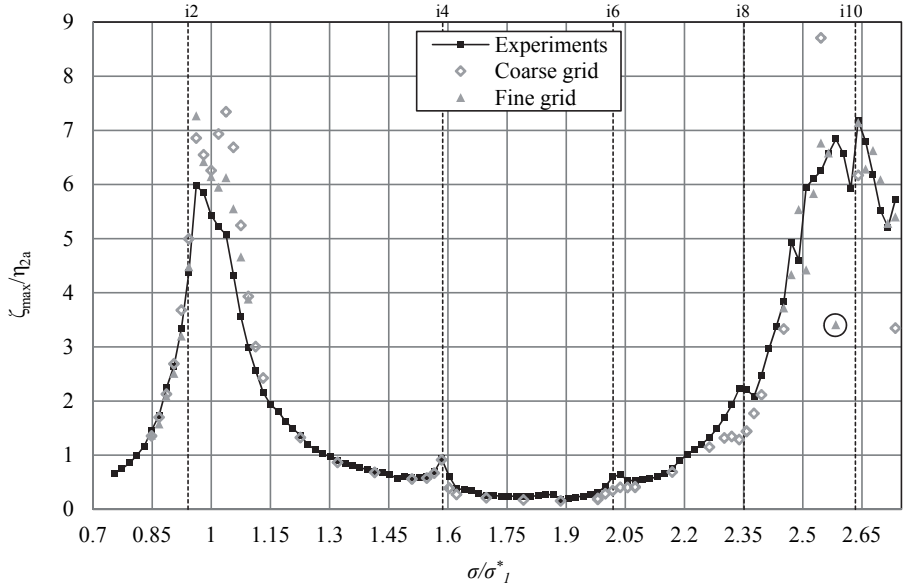

Figure 5-9. Comparison between numerical and experimental results. Curves present non-dimensional maximum steady-state wave elevations ζ_{max}/η_{2_a} as a function of non-dimensional forcing frequency σ/σ_1^*. $Sn = 0.4725$, $\varepsilon = 0.01$, $h/l = 0.12$. The vertical dashed lines i_j, $j = 2, 4, 6, 10$ mark frequencies where the secondary resonance of higher even modes is possible. The circled marker shows where the numerical simulations fail.

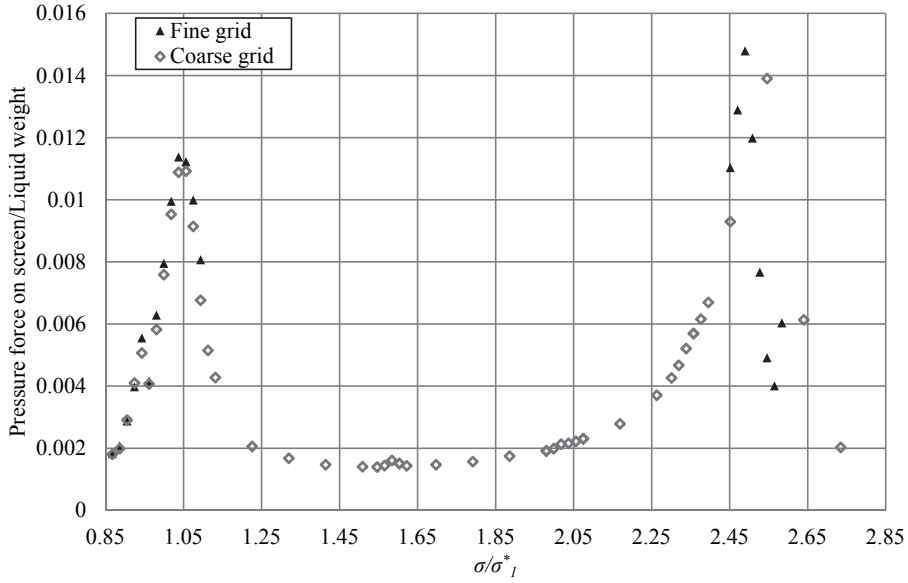

Figure 5-10. Pressure force on the screen non-dimensionalized by total liquid weight as a function of non-dimensional forcing frequency σ/σ_1^*. Coarse and fine grids use 2 and 6 cells inside the gap. $Sn = 0.4725$, $\varepsilon = 0.01$, $h/l = 0.12$.

Even though hydrodynamic forces on the screen were not measured in the experiments, result of CFD computations for pressure force is presented here to provide more details. Figure 5-10 compares the horizontal pressure force on the wetted screen surface for a coarse grid with 2 cells in the slot and for a finer grid with 6 cells in slot. Shear forces are believed to be small and neglected in the computations. Two resonant areas are present around σ_1^* and σ_3^* equivalent to non-dimensional values of $\sigma/\sigma_1^* = 1$ and $\sigma/\sigma_1^* = 2.5999$. The focus is put on the lowest resonant frequency at σ_1^*. Comparing the results around $\sigma/\sigma_1^* \approx 1$ for maximum steady-state wave elevations (see Figure 5-9) and maximum steady-state pressure force on the screen (see Figure 5-10), the difference in ζ_{max}/η_{2_a} between coarse and fine grid around is almost 20% while the difference in horizontal force is almost negligible between the results obtained for fine and coarse grid. This result brings up two concluding arguments. First, the captured forces on the screen are weakly sensitive to the number of vertical cells inside the slot. However, this might be violated if one uses a much finer grid at the screen region. Second, the captured flow details in the screen region which is convected toward the tank walls every half a cycle of oscillations affect the measured wave elevations at the tank walls.

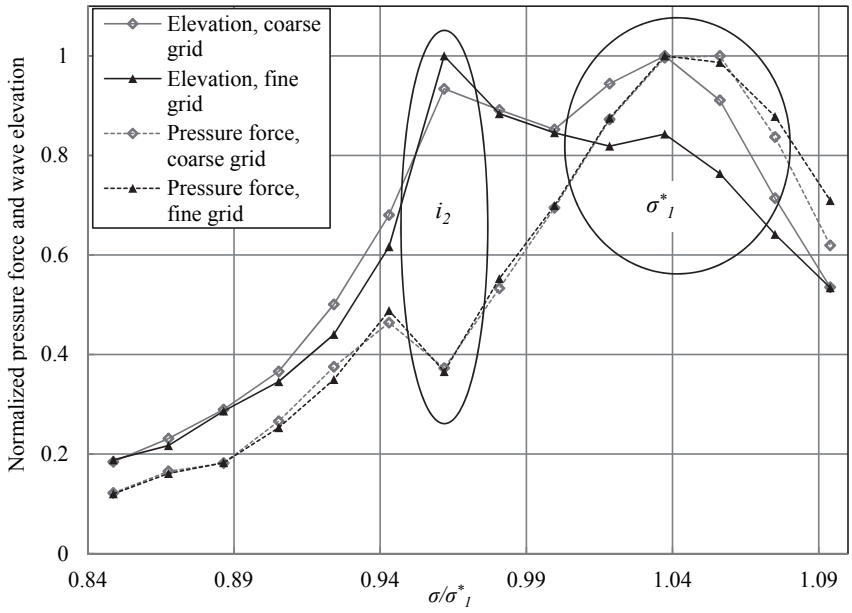

Figure 5-11. Normalized maximum steady-state pressure force on screen and maximum steady-state wave elevation at vertical walls. $Sn = 0.4725$, $\varepsilon = 0.01$, $h/l = 0.12$.

The normalized wave elevations in Figure 5-11 show two peak resonances due to secondary resonance of the second mode of sloshing in clean tank highlighted by the i_2-area and main resonance at the lowest natural mode of the clean tank which is highlighted by the σ_1^*-area. While the wave elevations show a peak at i_2-area, the pressure force experiences a drop. The reason is the excitation of the second mode of sloshing through secondary resonance. Asymptotically speaking, the second mode does

not cause cross flow through the screen and therefore it does not contribute to the pressure force. However the wave elevation at vertical walls increases due to this excitation. Due to secondary resonance the energy is transferred more into the second mode and the first mode becomes weaker. This can explain the drop on the force curves at the i_2-area. The pressure force curve has its maximum at the σ_1^*-area. At this area the first mode is the most energetic and applies stronger cross-flow through the screen which results in a larger pressure force.

5.3.3.2.1 Special free surface effects; sub-harmonic amplification

Analysis of experimental results for $Sn = 0.4725$, $\varepsilon = 0.01$, $h/l = 0.12$ in chapter 4 revealed presence of strong non-linearities such as nonlinear amplification of extra harmonics (sub and super harmonics) around $\sigma_3^*/\sigma_1^* = 2.5999$.

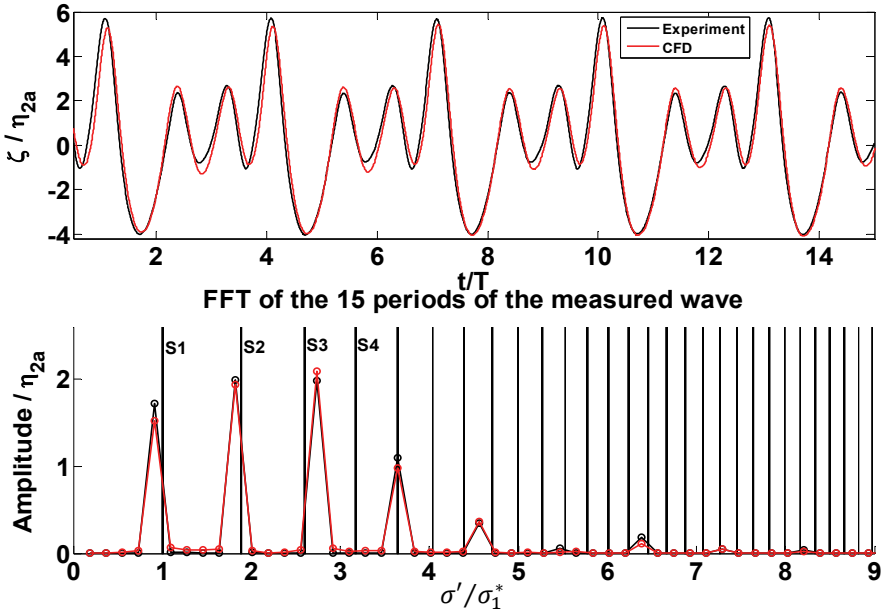

Figure 5-12. Comparison between numerical and experimental results. Amplification of sub-harmonics of the forcing frequency. Top panel: Non-dimensional wave elevation at the vertical wall, Bottom panel: Non-dimensional amplitude of the frequency components in frequency domain. The vertical lines, $S_1, S_2, \ldots$ in the lower panel identify the linear natural sloshing frequencies in the clean tank. $h/l = 0.12, \varepsilon = 0.01, Sn = 0.4725, \sigma/\sigma_1^* = 2.7348$. σ' is the frequency content of the measured signal calculated by FFT.

Depending on the forcing frequency, excitation of extra harmonics either results in waves with maximum steady-state elevations more than one forcing period apart in the recorded time series (Figure 5-12) or appearance of modulated waves with long beating periods(Figure 5-13). The CFD model can capture the extra harmonics for few number of tested forcing frequencies that, for instance, shown in Figure 5-12 for $\sigma/\sigma_1^* = 2.6971$ and in Figure 5-13 for $\sigma/\sigma_1^* = 2.7348$. The agreement between the experimental and numerical results is good for both cases. Ratios between the frequency of the strongest amplified extra harmonics and the forcing frequency in Figure 5-12 are k =1/3, 2/3, 4/3 and 5/3. Figure 5-13 shows formation of beating behavior due to presence of more extra harmonics oscillating with $k\sigma$ where $k = 0.32, 0.36, 0.64, 0.68,$

1.32, 1.36, 1.64 and 1.68. The numerical results shown in Figure 5-13 are in a better agreement with experiments for the last periods of simulation as the transient effects are dying out.

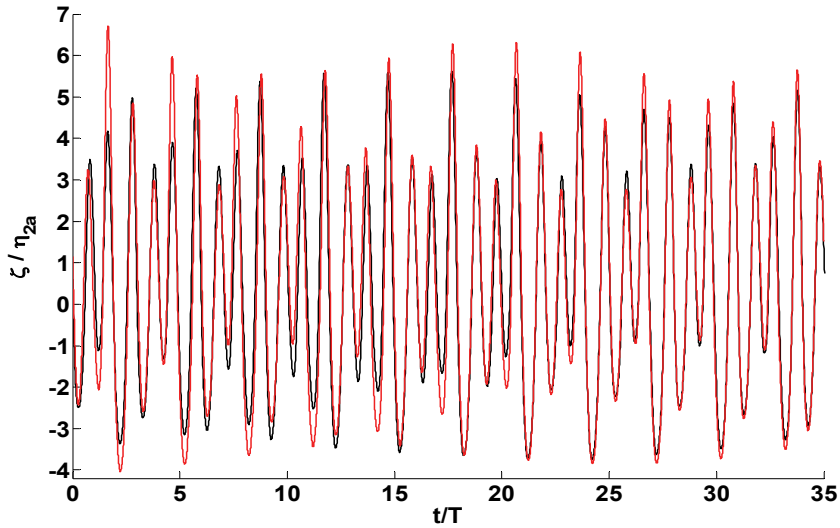

Figure 5-13. Comparison between numerical (red) and experimental (black) results. The graph presents the non-dimensional wave elevations ζ/η_{2_a} versus time non-dimensionalized by the forcing period T. $h/l = 0.12$, $\varepsilon = 0.01, Sn = 0.4725,\ \ , \sigma/\sigma_1^* = 2.6971$.

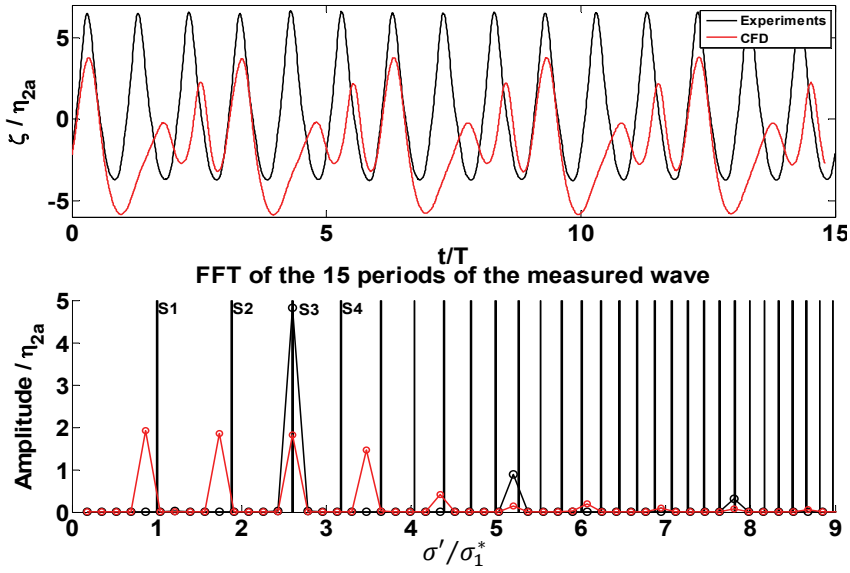

Figure 5-14. Amplification of sub-harmonics of the forcing frequency. top panel: Non-dimensional wave elevation at the vertical wall, Bottom panel: Non-dimensional amplitude of the frequency components in frequency domain. The vertical lines, $S_1, S_2, \ldots$ in the lower panel identify the linear natural sloshing frequencies in the clean tank. $h/l = 0.12, \varepsilon = 0.01, Sn = 0.4725, \sigma/\sigma_1^* = 2.5839$. σ' is the frequency content of the measured signal calculated by FFT.

The numerical results are not satisfactory for $2.4519 < \sigma/\sigma_1^* < 2.6217$. For instance, numerical simulations predict extra harmonic amplifications for $\sigma/\sigma_1^* = 2.6028$ ($\sigma/\sigma_3^* = 1.0011$) which is not supported by experiments. This is shown in Figure 5-14. The numerical studies show that sufficiently small time step size or CFL number is crucial to capture the nonlinear excitation of extra harmonics. The numerical results in Figure 5-12 and Figure 5-13 were produced by enforcing maximum CFL numbers smaller or equal to 0.35.

5.3.3.2.2 Turbulence

Numerical simulations based on laminar flow indicate that turbulence may matter when screens with coarse slat-slot arrangements are used. The numerical results show sloshing wave elevations with clear unsteady behavior which is not present in the experiments.

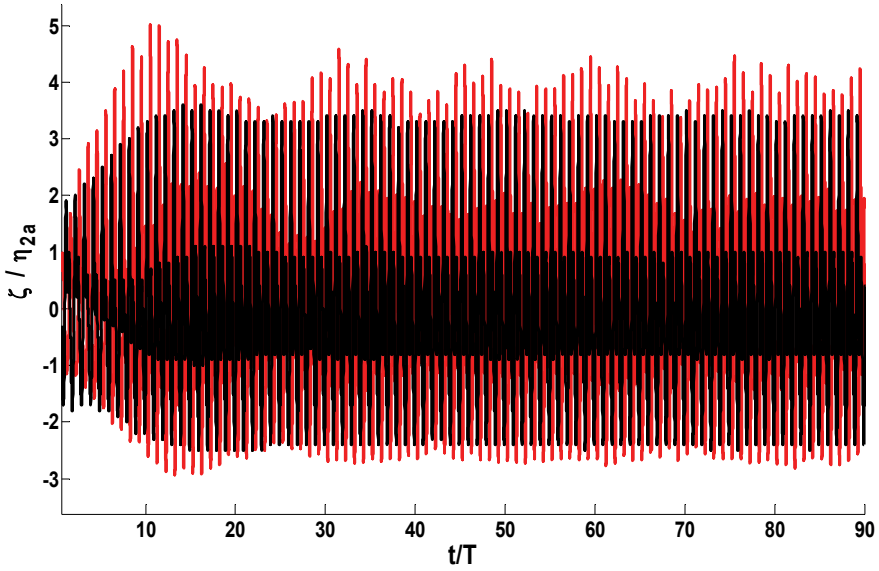

Figure 5-15. Unsteady behavior of numerical results for screen with coarse slat-slot arrangement. Non-dimensional wave elevation at the vertical wall ζ/η_{2_a} versus number of forcing periods t/T. Red: CFD, Black: Experiments. $h/l = 0.12, \varepsilon = 0.01, Sn = 0.5817, \sigma/\sigma_1^* = 0.943$.

Figure 5-15 compares time history of the wave elevations computed at one centimeter distance from a vertical end wall with wave elevations measured in experiments. The geometry of this screen is shown in the left panel of Figure 2-2; the second screen from the left with solidity ratio of 0.5817. Non-dimensional water depth and forcing amplitude are $h/l = 0.12, \varepsilon = 0.01$. The forcing frequency is near the lowest natural clean-tank sloshing frequency, i.e. $\sigma/\sigma_1^* = 0.943$, which means that the cross-flow through the screen is large. The transient effects in the numerical computations are not dying out as shown in Figure 5-15 while steady-state wave elevations appear after almost 25 periods of forcing motion in the experiments. The latter might be related to the size and diffusion of vorticity associated with eddies shed from the screen edges as well as cancellation of the oppositely circulating eddies shed

from the edges of the screen slats. One should note that the zero velocity initial conditions applied in the numerical simulations which is different than experiments. This difference can affect the time needed for the transients to die out. However, this is not the reason for the transients seen in the numerical results presented in Figure 5-15.

A snap shot of the vorticity distribution in the tank corresponding to numerical results presented in Figure 5-15 is shown in Figure 5-16. As one can see in Figure 5-16, the flow is crossing the screen from the right side of the screen to its left side at the moment. Due to this cross flow, group of eddies are shed from the screen and appear on the left side as shown in Figure 5-16. The distribution of vorticity due to these eddies is very non-uniform. This non-uniform vortex shedding from the slat edges together with laminar flow assumption in the numerical simulations do not let the eddies to die out as they do when turbulence causes faster diffusion of the vorticity.

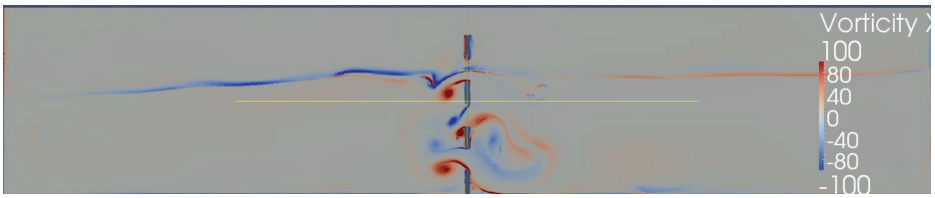

Figure 5-16. Vorticity distribution in the numerical domain with a screen of coarse slat-slot arrangement. $h/l = 0.12, \varepsilon = 0.01, Sn = 0.5817, \sigma/\sigma_1^* = 0.943$.

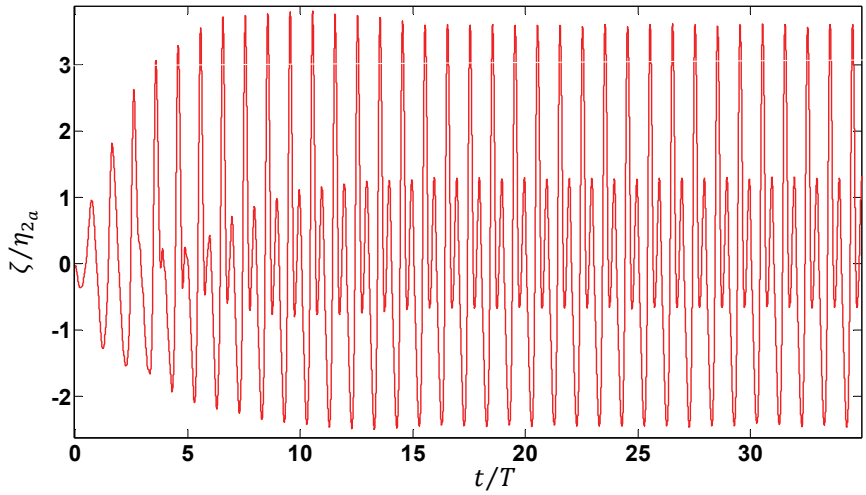

Figure 5-17. Numerical results. Effect of fine slat-slot arrangement on steadiness of the wave elevations. Non-dimensional wave elevation at the vertical wall ζ/η_{2_a} versus number of forcing periods t/T. Solidity ratio is 0.575. $h/l = 0.12, \varepsilon = 0.01, \sigma/\sigma_1^* = 0.943$.

In order to examine the effect of slat-slot arrangement on the steadiness of the wave elevation responses, a numerical simulation is conducted for a screen for which the screen's geometry is forced to have almost the same solidity ratio, i.e. $Sn = 0.575$, but with a finer slat-slot arrangement. The non-dimensional wave elevations ζ/η_{2_a} as a

function of number of forcing periods t/T are shown in Figure 5-17 for the new screen. The numerical results show that steady-state waves appear after almost 20 periods of forcing motion from the start. The vorticity distribution for the fine slat-slot arrangement is shown in Figure 5-18. The structure of shed eddies is much more uniform for the fine slat-slot arrangement relative to the coarse slat-slot arrangement (see Figure 5-16). It is noted that the plots of vorticity distribution shown in Figure 5-16 and Figure 5-18 were produced at almost the same time instant. Due to more uniform distribution of vorticity, the generated eddies from the edges of neighbor slats effectively cancel out each other leading to more uniform flow with weaker transients. The latter means even though laminar model is used, fine arrangements of slat and slots can reduce the strength of turbulence-dependent transients caused by vortex shedding.

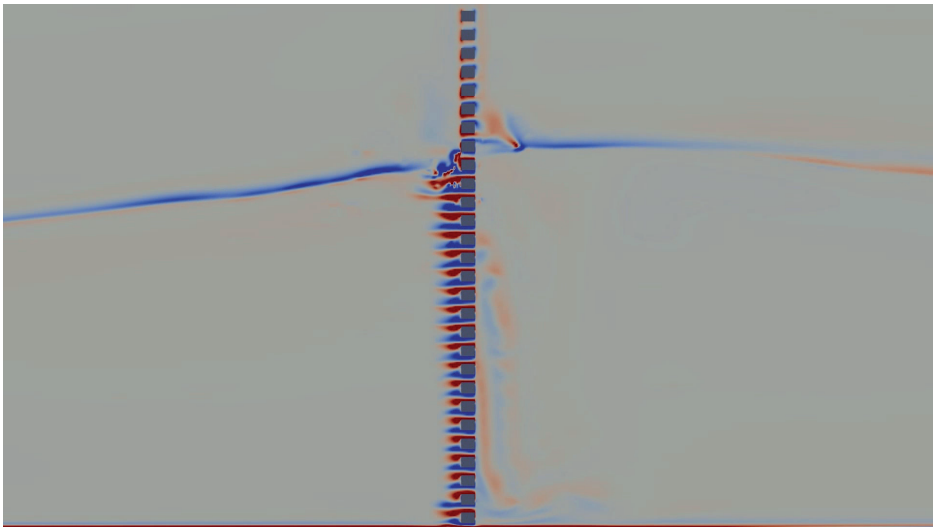

Figure 5-18. Vorticity distribution in the numerical domain with a screen of fine slat-slot arrangement. The pattern of colors is the same as in Figure 5-16. The maximum and minimum color thresholds are set at (100 s^{-1}) and (-100 s^{-1}). $h/l = 0.12, \varepsilon = 0.01, Sn = 0.575, \sigma/\sigma_1^* = 0.943$.

b. $Sn = 0.7875$

Figure 5-19 presents non-dimensional maximum steady-state wave elevations ζ_{max}/η_{2_a} versus non-dimensional forcing frequency σ/σ_1^* for $Sn = 0.7875$. All resonant peaks in the selected frequency range in Figure 5-19 are due to nonlinear effect associated with secondary resonance. Both coarse and fine grids are able to capture the first peak at i_2 with a good accuracy. The finer grid provides a good estimation for ζ_{max}/η_{2_a} with 10% error relative to experimental values. The resonance at i_4 is well predicted by the fine grid. Experiments show a small drop close at $\sigma/\sigma_1^* = 1.7$ which is predicted by the fine grid as well. However, the simulations estimate this jump at a smaller frequency. The resonance peak at i_8 is also captured by the fine grid. For this peak, the predicted resonant frequency is slightly smaller than that of the experiments. Experiments show a jump at i_8 as the frequency increases. This jump is captured by the

fine grid as well but with a clear over estimation. The quality of the numerical results on the right side of i_8 becomes more inaccurate. In general, the numerical simulations provide better results for smaller forcing frequencies.

Figure 5-20 presents non-dimensional pressure force on the screen for both coarse and fine grids. The two grids result in very similar values. This was seen for $Sn = 0.4725$ previously. Unlike the results shown for $Sn = 0.4725$, no clear resonant areas are present for pressure force in Figure 5-20 and it increases almost linearly with increasing forcing frequency. Considering the wave responses in Figure 5-19 a similar increase in the wave responses is seen for increasing forcing frequency. This is clearer for $\sigma/\sigma_1^* > 1.5$ in Figure 5-19. According to experimental and numerical wave responses in Figure 5-19 primary clean-tank sloshing resonance areas are highly damped and almost not present. This means strong cross flows through the screen which directly apply a pressure loss on either sides of the screen leading to pressure forces are not present.

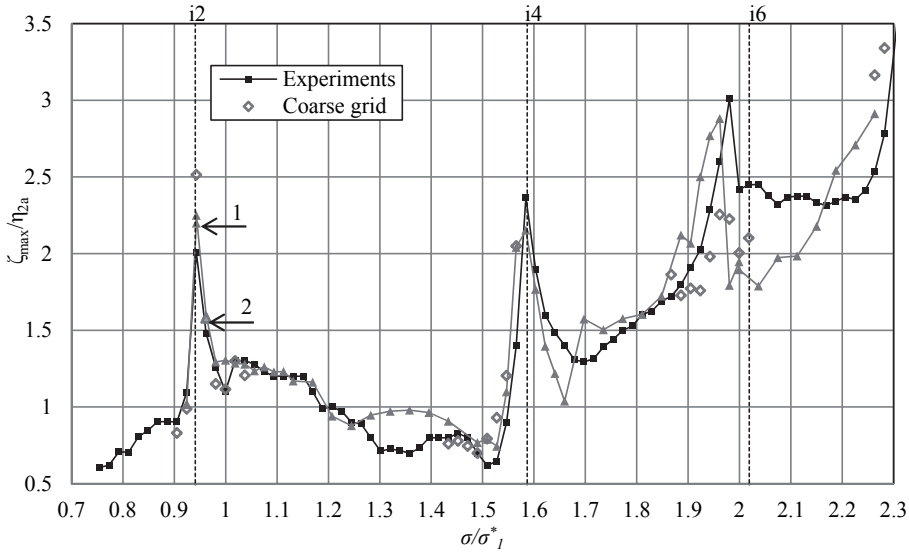

Figure 5-19. Comparison between numerical and experimental results. Curves contain non-dimensional maximum steady-state wave elevations ζ_{max}/η_{2_a} as a function of non-dimensional forcing frequency σ/σ_1^*. $Sn = 0.7875, \varepsilon = 0.01, h/l = 0.12$.

Two response points on the pressure force curve are marked in Figure 5-20. Point number 1 and 2 correspond to the peak point at i_2 and the point next to it on the right side as marked in Figure 5-19. As one can see in Figure 5-19 and Figure 5-20, the maximum wave response at the vertical walls, around i_2, occurs for point 1 while the same frequency in Figure 5-20 gives almost the minimum value for the pressure force. On the other hand, when the frequency increases and the maximum wave elevation drops down to point 2, the pressure force experience a positive jump to point 2 as shown in Figure 5-20. This is again due to secondary resonance of mode number 2 that causes a peak point for the wave elevation at the wall and conversely a minimum for pressure force on the screen. This fact is similar to the one discussed previously for $Sn = 0.4275$. (See Figure 5-11 and related discussion).

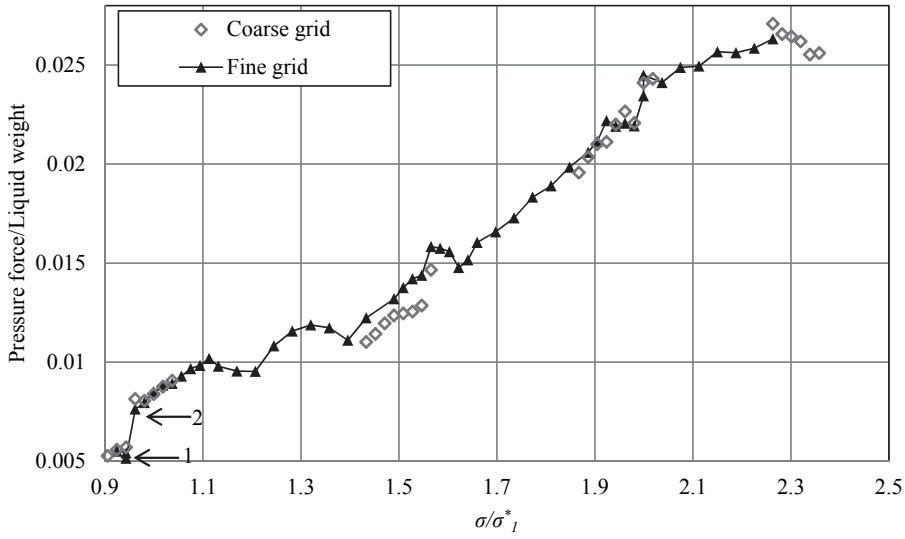

Figure 5-20. Pressure force on the screen non-dimensionalized by total liquid weight as a function of non-dimensional forcing frequency σ/σ_1^*. Coarse and fine grids use 2 and 6 cells inside the gap. $Sn = 0.4725$, $\varepsilon = 0.01$, $h/l = 0.12$.

5.3.3.3 Computational time

The computational time is the total time required for a single simulation. Each simulation is performed for one forcing frequency while the solidity ratio, forcing amplitude and water depth are kept fixed. Because steady-state sloshing has to be reached, the tank should be excited for sufficient number of forcing periods for a single forcing frequency. This is a function of the hydrodynamic damping existing in the system. Considering $Sn = 0.4725$, between 30 to 70 forcing cycles are enough to reach steady-state waves in the numerical simulations. The lowest limit of 30 cycles belongs to simulations ran for $Sn = 0.4725$ when forcing frequency is varying around $\sigma/\sigma_1^* \approx 1$. The latter is related to the large flow rate through the screen accompanied with strong vortex shedding. The 30 cycles limit also belongs to forcing frequency zones away from the primary resonances where responses are small. For $Sn = 0.7875$, longer simulation times are required to reach steady-state waves. The main reason is mainly the reduced cross-flow through the screen. In average, 50 cycles of forcing period has been used to produce steady-state responses.

A key information for a numerical simulation is the number of time steps needed to numerically simulate one forcing period. In addition how much time is spent to simulate one time step of solution is also important. Presence of the screen in the tank middle and smallness of the CVs at the screen zone needs very small time steps in order to achieve a stable solution. For $Sn = 0.4725$ the largest responses occur at the first and the third natural sloshing frequencies of the clean tank. Simulations were carried out either on a desktop computer equipped with "2.53GHz Intel(R) Xeon(R) CPU E5630" processor (called CPU1 hereafter) or on a Linux cluster equipped with "2.4 GHz AMD Opteron 2431 (Istanbul)" (called CPU2 hereafter). The average time step

$\Delta t_{average}$, CPU time needed for simulation of each time step t_{cpu} of the solution, average number of time steps used to simulate one cycle of forcing N_{cycle} and time needed for simulation of 30 cycles of the forcing $t_{30cycles}$ are calculated and reported below.

Considering $Sn = 0.4725$, the CPU1 machine with 8 parallel computations were used for frequencies around σ_1^*. The maximum CFL number was fixed to 0.5 and the grid had 6 cells inside the gap. For frequencies around σ_3^* mostly the CPU2 machine with 12 parallel domains were used. The maximum CFL number was fixed to 0.35 and the grid has 6 cells inside the gap. The average simulation time parameters are listed in Table 5-5.

Table 5-5. Simulation time parameters for $Sn = 0.4725$. $\Delta t_{average}$, t_{cpu} are respectively the average time step in one simulation and CPU time needed for simulation of each time step in seconds. N_{cycle} is the average number of time steps used to simulate one cycle of forcing. $t_{30cycles}$ is time needed for simulation of 30 cycles of the forcing.

Forcing frequency	$\Delta t_{average}$(s)	t_{cpu}(s)	N_{cycle}	$t_{30cycles}$(h)	CPU, number of sub-domains
$\frac{\sigma}{\sigma_1^*} \approx 1$	3.7609e-04	0.4170	5017	17.4	Intel, 8
$\frac{\sigma}{\sigma_1^*} \approx 2.5999$	1.5745e-04	0.2929	4619	11.3	AMD, 12

This information shows that the simulations need very long computational times even though parallel computations are used. For instance simulations for 10 forcing frequencies around σ_1^* using CPU1 distributing the simulation over 8 domains in parallel needs almost 7 days to be completed. This issue forced the author to include only two solidity ratios in the simulations.

For $Sn = 0.7875$, with maximum CFL number of 0.5 and 6 cells inside the gap. The simulation parameters for this solidity ratio is listed in Table 5-6.

Table 5-6. Simulation time parameters for $Sn = 0.7875$. The definition of these parameters is given in caption of Table 5-5.

Forcing frequency	$\Delta t_{average}$(S)	t_{cpu}(S)	N_{cycle}	$t_{30cycles}$(h)	CPU, number of sub-domains
$0.924 < \frac{\sigma}{\sigma_1^*} < 1.4711$	5.21e-04	0.226	3330	6.23	Intel, 8
$1.6975 < \frac{\sigma}{\sigma_1^*} < 2.2633$	2.73e-04	0.245	3570	7.33	AMD, 12

5.4 Closure

The VOF method was shown capable of capturing non-linear, non-violent free-surface effects in steady-state sloshing in presence of a screen in the middle of a rectangular tank. These non-linear effects include secondary resonance of higher modes and non-linear amplification of extra sub- and super-harmonics of the forcing motion. The latter effect can be captured by sufficiently accurate time integration which was achieved by setting a small enough CFL number.

In general, coarse grids have been used in this study. The minimum ratio between the smallest edge of a CV at a screen slot and the slot height is 1/6 in most of the simulations. For the small forcing amplitude of $\varepsilon = 0.01$, the numerical results for $Sn = 0.4725$ gives acceptable results around the main resonant areas at $\sigma/\sigma_1^* \approx 1$ and $\sigma/\sigma_1^* \approx \sigma_3^*/\sigma_1^*$. In general, better agreement between numerical and experimental results over the total range of tested forcing frequencies is obtained for $Sn = 0.7875$ which might be related to smaller cross-flow through the screen.

Simulations ran for a coarse grid and a finer grid show almost negligible difference in the calculated pressure forces on the screen while the calculated wave elevations at the vertical walls show 10% difference.

In this numerical study, the two-dimensional cross-section of the screen was modeled with all geometrical details. The refined grids at the screen enforce very small time steps to obey the maximum desired local CFL number. Due to very small time steps, the simulations are very time consuming. For example this fact limited the author to run simulations only for $Sn = 0.4725$ and $Sn = 0.7875$.

6 Concluding remarks and suggestions for future work

6.1 Concluding remarks

Model tests were carried out in a rectangular tank with a screen in the middle with lateral excitation for various forcing frequencies including the first three lowest natural frequencies of clean-tank sloshing. Two-dimensional steady-state sloshing is considered. The main measured physical parameter is the elevation of the sloshing waves at the vertical end walls. The tested depths are in the category of finite, intermediate and shallow water. Very small, small and relatively large forcing amplitudes were considered in the experiments to study linear and non-linear sloshing. Solidity ratios of the screen vary between 0.45 and 0.95. This variation made it possible to study the effect of solidity ratio on the natural frequencies of the tank-liquid-system. The results for the smallest forcing amplitude to tank-length ratio $\varepsilon = 0.001$ showed that by increasing the solidity ratio toward 1, the lowest natural frequency of clean-tank sloshing disappears and the third natural frequency starts moving gradually toward the lowest natural frequency of a compartment with a length equal to half the length of the main tank. As a result the resonant frequencies and modes change drastically. This is called compartmentation. Compartmentation was shown by experiments to be a function of non-dimensional forcing amplitude ε. Larger forcing amplitudes cause compartmentation at a smaller solidity ratio.

Running model tests for two sets of screens with different geometrical details, i.e. different slat-slot arrangements, but with almost the same solidity ratios reveals that the results are much more dependent on the solidity ratio rather than the geometrical details of the screens. These test runs were performed in finite water depth $h/l = 0.4$ and for forcing amplitude $\varepsilon = \eta_{2_a}/l = 0.001$.

The experimental results which represent the main part of this thesis are new and had not been reported in the literature before or during the time of current study. The produced results can be used as references for validation purposes.

The theoretical study based on multimodal method and comparison with the experiments showed applicability of linear free-surface assumption for simulation of very small forcing amplitudes in finite water depth, i.e. $\varepsilon = 0.001$ and $h/l = 0.4$. For these conditions, experimental measurements shows wave responses of linear character. The theoretical model assumes an inviscid incompressible liquid with irrotational flow (potential flow) except at the screen zone. Applying this model, an important finding is that modeling the screen as a local pressure loss which is qudratically related to the approach velocity U in the tank middle, $\Delta p = \frac{1}{2}\rho U|U|$, leads to satisfactory results for very small forcing amplitudes and solidity ratios not too close to 1. For $Sn \to 1$ the theoretical results at the lowest resonant frequency of a compartment with a half tank length are much larger than reality due to the linear free-surface assumption and the fact

that the screen causes negligible damping. The linear model provides qualitative results for $\varepsilon \geq 0.01$ in finite water depth.

In general forcing amplitudes $\varepsilon \geq 0.01$ lead to non-linear free surface effects. Relevant to this, new phenomena in connection with sloshing in screen-equipped tank were discovered and discussed. The experimental results showed that for sufficiently large forcing amplitudes, i.e. $\varepsilon \geq 0.01$ (as observed in the present study) the presence of the screen leads to strong excitation of higher harmonics of the liquid flow at certain forcing frequencies that can be related to nonlinear amplification of higher modes of sloshing. This phenomenon which is called secondary resonance needs relatively larger amplitudes to occur in a clean tank. The result of screen-caused secondary resonance is formation of narrow banded resonant areas at frequencies away from the first three natural frequencies of the clean-tank sloshing. A possible reason is that the symmetric modes do not lead to a cross-flow through the screen and, therefore, are almost undamped, in contrast to the antisymmetric ones. This implies that the same-order forcing of symmetric and antisymmetric modes should give a larger response of the symmetric modes.

An adaptive non-linear modal method for finite liquid depth modified for presence of the screen and secondary resonance can predict the resonant steady-state wave elevations with an acceptable accuracy in terms of the resonant frequencies and wave amplitudes. The forcing frequency range where the model produces acceptable results does not cover frequencies near the 3rd natural frequency of clean-tank sloshing. The main difficulty around this natural frequency is related to the complexity of the modal system and amount of contribution of several modes in the modal system in addition to free-surface nonlinreaties at the screen zone. However this nonlinear model can explain non-linear sloshing for $\varepsilon \leq 0.01$ for $0.75 < \sigma/\sigma_1^* < 1.35$. This non-linear modal model includes the effect of geometrical details of the screen under the mean free surface to account for changes of anti-symmetric natural modes due to presence of the screen. This inclusion improves the predicted resonant frequencies. The non-linear model also assumes that the symmetric modes are not affected by the screen.

The theoretical models, both linear and non-linear, are applicable in finite water depth. The linear model provides qualitative results for $\varepsilon = 0.03$ and $h/l = 0.35$. For $\varepsilon = 0.03$, the non-linearity due to the free-surface is very strong and constructing a non-linear model was not possible due to the complexity of the modal system. Large forcing amplitudes cause special non-linear free-surface effects such as very thin run-ups on the vertical walls and on the screen, wave breaking, jet flow through the screen from water to air impacting the underlying free-surface and fragmentation of the free surface. These effects cannot be included in the modal method and were neglected. Therefore when these special free-surface effects were large, the modal method failed to capture the experimental results.

Local special free-surface effects at the screen position can cause multiple steady-state responses in a screen-equipped tank on the two sides of the screen. As a general rule, two distinct sloshing amplitudes can happen if sloshing in both compartments is close to the primary resonant frequencies of the compartments and screen-caused damping is relatively small due to reduced cross-flow through the screen. This means that the solidity ratio should be large. For these conditions transient effects can change the damping content in each compartments and the solution in one of the compartments

experiences a jump in the response amplitude while the response in the other compartment does not experience a jump. This phenomenon for screen-equipped tanks has been observed first in this study and has not been found reported in the literature. Any theoretical or numerical model needs to model the details of the flow at the screen zone to capture multiple sloshing solutions in the compartments.

Small and relatively large forcing amplitudes were tested in shallow-water conditions ($h/l = 0.12$ and $h/l = 0.125$). Secondary resonance is more pronounced in shallow water than in finite depth and causes clear extra resonance peaks in the total range of tested forcing frequencies especially when the solidity ratio is between 0.7 and 0.9. A new phenomenon is amplifications of "extra" harmonics of the forcing frequency σ in the wave responses that are oscillating with $k\sigma$. These harmonics are called extra because k values are not integer values unlike the natural higher harmonics where $k = 1, 2, \ldots$. This phenomenon was observed around the third natural clean-tank sloshing frequency. The forcing frequency ranges associated with amplifications of "extra" harmonics are functions of solidity ratio as well. These forcing frequency ranges were collected and documented for each solidity ratio in chapter 4.

In shallow water, $h/l = 0.125$ and in case of relatively large forcing amplitude, $\varepsilon = 0.05$, free-surface impact events on the vertical end walls and on the screen were observed. For the smallest solidity ratio, $Sn = 0.4752$, flip-through like impact events occur on the vertical end walls when the forcing frequency is near the lowest natural frequency of clean-tank sloshing. Increasing the solidity ratio to larger than 0.7 removes the impact events on the vertical walls but causes impact events on the screen. The forcing frequency range associated with the impacts on the screen is clearly larger than the lowest natural frequency. When compartmentation of sloshing occurs, new impact events are observed on the vertical walls for frequencies around the lowest natural frequency of a compartment. These impact events are documented in chapter 4 using visual investigations.

Estimations of the magnitude of impact pressures due to impact events on the tank walls at the lowest natural frequency of clean-tank sloshing were made using pressure impulse theory (Cooker & Peregrine, 1995). The estimation predicts impact pressures to be comparable to previous measurements in clean tanks by Abramson et al., (1974) for similar shallow liquid depths, excitation amplitudes and frequencies.

Non-violent sloshing in shallow water, i.e. $h/l = 0.12$ and $\varepsilon = 0.01$, was selected to perform numerical simulations using CFD (Computational Fluid Dynamics). The VOF (Volume of Fluid) free-surface capturing method was applied. The numerical code used for simulations was OpenFOAM which is an open source software. The VOF model was shown to be able to capture nonlinear effects such as secondary resonance with acceptable agreement with experiments for solidity ratios 0.4725 and 0.7875 in $h/l = 0.12$ and for small non-dimensional forcing amplitude $\varepsilon = 0.01$. Even though the results were satisfactory, there were some major issues with the CFD simulations that have been applied in this study:

- Long-time computational time was needed for performing every single simulation which makes it expensive for parametric studies. For instance, a single simulation for fixed forcing amplitude and frequency can take up to 17 hours for 30 cycles of the forcing motion on a desktop computer equipped with

"2.53GHz Intel(R) Xeon(R) CPU E5630" processor even if parallel computations are used.

- In addition, extensive preliminary simulations were needed to find out which numerical discretization schemes should be chosen to achieve both stability and accuracy; also how fine the numerical grid should be near the screen to achieve acceptable accuracy in the numerical results required many preliminary simulations.

One important conclusion was that a laminar model did not provide steady-state wave responses oscillating with the forcing frequency if a screen with coarse slat-slot arrangements were used. The reason is believed to be associated with diffusion of vortices and cancellation of lateral vortices/eddies shedding from the screen slats. The latter effect is stronger in turbulent than in laminar flow. The real rotational flow away from the boundary layer is believed to be turbulent in our studied cases.

6.2 Future work

This study was limited to two-dimensional steady-state sloshing in a rectangular tank without force and pressure measurements on the vertical walls and on the screen. Following plans can be made for more future work by performing new experimental and theoretical works:

1. An experimental set-up for measuring local pressures on the screen and vertical walls to provide sufficient information regarding probability of occurrence of slamming pressures during the observed impact events for the large amplitude-to-length ratio $\varepsilon = 0.05$ in shallow water.
2. Two-dimensional experiments in the same tank with forcing signal constructed from a scaled down sea-state or spectrum can be performed.
3. Conducting steady-state sloshing tests in three-dimensional screen-equipped tanks. Real tank shapes such as cubic chamfered tanks and cylindrical tanks with perforated walls dividing the tank into sectors out to be investigated. The three-dimensional studies can be extended to tests with irregular forcing signals representing realistic ship motions in different sea states.

Considering numerical simulations using CFD, one may try to apply an abrupt pressure loss boundary condition instead of modeling the screen with all geometrical details in order to reduce the computational time. This was not applied in this thesis, because a difficulty with a highly advanced written code such as OpenFOAM (used in this thesis) was the unknown time which might be needed to understand the code deeply to define a new boundary condition.

Bibliography

Abrahamsen, B. (2011). *Sloshing Induced Tank-roof Impact with Entrapped Air Pocket.* Trondheim: Norwegian University of Science and Technology, NTNU.

Abramson, H. N. (1966). *Dynamic Behavior of Liquids in Moving Containers with Applications to Space Vehicle Technolegy.* Washington: NASA.

Baines, W. D., & Peterson, E. G. (1951). An investigation of flow through screens. *Transactions of the ASME* .

Bearman, P. W., Graham, J. M., Obasaju, E. D., & Drossopoulos, G. M. (1984). The influence of corner radius on the forces experienced by cylindrical bluff bodies in oscillatory flow. *Applied Ocean Research , 6* (2), 83-89.

Behrens, T. (2009). *OpenFOAM's Basic Solvers for Linear Systems of Equations.* Retrieved from www.tfd.chalmers.se.

Blevins, R. D. (2000). *Applied Fluid Dynamics Handbook.* Krieger Publishing Company.

Chester, W., & Bones, J. A. (1968). Resonant Oscillations of Water Waves. II. Experiment. *Proceedings of the Royal Society of London. Series A, Mathematical and Physical Sciences*, *306*, pp. 23-39. London.

Colagrossi, A., Lugni, C., Dousset, V., Bertram, V., & Faltinsen, O. (2003). Numerical and experimental study of sloshing in partially filled rectangular tanks. *In proceedings of 6th Numerical Towing Tank Symposium.* Rome.

Cooker, M. J., & Peregrine, D. H. (1995). Pressure-impulse theory for liquid impact problems. *Journal of Fluid Mechanics , 297*, 193-214.

Dodge, F. T. (2000). *The New Dynamic Behavior of Liquids in Moving Containers.* San Antonio, Texas: Southwest Research Institute.

Ezersky, A., Slunyaev, A., Mouazé, D., & Chokchai, W. (2009). Occurrence of standing surface gravity waves modulation in shallow water. *European Journal of Mechanics - B/Fluids , 28* (4), 521-531.

Faltinsen, O. M. (1989). *Sea Loads on Ships and Offshore Structures.* Cambridge University Press.

Faltinsen, O. M., & Timokha, A. N. (2001). An adaptive multimodal approach to nonlinear sloshing in a rectangular tank. *Journal of Fluid Mechanics , 432*, 167-200.

Faltinsen, O. M., & Timokha, A. N. (2011). Natural sloshing frequencies and modes in a rectangular tank with a slat-type screen. *Journal of Sound and Vibration , 330* (7), 1490-1503.

Faltinsen, O. M., & Timokha, A. N. (2009). *Sloshing.* Cambridge University Press.

Faltinsen, O. M., Firoozkoohi, R., & Timokha, A. N. (2011). Analytical modeling of liquid sloshing in a two-dimensional rectangular tank with a slat screen. *Journal of Engineering Mathematics , 70*, 93-109.

Faltinsen, O. M., Firoozkoohi, R., & Timokha, A. N. (2011). Effect of central slotted screen with a high solidity ratio on the secondary resonance phenomenon for liquid sloshing in a rectangular tank. *Physics of Fluids , 23* (6), 13.

Faltinsen, O. M., Firoozkoohi, R., & Timokha, A. N. (2011). Steady-state sloshing in a rectangular tank with a slat-type screen in the middle:Quasilinear modal analysis and experiments. *Physics of Fluids , 23* (4), 19.

Fediw, A. A., Isyumov, N., & Vickery, B. J. (1995). Performance of a tuned sloshing water damper. *Journal of Wind Engineering and Industrial Aerodynamics , 57*, 237-247.

Ferziger, J. H., & Peric, M. (2002). *Computational Methods for Fluid Dynamics.* Springer.

Firoozkoohi, R., & Faltinsen, O. M. (2010). Experimental and numerical investigation of the effect of swash bulkhead on sloshing. *20th International Offshore and Polar Engineering Conference, ISOPE-2010, June 20, 2010 - June 25, 2010. 3*, pp. 252-259. Beijing: International Society of Offshore and Polar Engineers.

GL. (2003). *Rules for Classification and Construction, Ship Technology.* Germanischer Lloyd.

Hirt, C. W., & Nichols, B. D. (1981). Volume of fluid (VOF) method for the dynamics of free boundaries. *Journal of Computational Physics , 39* (1), 201-225.

Idelchik, I. E. (1996). *Handbook of Hydraulic Resistance.* Begell House INC.

IHI. (2000). *SPB Technology.* Retrieved from http://www.ihi.co.jp

Issa, R. I. (1986). Solution of the implicitly discretised fluid flow equations by operator-splitting. *Journal of Computational Physics , 62* (1), 40-65.

Kaneko, S., & Ishikawa, M. (1999). Modeling of tuned liquid damper with submerged nets. *Journal of Pressure Vessel Technology , 121* (3), 334-343.

Kaneko, S., & Mizota, Y. (2000). Dynamical modeling of deepwater-type cylindrical tuned liquid damper with a submerged net. *Journal of Pressure Vessel Technology , 122* (1), 96-104.

Keulegan, G. H. (1959). Energy dissipation in standing waves in rectangular basins. *Journal of Fluid Mechanics , 6* (1), 33-50.

Laws, E. M., & Livesey, L. J. (1978). Flow through Screens. *Annual review of Fluid Mechanics , 10*, 247-266.

Lepelletier, T., & Raichlen, F. (1988). Nonlinear oscillations in rectangular tanks. *Journal of Engineering Mechanics , 114* (1), 1-23.

Liu, D., & Lin, P. (2009). Three-dimensional liquid sloshing in a tank with baffles. *Ocean Engineering , 36* (2), 202-212.

Love, J. S., & Tait, M. J. (2010). Nonlinear simulation of a tuned liquid damper with damping screens using a modal expansion technique. *Journal of Fluids and Structures , 26* (7-8), 1058-1077.

Love, J. S., Tait, M. J., & Toopchi-Nezhad, H. (2011). A hybrid structural control system using a tuned liquid damper to reduce the wind induced motion of a base isolated structure. *Engineering Structures , 33* (3), 738-746.

Lugni, C., Brocchini, M., & Faltinsen, O. M. (2006). Wave impact loads: The role of the flip-through. *Physics of Fluids , 18* (12), 17.

Maravani, M., & Hamed, M. S. (2010). Numerical modeling of sloshing motion in a tuned liquid damper outfitted with a submerged slat screen. *International Journal for Numerical Methods in Fluids , 65* (7), 834–855.

Molin, B. (2010). Hydrodynamic modeling of perforated structures. *Applied Ocean Research , 33*, 1-11.

Muzaferija, S., & Peric, M. (1998). Computation of free-surface flows using interface-tracking and interface-capturing methods. In O. Mahrenholtz, & M. Markiewicz, *Nonlinear Water Wave Interactions*. Southampton: Computational Mechanics Publications.

Onno, U. (1997). *Numerical Prediction of Two-Fluid Systems with Sharp Interfaces, PhD thesis*. London: Imperial College of Science.

OpenCFD. (n.d.). *OpenFOAM Documentation*. Retrieved from OpenFOAM- The Open Source Computational Fluid Dynamics (CFD) Toolbox: http://www.openfoam.org/docs/

OpenCFD. (n.d.). OpenFOAM Source Code.

Peregrine, D. H. (2003). Water-wave impact on walls. *Annual Review of Fluid Mechanics , 35* (1), 23-43.

Peric, M., Zorn, T., el Mokhtar, M., Schellin, T. E., & Kim, Y. (2009). Simulation of sloshing in LNG-tanks. *Journal of Offshore Mechanics and Arctic Engineering , 131* (3).

Rousche, H. (2002). *Computational Fluid Dynamics of Dispersed Two-Phase Flows at High Phase Fractions, PhD thesis*. London: Imperial College of Science.

Tait, M. J., El Damatty, A. A., Isyumov, N., & Siddique, M. R. (2005). Numerical flow models to simulate tuned liquid dampers (TLD) with slat screens. *Journal of Fluids and Structures , 20* (8), 1007-1023.

Tanaka, N., Ikeda, Y., & Nishino, K. (1983). *Hydrodynamic Viscous Force Acting on Oscillating Cylinders with Various Shapes*. Department of Naval Architecture, University of Osaka.

Verhagen, J. H., & van Wijngaarden, L. (1965). Nonlinear oscillations of fluid in a container. *Journal of Fluid Mechanics , 22* (4), 737-751.

Wood, D., Peregrine, D., & Bruce, T. (2000). Wave impact on a wall using pressure-impulse theory. I: Trapped air. *Journal of Waterway, Port, Coastal, and Ocean Engineering , 126* (4), 182-190.

Appendix

1. Firoozkoohi, R., & Faltinsen, O. M. (2010). Experimental and numerical investigation of the effect of swash bulkhead on sloshing. *20th International Offshore and Polar Engineering Conference, ISOPE-2010, June 20, 2010 - June 25, 2010. 3*, pp. 252-259. Beijing: International Society of Offshore and Polar Engineers.

Proceedings of the Twentieth (2010) International Offshore and Polar Engineering Conference
Beijing, China, June 20–25, 2010

ISBN 978-1-880653-77-7 (Set); ISSN 1098-6189 (Set); www.isope.org

Experimental and Numerical Investigation of the Effect of Swash Bulkhead on Sloshing

Reza Firoozkoohi and Odd Magnus Faltinsen
Center for Ships and Ocean Structures & Department of Marine Technology, Norwegian University of Science and Technology (NTNU), Trondheim, Norway

ABSTRACT

The effect of swash bulkheads on sloshing in a two-dimensional rectangular tank is studied. Damping due to the bulkheads and change in the lowest natural sloshing frequencies are accounted for using the quasi-linear modal theory by Faltinsen and Timokha (2009) and compared to new experimental results. An objective is to find which solidity ratio[1] (Sn) gives the smallest sloshing waves at the two lowest natural sloshing frequencies. This solidity ratio is a function of non-dimensional lateral excitation amplitude and liquid depth-to-tank breadth ratio. In fact the quasi-linear modal theory (Faltinsen and Timokha, 2009) is justified and the conditions of applicability of the theory are determined.

KEY WORDS: Sloshing; swash bulkhead; linear modal theory; experiments.

INTRODUCTION

Sloshing matters in the design of ship tanks transporting liquids and fuels like LNG, LPG and oil. Sloshing means in our context "Violent or resonant motion of a liquid free surface inside a storage tank of a ship due to an excitation load with a frequency close to the lowest natural frequencies of the tank-liquid system". There is a mutual interaction between ship motions and sloshing. Liquid impact on the tank walls and the roof can happen as results of different sloshing scenarios. Sloshing-induced slamming and resulting structural stresses is of particular concern for prismatic LNG tanks. As a consequence, there are limitations on the filling depth of the tanks.
Internal structures such as baffles, columns and swash bulkheads[2] cause dissipation of the kinetic and potential energy by means of flow separation. The consequence is damping of the sloshing. A swash bulkhead has the additional important effect of changing the natural sloshing frequencies to a frequency domain where less severe ship motions occur.
Baffles have in general a small damping effect on sloshing relative to swash bulkheads (Faltinsen and Timokha, 2009). Swash bulkheads can be optimized to minimize sloshing. The result depends for instance on the tank motion, the liquid depth and the solidity ratio (Sn).
An early study about swash bulkhead in the marine field was by Akita (1967). He showed from a non-impact hydrodynamic pressure point of view how different shapes of perforations and different solid area percentages can reduce the pressure forces on the tank walls. In spacecraft applications, the effect of perforated walls on sloshing has been studied experimentally by Garza (1964) and Abramson and Garza (1965) for forced horizontal excitation of a vertical circular tank that is compartmented into sectors by means of radial walls 45°, 60° and 90° sector tanks. Their lateral excitation amplitudes were low relative to ship sloshing applications. Both the excitation amplitude and perforation of the sector walls affect the damping and the highest natural period. The natural period is here defined to correspond to when the liquid response has a maximum as a function of the forcing period. The fact that the excitation amplitude matters is a nonlinear effect associated with the flow through the perforated walls. As a rule-of thumb Dodge (2000) gives that if the total area of the perforations exceeds 10% of the area, the liquid tends to slosh between the compartments and the slosh natural frequency tends to approach the value of an un-compartmented tank.
Classification societies have rules regarding swash bulkheads. GL[3] expresses that the perforation area should not exceed 10 percent of the whole bulkhead area.
The theory of swash bulkheads and their effects on sloshing is not well developed so far. This study introduces a quasi-linear method with empirical quadratic nonlinear damping associated with the cross-flow through the swash bulkhead that can provide useful information on the effectiveness of swash bulkheads. The investigation begins by describing the theoretical method. The results of this numerical method will be compared with new experimental results.

NUMERICAL INVESTIGATION

The numerical analysis is developed for a 2D rectangular tank without chamfers and infinite tank roof height. The tank is laterally excited. The method is described in detail by Faltinsen and Timokha (2009).Here a summary of the theoretical model is given.

Summary of the Mathematical Procedure

The liquid domain is split into two equal domains Q_0^- and Q_0^+ by a

1 The ratio between the solid area and the total projected area of the swash bulkhead
2 Perforated bulkheads inside ship tanks used for damping the resonant liquid motion
3 Germanisher Lloyds

vertical perforated thin plate (screen) (see Fig. 1) with a solidity ratio $Sn = 1 - \Delta A/A$ where ΔA is the opening area and A is the total projected area of the plate including the opening area. Fig. 1 defines the coordinate system, the water depth h and the length a of each subdomain. Potential flow theory with linear free-surface conditions is assumed in Q_0^- and Q_0^+. There is an inflow-outflow rate between the domains Q_0^- and Q_0^+ that affects the behavior of the free surface and is a function of the forcing frequency and amplitude as well as the solidity ratio. The two transmission conditions at the perforated plate are:

- The pressure difference on the two sides of the screen is related by a pressure loss coefficient
- The horizontal absolute velocities on the two sides of the screen are equal

The relative horizontal velocity at the screen is averaged over the liquid depth and expressed as

$$\dot{\alpha}_0(t) = \frac{1}{h}\int_{-h}^{0} u_r(z,t)dz \tag{1}$$

where $u_r(z,t)$ is the horizontal velocity relative to the tank. The pressure loss condition at the screen is averaged over the liquid depth and expressed as

$$\frac{1}{h}\int_{-h}^{0}\left[\frac{\partial\Phi^+}{\partial t}|_{y=0} - \frac{\partial\Phi^-}{\partial t}|_{y=0}\right]dz = \frac{1}{2}K\dot{\alpha}_0|\dot{\alpha}_0| \tag{2}$$

Here the pressures on the left hand side of equation (2) have been expressed by Bernoulli's equation in the two liquid domains at the perforated plate.

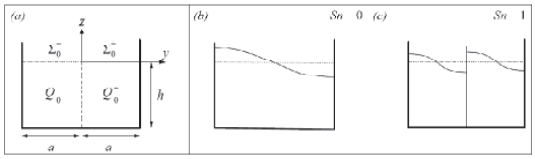

Fig. 1, A two-dimensional rectangular tank with a screen in the middle. Parts (b) and (c) illustrate the lowest natural modes in the limit cases $Sn = 0$ and $Sn = 1$, respectively.

The velocity potential and the free-surface elevation in the two liquid domains must account for the cross-flow at the perforated plate. The absolute velocity potentials in the two domains are expressed as

$$\varphi^{\pm} = y\dot{\eta}_2(t) + \Omega_d^{\pm}(y,z)\dot{\alpha}_0(t) \mp \dot{\alpha}_{-1}(t) + \sum_{k=1}^{\infty} R_k^{\pm}(t)\cos\left(\frac{\pi k y}{a}\right)\frac{\cosh\left(\pi k(z+h)/a\right)}{\cosh\left(\pi k h/a\right)} \tag{3}$$

Here $\eta_2(t)$ is the sway motion of the tank and

$$\Omega_d^{\pm}(y,z)\dot{\alpha}_0(t) = \mp\frac{\dot{\alpha}_0(t)}{2a}\left[(y \mp a)^2 - (z+h)^2\right] \tag{4}$$

The free-surface elevation can be described based on the in-flow or out-flow:

$$\zeta^{\pm}(y,t) = \pm\frac{h}{a}\alpha_0(t) + \sum_{j=1}^{\infty}\beta_j^{\pm}\cos\left(\frac{\pi j y}{a}\right) \tag{5}$$

Here, the first term on the right side of the free-surface elevation is a consequence of the piston-like motion at the perforated plate. The generalized coordinates $R_k^{\pm}(t)$ in the velocity potential and the generalized coordinates $\beta_j^{\pm}$ of the free-surface elevation can be related by the linear kinematic free-surface condition. The next step is to use the linear dynamic free-surface condition. This leads to the following relationship for $\alpha_{-1}(t)$ and differential equations for β_j^+ and β_j^-:

$$\ddot{\alpha}_{-1}(t) = -\frac{1}{2}a^{-1}\ddot{\alpha}_0(t)\left[\frac{1}{3}a^2 - h^2\right] + \frac{1}{2}a^{-1}\ddot{\eta}_2(t) + a^{-1}gh\alpha_0(t) \tag{6}$$

,

$$\ddot{\beta}_j^{\pm} + \sigma_{aj}^2\beta_j^{\pm} = \pm K_j(t) \tag{7}$$

where

$$K_j(t) = \frac{2}{\pi}\tanh\left(\frac{\pi j h}{a}\right)\left[-\frac{(-1)^j - 1}{j}\ddot{\eta}_2 + \frac{\ddot{\alpha}_0(t)}{j}\right] \tag{8}$$

and

$$\sigma_{aj}^2 = \frac{g\pi j}{a}\tanh\left(\frac{\pi j h}{a}\right) \tag{9}$$

is the square of the natural frequency of a sub-domain. The presented differential equations and pressure loss condition are used to derive steady-state solutions of $\alpha_{-1}(t)$, $\alpha_0(t)$ and the generalized coordinates $\beta_j^{\pm}$ under harmonic excitation.

Numerical Calculations

Influence of Physical Parameters. The physical parameters influencing the flow in the present problem are the ratio h/l between the liquid depth and the tank length, the non-dimensional forcing amplitude $\varepsilon = \frac{\eta_{2a}}{l}$, the non-dimensional forcing frequency $\frac{\sigma}{\sigma_{1(Sn=o)}}$ and the solidity ratio. Here $\sigma_{1_{(Sn=o)}}$ denotes the lowest natural sloshing frequency without the perforated plate. We will separately examine $\varepsilon = 0.001$ and $\varepsilon = 0.01$. Our cases correspond to $h/l = 0.4$. The frequency range is chosen so that two resonant sloshing conditions are included.

Results for $\varepsilon = 0.001$. The calculations were performed for the solidity ratios 0.328, 0.52, 0.712, 0.808, 0.854, 0.904, 0.928, 0.948 and 0.962. The pressure loss coefficients corresponding to the chosen solidity ratios are listed in Table 1. These coefficients represent experimental results by Blevins (2000) for two-dimensional cross-flow through a line of small rectangular objects with sharp edges. The ambient flow is spatially uniform and steady. These pressure loss values are not Reynolds number dependent because the separation of the flow always occurs when it passes the sharp edges. The fact that the ambient flow is neither uniform nor steady in our case represents an error source in adopting the pressure loss coefficients from Blevins.

Fig. 2 presents the steady-state maximum wave elevation at a distance of 1 cm from the vertical end walls. The tank length is 1m. The 1 cm distance is used to avoid the very thin wave-run up region when comparisons are made with the experiments (Wave run- up phenomenon cannot be modeled by the present theory). For low solidity ratios and the studied frequency range, two resonant frequencies exist corresponding to the first and approximately the third natural frequency of sloshing of the tank without the perforated plate. The largest responses at the first and the second resonant frequencies occur for the lowest solidity ratio. Increasing the solidity ratio will within a certain solidity-ratio range raise the damping due to the cross-flow at the perforated plate and cause smaller response amplitudes. However, there is a limit of the solidity ratio for this tendency and for Sn-values larger than that limit the response amplitude starts growing again. We can define a value Sn_{min} that corresponds to a solidity ratio that causes the lowest response at both the first and second resonances. The information about maximum responses and the resonant frequencies in Fig. 2 is collected in Table 1. According to this table, the smallest response at the two resonance frequencies occurs for $Sn = 0.904$. For $Sn = 0.904$, the peak point of the response at the first resonant frequency has disappeared and the second resonant frequency has drifted to a frequency at the second resonant frequencies for the tank without the perforated plate. The latter resonance frequency for a tank without the perforated plate cannot be excited by lateral excitation

according to linear theory. According to Fig. 2 and Table 1, increasing the solidity ratio to larger than Sn_{min}, results in larger frequency shift of the second resonant frequency and larger response amplitude. This means lower flow rate through the bulkhead and consequently smaller damping. In fact when the solidity ratio is larger than Sn_{min} and very close to one, the liquid tends to oscillate with the natural frequency of a compartmented tank.

The gray background data in Table 1 are related to a frequency range which is more close to the first natural frequency of a compartment, i.e. the second natural frequency of the original clean tank.

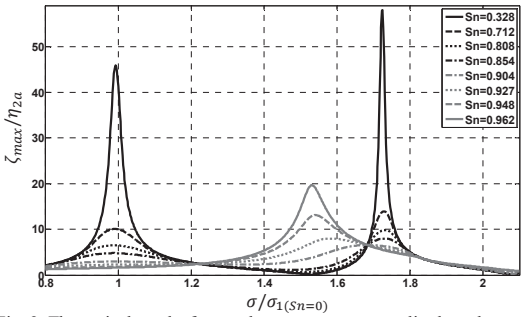

Fig. 2, Theoretical results for steady-state response amplitude at the distance of 1cm from a vertical end wall for different solidity ratios, $h/l = 0.4$ and $\varepsilon = 0.001$.

Table 1. Pressure loss coefficients, the corresponding solidity ratios based on Blevins's experimental results and the theoretical results for the first and the second resonant frequencies for $\varepsilon = 0.001$ and $h/l = 0.4$.

Sn	K	$(\frac{\sigma}{\sigma_{1(Sn=0)}})_1$	$\frac{\zeta_{max_1}}{\eta_{2a}}$	$(\frac{\sigma}{\sigma_{1(Sn=0)}})_2$	$\frac{\zeta_{max_2}}{\eta_{2a}}$
0.328	1	0.99	45.86	1.72	58.26
0.52	4.53	0.99	21.54	1.72	27.89
0.712	20.83	0.99	10.09	1.73	13.93
0.808	50.74	0.99	6.51	1.73	9.83
0.854	96	0.99	4.79	1.73	7.99
0.904	273.97	0.99	2.95	1.68	6.56
0.927	506.48	1.58	8	-	-
0.948	937.44	1.54	13.11	-	-
0.962	1443.45	1.53	19.67	-	-

***Results* for $\varepsilon = 0.01$.** Varying the forcing amplitude affects the amount of solidity ratio that gives the minimum response. Fig. 3 presents the results for $\varepsilon = 0.01$. For this forcing amplitude, the minimum wave amplitude responses at the two lowest natural frequencies take place for $Sn_{min} = 0.712$. According to Table 2, the peak value of the response at the lowest natural frequency has not disappeared but it is very small. The second maximum response is the smallest response when the forcing frequency varies between the second and the third natural frequency of a non-perforated tank. For $Sn_{min} = 0.712$, the second resonant frequency which has the smallest response in this frequency range, occurs $at\ \frac{\sigma}{\sigma_{1(Sn=o)}} = 1.71$ (Table 2). For $\varepsilon = 0.001$, and when $Sn_{min} = 0.904$, the maximum response takes place at $\frac{\sigma}{\sigma_{1(Sn=o)}} = 1.68$. It means that for a larger forcing frequency, the smallest response happens at a lower solidity ratio and with a smaller frequency shift relative to the approximate third natural frequency of sloshing of the tank without the perforated plate.

Comparing the peak points of the response in Fig. 2 and Fig. 3 show that, when $Sn <= (Sn_{min})_{\varepsilon=0.01}$ the damping is larger for $\varepsilon = 0.01$ which means larger forcing amplitude causes larger flow rate through the swash bulkhead

When $Sn > Sn_{min}$, the behavior is similar as for $\varepsilon = 0.001$, i.e. the flow rate through the bulkhead reduces and the maximum response amplitude is growing as the solidity ratio increases.

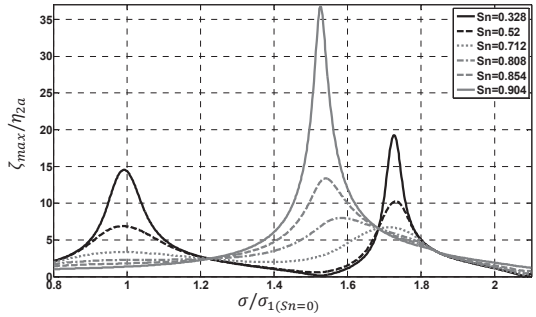

Fig. 3, Theoretical results for steady-state response amplitude at the distance of 1cm from a vertical end wall for different solidity ratios, $h/l = 0.4$ and $\varepsilon = 0.01$.

Table 2. Pressure loss coefficients, the corresponding solidity ratios based on Blevins's experimental results and the theoretical results for the first and the second resonant frequencies for $\varepsilon = 0.01$ and $h/l = 0.4$.

Sn	K	$(\frac{\sigma}{\sigma_{1(Sn=0)}})_1$	$\frac{\zeta_{max_1}}{\eta_{2a}}$	$(\frac{\sigma}{\sigma_{1(Sn=0)}})_2$	$\frac{\zeta_{max_2}}{\eta_{2a}}$
0.328	1	0.99	14.54	1.726	19.27
0.52	4.53	0.99	6.89	1.730	10.25
0.712	20.83	0.99	3.34	1.710	6.7
0.808	50.74	1.581	8.01	-	-
0.854	96	1.539	13.40	-	-
0.904	273.97	1.525	36.84	-	-
0.927	506.48	1.525	67.85	-	-
0.948	937.44	1.523	125.46	-	-
0.962	1443.45	1.523	193.10	-	-

The presented theory makes it possible to show how the second maximum response shifts in the frequency domain as the solidity ratio increases. Fig. 4 shows the variation of the second resonant frequency as a function of the forcing amplitude and the solidity ratio. The figure shows that the second resonant frequency experiences a large change around a specific solidity ratio. This change behaves more gradually for the larger forcing amplitude.

Uniform flow assumption through the bulkhead and its effect on the numerical results. At the relative depth ($\frac{h}{l} = 0.4$) , the exact value of the first, the second and the third non-dimensional natural frequencies $\frac{\sigma}{\sigma_{1(Sn=o)}}$ are 1, 1.5237 and 1.8774. We had expected to see the maximum

responses at these frequencies.

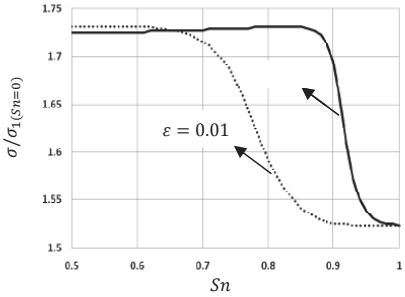

Fig. 4, The variation of the non-dimensional second resonant frequency versus the solidity ratio at liquid depth-to-tank length ratio $h/l = 0.4$ for different non-dimensional forcing amplitudes $\varepsilon = \eta_{2a}/l$.

However, Fig 2 and 3 show that the resonant frequencies are not completely matched with all these frequencies. The reason is that the assumed piston-like (uniform) flow between the compartments does not properly account for the fact that the flow velocity decreases exponentially as we go down towards the tank bottom. This error is larger for higher modes and larger depth-to-tank length ratios. For instance, Table 2 and Table 3 confirm that this error is larger for the third natural frequency. Numerical experiments show that the uniform flow assumption leads to only 0.1% error for the lowest natural frequency if $\frac{h}{l} < 0.5$. The error increases with liquid depth (up to 1% for fairly deep water). It is also larger, up to 5-7%, for higher modes (Faltinsen and Timokha, 2009). The error due to the uniform flow assumption through the bulkhead is more of concern for low solidity ratios.

Applicability of the Theoretical Results

We have demonstrated that conditions causing small sloshing are tank amplitude dependent. We have limited our studies to harmonic lateral excitation with steady-state conditions in two-dimensional flow conditions. The tank is rectangular, but Faltinsen and Timokha (2009) have shown that a chamfered tank bottom has a minor influence on natural modes and frequencies. In reality, we must consider a family of design sea state conditions with corresponding time-domain realizations of the tank motions. Further, the liquid depth-to-tank length ratio must be varied. The described generalizations are possible by means of the presented theory. However, an important question is to what extent free-surface nonlinearities matter. The latter will be addressed by comparing with model tests.
One may in principle use validated CFD methods to find an optimum solidity ratio. However, a CFD solver is very time-consuming which limits its applicability for systematic investigations. The described quasi-linear method has therefore an advantage for systematic studies of optimum conditions.

EXPERIMENTAL INVESTIGATION

Experimental Setup

Forced lateral harmonic tank motion $\eta = \eta_{2a}\cos(\sigma t)$ is studied. The swash bulkhead is in the middle of the tank as shown in Fig. 5. The interior tank length in the excitation direction is 1m. The tank is installed in a 2D sloshing rig located at the Marine Technology Centre in Trondheim, Norway. Inside the tank two resistant wave probes with accuracy of one mm have been installed 1cm away from the vertical walls (Fig. 5) in order to avoid the effect of local wave run-ups on the walls.

Selection of the Swash Bulkhead Perforations and the Tank Dimensions. In order to achieve a two-dimensional flow through the swash bulkheads, the opening area is horizontal with constant height covering the tank breadth which is defined as the tank length perpendicular to the excitation direction (Fig. 5). A given solidity ratio can be the consequence of many different opening arrangements. Fig. 6 shows the arrangement of the openings and their dimensions for different solidity ratios. In the figure, the solidity ratio increases from left to right. As an example, the dimensions of the openings are given for $Sn = 0.328$. The distribution of the openings is more uniform for low solidity ratios. Due to the technical limitations in the drilling of openings with very small dimensions, the number of openings was reduced for large solidity ratios and as a consequence this will increase the non uniform inflow-outflow between the compartments.

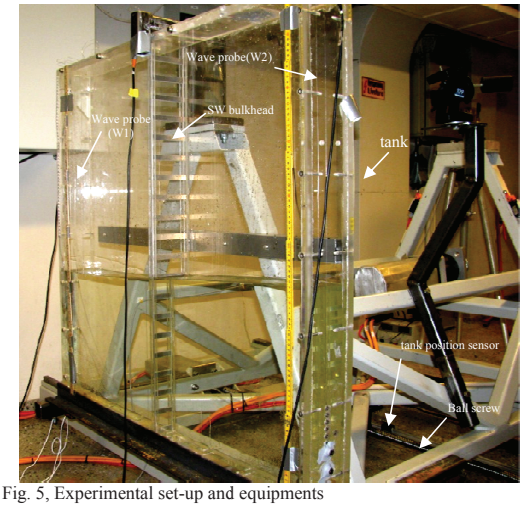

Fig. 5, Experimental set-up and equipments

The tank breadth should be small in order to achieve two-dimensional flow conditions. For instance, a prismatic tank with a nearly square base and no interior structures may develop important nonlinear three-dimensional flow such as swirling, diagonal waves and chaos for lateral excitation along a tank wall (Faltinsen and Timokha, 2009). However, we must avoid that the tank is so narrow that viscous effects associated with the boundary layers at the tank walls matter. As a measure of the viscous boundary layer thickness we consider a period of 1.83 seconds. It follows by Froude scaling and a ratio between the full scale length and the model length ($\frac{l_p}{l_m}$) equal to 30 that a model period of 1.83 seconds corresponds to a full scale period of 10 seconds. Using linear boundary layer theory for laminar harmonically oscillating flow gives a geometrical measure of the boundary layer thickness of approximately 0.0035m. Therefore, a width of 10 cm is sufficient to have 99.3 per cent of the tank breadth out of the boundary layer. A tank with the dimensions of 1.0m x 0.98m x 0.1m (length x height x breadth) were chosen. The damping due to viscous energy dissipation along the tank walls is very small and negligible in our context (Faltinsen and Timokha, 2009). There occur meniscus effects at the intersection

between the tank walls and the free surface leading to three-dimensional waves with very small wave height and wave length relative to the gravity waves. The error due to meniscus effects is therefore believed negligible.

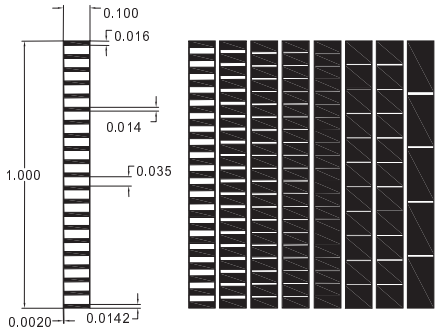

Fig. 6, Swash bulkheads and distribution of the openings for different value of solidity ratios. From left to right the solidity ratios are: 0.328, 0.52, 0.712, 0.808, 0.854, 0.904, 0.927, 0.948 and 0.962.The dimensions are in meters. The solid area is in black.

Performing the Experiments

Generally the steady-state response elevation of sloshing waves is recorded for different forcing frequencies in specific frequency intervals. All of these intervals together should cover a frequency range of $0.6\,Hz \le f \le 1.7\,Hz$ ($\cong 0.8 < \frac{\sigma}{\sigma_{1(Sn=0)}} < 2.1$). An important consideration is that the steady-state solution may belong to different solution branches due to nonlinear free-surface effects. Which steady-state solution is obtained depend on the transient time history. We will illustrate the fact that different steady-state solution exist by using a nonlinear multimodal theory with damping for a finite depth larger than the critical depth $h/l = 0.3368$ (Faltinsen and Timokha, 2009). There are no interior structures. The typical soft-spring behavior in the vicinity of the lowest natural sloshing frequency is shown in Fig.7.

The maximum response occurs at a frequency lower than the natural frequency $\sigma_1$according to linear theory. If the forcing frequency σ is decreased continuously from a frequency higher than σ_1, the response amplitude will reach a maximum and then jump from A_2 to a smaller value A_3(Fig. 7). In the opposite direction, by increasing the forcing frequency a jump at the turning point T to a higher value A_1 takes place and then it decreases smoothly with increasing forcing frequency. In Fig. 7 is also shown a solution branch which can never occur due to the fact that the corresponding steady-state solutions are unstable. This unstable solution branch starts from T to A_2 and is between the higher and lower solution branches in this frequency range. However, for a sufficiently high damping the jump phenomenon, i.e. the hysteresis effect, does not occur. What we are saying is if the cross-flow past the perforated plate causes sufficiently large damping, we will not see jumps. However, we must conduct the experiments properly in order to be able to detect jumps and not just start the forcing of the tank with a given forcing frequency. What we are interested in is the largest possible steady state amplitude. Based on the previous explanation, the maximum possible steady state amplitude occurs if the forcing frequency decreases continuously. Fig. 7 illustrates that two stable steady-state solutions may exist in a certain frequency range. We will illustrate experimentally the latter fact for the highest excitation amplitude by showing two different steady-state solutions in the two compartments for a range of solidity ratios.

As an example, for $\frac{h}{l} = 0.4$, $\varepsilon = 0.001$, the tank is excited by a long sinusoidal input signal. The signal starts from a frequency larger than the third natural frequency of the tank without swash bulkhead and lasts for about 300 cycles at this frequency. In this way the response elevation reaches steady-state conditions after about 100-150 cycles and then the maximum wave-elevation in the steady state region is found. Then the frequency decreases to a lower value and again this frequency lasts for about 300 cycles to reach steady state responses. The step of frequency changes is smaller around the peak points of the response in order to have the precise value of the resonance frequencies. In this way a long input signal is required to cover the whole frequency range.

For $\varepsilon = 0.01$, when the forcing frequency is around a resonant frequency, a real steady-state condition cannot be met because of the steep waves and wave breaking, strong transients and progressive waves and unsteady effects of the swash bulkhead on the flow. Therefore, a mean value amongst all the maximum responses is used.

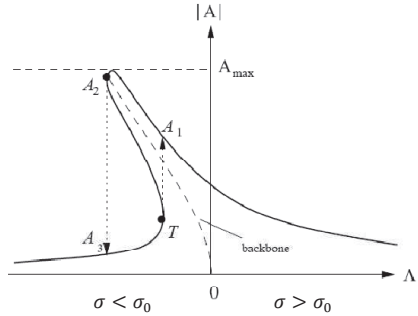

Fig. 7, Different solution branches for steady-state amplitude around the lowest natural frequency. σ_0 is the lowest natural frequency. Λ is detuning parameter: $\Lambda = (\sigma_0^2 - \sigma^2)/(\varepsilon^{\frac{2}{3}}\sigma^2)$. The depth is larger than the critical depth (Faltinsen and Timokha, 2009).

Experimental Results and Analysis

A. $\boldsymbol{\varepsilon = 0.001}$. Fig. 8 presents the maximum wave elevation for the first series of experiments for Sn values of 0.328, 0.712, 0.904, 0.927, 0.948, 0.962, $\varepsilon = 0.001$ and $\frac{h}{l} = 0.4$. Since the forcing amplitude is very small and the accuracy of the wave probes is 1 mm, it is difficult to detect the smallest response in particular when the difference between the peaks is very small. For most of the solidity ratios, the curves are nearly flat around the two resonant frequencies and single frequencies corresponding to the maximum responses is not possible to report. Therefore a frequency range is notified in Table 3 around each resonant frequency. When there are no peaks, no frequency range is reported. The resonant frequencies are categorized for the first and the second resonant frequencies in Table 3. The gray background data corresponding to $Sn = 0.948$ and $Sn = 0.962$ indicate that the frequency of maximum response is in a frequency range that is in the neighborhood of the lowest natural frequency of a compartment. In the above-mentioned theory this shift of the lowest frequency of maximum response to the lowest natural frequency of a compartment occurs at a lower solidity ratio, i.e. $Sn = 0.904$. However, the theoretical results depend on the selection of the K-values.

Sn_{min}=0.927 gives the lowest response which is in a frequency range smaller than the range of the second maximum frequency response for lower solidity ratios (Table 3). No peak point can be detected around

the first maximum frequency for $Sn = 0.927$. Theoretical calculations predict $Sn = 0.904$ as the optimum value which is not far from the experimental results. In brief, comparing the results of theory and experiments for $\varepsilon = 0.001$ is summarized in Table 4.

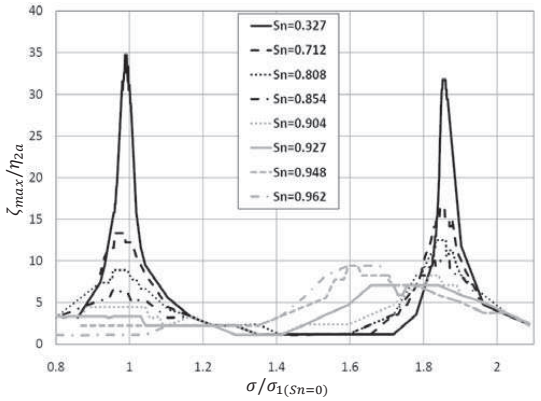

Fig. 8, Non-dimensional maximum wave elevation at a distance of 1 cm from the vertical walls in experiments for $h/l = 0.4$, $\varepsilon = \eta_{2a}/l = 0.001$.

Table 3. Experimental results for ε=0.001 and $h/l = 0.4$. F1 and F2 ranges describes the frequency ranges around the first and the second resonant frequencies.

Sn	F1 range $\sigma/\sigma_{1(Sn=0)}$	$\frac{\zeta_{max}}{\eta_{2a}}$	F2 range $\sigma/\sigma_{1(Sn=0)}$	$\frac{\zeta_{max}}{\eta_{2a}}$
0.328	0.988-0.993	34.8	1.852-1.86	31.8
0.52	0.98-0.981	25.6	1.85-1.856	27.1
0.712	0.96-0.988	13.3	1.845-1.857	16.5
0.808	0.955-0.994	8.9	1.833-1.861	12.5
0.854	0.957-0.994	6.32	1.83-1.87	10
0.904	-	-	1.817-1.841	8.24
0.927	-	-	1.695-1.841	7.06
0.948	1.596-1.620	9.41	-	-
0.962	1.596-1.682	9.41	-	-

Fig. 9 shows that by finding an appropriate pressure loss coefficient K it is possible to fit the results of the experiments with the theoretical results for the lowest resonance frequency. However, with this pressure loss coefficient the peak point on the second resonant frequency (third natural frequency of sloshing for a tank without interior structures) does not agree with the experiments neither for the frequency nor for the response amplitude. The fitting is also done for $Sn > 0.904$ where only one clear peak point exists. Table 5 presents the numerical results including the frequency range of the peak points for both theory and experiments where the fitted pressure loss coefficients have been used. Calculations for finding a pressure loss coefficient show that the theoretical results are not very sensitive to the pressure loss coefficient for large solidity ratios around Sn_{min}. It means that large changes of pressure loss can make a very small change in the amplitude response and its corresponding resonant frequency (when Sn is around Sn_{min}).

Table 4. The optimum solidity ratio and the non-dimensional frequency range of maximum response for $\varepsilon = 0.001$

Items	Theory	Experiments
Sn_{min}	0.904	0.927
Resonant frequency (range) $(\sigma/\sigma_{1(Sn=0)})$	1.68	1.695-1.841

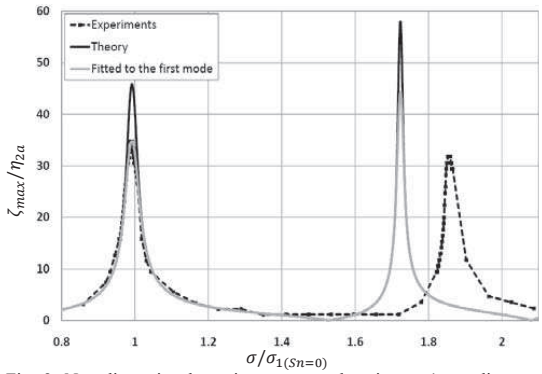

Fig. 9, Non-dimensional maximum wave elevation at 1 cm distance from the tank end wall. Theoretical results with empirical and fitted pressure loss coefficients, together with experimental results for $h/l = 0.4$., $\varepsilon = \eta_{2a}/l = 0.001$ and Sn value of 0.328.

Table 5. Empirical and fitted pressure loss coefficients for the first resonant frequency. For Sn>0.904, only one resonant response exists.

Sn	K(Blevins)	K(fitted)	Frequency (Range) Theory	Frequency (Range) Experiments
0.328	1	1.73	0.99	0.988-0.993
0.52	4.53	3.2	0.99	0.98-0.981
0.712	20.83	11.9	0.99	0.96-0.988
0.808	50.74	26.8	0.99	0.955-0.994
0.854	96	54	0.99	0.957-0.994
0.904	273.97	87	1.73	1.817-1.841
0.927	506.48	400	1.615	1.695-1.841
0.948	937.44	520	1.578	1.596-1.62
0.962	1443.45	630	1.56	1.596-1.682

B. $\boldsymbol{\varepsilon = 0.01}$**.** It is expected from the above-mentioned theory that by increasing the forcing amplitude, the largest damping might in general be achieved for a lower solidity ratio (Fig. 3). Experiments prove this fact in general. Also, the experiments confirm the theoretical results predicting that the damping is larger for larger forcing amplitude at low solidity ratios (when $Sn <= (Sn_{\min})_{\varepsilon=0.01}$). This is obvious by comparing the results in Fig. 10 or Fig. 11 with the results in Fig 8.
The quasi-linear theory predicts equal responses in both compartments of the tank no matter what the forcing amplitude is. The experiments confirm this fact for $\varepsilon = 0.001$. However, the experiments for $\varepsilon = 0.01$ shows that the response wave elevations in the two compartments can be different around resonance frequencies. This difference can be very large for certain solidity ratios. Fig. 10 and Fig. 11 exhibit the results for the left and right compartments, respectively. The three thick solid lines illustrate the positions of the first, the second and the third natural

frequencies of the clean tank.

The experimental results for $\varepsilon = 0.01$ contain interesting information about the behavior of the tank-liquid system in both compartments. Starting the investigation from the lowest solidity ratio, the steady-state amplitude-jump has happened for the third resonant frequency of sloshing unlike the results for $\varepsilon = 0.001$ that never show an amplitude jump. When $\varepsilon = 0.01$ and the forcing frequency is in the vicinity of the second natural frequency, the damping is not sufficiently large for the system to behave like a linear system. Nonlinearities will then, according to nonlinear multimodal theory, transfer energy between different sloshing modes and limit the response at the resonant mode according to linear theory. Another peculiar phenomenon is a small jump on the right side of the former jump on the same curve ($Sn = 0.328$). This is connected with the presence of the swash bulkhead (repeating the experiments without bulkheads do not show this small jump).

For $Sn = 0.52$ the amplitude jump does not occur and the peak point moved a little towards a higher frequency range and also, the peculiar small jump is still there but with smaller amplitude. The result for $Sn = 0.52$ in the left compartment shows a small growing bump around the first natural frequency of a compartment without perforated wall.

$Sn = 0.712$ introduces a new jump in the frequency range close to the third natural frequency but this time the response jumps to a higher value. At the non-dimensional forcing frequency 1.277, a new peak point is introduced to the system which is not connected to any natural frequencies of the system. This peak exists in the same frequency range for $Sn = 0.808 \sim 0.927$ but it disappears for $Sn = 0.948$ and larger solidity ratios.

Unequal steady-state amplitude in the compartments can be identified clearly at $Sn = 0.808$ and $Sn = 0.948$. Since at these solidity ratios different interesting information is present, it would be better to present the results for these solidity ratios in separate figures.

In Fig. 12 which is for $Sn = 0.808$, along with decreasing of the frequency, five zones with high responses can be detected. From right to left, the first one is related to the third mode of sloshing, the second one stands for the second mode, the third one is another new peak point, the fourth one is the same peculiar peak point as for $Sn = 0.712 \sim 0.927$ and finally the fifth one which is new again and it is at the right side of the first natural mode of the original tank. These new and unexpected peak points might be due to the combination of different modes and harmonics due to the presence of the bulkhead. The difference between the responses in the two compartments ($Sn = 0.808$) is getting very large when $0.1471 < \frac{\sigma}{\sigma_{1(Sn=0)}} < 0.1571$.

Around the non-dimensional frequency of 1.497 the response on the right side is approximately two times the response in the other side. In fact the large response on the right side holds in a wider range than the left side. The important matter for $Sn = 0.808$ is that it provides the smallest response in both compartments (Fig. 10 and 11).

Therefore experimental results predict a larger solidity ratio as the $Sn_{\min}$ (theory predicts $Sn_{\min} = 0.712$). The difference in the maximum response for the optimum conditions in theory and experiments is not large. Comparisons between the results for $\varepsilon = 0.01$ for experiments and the theory are summarized below in Table 6.

The other very interesting results appear for $Sn = 0.948$ when the highest response in the left compartment is about four times the response in the right one (Fig. 13). It can be seen that for forcing frequencies around the second natural frequency, when one of the responses starts getting larger, the other one goes in the opposite way and gets smaller. One may say that larger inflow through the bulkhead from one side to the other side causes a large damping to the compartment with the lower response. Even more, the maximum elevation in the left compartment for $Sn = 0.948$ is larger than the maximum elevation for $Sn = 0.962$. This does not follow the predictions of the quasi-linear theory that the largest response occurs for the largest solidity ratio. An interesting fact is that repeating the experiments does not give the same results in the same compartment. It illustrates that different steady-state solutions exist due to free-surface nonlinearities for a given forcing frequency as illustrated for a clean rectangular tank in Fig. 7.

Table 6. The optimum solidity ratio and the non-dimensional frequency range of maximum response for $\varepsilon = 0.01$

	Theory	Experiments(Left)	Experiments(Right)
Sn_{min}	0.712	0.808	0.808
Resonant frequency (range) $(\sigma/\sigma_{1(Sn=0)})$	1.71	1.571-1.620	1.497-1.633

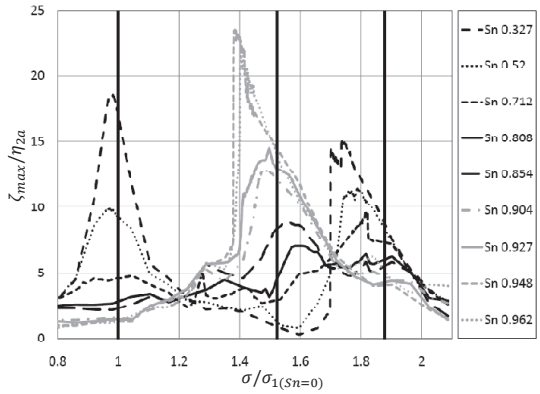

Fig. 10, Maximum elevation in the left compartment for $\varepsilon = 0.01$ and $h/l = 0.4$.

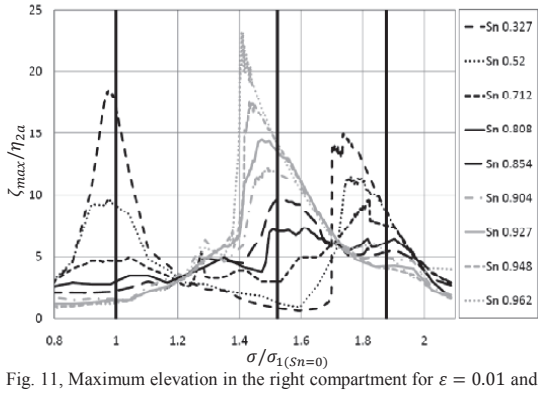

Fig. 11, Maximum elevation in the right compartment for $\varepsilon = 0.01$ and $h/l = 0.4$..

The higher jump at the third resonant frequency for $Sn = 0.328$ and for largest solidity ratios i.e. $Sn = 0.948$ and $Sn = 0962$ is due to the soft-spring effect but the other jumps observed here can be due to the presence of the bulkheads. There were no jumps or any unexpected nonlinear phenomena in the case of $\varepsilon = 0.001$ in the experimental

results. This emphasizes the important role of large forcing amplitude in amplifying the nonlinear effects.

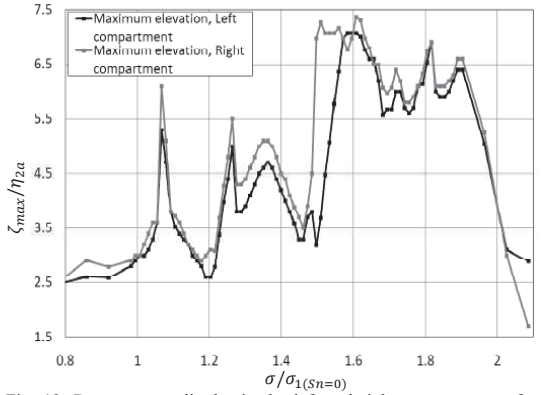

Fig. 12, Response amplitudes in the left and right compartments for $\varepsilon = 0.01$, $Sn = 0.808$ and $h/l = 0.4$.

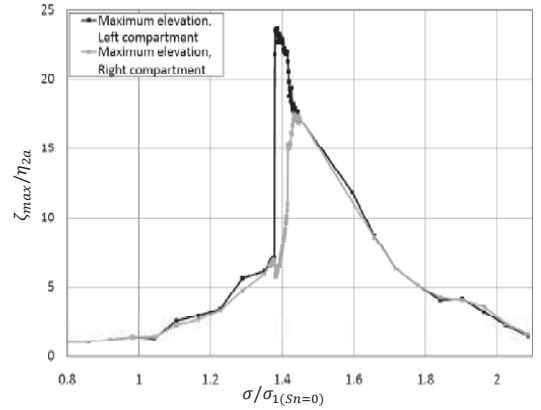

Fig. 13, Response amplitudes in the left and right compartments for $\varepsilon = 0.01$, $Sn = 0.948$ and $h/l = 0.4$.

CONCLUSIONS

The presented quasi-linear theory provides guidance on the optimum solidity ratio Sn_{min} and resonant frequency (ies) range. Table 7 shows the relatively good performance of the theory in determining Sn_{min} for very low forcing amplitude and for a higher forcing. The predicted resonant frequency by theory is not bad relative to the experimental results for the lowest forcing amplitude but it is a little far from the experimental results for the larger forcing.

For low solidity ratios the theoretical results are sensitive to the pressure loss coefficient. This sensitivity is low when the solidity ratio is in the vicinity of Sn_{min}. Blevins (2000) notified that the accuracy of the presented pressure loss coefficients are $\pm 20\%$ and the error is higher when the solidity ratio is larger than 0.9 or smaller than 0.15. As a consequence, the theory can give fair predictions about the range of minimum response in terms of solidity ratio and the frequency range of maximum responses even for relatively large forcing amplitude.

Nonlinear effects can cause large differences between the steady-state oscillations in the two compartments when the forcing amplitude is not very small and the solidity ratio is not small, let say larger than 0.712 for $\varepsilon = 0.01$. The interesting examples are $Sn = 0.808$ and $Sn = 0.948$, where the difference between the responses in the two compartments can be very large ($\varepsilon = 0.01$).

Table 7. Optimum solidity ratios for theory and experiments. Frequency ranges are non-dimensional ($\sigma/\sigma_{1(Sn=0)}$)

	Theory	Experiments(Left)	Experiments(Right)
Sn_{min} ($\varepsilon = 0.001$)	0.904	0.927	0.927
Resonant frequency (range) ($\varepsilon = 0.001$)	1.68	1.695-1.841	1.695-1.841
Sn_{min} ($\varepsilon = 0.01$)	0.712	0.808	0.808
Resonant frequency (range) ($\varepsilon = 0.01$)	1.71	1.571-1.620	1.497-1.633

Assuming uniform flow through the bulkheads in the theory causes an error in the predicted resonant frequency for higher modes and large depths ($h/l > 0.5$). Including the effect of exponential decreasing of the flow velocity in the theory can make this error smaller.

In this study, the shape of perforations is chosen to be rectangular to have a two-dimensional flow condition. Other shapes of perforations may change the results. In addition, we are able to have uniform distribution of openings for low solidity ratios but not for the large solidity ratios due to technical limitations in cutting very narrow openings in the plates. This can cause different local effects on the inflow-outflow for these large solidity ratios.

REFERENCES

Abramson, H.N. and Garza, L.R. (1965). "Some measurements of liquid frequencies and damping in compartmented cylindrical tanks," AIAA Journal. Spacecraft and Rockets 2, 453-455.

Akita, Y (1967). "Dynamic pressure of cargo oil due to pitching and effectiveness of swash bulkhead in long tanks," Japan Shipbuilding and Marine Engineering, Vol 2, No 5, p 42-55.

Blevins, RD (2000). "*Applied Fluid Dynamics Handbook*," Malabar, FL:Kreiger.

Dodge, F.T. (2000) "*The New Dynamic Behavior of Liquids in Moving Containers*," Southwest Research Institute, San Antonio, Texas, USA.

Faltinsen, OM, Timokha, AN (2009)."*Sloshing*," Cambridge university press".

Garza, LR (1964). "Measurements of liquid natural frequencies and damping in compartmented cylindrical tanks," Technical Report No. 8. Southwest Research Institute, San Antonio, Texas, USA.

2. Faltinsen, O. M., Firoozkoohi, R., & Timokha, A. N. (2011). Analytical modeling of liquid sloshing in a two-dimensional rectangular tank with a slat screen. Journal of Engineering Mathematics , 70, 93-109.

J Eng Math (2011) 70:93–109
DOI 10.1007/s10665-010-9397-5

Analytical modeling of liquid sloshing in a two-dimensional rectangular tank with a slat screen

O. M. Faltinsen · R. Firoozkoohi · A. N. Timokha

Received: 19 March 2010 / Accepted: 17 July 2010 / Published online: 4 August 2010

Abstract Potential-flow theory is employed with linear free-surface conditions, multimodal method, and a screen-averaged pressure-drop condition to derive an analytical modal model describing the two-dimensional resonant liquid motions in a rectangular tank with a vertical slat-type screen in the tank middle. The tank is horizontally excited in a frequency range covering the two lowest natural sloshing frequencies. The model consists of a system of linear ordinary differential [modal] equations responsible for liquid sloshing in compartments, as well as a nonlinear ordinary differential equation describing the liquid flow between the compartments. New experimental model tests on steady-state wave elevations near the tank wall are reported for the solidity ratios $0.328 \leq \mathrm{Sn} \leq 0.963$ where Sn is the ratio between the solid area and the full area of the screen. The experiments generally support the applicability of the model. The discrepancy can be explained by the free-surface nonlinearity. The screen acts as a damping mechanism for low and intermediate solidity ratios, but it causes an increase in the lowest resonant sloshing frequency at higher solidity ratios as if the screen had been replaced by an unperforated wall.

Keywords Multimodal method · Perforated screen · Sloshing

1 Introduction

Screens and perforated plates can provide important damping of sloshing in a tank. They may also affect the natural sloshing frequencies. An important parameter is the solidity ratio, Sn, which is the ratio of the area of the shadow projected by the screen on a plane parallel to the screen to the total area contained within the frame of the screen. The solidity ratio is between zero and one, where $\mathrm{Sn} = 0$ means no screen and $\mathrm{Sn} = 1$ means that the screen becomes an unperforated wall.

Perforated plates have been studied in the past century in the context of liquid sloshing in cylindrical fuel tanks of spacecraft (see the NASA report [1, Sect. 4.4]). Other hydrodynamic-screen applications are associated with anti-rolling tanks of ships, tuned liquid dampers (TLD) of tall buildings, swash bulkheads of ships, and perforated plates of oil–gas separators on a floating platform (see for instance [2–5]). A design requirement for anti-rolling tanks and TLDs is that the lowest natural sloshing frequency should not be significantly affected by the screen and

O. M. Faltinsen (✉) · R. Firoozkoohi · A. N. Timokha
Centre for Ships and Ocean Structures and Department of Marine Technology, Norwegian University of Science and Technology, 7491 Trondheim, Norway
e-mail: odd.faltinsen@ntnu.no

approximately equal to the roll natural frequency and the lowest important structural natural frequency, respectively. The damping should be large. The consequence is that either the wave-induced roll motions of a ship or wind- and earthquake-excited vibrations of tall buildings are clearly reduced. A rough guideline is that the solidity ratio ought to be about 0.5. The objectives for a swash bulkhead in cargo liquid tanks of ships and perforated plates in oil–gas separators on floating platforms are to provide sloshing damping as well as to change the lowest natural sloshing frequency to a higher frequency range where the wave-induced ship and platform velocities and accelerations are less severe. The consequence is a high solidity ratio.

Our focus is on analytical modeling of liquid sloshing in a rectangular tank with a slat screen (interested readers may find a review on appropriate CFD methods in the recent paper by Maravani and Hamed [5]) to be applicable for $\mathrm{Sn} \geq 0.3$. The excitation is horizontal and harmonic, and the flow is nearly two-dimensional.

Existing analytical modeling techniques typically assume that the screen has a minor effect on the natural sloshing frequencies. Under this assumption, we may use the flow in a clean tank as an ambient flow and estimate the energy dissipation due to the screen. This estimate can be done by empirical drag-force formulations that account for flow parameters such as the Reynolds number and the geometrical screen shape [6, Chap. 6], or employing the empirical pressure-drop condition [3,4,7,8]. Thereafter, the found damping rates can be incorporated into either modal [6,9] or equivalent (pendulum, spring-mass etc.) mechanical systems [3,4] by using an equivalent linearization technique in steady-state conditions. Such a procedure based on empirical drag formulation is exemplified in [6, Sect. 6.8] for a screen placed in the middle of a rectangular tank with two-dimensional ambient flow. The ambient flow was described by the linear potential-flow theory of an incompressible liquid. The relatively small effect of viscous boundary-layer damping was incorporated. There was good agreement with the experimental values of damping ratio, steady-state wave amplitude and longitudinal force for a rectangular tank with a wire mesh screen by Warnitschai and Pinkaew [2]. The experimental conditions for forced tank oscillations was a water depth-to-tank length ratio of 0.3, and longitudinal forcing amplitude divided by tank length equal to 0.005. The solidity ratio was 0.48.

A different procedure has to be followed for higher solidity ratios when the screen significantly affects the resonance sloshing frequencies which tends to the natural frequencies in the compartmental tanks, i.e., the tanks that result from replacing the screen with an unperforated wall. A large change in the pressure and free-surface profiles occurs then across the screen. Which lower solidity ratio causes this change in two-dimensional flow depends during harmonic excitation on the liquid depth-to-the tank width ratio and the ratio between the lateral forcing amplitude and the tank width. When the change in the lowest resonance sloshing frequency occurs, the sloshing is less severe relative to a clearly lower or higher solidity ratio.

The *main goal* of this paper is to show that employing multimodal methods makes it possible to derive an analytical [modal] model for sloshing in a rectangular tank with a screen which can be applied for any solidity ratio. The corresponding modal system is derived from the original boundary-value problem with linear free-surface conditions by employing the pressure-drop condition as a transmission condition at the screen in a domain decomposition scheme. The pressure-drop condition describes the effect of the jet flow through the screen at higher solidity ratio, and the flow separation (wake) at lower solidity ratios. The modal system explicitly handles discontinuity of the free surface (pressure). New experiments with slat-type screens are reported which support the applicability of the derived modal system when the free-surface nonlinearity does not have a dominant effect.

We start the analysis with the linear sloshing boundary problem formulated for each compartment (Sect. 2.1) and, in addition, introduce two transmission conditions (Sect. 2.2) at the screen. The first transmission condition (Neumann-type) implies continuity of normal velocity, but the second (Dirichlet-type) condition governs the screen-averaged pressure drop. In Sect. 2.2, we discuss applicability of the second condition for the slat screen used in our experiments.

There is a variety of external wave problems with screens and porous barriers that have been studied by using an analytical technique with the corresponding transmission conditions. In the list of these studies, we should mention the *papers by E. Tuck* [10,11] whose concept of the transmission conditions is, for instance, realized in [12]. Reviews on wave interaction with porous media are given in [13], or in the more recent book [14] where the transmission conditions are based on Darcy's law. Another approach to the pressure-drop condition developed for wind-tunnel engineering is outlined in the review [15] as well as in the handbook [16, pp. 314–316]. It assumes a uniform steady

flow. Based on this approach, a version of the pressure-drop conditions for external wave problems is adopted in [17,18]. The latter papers deal with porous-type screens characterized by small sharp-edged openings providing the flow separation through the holes so that the rotational wakes and jets remain in a neighborhood of the screen. For these screens, a local-averaging procedure is possible (as described by Molin [17]) leading to a pressure-drop condition to be mathematically satisfied at each point of the screen. Our approach averages the pressure-drop condition over the mean submerged screen area by accounting for the exponential decay of the velocity field.

As will be shown in Sect. 2.3, employing the screen-averaged pressure-drop condition leads to non-unique solutions of the linear sloshing problem under consideration. To avoid non-uniqueness, we assume that the velocity profile at the slat screen keeps the same shape for $0 \leq \mathrm{Sn} \leq 1$. In other words, our hypothesis is that the velocity profile (exponentially decaying from the free surface to the bottom) remains close to that occurring for steady-state sloshing in the smooth tank ($\mathrm{Sn} = 0$). This assumption is not in conflict with the asymptotic limit $\mathrm{Sn} \to 1$. The formula for the pressure loss coefficient K of the screen is taken from [19,20]. Even though the formula is for a steady flow, its applicability for unsteady wave flows was experimentally confirmed in [3].

In Sect. 3, we derive the modal system described above. Because linear free-surface conditions are assumed, the system includes two subsystems of linear ordinary differential equations which governs liquid sloshing in the compartments. This sloshing is excited by both horizontal motions of the tank and cross-flow at the screen. The free-surface elevation described by these subsystems has a jump in the tank middle at the assumed screen position. The presence of the jump is consistent with the fact that there is a pressure drop across the screen. The subsystems are coupled by a nonlinear ordinary differential equation with respect to a generalized coordinate responsible for the liquid flow through the screen.

In Sect. 4, we report new experimental model tests, and compare the experimental measurements on steady-state wave elevations at the tank wall with those following from our modal theory. Agreement is satisfactory and the experiments generally support the theory for smaller forcing amplitude (the forcing amplitude-to-the-tank-width ratio η_{2a}/l is about 0.001). Theoretical predictions for the larger forcing amplitude ($\eta_{2a}/l = 0.01$) are consistent in some cases with the primary Fourier harmonics of the measured output signal. The higher harmonics in the measured resonant wave elevations contribute up to 35% and, we believe (see discussion in [21,22]), they are associated with amplification of the higher modes due to the free-surface nonlinearity. The linear potential-flow theory used here is only relevant in resonant conditions if the damping is sufficiently large. Otherwise nonlinear free-surface effects are dominant [6]. We do not know appropriate analytical studies on nonlinear liquid sloshing in tanks with perforated screens. The proposed analytical modal scheme generally allows for the corresponding generalization.

2 Statement of the problem

We consider a two-dimensional rigid rectangular tank with a width $l = 2a$ and a mean liquid depth h (see Fig. 1). A perforated plate (screen) is mounted vertically in the tank middle. The tank is forced horizontally with small amplitudes relative to the tank width. The liquid is incompressible with irrotational flow except in limited jet or wake regions caused by cross-flow at the screen. The free-surface nonlinearity is neglected. Assuming purely piston-like transverse flow velocity at the screen, a steady-state analysis was performed in [6]. The forthcoming study is more

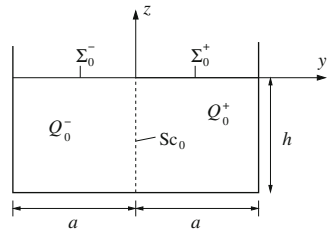

Fig. 1 Geometric definitions for the sloshing analysis with a screen Sc_0 in the middle of the tank dividing the tank into two compartments

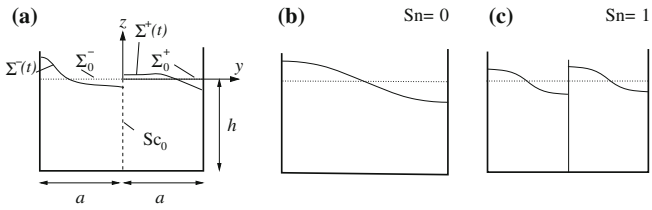

Fig. 2 Typical instantaneous wave profiles for two-dimensional sloshing in a rectangular tank due to horizontal excitation. Screen Sc_0 with $0 < Sn < 1$ in the middle is installed (part **a**). Parts **b** and **c** illustrate primary antisymmetric wave profiles for the limit cases $Sn = 0$ and $Sn = 1$, respectively

general. It accounts more properly for the fact that the transverse velocity at the screen decays with depth which matters in particular for larger liquid depths and at higher sloshing frequencies. This latter fact results in a correct prediction of the second natural sloshing frequency, in the present study with $h/l = 0.4$ and a frequency range that covers the two lowest natural sloshing frequencies. In addition, the presented modal method may handle transient waves.

2.1 Boundary-value problem in compartments

The corresponding linear liquid theory deals with the following boundary-value problems in the unperturbed liquid domains $Q_0^{\pm}$ (see Fig. 1).

The theory introduces the *absolute velocity* potentials $\Phi^{\pm}(y, z, t)$ in $Q_0^{\pm}$, which should satisfy the Laplace equation and the Neumann boundary conditions on the wetted tank surface

$$\nabla^2\Phi^{\pm} = 0 \text{ in } Q_0^{\pm}; \quad \frac{\partial\Phi^{\pm}}{\partial z} = 0 \ (z = -h); \quad \frac{\partial\Phi^{\pm}}{\partial y} = \pm\dot{\eta}_2 \ (y = \pm a), \tag{1}$$

where $\eta_2(t)$ describes the horizontal motions of the rigid tank.

Furthermore, the theory defines the free-surface elevations $z = \zeta^{\pm}(y, t)$ and states the kinematic,

$$\frac{\partial\Phi^{\pm}}{\partial z} = \frac{\partial\zeta^{\pm}}{\partial t} \quad (z = 0), \tag{2}$$

and dynamic,

$$\frac{\partial\Phi^{\pm}}{\partial t} + g\zeta^{\pm} = 0 \quad (z = 0), \tag{3}$$

boundary conditions on the unperturbed free surfaces $\Sigma_0^{\pm}$. These conditions couple $\Phi^{\pm}(y, z, t)$ and $\zeta^{\pm}(y, t)$ separately for the two compartments. Here, g is the gravity acceleration.

Further, the liquid conservation condition should be fulfilled

$$\int_{-a}^{0} \zeta^{-}\mathrm{d}y + \int_{0}^{a} \zeta^{+}\mathrm{d}y = 0. \tag{4}$$

The problem (1)–(3) requires initial conditions expressing the initial perturbation (function $\zeta_0(y)$) and its initial velocity (function $\zeta_1(y)$) of the free surface to be given, i.e.,

$$\zeta(y, 0) = \zeta_0(y), \quad \frac{\partial\zeta}{\partial t}(y, t) = \zeta_1(y). \tag{5}$$

Even though the free surface is discontinuous at Sc_0 (see Fig. 2a), the initial conditions should, due the required time to generate a pressure drop at the screen, involve smooth functions $\zeta_0(y)$ and $\zeta_1(y)$ on the whole interval $(-a, a)$. That is why the $\pm$-sign in conditions (5) is omitted.

2.2 Transmission conditions on Sc_0

As long as $\mathrm{Sn} = 0$ (smooth rectangular tank), the velocity potential and its normal derivative are continuous in the middle provided by an appropriate combination of Neumann and Dirichlet-type boundary conditions (see mathematical details in [23, Chap. 2]). Another limit case, $\mathrm{Sn} = 1$, suggests a rigid non-perforated wall in the middle which requires the zero normal derivative; there is no Dirichlet condition stated in this case. For both limit cases (see Fig. 2b, c), there exist analytical [modal] models reducing the linear sloshing problem (1)–(4) to the corresponding linear [modal] systems of linear ordinary differential equations [6, Chap. 5].

As long as the solidity ratio is between 0 and 1, the first transmission condition does not change, i.e.,

$$u_r(z,t) + \dot{\eta}_2(t) = \frac{\partial \Phi^-}{\partial y} = \frac{\partial \Phi^+}{\partial y} \quad (y = 0), \tag{6}$$

providing equal flux across Sc_0. Here $u_r(z,t)$ is the relative normal velocity on Sc_0.

The second condition should reflect the fact that the hydrodynamic pressure undergoes a jump. This condition is normally formulated for uniform flows which should, generally, be perpendicular to the flat screen. In accordance with definitions in [16] the pressure drop at the screen is

$$P^- - P^+ = \frac{1}{2}\rho K U|U|. \tag{7}$$

Here, $U = U(t)$ is the horizontal liquid velocity at the screen, $P^\pm = P^\pm(t)$ is the pressure at different sides of the screen so that the right direction is assumed to be positive, $K \geq 0$ is the so-called pressure-loss coefficient depending on the screen geometry, the solidity ratio Sn, the Reynolds number and, generally, the Keulegan–Carpenter number KC which may be defined as $\mathrm{KC} = U_M T/D$ where U_M is the amplitude of U, T is the forced oscillation period and D is a characteristic length of the screen such as the slat height. When the uniform in-flow velocity is not perpendicular to the flat screen, the pressure-loss coefficient becomes also a function of the in-flow angle.

When discussing the condition (7), we should remark that all the forces due to viscous effects are commonly expressed as quadratic functions of a reference velocity. An example for that is the Morison's equation commonly used for offshore structures. Formulations such as these rely on experimental values for drag coefficients. The formulations must give a good fit to experimental data. Then comes what parameters affect the drag coefficient. As we have mentioned, that is, for instance, the Reynolds number, the Keulegan–Carpenter number, the structural form (see [21, Chap. 7] where this is extensively discussed). Here we talk about a pressure-loss coefficient which has a similarity with the drag formulation in Morison's equation when viscous-flow separation matters. It is once more an empirical formulation that has been extensively investigated for ambient steady and space-independent flow [16]. Using linear formulations will not fit experimental data.

Our focus is on the slat screens depicted in Fig. 3. They are characterized by openings with sharp edges where flow separation occurs. The latter fact implies that the Reynolds-number dependence of the pressure-loss coefficient is negligible. The values of K for the slat screens with $\mathrm{Sn} > 0.3$ and $\mathrm{KC} > 2$ (with characteristic dimension equal to the slat height) are, according to [3] (the authors refer to [19,20] where the following expressions were established for steady flow), approximated by the formulas

$$K = \left(\frac{1}{\mathrm{Cc}\,(1-\mathrm{Sn})} - 1\right)^2, \quad \mathrm{Cc} = 0.405\exp(-\pi\,\mathrm{Sn}) + 0.595. \tag{8}$$

The pressure-loss coefficient monotonically increases with the solidity ratio from zero (at $\mathrm{Sn} = 0$) to infinity (at $\mathrm{Sn} = 1$).

Even though formulas (8) are originally proposed for steady uniform flows, it was illustrated in [3] by experiments for certain values of the solidity ratios that (8) is applicable in a screen-averaged sense (with mean values of the velocity and pressure over Sc_0) for sloshing problems with vertical screens, namely, it holds

$$\frac{1}{h}\int_{-h}^{0}\left[\frac{\partial \Phi^+}{\partial t} - \frac{\partial \Phi^+}{\partial t}\right]\mathrm{d}z = \frac{1}{2}KU|U|, \quad \text{where } U = \frac{1}{h}\int_{-h}^{0} u_r\,\mathrm{d}z. \tag{9}$$

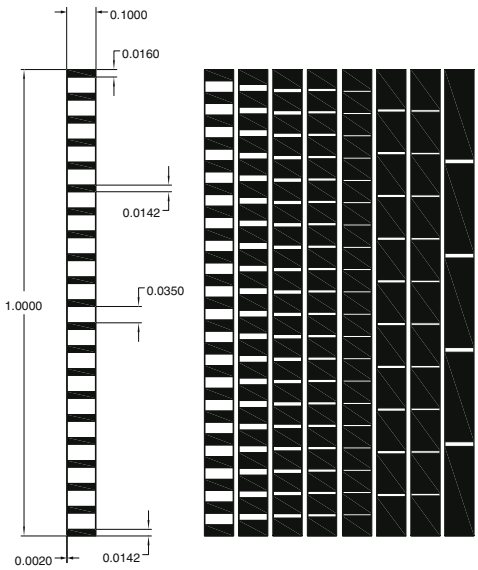

Fig. 3 A schematic distribution of the openings for different value of solidity ratios in our experimental slat screen. The dimensions are in meters. The screen thickness is 5 mm; it is neglected in our analysis. Because there is a limited number of slats, the solidity ratio varies with the mean liquid depth depending on how many openings become submerged. For the liquid depth 0.4 m, the solidity ratio is (from *left to right*) 0.328, 0.52, 0.713, 0.808, 0.855, 0.905, 0.928, 0.948 and 0.963

This condition will be adopted in our forthcoming analysis.

The pressure-drop condition plays the role of damping at small and intermediate solidity ratios. When Sn tends to 1, the flow experiences the screen as a barrier that is difficult to flow through. The consequences are small damping due to cross-flow and that the flow as a first approximation behaves as if the screen is an unperforated wall. The result is that the lowest resonant frequency changes to that in the separated compartments. The change of the resonant frequencies depends on the forcing amplitude, i.e., it cannot be explained by linear theory. Both theory and experiments confirm this fact.

2.3 Non-uniqueness and additional assumptions

According to the multimodal method, the velocity potentials $\Phi^{\pm}$ should be presented by a Fourier-type series in the natural sloshing modes (see [6, Chap. 5]). For the whole tank without screen, there are antisymmetric (relative to the Oz-axis) and symmetric natural modes. The antisymmetric (odd) modes take the form

$$\varphi_i(y,z) = \sin\left(\frac{1}{2}\pi(2i-1)y/a\right)\frac{\cosh\left(\frac{1}{2}\pi(2i-1)(z+h)/a\right)}{\cosh\left(\frac{1}{2}\pi(2i-1)h/a\right)}, \quad i=1,2,\ldots. \tag{10}$$

Only these modes are directly excited within the framework of the linear sloshing approximation as $\mathrm{Sn}=0$.

The symmetric (even) natural modes are

$$\phi_i(y,z) = \underbrace{\cos(\pi i y/a)}_{f_i(y)}\frac{\cosh(\pi i(z+h)/a)}{\cosh(\pi i h/a)}, \quad i=1,2,\ldots. \tag{11}$$

These modes are not excited (within the framework of linear sloshing theory) for $\mathrm{Sn}=0$, but, whereas $\mathrm{Sn}=1$, projections of these modes,

$\phi_i^{\pm} = \phi_i|_{Q_0^{\pm}}, \quad f_i^{\pm} = f_i|_{\Sigma_0^{\pm}},$

constitute the full set of the natural sloshing modes for sloshing in the compartment tanks followed by replacing the screen with a rigid non-perforated wall in the middle. This means that the natural sloshing modes $\phi_{2n-1}^{\pm}$ are directly excited by lateral tank motions for the limit case $\mathrm{Sn}=1$ (see the wave profile associated with $\phi_1^{\pm}$ in Fig. 2c).

The natural modes φ_i and ϕ_i correspond to the natural sloshing frequencies σ_{2i-1} and σ_{2i}, respectively, where

$$\sigma_k^2 = g\kappa_k, \quad \kappa_k = \frac{\pi k}{2a}\tanh\left(\frac{\pi k h}{2a}\right), \quad k \geq 1. \tag{12}$$

The antisymmetric modes φ_i determine the relative *horizontal velocity* in the tank middle, but give zero contribution to the hydrodynamic pressure at Sc_0. Contrary, the symmetric modes ϕ_i do not affect the relative horizontal velocity at $y = 0$, but determine the linear hydrodynamic *pressure* (Dirichlet trace of the velocity potential) in the tank middle. Because the transmission conditions (6) and (9) imply continuous horizontal velocity, but discontinuous pressure, the absolute velocity potentials $\Phi^{\pm}$ take the form

$$\Phi^{\pm}(y,z,t) = \dot{\eta}_2 y + \sum_{i=1}^{\infty} \dot{V}_i(t)\varphi_i(y,z) + \sum_{i=0}^{\infty} R_i^{\pm}(t)\phi_i^{\pm}(y,z) \quad \text{in } Q_0^{\pm}, \tag{13}$$

where V_i and $R_i^{\pm}$ are originally unknown time-dependent functions (generalized coordinates). Here, $\dot{\eta}_2 y$ expresses the liquid motions as a solid body. Modal solution (13) automatically satisfies (1) and (6).

The relative horizontal velocity u_r at $y = 0$ is

$$u_r(z,t) = \frac{\pi}{2a}\sum_{i=1}^{\infty} \dot{V}_i(t)\,\frac{(2i-1)\cosh\left(\frac{1}{2}\pi(2i-1)(z+h)/a\right)}{\cosh\left(\frac{1}{2}\pi(2i-1)h/a\right)}. \tag{14}$$

Because the $\{\cosh(\lambda_i y),\ \lambda_0 < \lambda_1 < \cdots\}$–type exponential functions constitute a complete set of functions on the interval $[0, a]$ for any positive a (see [24, Chap. 1]), any function $u_r(z,t)$ can uniquely be presented in the series (14) on the interval $[-h, 0]$. Let us fix $\{V_i(t),\ i \geq 1\}$ and find $\zeta^{\pm}(y,t)$ and $R_m^{\pm}(t)$ by solving (2)–(4). Appropriate solution is possible by using, for instance, a Fourier technique from [6, Sect. 5.4.2.4] developed for the problem on liquid sloshing due to deformations of the side wall governed by the normal velocity $u_r(z,t)$. Due to this solution, $\zeta^{\pm}(y,t)$ and $R_m^{\pm}(t)$ become linearly dependent functions of the generalized coordinates $\{V_i(t), i \geq 1\}$. Furthermore, substituting $R_m^{\pm}(t)$ in the modal representation (10) and the integral-type transmission condition (9), we arrive at a single scalar relation coupling the infinite set of functions $\{V_i\}$. This single relation for the infinite set of input generalized coordinates can *not* provide a *unique solution*.

To get a unique solution from this single relation, $V_i(t)$ must be functions dependent on a single generalized coordinate $\beta_{-1}(t)$. Appropriate $\beta_{-1}(t)$ may be obtained from the assumption that the velocity profile at Sc_0 (but not the amplitude!) weakly depends on K (or Sn), namely, remains close to that occurring for the steady-state solution in the limit case $K = 0$. Adopting this velocity profile poses no conflict with another limit case $K \to \infty$ ($\mathrm{Sn} = 1$). Passage to $\mathrm{Sn} = 1$ implies that the amplitude parameter $\beta_{-1}(t)$ tends to zero.

Faltinsen and Timokha [6, Sect. 5.4] give the steady-state solution for $\mathrm{Sn} = 0$ (smooth rectangular tank) occurring due to harmonic forcing. The corresponding relative velocity potential $\varphi = \Phi - \dot{\eta}_2 y$ is then as follows

$$\varphi(y,z,t;\sigma) = \underbrace{\left(-\sigma\eta_{2a}\sin(\sigma t)\frac{8N_r}{\pi^2}\right)}_{\mathrm{f}(t)} \underbrace{\sum_{i=1}^{\infty} \frac{a(-1)^i \sin\left(\frac{1}{2}\pi(2i-1)y/a\right)}{N_r(2i-1)^2(1-\bar{\sigma}_{2i-1}^2)}\,\frac{\cosh\left(\frac{1}{2}\pi(2i-1)(z+h)/a\right)}{\cosh\left(\frac{1}{2}\pi(2i-1)h/a\right)}}_{\varphi_{-1}(y,z;\sigma)}. \tag{15}$$

Here, $\eta_2(t) = \eta_{2a}\cos(\sigma t)$, where σ is the forcing frequency, and η_{2a} is the forced sway amplitude of the tank; $\bar{\sigma}_i = \sigma_i/\sigma$, and

$$N_r = \sqrt{\sum_{i=1}^{\infty} \frac{1}{(2i-1)^4(1-\bar{\sigma}_{2i-1}^2)^2}}$$

is the norm providing the finiteness of φ_{-1} for any forcing frequency σ. The function φ_{-1} in (15) depends on the forcing frequency σ and determines the *relative horizontal velocity* at $y = 0$ expressed in terms of $\mathrm{f}(t)$ and φ_{-1}

$$u_r(z,t;\sigma) = \mathrm{f}(t)\left.\frac{\partial\varphi_{-1}}{\partial y}\right|_{y=0} = \mathrm{f}(t)\underbrace{\sum_{i=1}^{\infty} \frac{\pi(-1)^i}{2N_r(2i-1)(1-\bar{\sigma}_{2i-1}^2)}\,\frac{\cosh\left(\frac{1}{2}\pi(2i-1)(z+h)/a\right)}{\cosh\left(\frac{1}{2}\pi(2i-1)h/a\right)}}_{U_r(z;\sigma)}. \tag{16}$$

Equation (16) defines $U_r(z)$ which represents the *horizontal velocity profile* along the interval $[-h, 0]$ for the considered steady-state sloshing with Sn $= 0$, namely, without screen. The time-dependent function f(t) is then an amplitude parameter defined by (15). As we discussed above, we impose the horizontal velocity profile U_r to keep the same shape for $0 <$ Sn < 1, i.e., when there is a screen. The screen effect is therefore associated with a modification of the time-dependent function f(t). We replace the harmonic function f(t) by an unknown generalized coordinate $\dot{\beta}_{-1}(t)$ governing the magnitude of the profile $U_r(z)$ when Sn is not zero. Comparing (14) and (16) leads to the conclusion

$$\dot{V}_i = \dot{\beta}_{-1}(t)\frac{a(-1)^i}{N_r(2i-1)^2(1-\tilde{\sigma}_{2i}^2)}. \tag{17}$$

The assumption (17) makes the problem (1)–(4), (6), (9) uniquely solvable with the corresponding initial conditions (5). The velocity potential (13) then takes the form

$$\Phi^{\pm}(y,z,t) = \dot{\eta}_2 y + \dot{\beta}_{-1}(t)\varphi_{-1}(y,z) + \sum_{i=0}^{\infty} R_i^{\pm}(t)\phi_i^{\pm}(y,z) \quad \text{in } Q_0^{\pm}. \tag{18}$$

3 Analytical modal model

According to the multimodal methods, the free surfaces $\Sigma^{\pm}(t)$ (see Fig. 2) are described (in the tank-fixed coordinate system Oyz) by the Fourier-type representation

$$z = \zeta^{\pm}(y,t) = \beta_{-1}(t)f_{-1}(y) + \sum_{i=1}^{\infty}\beta_i^{\pm}(t)f_i(y), \tag{19}$$

where $f_{-1}(y) = \partial\varphi_{-1}/\partial z$ at $z = 0$ and $\beta_{-1}(t)$ is the same as in (18).

The component $\beta_{-1}(t)f_{-1}(y)$ is continuous on $(-a, a)$ for any instant t. It is responsible for the wave elevations due to liquid flow between the compartments, the time-dependent mean liquid level in the compartments, and provides the volume-conservation condition with

$$\int_{-a}^{0} f_{-1}(y)\mathrm{d}y = -\int_{0}^{a} f_{-1}(y)\mathrm{d}y \neq 0.$$

Projections of $f_i(y),\ i \geq 1$ on $(-a, 0)$ and $(0, a)$ are exactly the natural surface modes on Σ_0^- and Σ_0^+, respectively. These satisfy volume conservation in the compartments, namely, $\int_{-a}^{0} f_i\mathrm{d}y = \int_0^a f_i\mathrm{d}y = 0,\ i \geq 1$.

Substituting (19) and (18) in relations (2) and (3) and using orthogonality of $\{f_n(y), n \geq 0\}$ on the intervals $[-a, 0]$ and $[0, a]$ gives

$$\dot{R}_0^{\pm} = \pm\left[-\frac{1}{2}\ddot{\eta}_2 + v_0^*\ddot{\beta}_{-1} + g v_0\beta_{-1}\right], \quad R_n^{\pm} = \frac{\dot{\beta}_n^{\pm}}{\kappa_{2n}} \tag{20}$$

and the following system of linear modal equations

$$\ddot{\beta}_n^{\pm} + \sigma_{2n}^2\beta_n^{\pm} = \pm 2\kappa_{2n}\left(a_n\ddot{\eta}_2 + v_n^*\ddot{\beta}_{-1} + g v_n\beta_{-1}\right), \quad n \geq 1, \tag{21}$$

where

$$a_n = \int_{-a}^{0} y f_n\mathrm{d}y = -\frac{(-1)^n - 1}{\pi^2 n^2}a, \tag{22}$$

$$v_n^* = \int_{-a}^{0}\varphi_{-1}f_n\mathrm{d}y = \frac{2a}{\pi N_r}\sum_{i=1}^{\infty}\frac{(-1)^{i+1}}{((2i-1)^2 - 4m^2)(2i-1)(1-\tilde{\sigma}_{2i-1}^2)},$$

$$v_n = \int_{-a}^{0}\left.\frac{\partial\varphi_{-1}}{\partial z}\right|_{z=0} f_n\mathrm{d}y = \frac{1}{N_r}\sum_{i=1}^{\infty}\frac{(-1)^{i+1}\tanh(\frac{1}{2}\pi(2i-1)h/a)}{((2i-1)^2 - 4m^2)(1-\tilde{\sigma}_{2i-1}^2)}.$$

The modal system (21) governs the generalized coordinates determining the component $\sum_{i=1}^{\infty}\beta_i^{\pm}(t)f_i(y)$ in representation (19). This component satisfies the volume-conservation conditions on Σ_0^- and Σ_0^+, and, therefore, does not describe the time-dependent change of the mean liquid levels in the compartments. It looks similar to the case when the compartments are separated by a rigid non-perforated wall. However, in our case, $\beta_n^{\pm}$ also depend on the inflow/outflow through Sc_0 associated with the generalized coordinate $\beta_{-1}(t)$. Formulas (20) give $R_n^{\pm}(t),\ n\geq 0$ in Eq. (18) as functions of $\beta_n^{\pm}(t)$ and $\beta_{-1}(t)$.

Furthermore, the right-hand sides in (21) are proportional to

$$a_n\ddot{\eta}_2+v_n^*\ddot{\beta}_{-1}+gv_n\beta_{-1}=\int\limits_{\Sigma_0^-}\left(y\ddot{\eta}_2+\varphi_{-1}\ddot{\beta}_{-1}+g\frac{\partial\varphi_{-1}}{\partial z}\beta_{-1}\right)f_n\mathrm{d}S. \tag{23}$$

When $\dot{\beta}_{-1}(t)$ coincides with $\mathrm{f}(t)$, i.e., when there is no screen for a horizontal harmonic forcing, expression (23) vanishes. As a consequence, the right-hand sides in modal equations (20) becomes zero. This means that we can expect amplification of $\beta_n^{\pm},\ n\geq 1$ only for non-small solidity ratios.

Using formulas (20) in representation (18) and substituting them in the transmission condition (9) gives the following ordinary nonlinear differential equation with respect to $\beta_{-1}(t)$

$$2hv_0^*\ddot{\beta}_{-1}-\left[\frac{K}{2h}\int\limits_{-h}^{0}U_r(z)\mathrm{d}z\left|\int\limits_{-h}^{0}U_r(z)\mathrm{d}z\right|\right]\dot{\beta}_{-1}|\dot{\beta}_{-1}|+2ghv_0\beta_{-1}-ah\ddot{\eta}_2+a^2\sum_{n=1}^{\infty}\frac{\ddot{\beta}_n^+-\ddot{\beta}_n^-}{(\pi n)^2}=0. \tag{24}$$

An equivalent form of (24) can be written as follows

$$\left[a(\sigma)\ddot{\beta}_{-1}+b(\sigma)\dot{\beta}_{-1}(t)|\dot{\beta}_{-1}(t)|+c(\sigma)\beta_{-1}+d(\sigma)\ddot{\eta}_2\right]+ga\sum_{n=1}^{\infty}\frac{\tanh(\pi nh/a)}{\pi n}\left(\beta_n^--\beta_n^+\right)=0, \tag{25}$$

where $\beta_n^{\pm}(t)$ are solutions of (21) and

$$a(\sigma)=\int\limits_{-a}^{0}\varphi_{-1}|_{z=0}\mathcal{F}(y)\mathrm{d}y=2hv_0^*+4a\sum_{n=1}^{\infty}\frac{\tanh(\pi nh)}{\pi n}v_n^*, \tag{26}$$

$$b(\sigma)=-\frac{K}{2h}\int\limits_{-h}^{0}U_r(z)\mathrm{d}z\left|\int\limits_{-h}^{0}U_r(z)\mathrm{d}z\right|, \tag{27}$$

$$c(\sigma)=\int\limits_{-a}^{0}\left.\frac{\partial\varphi_{-1}}{\partial z}\right|_{z=0}\mathcal{F}(y)\mathrm{d}y=g\left[2hv_0+4a\sum_{n=1}^{\infty}\frac{\tanh(\pi nh)}{\pi n}v_n\right], \tag{28}$$

$$d(\sigma)=\int\limits_{-a}^{0}y\mathcal{F}(y)\mathrm{d}y=-ah+8a\sum_{i=1}^{\infty}\frac{\tanh(\pi(2i-1)h)}{\pi^3(2i-1)^3} \tag{29}$$

with

$$\mathcal{F}(y)=2h+4a\sum_{n=1}^{\infty}\frac{\tanh(\pi nh)}{\pi n}\cos(\pi ny).$$

The system of differential equations (21), (25) couples the generalized coordinates $\beta_{-1}(t)$, $\beta_n^{\pm}(t)$, $n\geq 1$. It can be solved by any numerical method subject to the initial conditions $\beta_{-1}(0)=\beta_{-1}^{(0)},\ \beta_n(0)=\beta_n^{(0)}, n\geq 1$, and $\dot{\beta}_{-1}(0)=\beta_{-1}^{(1)},\ \dot{\beta}_n(0)=\beta_n^{(1)}, n\geq 1$. In our calculations, we used the fourth-order Runge–Kutta method. These initial conditions govern the initial free-surface shape and initial free-surface velocity defined by (5) and (19).

4 Steady-state sloshing due to harmonic horizontal excitation

4.1 Preliminaries

We consider steady-state sloshing due to harmonic sway excitation $\eta_2(t) = \eta_{2a}\cos(\sigma t)$, where η_{2a} is the forcing amplitude, and the forcing frequency σ is in a range including the two lowest natural sloshing frequencies, σ_1 and σ_2. The steady-state sloshing corresponds to the $2\pi/\sigma$-periodic solution of the system (21), (25).

As before, there are two limit cases associated with sloshing in a smooth tank (there is no screen, $K = 0$) and sloshing in two smooth compartments without cross-flow (the screen is an unperforated wall, $K = \infty$, $\mathrm{Sn} = 1$). Straightforward (but tedious) algebra shows that, if $K = 0$ ($\mathrm{Sn} = 0$), the steady-state (periodic) solution of (21), (25) is $\dot{\beta}_{-1} = \mathrm{f}(t)$ and $\beta_n^{\pm}(t) = 0$, $n \geq 1$. This solution implies the resonant behavior at σ_1, but not at σ_2, because the symmetric modes are not excited within the framework of linear sloshing theory.

Passage to $K = \infty$ ($\mathrm{Sn} = 1$) in (25) leads to $\dot{\beta}_{-1}(t) = 0$ which gives together with the fact that both compartments, by definition, contain the same liquid volumes, that $\beta_{-1}(t) = 0$. Substituting $\beta_{-1}(t) = 0$ in modal equations (21) gives the well-known linear modal equations for sloshing in smooth rectangular tanks (compartments) with the width a and the filling liquid depth h; see [6, Chap. 5]. For this case, the limit $\sigma \to \sigma_2$ leads to the linear resonance response by modes $\phi_1^{\pm} = \phi_1|_{Q_0^{\pm}}$ with wave profiles shown in Fig. 2c, but there is no resonance at $\sigma = \sigma_1$.

4.2 Model tests

A rectangular tank was installed in a rig located at the Marine Technology Center in Trondheim, Norway. The Plexiglas-made tank dimensions are $1.0\,\mathrm{m} \times 0.98\,\mathrm{m} \times 0.1\,\mathrm{m}$ (width × height × breadth). The tank was forced horizontally with a sinusoidal signal. To provide a nearly two-dimensional sloshing, a slat screen (Fig. 3) was used. Meniscus effects at the intersection between the free surface and the tank walls are secondary and cause three-dimensional capillary waves that are riding on the gravity waves.

The tank was equipped with two resistant wave probes installed 1 cm away from the end walls in order to avoid possible local run-up effects which cannot be described by this theory. The wave elevation is recorded with a sampling rate of 100 Hz and measured relative to the unperturbed free surface. The error in the measured wave elevation is less than 1 mm.

Our focus is on model tests with $h/l = 0.4$ and nondimensional forcing amplitudes close to $\eta_{2a}/l = 0.001$ and 0.01. The frequency range covers the two lowest natural sloshing frequencies. The wide range of tested solidity ratios of the submerged screen part, as it is accepted in our two-dimensional sloshing analysis with $h/l = 0.4$, is listed in the caption of Fig. 3. Note that the actual experimental setup included narrow (about 5 mm) vertical rigid constraints mounting the screen to the tank walls. The effects of these constraints on perturbing a local three-dimensional flow at the mounting lines, as well as on the solidity ratio of the considered screens as three-dimensional structures, are neglected. The fact that the slot height is not perfectly constant across the screen is an error source for high-solidity ratios.

To account for the free-surface nonlinearity hysteresis effect (see [6, Chap. 8]), the forcing frequency for a prescribed forcing amplitude changes 'stepwise' after reaching an experimental steady-state regime. The signal with a fixed forcing frequency lasts for about 300 cycles; 200 cycles were sufficient to reach the steady-state condition. After 300 cycles, the forcing frequency changes to a lower value. The reason for decreasing the forcing frequency is to detect the maximum wave elevation. The latter fact follows from the character of the nonlinear steady-state response at a depth larger than the critical depth for sloshing in a smooth two-dimensional rectangular tank (see [6, Chap. 8]). The initial runs were performed with frequency steps of about 0.05 Hz which enabled localization of the peaks in the steady-state wave-amplitude response. Afterwards, the frequency steps were in the range of 0.01Hz to 0.001Hz, in the frequency domains where the initial tests have detected the resonance peaks in order to more accurately quantify the response peaks. The forcing amplitude might slightly change for technical reasons when switching to another forcing frequency.

4.3 Comparison with experiments

Numerical steady-state solutions are found by using direct numerical simulations by the modal system (21), (25). Our simulations adopt the experimental stepwise change of the forcing frequency and corresponding amplitude with the consequence that simulations with each new forcing parameters employed the initial conditions from the previous steady-state solution. Because (21) and (25) imply a dissipative mechanical system, the long-time simulations always led to a periodic (steady-state) numerical solution. Usually, about 300 cycles are required to get this solution within a two-digits accuracy. This is generally consistent with experiments. The final simulations include up to 1500 cycles providing a four-five digits accuracy for the periodic solution.

When $h/l = 0.4$, the lowest theoretical resonances for Sn $= 0$ and Sn $= 1$ are at $\sigma/\sigma_1 = 1$ and $\sigma/\sigma_1 = \sigma_2/\sigma_1 \approx 1.52$ with $\sigma_1 = 5.12$ (rad/s), respectively.

Comparison of theoretical and experimental maximum steady-state wave elevation as a function of forcing frequency is presented in Figs. 4, 5, 6, 7, and 8. The figures show the theoretical values (solid lines), the actual measured maximum wave elevations (empty boxes) at the wave probe (in left compartment), and the amplitude of the primary harmonics of the experimental output signal (associated with $\exp(\mathrm{i}\sigma t)$, $\mathrm{i}^2 = -1$) marked by the filled boxes. The figures give also information on the experimental forcing amplitude as a function of the forcing frequency.

The experiments showed in some cases that different steady-state solutions occur in the compartments in a neighborhood of $\sigma/\sigma_1 = \sigma_2/\sigma_1 = 1.52$. The presence of two stable steady-state solutions is a well-known fact for sloshing in a two-dimensional rigid rectangular tank (here, the compartments) with a finite liquid depth [21,22]. The reason is the free-surface nonlinearity which is not included in the present theory. The corresponding experimental records with different steady-state results in the two compartments are therefore not included in the present comparison.

4.3.1 Lower values of the solidity ratio

Figure 4 shows experimental and numerical values of the maximum wave elevations for Sn $= 0.328$ and 0.52 ($K = 1.025$ and 4.371, respectively). Both theory and experiments give in the considered frequency range only a resonant peak at $\sigma/\sigma_1 = 1$, i.e., there is no resonant amplification at $\sigma_2/\sigma_1 = 1.52$. This means that the generalized coordinate $\beta_{-1}(t)$ describing the cross-flow at the screen dominates, while $\beta_n^{\pm}$, $n \geq 1$ are of lower importance. Because $\beta_n^{\pm}$, $n \geq 1$ determine the jump of the free surface at the screen, this jump does not provide a dominant contribution to the sloshing. The pressure loss coefficient K plays the role of damping at the corresponding quadratic damping term in (25).

Figure 4 (panels a and b) shows that the numerical results by the analytical modal model generally agree with the experiments for the smaller nondimensional forcing amplitude $\eta_{2a}/l \approx 0.001$. We see larger theoretical values relative to experiments in case (a) for Sn $= 0.328$. This fact can, in part, be related to non-accurate prediction of K by empirical formulas (8). As we reported ahead of (8), the values of the empirical formula do not depend on the Reynolds number and assume KC > 2. An alternative is the table with empirical K in [16, pp. 314–316]. The latter values do not depend on KC and the Reynolds number. We could have tried to fit the K-value to agree with the experimental results and, in that way, for instance, detect a KC-dependence. However, a procedure like that is questionable because it does not account for the fact that a reason for discrepancies can be due to nonlinear free-surface effects. In the presented calculations from Fig. 4a, $K = 1.025$ leads to $\zeta_a/\eta_{2a} = 50$ for $\sigma/\sigma_1 = 1$, but $K = 1.32$ (this value of K follows from the empirical loss coefficients in [16, p. 314]) gives $\zeta_a/\eta_{2a} = 43.5$. Because β_{-1} dominates, one can, in a qualitative analysis, neglect the $\beta_n^{\pm}$-quantities from (25) which, as explained previously, are responsible for the free-surface jump at the screen. This means that (25) becomes similar to a single-dimensional mass–spring system with quadratic damping where the damping coefficient is proportional to K and, therefore, the screen should act as a damper. As shown in [25, Chap. 3] for a lightly damped one-degree of mass–spring system, the resonant nondimensional response ζ_a/η_{2a} should then be proportional to $1/\sqrt{K\eta_{2a}/l}$. The nondimensional resonant response is consistent with this general prediction.

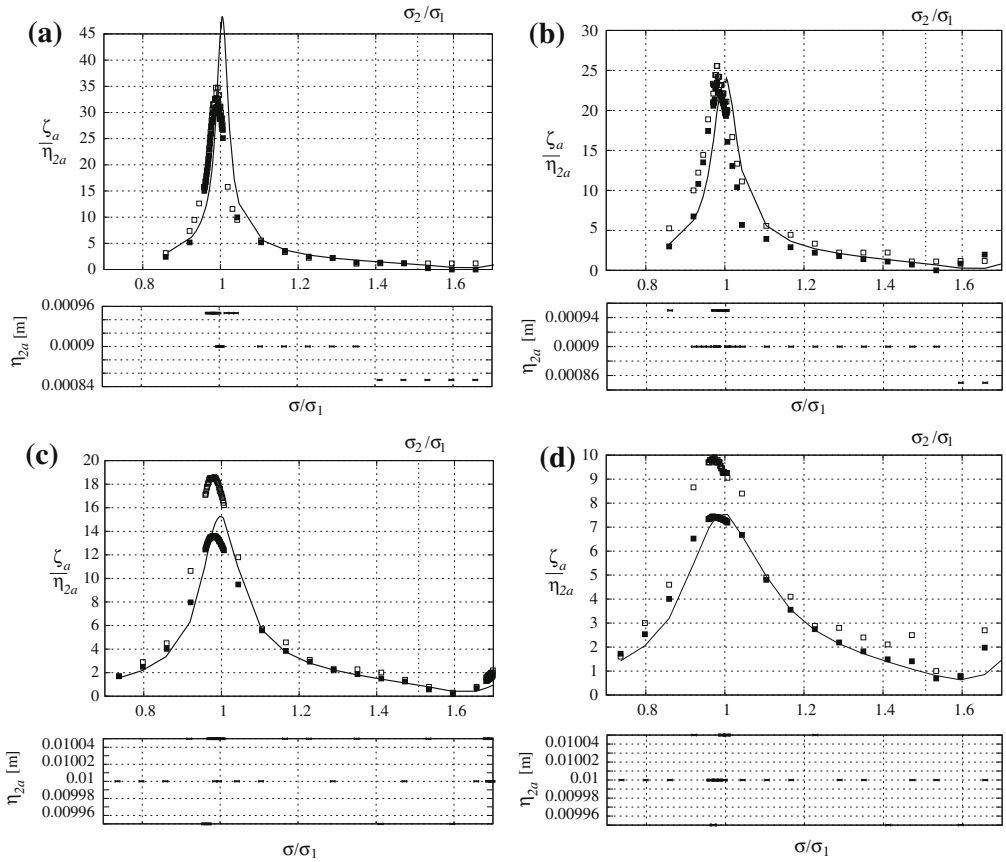

Fig. 4 Nondimensional theoretical (*solid line*) and experimental (*filled and empty boxes*) maximum wave elevations (denoted as ζ_a) at the wave probe 1 cm away from the wall versus nondimensional forcing frequency σ/σ_1. The *empty boxes* represent the actual measured maximum wave elevations, but the *solid* (*filled*) *boxes* denote amplitude of the primary Fourier harmonics of the measured signal. Because the experimental horizontal forcing amplitude η_{2a} slightly varies with changing the forcing frequency, their dimensional values are also presented; this variation is taken into account in the numerical analysis. Panels **a** and **b** present the case of smaller forcing amplitudes ($\eta_{2a}/l \approx 0.001$), but **c** and **d** demonstrate the case of larger forcing amplitudes ($\eta_{2a}/l \approx 0.01$). The left panels **a** and **c**, corresponds to Sn $= 0.328 (K = 1.025)$. The right panels, **b** and **d**, show results for Sn $= 0.52$ ($K = 4.371$)

A major reason why the experimental and theoretical peak values and corresponding frequencies do not agree perfectly are believed to be due to free-surface nonlinearities. The latter is well known from the potential-flow sloshing in a smooth (clean) tank, when a linear sloshing theory based on potential flow wrongly predicts an infinite resonance response. Nonlinear resonant free-surface effects cause transfer of energy to other, higher modes than the primary excited, dominant mode and, thereby, limit the response of the primary excited mode at the lowest resonant frequency. Another consequence of nonlinear sloshing in a clean tank with $h/l > 0.3368\ldots$ is a drift of the peak response to a lower frequency than the lowest natural frequency σ_1. The latter effect is evident in the experimental results. If the dissipation (damping) due to cross-flow through the screen had been sufficiently high, i.e., larger than theoretically predicted in this case, the nonlinear free-surface effect would be negligible.

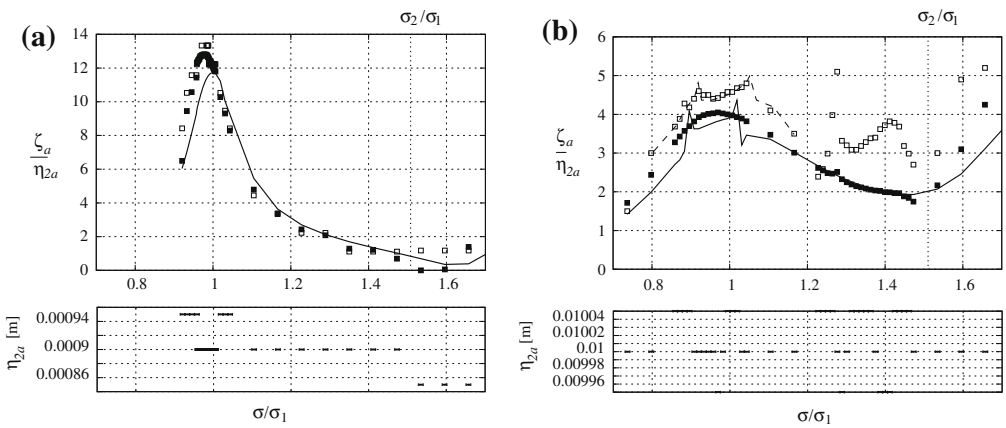

Fig. 5 Nondimensional theoretical (*solid line*) and experimental maximum wave elevations (denoted as ζ_a) at the wave probe versus nondimensional forcing frequency σ/σ_1. The *empty boxes* represent the measured maximum wave elevations, but the *solid boxes* denote amplitudes of the primary harmonics, $\exp(\mathrm{i}\sigma t)$. The experimental variation of the forcing amplitudes is taken into account in the numerical analysis. Sn $= 0.713$ ($K = 19.89$). Panel **a** corresponds to the lower excitation amplitudes, $\eta_{2a}/l \approx 0.001$, and panel **b** implies $\eta_{2a}/l \approx 0.01$

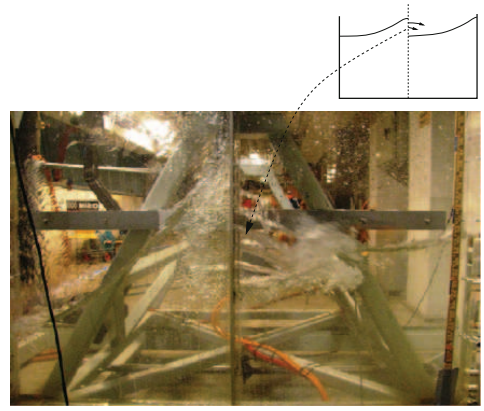

Fig. 6 The experimentally observed fallout of the liquid going through the screen into the air domain of the opposite compartment and subsequently impacting on the underlying free surface

Furthermore, increasing the forcing amplitude may lead to a nonlinear amplification of higher modes which give a non-negligible contribution to the maximum steady-state wave elevation. This contribution is associated with higher harmonics. The cases (c) and (d) in Fig. 4 are for the larger nondimensional forcing amplitude $\eta_{2a}/l \approx 0.01$. In these cases, the analytical modal model gives lower nondimensional values of the maximum steady-state elevation at the wave probes relative to the experimental measurements. To explain why this happens, we had to perform a Fourier analysis and extract the primary Fourier harmonics contribution from the measured output signal. It is marked by the filled boxes. Cases (a) and (b) show that the primary harmonics (associated with primary excited mode) clearly dominates for smaller forcing amplitude. This is not so for the larger forcing amplitude in cases (c) and (d), where higher harmonics (associated with higher modes) give sufficient contribution. Amplification of

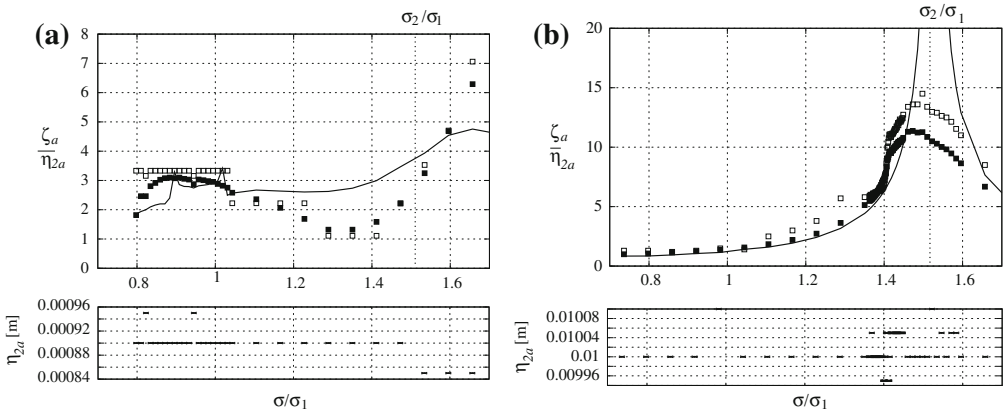

Fig. 7 The same as in Fig. 5, but for Sn = 0.928 ($K = 462.8$). In case **b**, the maximum peak at $\sigma/\sigma_1 = \sigma_2/\sigma_1 = 1.52$ is computed to be $\zeta_a/\eta_{2a} = 50$

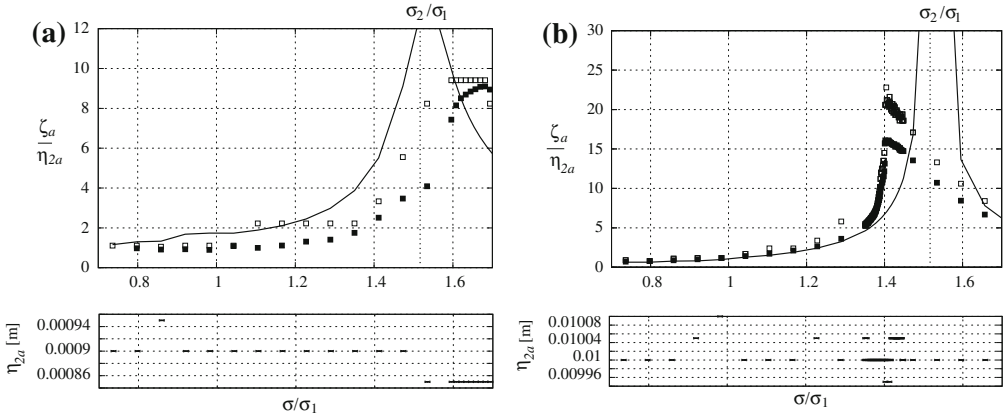

Fig. 8 The same as in Fig. 5, but for Sn = 0.963 ($K = 1{,}846$). In case **a**, the maximum peak at $\sigma/\sigma_1 = \sigma_2/\sigma_1 = 1.52$ is computed to be $\zeta_a/\eta_{2a} = 23$, but case **b** gives this theoretical maximum equal to 102

these harmonics with increasing forcing amplitude was extensively discussed in [27]. It was shown that this is a nonlinear free-surface effect. To describe this amplification, one should use the nonlinear multimodal theory which links the higher harmonics with nonlinear energy transfer from the lowest, primary excited mode to higher modes. Our theoretical model with linear free-surface conditions and damping due to the cross-flow through the screen demonstrates a good agreement with the primary harmonics contribution associated with the primary excited mode.

4.3.2 Intermediate values of the solidity ratio

Increasing the solidity ratios to Sn $= 0.713 (K = 19.89)$ leads to the theoretical and experimental nondimensional maximum steady-state wave elevations shown in Fig. 5. The generalized coordinate $\beta_{-1}(t)$ dominates with respect to $\beta_n^{\pm}(t)$ in case (a), and, therefore, the system behaves as a one-degree lightly damped mass-spring system with quadratic damping. The consequence is that the resonant nondimensional response ζ_a/η_{2a} is proportional to

$1/\sqrt{K\eta_{2a}/l}$ which is consistent with the theoretical results in Fig. 4 for lower solidity ratios. The experimental results in case (a) show small influence of higher harmonics and there is good agreement with quasi-linear theory.

The larger excitation amplitude in Fig. 5b leads to $\beta_{-1} \sim \beta_n^{\pm}$ with many dominant generalized coordinates. A consequence of coupling between modes is a double-peak response at the lowest natural sloshing frequency σ_1. The experimental primary harmonic response is, in general, in good agreement with the theoretical prediction. However, the experiments demonstrate the presence of non-negligible higher harmonics, for instance at $\sigma/\sigma_1 = 1.28$ and 1.4. A plausible reason is nonlinear free-surface effects. We do not know to what extent the water flow through the air illustrated in Fig. 6 matters. A water-jet flow that originates from the screen opening impacts on the underlying free surface and, thereby, can excite higher-harmonics wave (see discussion in [26]).

4.3.3 Larger values of the solidity ratio

Passage to higher solidity ratios is studied in Figs. 7 and 8. Figure 7a corresponds to Sn = 0.928 and $\eta_{2a}/l = 0.001$. When σ/σ_1 is in the vicinity of 1, $\beta_{-1} \sim \beta_n^{\pm}$ in the theoretical model. The consequence is that both cross-flow quadratic damping due to the screen and coupling between many generalized coordinates of the liquid motions matter. The result is a relatively small nondimensional wave amplitude response with the presence of a double peak. The agreement with the experiments is reasonable. The theoretical response is largest at $\sigma/\sigma_1 = 1.65$, i.e., at a higher frequency than the second natural sloshing frequency $\sigma_2 = 1.52\sigma_1$. The experimental results do not show a clear effect of higher harmonics and agree that there is a peak response at $\sigma/\sigma_1 = 1.65$. However, the magnitudes of theoretical and experimental wave elevations differ at the second natural frequency with the experimental results being clearly higher. A reason can be errors in the theoretical damping model in the considered frequency range. Furthermore, there is a clear minimum in the experimental results at $\sigma/\sigma_1 = 1.35$ which is not supported by the theoretical model.

A very large theoretical amplification occurs at $\sigma/\sigma_1 = 1.52$ for the cases presented in Figs. 7b and 8a, b. The reason is associated with the fact that $\beta_n^{\pm} \gg \beta_{-1}$ in the theoretical model which can be explained as follows. Because there is a larger coefficient K in the front of the quadratic damping term in (25), the generalized coordinate β_{-1} is highly damped to become of non-dominant (higher order) with respect to $\beta_n^{\pm}$, $n \geq 1$. The latter generalized coordinates are solutions of the linear equations (21) without damping terms and, therefore, the $\beta_i^{\pm}$-related oscillations can only be reduced due to energy transfer to β_{-1}. The pressure-drop condition no longer plays the role of a damping mechanism, as it happened for lower and intermediate solidity ratios. An indication of the fact that the cross-flow at the screen does not act as a quadratic one-dimensional damping mechanism at $\sigma = \sigma_2$ is that we predict an increased nondimensional response ζ_a/η_{2a} with increasing forcing amplitude η_{2a}/l. The generalized coordinates $\beta_n^{\pm}$ governed by the linear non-damped linear oscillator equations (21) should determine both the primary response as well as the corresponding resonance peak which is now expected at $\sigma = \sigma_2$. The latter fact means that the screen can in a first approximation be considered as an unperforated wall which isolates wave motions in the compartments whose interplay is now associated with a higher-order flow component β_{-1}. It was shown in [6, Sect. 6.8] that increasing the excitation amplitude causes a decrease in the threshold value of the solidity ratio for which the screen changes its role from a damper to an isolator of the compartment tank. This explains why we see a clear resonance peak at $\sigma/\sigma_1 = \sigma_2/\sigma_1 = 1.52$ and not at $\sigma/\sigma_1 = 1$ in Fig. 7b. Case (a) in Fig. 7 with $\eta_{2a}/l = 0.001$ corresponds to a Sn-value where the dominant resonant response changes from being at $\sigma/\sigma_1 = 1$ to $\sigma/\sigma_1 = 1.52$.

The experimental results in a frequency range around the second natural frequency do not agree well with the theoretical results in Figs. 7b and 8a, b. The experiments show a frequency of the peak response that is lower than σ_2 for $\eta_{2a}/l = 0.01$ (Figs. 7b, 8b) and larger than σ_2 for $\eta_{2a}/l = 0.001$ (Fig. 8a). Furthermore, the maximum experimental values are clearly lower than the theoretical values. The presence of higher-harmonics contribution in the experiments indicates nonlinear free-surface effects causing transfer of energy from lowest primary excited mode to higher modes. The experimental behavior for $\eta_{2a}/l = 0.01l$ is consistent with a theoretical nonlinear behavior of resonant sloshing for depths that are larger than the critical depth in a rectangular tank with small damping. For instance, jumps between stable steady-state solution branches occur according to the multimodal method with nonlinear free-surface nonlinearity effects described in [6, Chap. 8]. The response has similarities

with the response of a Duffing-type nonlinear oscillator. Because there is a small flow exchange between the tank compartments, the relevant theoretical tanks are the compartment tanks. We are not able to theoretically explain why the maximum experimental response occurs for a frequency larger than the second natural frequency in Fig. 8a with $\eta_{2a}/l = 0.001$ and $\mathrm{Sn} = 0.963$.

5 Concluding remarks

A modal model based on linear free-surface conditions has been derived to describe sloshing in a two-dimensional rectangular tank with a slat-type screen in the middle. An empirical pressure-drop condition as well as continuity of the transverse velocity were used as transmission conditions between the two compartments. The derived modal model consists of two modal systems to describe sloshing in the two compartments, and an ordinary differential equation governing the generalized coordinate $\beta_{-1}(t)$ responsible for liquid flow between compartments. The first modal systems are similar to that in [6, Chap. 5], but with other right-hand sides. These right-hand sides include terms depending on $\beta_{-1}(t)$. The last differential equation with respect to $\beta_{-1}(t)$ contains the nonlinear, $\dot{\beta}_{-1}|\dot{\beta}_{-1}|$–term coming from the pressure-drop condition.

The theoretical pressure-drop condition across the screen plays the role of a damper for low and intermediate solidity ratios. For low solidity ratio, this role is similar to that in a single-degree mass–spring system with quadratic damping. A consequence of the latter fact is that the resonant nondimensional response ζ_a/η_{2a} is proportional to $1/\sqrt{K\eta_{2a}/l}$ where K is the pressure-drop coefficient. The same similarity to a spring–mass system is applicable for intermediate solidity ratios and smaller forcing amplitudes ($\eta_{2a}/l = 0.001$ in our studies). However, increasing the forcing amplitude makes inapplicable the single-degree mechanical analogy. There are then many generalized coordinates and corresponding natural modes which should give comparable dominant contributions, and the actual response results from a complex interplay between them. The pressure-drop condition does not act as a damping mechanism for higher solidity ratios, but causes the lowest resonance sloshing frequency to increase to the lowest sloshing frequency in the tank compartments isolated by the screen as an unperforated wall. Which lower solidity ratio causes the change in the resonance frequency under harmonic sway excitation in a two-dimensional tank depends on the liquid depth-to-the-tank-width ratio and the ratio between the sway amplitude and the tank width.

Even though we use linear free-surface conditions and a screen-averaged pressure-drop condition, comparison of the numerical results by the derived analytical modal model and *new* experimental model tests on steady-state wave elevations show satisfactory agreement in many cases. The most serious discrepancy can be explained by the free-surface nonlinearity. Mathematically, the nonlinearity at the second natural frequency σ_2 (for larger solidity ratios) can be handled by replacing the left-hand sides of (21) with the corresponding adaptive modal system taken from paper [27]. However, we anticipate a non-trivial analysis accounting for a very special liquid flow associated with a liquid jet that originates at the screen, goes through the air and subsequently impacts on the underlying free surface (see Fig. 6).

Because of the specific slat-type screen, we adopted a mean (screen-averaged) pressure-drop condition. Generally speaking, the sloshing problem needs a modification of this condition that accounts for the local approach velocity and pressure drop at each opening in the screen.

References

1. Abramson H (1966) The dynamic behavior of liquids in moving containers. Washington DC, NASA SP-106
2. Warnitchai P, Pinkaew T (1998) Modelling of liquid sloshing in rectangular tanks with flow-dampening devices. Eng Struct 20:593–600
3. Tait MJ, El Damatty AA, Isyumov N, Siddique MR (2005) Numerical flow models to simulate tuned liquid dampers (TLD) with slat screens. J Fluids Struct 20:1007–1023
4. Tait MJ (2008) Modelling and preliminary design of a structure-TLD system. Eng Struct 30:2644–2655

5. Maravani M, Hamed MS (in press) Numerical modeling of sloshing in a turned liquid damper outfitted with a submerged slat screen. Int J Numer Methods Fluids. doi:10.1002/fld.2250
6. Faltinsen OM, Timokha AN (2009) Sloshing. Cambridge University Press, New York
7. Kaneko S, Ishikawa M (1992) Modelling of tuned liquid damper with submerged nets. ASME PVP 247:185–203
8. Kaneko S, Ishikawa M (1999) Modelling of tuned liquid damper with submerged nets. Trans ASME, J Press Vessel Technol 121:334–341
9. Kaneko S, Mizota Y (2000) Dynamical modelling of deepwater-type cylindrical tuned liquid damper with a submerged net. Trans ASME, J Press Vessel Technol 122:96–104
10. Tuck EO (1971) Transmission of water waves through small apertures. J Fluid Mech 49:65–74
11. Tuck EO (1975) Matching problems involving flow through small holes. Adv Appl Mech 15:89–157
12. Evans DV (1990) The use of porous screens as wave dampers in narrow wave tanks. J Eng Math 24:203–212
13. Chwang AT, Chan AT (1998) Interaction between porous media and wave motion. Annu Rev Fluid Mech 30:53–84
14. Straughan B (2008) Stability and wave motion in porous media. Springer Verlag, Berlin
15. Laws EM, Livesey JL (1978) Flow through screens. Annu Rev Fluid Mech 10:247–266
16. Blevins RD (1992) Applied fluid dynamics. Krieger Publishing Company, Malabar, FL
17. Molin B (2001) On the added mass and damping of periodic arrays of fully or partially porous disks. J Fluid Struct 15:275–290
18. Kimmoun O, Molin B, Moubayed W (2001) Second-order analysis of the interaction of a regular wave train with a vertical perforated wall. In: Proceedings of 8$^{\text{èmes}}$ Journèes de l'Hydrodynamique, 5, 6, 7 March 2001, Nantes
19. Baines WD, Peterson EG (1951) An investigation of flow though screens. ASME Trans 73:467–479
20. Weisbach J (1855) Die Experimental-Hydraulik. Engelehardt, Freiburg
21. Faltinsen OM (1974) Nonlinear theory of sloshing in rectangular tanks. J Ship Res 18:224–241
22. Faltinsen OM, Rognebakke OF, Lukovsky IA, Timokha AN (2000) Multidimensional modal analysis of nonlinear sloshing in a rectangular tank with finite water depth. J Fluid Mech 407:201–234
23. Agranovich MS (1996) Elliptic boundary problems. In: Encyclopedia of mathematical sciences, vol 79. Springer, Berlin, pp 1–146
24. Karlin S, Studden WJ (1966) Tschebyscheff systems with applications in analysis and statistics. Wiley, New York
25. Faltinsen OM (1990) Sea loads on ships and offshore structures. Cambridge University Press, New York
26. Faltinsen OM, Rognebakke OF, Timokha AN (2006) Transient and steady-state amplitudes of resonant three-dimensional sloshing in a square base tank with a finite fluid depth. Phys Fluids 18, Art. No. 012103:1–14
27. Faltinsen OM, Timokha AN (2001) Adaptive multimodal approach to nonlinear sloshing in a rectangular tank. J Fluid Mech 432:167–200

3. Faltinsen, O. M., Firoozkoohi, R., & Timokha, A. N. (2011). Steady-state sloshing in a rectangular tank with a slat-type screen in the middle:Quasilinear modal analysis and experiments. Physics of Fluids , 23 (4), 19 pages.

AIP | Physics of Fluids

Steady-state liquid sloshing in a rectangular tank with a slat-type screen in the middle: Quasilinear modal analysis and experiments

O. M. Faltinsen, R. Firoozkoohi, and A. N. Timokha

Citation: Phys. Fluids **23**, 042101 (2011); doi: 10.1063/1.3562310
View online: http://dx.doi.org/10.1063/1.3562310
View Table of Contents: http://pof.aip.org/resource/1/PHFLE6/v23/i4
Published by the American Institute of Physics.

Steady-state liquid sloshing in a rectangular tank with a slat-type screen in the middle: Quasilinear modal analysis and experiments

O. M. Faltinsen,[a] R. Firoozkoohi, and A. N. Timokha
Centre for Ships and Ocean Structures and Department of Marine Technology, Norwegian University of Science and Technology, NO-7091 Trondheim, Norway

(Received 24 September 2010; accepted 11 February 2011; published online 5 April 2011)

Two-dimensional resonant liquid sloshing in a rectangular tank equipped with a central slat-type screen is studied theoretically and experimentally with focus on *nonsmall* solidity ratios of the screen ($0.5 \lesssim \mathrm{Sn} \lesssim 0.95$), nonlarge number of slots ($N \lesssim 50$), and steady-state conditions. The tank is horizontally and harmonically excited with frequencies in a range covering the two lowest primary-excited natural sloshing resonance frequencies in the corresponding clean tank. The liquid depth is finite. Theoretical analysis is based on the multimodal method with linear free-surface conditions and a quadratic pressure drop condition at the screen expressing an "integral" effect of the screen-induced cross-flow separation (or jet flow). New experimental data on the maximum wave elevations at the wall are compared with the theoretical predictions. Very good agreement is shown for the smallest forcing amplitudes (the forcing amplitude-to-tank width ratio is ≈ 0.001). Increasing the nondimensional forcing amplitude to ≈ 0.01 leads to discrepancies due to secondary resonance causing the energy context from the two primary-excited antisymmetric modes to other, first of all, symmetric modes. A further increase of the nondimensional forcing amplitude to 0.03 leads to more complex secondary resonance effects. Specific surface wave phenomena, e.g., wave breaking, are experimentally observed and documented by photographs and videos.
 [doi:10.1063/1.3562310]

I. INTRODUCTION

Rectangular tanks with screens are used for antirolling tanks of ships and tuned liquid dampers (TLDs) of tall buildings. Properly tuned sloshing is an efficient tool for suppressing oscillations of the carrying structure. For these applications, a design requirement is that the lowest resonant sloshing frequency should almost not be affected by screens, i.e., it must remain almost the same as for the clean tank and relatively close to the most important structural natural frequency and the roll natural frequency. A rough guideline is then that the screen *solidity ratio* Sn, i.e., the ratio of the area of the shadow projected by the screen on a plane parallel to the screen to the total area contained within the frame of the screen is relatively small, $\mathrm{Sn} \lesssim 0.5$. The free-surface nonlinearity may be important.[1] This especially matters for antirolling and ship tanks when the nondimensional tank motion magnitudes (scaled by the cross-dimensional tank length l) are clearly larger than for TLDs.

The cargo ship liquid tanks with swash bulkheads is another application dealing with sloshing in rectangular tanks. A swash bulkhead is a bulkhead with holes and has from a hydrodynamic point of view similarities with a screen. The objectives are to provide sloshing damping as well as to *change the lowest resonance frequency* to a higher frequency range where the wave-induced ship velocity and acceleration are less severe. The consequence is that, in contrast to TLDs, slotted swash bulkheads are characterized by a higher solidity ratio, e.g., $\mathrm{Sn} \approx 0.9$. The optimum solidity ratio is not the highest value $\mathrm{Sn} = 1$ which means that the screen becomes a solid wall dividing the liquid domain into independent compartments. Similar devices as swash bulkheads are, for instance, used in fuel tanks of rockets and oil-gas separators on floating platforms.

Bearing in mind the swash bulkheads in rectangular ship tanks, we focus in the present paper on the *steady-state* two-dimensional liquid sloshing in a rectangular tank with a central slat-type screen and the specific geometric and physical parameters which are, in contrast to earlier TLDs studies, characterized by

- $0.5 \lesssim \mathrm{Sn} \lesssim 0.95$;
- a limited number of openings (slots, gaps) in the screen ($N \lesssim 50$);
- finite liquid depths;
- a wider forcing frequency range covering not only the lowest natural sloshing frequency for the corresponding clean tank, σ_1^*, but also the next primary excited natural sloshing frequency σ_3^*.

The latter frequency range is needed because, in contrast to a TLD with lower solidity ratios, frequencies corresponding to the resonant sloshing responses with $0.5 \lesssim \mathrm{Sn} \lesssim 0.95$ are expected to be away from those for the corresponding clean tank. The lateral excitations are considered. A particular goal is to understand the physics of liquid sloshing dynamics versus the input parameters, the solidity ratio Sn, the forcing frequency σ, and the forcing amplitude η_{2a} with emphasis on the resonance frequencies as a function of Sn. Understanding the role of the free-surface nonlinearity is an-

[a]Electronic mail: odd.faltinsen@ntnu.no.

other particular goal. Three different nondimensional amplitudes, $\eta_{2a}/l=0.001$, 0.02, and 0.03 were tested in the experiments.

To the best of the authors' knowledge, the literature on the liquid sloshing dynamics in tanks with screens of solidity ratio higher than 0.5 is rare. Typical examples in the papers by Kaneko and Ishikawa,[2] Tait *et al.*,[3] Love and Tait,[1] and Warnitchai and Pinkaew[4] are associated with TLDs and Sn $\lesssim 0.5$. They extensively employ the fact that the natural sloshing frequencies and modes remain *almost the same* as for the corresponding clean tank (without screen). The focus is mainly on the resonance response with the forcing frequencies close to the first natural frequency of the corresponding clean tank, σ_1^*. For analyzing this resonance, Kaneko and Ishikawa,[2] Tait *et al.*,[3] and Love and Tait[1] use different linear and nonlinear modal methods in which the corresponding modal equations are derived (Love and Tait[1] takes the nonlinear modal system by Faltinsen and Timokha[5]) based on the natural sloshing modes of the corresponding clean tank. These modal solutions make it possible to estimate the pressure field at the screen and, using the pressure drop condition, derive quadratic damping term in the corresponding modal equations. The pressure drop condition appears as a generalization of the viscous drag term in Morison's equation. This condition requires empirical information on the so-called pressure drop coefficient which, for instance, is well-known for an orifice meter device and the modeling of the screen effect in air ventilation systems. Reviews on usage of this condition can be found in Refs. 6 and 7. Additional examples of using this condition for liquid sloshing dynamics and external surface wave problems can be found in the papers by Molin[8] and Faltinsen *et al.*[9]

When $\mathrm{Sn}\to 1$, the screen becomes a rigid wall. The modal solution employing the natural sloshing modes of the corresponding clean tank used in the aforementioned TLD analysis is then not more applicable. The resonant peaks are then expected not at σ_{2i-1}^* (odd natural sloshing frequencies of the clean tank). This fact was first documented in the famous NASA Report[10] for a circular sectored tank. An attempt to describe the general *trend* in changing the *resonant* sloshing frequencies with increasing Sn in a rectangular tank with two-dimensional flows is given in Sec. 6.8 of Ref. 11. The screen was installed in the middle of the rectangular tank. Linear sloshing theory was employed. The idea was to consider the modal solutions in the two screen-separated compartments and, thereafter, match these solutions at the screen by using continuity of the mean flux velocity and the averaged pressure drop condition which should play the role of transmission boundary conditions. An extension of this approach was done by Faltinsen *et al.*[9] Realizing this idea showed success in describing (i) the resonance response amplitude for σ close to σ_1^* (the first natural frequency for the corresponding clean tank), and (ii) the general qualitative fact of disappearance of the resonance peaks at σ_1^* and σ_3^* and appearance of the resonance peak at σ_2^* (which is the lowest natural sloshing frequency for the compartments) as $\mathrm{Sn}\to 1$. Due to quadratic nature of the pressure drop condition, the results on the resonance peaks depend on the forcing amplitude. Furthermore, working on Ref. 9, we found out that this approach is not precise in identification of the resonance peak positions as the forcing amplitude becomes smaller and Sn tends to 1. Even though the experimental forcing amplitude was sufficiently small (the forcing amplitude-to-tank width is about 0.001), this theoretical approach gave wrong resonance peak position in a frequency range about σ_3^*. Explanation comes from the fully linear analysis by Faltinsen and Timokha[12] who study the *linear* natural sloshing frequencies and modes neglecting flow separation (jet flow) at the slotted screen in the spirit of earlier papers on either surface-piercing barriers[13] or baffles.[14] Faltinsen and Timokha[12] showed in their linear analysis that, when $\mathrm{Sn}\lesssim 0.5$, the screen-corrected natural sloshing frequencies remain almost the same as for the corresponding clean tank (consistent with earlier TLD analysis), but, when Sn increases in the range $0.5\lesssim \mathrm{Sn}<1$, the first natural sloshing frequency σ_1 (and the corresponding mode) in the screen-equipped tanks continuously vanishes, $\sigma_1\to 0$, but the third one, $\sigma_3\to\sigma_2^*$, as $\mathrm{Sn}\to 1$. Because Faltinsen and Timokha[12] do *not* use the nonlinear pressure drop condition, this result on the natural sloshing frequencies and modes is independent of the forcing amplitude, i.e., it is the limit case on the resonance frequencies when the forcing amplitude tends to zero. The change of the theoretical natural frequencies by this linear theory is quantitatively consistent with experiments conducted with their smallest forcing amplitude $\eta_{2a}/l\approx 0.001$.

The transformations of the natural sloshing modes and frequencies within the linear approximation by Faltinsen and Timokha[12] are an important factor which should be accounted for in description of the forced resonant liquid sloshing and accurate identification of the resonance sloshing frequencies for $0.5\lesssim \mathrm{Sn}<1$. As we will show in the present paper, accounting for both these transformations and the pressure drop at the screen makes the multimodal technique much more complicated. The transformations are, however, not important for TLDs, thus, when $0<\mathrm{Sn}\lesssim 0.5$, the interested reader can use, e.g., the modal theories Kaneko & Ishikawa,[2] Tait *et al.*,[3] and Love and Tait,[1] instead of following the present analysis.

The experimental setup, measured wave elevations at the walls, and video observations are reported in Secs. III and IV. The latter section includes also comparison with quasilinear multimodal theory constructed in Sec. II. The quasilinear multimodal theory is constructed based on the natural sloshing modes by Faltinsen and Timokha[12] and the well-known linear multimodal method whose description is given, e.g., in Chap. 5 of Ref. 11. A novelty is that we also account for the pressure drop condition by selecting the approach-velocity component from the singular (at the sharp slot edges) natural sloshing modes by Faltinsen and Timokha.[12] The quasilinear theory accounts therefore for the change of the natural sloshing modes (frequencies) versus the screen geometry as well as an "integral" effect of the local flow separation (or jet flow) by means of the pressure drop condition. However, this theory neglects the free-surface nonlinearity. Adopting the pressure drop condition implicitly assumes that the liquid motions in the whole tank are generally well described by the potential incompressible inviscid hydrodynamic model and that flow separation (or jet flow) at

the screen is only localized in a relatively small neighborhood of the screen.

Even though we postulate the linearized free-surface conditions, the nonlinear pressure drop condition introduces the $(\cdot|\cdot|)$-type quadratic quantities in terms of the generalized velocities in the corresponding modal equations. For TLD-related applications with resonant excitation at the lowest natural frequency, one can, e.g., follow Tait *et al.*[3] to get simpler expressions depending only on the dominant modes. These quantities can then be interpreted as quadratic damping terms causing finite resonant response at σ_1^* (see a review on the quadratic damping for linear oscillators in Ref. 15). An alternative approach is to use a Morison-equation formulation instead of the pressure drop condition at the screen with $0<\mathrm{Sn}\lesssim 0.5$ (see Sec. 6.7 of Ref. 11). The latter approach provided very satisfactory agreement with experiments by Warnitchai and Pinkaew.[4] In the present paper, the hydrodynamic coefficients of the modal equations, including the natural frequencies σ_i, change with Sn, the number and position of the slots. The quadratic terms should then include all the generalized coordinates and, along with damping, cause an energy redistribution between different screen-modified natural sloshing modes.

Agreement between the quasilinear theory and experiments is almost ideal for the smallest forcing amplitude-to-tank width ratio equal to 0.001 (the liquid depth-to-the tank width ratio is 0.4). The results are reported in Sec. IV A. Discrepancies for the lowest and largest tested Sn, $\mathrm{Sn}=0.4725$ and 0.95125, are explained by the free-surface nonlinearity causing a soft-spring type response behavior similar as for theoretical steady-state sloshing in clean rectangular tanks with a finite depth (see, e.g., Chap. 8 in Ref. 11). Increasing the nondimensional forcing amplitude to 0.01 (Sec. IV B) leads to a series of new experimentally observed free-surface phenomena. The paper presents the corresponding photographs and videos. Implicitly, these free-surface phenomena, e.g., wave breaking, runup with jets at the walls, indicate importance of the free-surface nonlinearities. The observed free-surface phenomena are mainly documented in the frequency range covering σ_2^* and σ_3^*. The latter is explained by the fact that resonance at $\sigma\approx\sigma_1^*$ leads to a larger cross-flow at the screen, and, therefore, causes a larger damping due to flow separation (or jet flow). The experimental response curves are characterized by extra resonance peaks in this frequency range. The modal analysis shows that these peaks are a consequence of the secondary resonance due to the second-order free-surface nonlinearity. According to Faltinsen and Timokha,[5] this kind of the secondary resonance amplifies symmetric natural sloshing modes which are not directly excited by the horizontal tank forcing. Theoretical description of the secondary resonance may require the so-called adaptive nonlinear multimodal modeling elaborated by Faltinsen and Timokha[5] for the clean rectangular tank. However, the quasilinear theory describes the general trend in changing the main resonance peak position.

In Sec. IV C, we present experimental data for the largest tested forcing amplitude, $\eta_{2a}/l=0.03$, which were conducted with the liquid depth-to-the tank width, $h/l=0.35$. The experimental observations show very steep waves with strong wave breaking, runup as well as overturning and formation of gas pockets. Implicitly, this indicates amplifications of the higher natural modes via the free-surface nonlinearity mechanism. The quasilinear theory shows qualitatively how the resonance frequencies change with Sn, but cannot be used to quantify the steady-state wave amplitude response. Further, the experiments detect the multiple resonance peaks for $0.5\lesssim\mathrm{Sn}\lesssim 0.9$ as well as the multibranching of the corresponding experimental response curves. In contrast to the case with $\eta_{2a}/l=0.01$, this cannot be easily explained by the secondary resonance phenomena due to the second-order nonlinearity. A dedicated study is required.

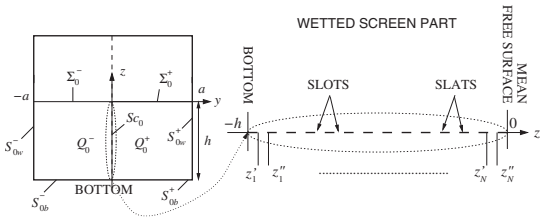

FIG. 1. The rectangular tank with a slat-type screen in the middle. Basic geometric notations.

II. QUASILINEAR MULTIMODAL THEORY

A. Preliminaries

1. Basic notations and limit cases

Two-dimensional liquid sloshing is considered in a rectangular tank of width $l=2a$ with a slat-type screen installed at the tank middle as shown in Fig. 1. The figure introduces geometric notations and the body-fixed coordinate system. The rectangular tank is forced horizontally with displacements $\eta_2(t)$. The screen appears as a thin solid plate with a series of perforated horizontal slots. The screen thickness is neglected. In the linear free-surface analysis, we consider only the mean wetted screen part Sc_0 and assume that it has N submerged slots. When the set So_0 denotes all the wetted rigid slats, and Op_0 is the total set of submerged slots $(\mathrm{Sc}_0=\mathrm{Op}_0\cup\mathrm{So}_0)$, this numerical sequence defines them as follows:

$$\mathrm{So}_0=\{(0,z):-h\le z\le z_1',\ z_1''\le z\le z_2',\ \dots,\ z_N''\le z\le 0\},$$
$$\mathrm{Op}_0=\{(0,z):-h\le z_1'<z<z_1'',\ \dots,\ z_N'<z<z_N''\le 0\}, \tag{1}$$

where h is the liquid depth. Based on definition (1), we can introduce the solidity ratio of the mean wetted screen part as follows:

$$\mathrm{Sn}=\frac{h-\Sigma_{j=1}^{N}(z_j''-z_j')}{h}. \tag{2}$$

As we see, the solidity ratio is a function of h.

An inviscid and incompressible liquid with irrotational flow is assumed everywhere in the mean liquid domain $Q_0=Q_0^-\cup Q_0^+$ *except* in a small neighborhood of the screen Sc_0. The *linear sloshing* theory is adopted, namely, the wave slope is assumed asymptotically small (see Chap. 5 in Ref.

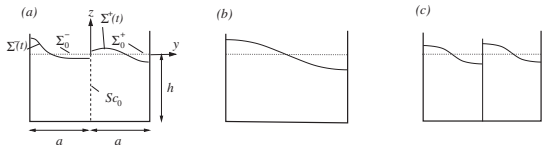

FIG. 2. Schematic instant wave profiles for two-dimensional liquid sloshing in a rectangular tank with horizontal excitation. Screen Sc_0 with $0<Sn<1$ in the middle is installed [part (a)]. Parts (b) and (c) illustrate the first antisymmetric wave profiles for the limit cases Sn=0 and Sn=1, respectively.

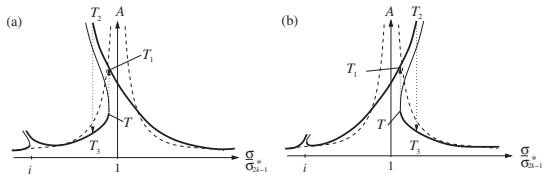

FIG. 3. Schematic response curves for a clean rectangular tank giving the steady-state resonance wave amplitude response A vs σ/σ^*_{2k-1} based on two-dimensional potential flow of an incompressible liquid. The dashed line shows results following from the linear sloshing theory. The solid lines represent response curves following from the nonlinear asymptotic theory, where the bold solid line notes stable steady-state solutions. A hysteresis effect is possible denoted by the points T, T_1, T_2, and T_3. The point i marks possibility of the secondary resonance whose concept for sloshing problem is elaborated and studied in detail by Faltinsen and Timokha (Ref. 5). The secondary resonance implies amplification of higher modes when a superharmonics becomes close to a higher natural sloshing mode. Depending on the nondimensional liquid depth h/l, we can have (a) soft-spring type behavior ($0.3368\ldots \lesssim h/l$ for $k=1$), or (b) hard-spring type behavior ($h/l \lesssim 0.3368\ldots$ for $k=1$).

11). The effect of viscous boundary layers at the tank walls and bottom is assumed negligible (see Chap. 6 in Ref. 11)

Physically, there exist two limit cases associated with Sn=0 (no screen) and Sn=1 (solid central wall). Typical wave profiles are depicted in Fig. 2. Panels (b) and (c) are related to the lowest natural sloshing modes for the two limit cases. When Sn=0, the natural sloshing modes (within an arbitrary nonzero constant C_i) are expressed as

$$\varphi_i = \varphi_i^* = C_i \cos\left(\frac{\pi i}{l}(y+a)\right)\cosh(\pi i(z+h)/l), \qquad (3)$$

$$\kappa_i = \kappa_i^* = \frac{\pi i}{l}\tanh\left(\frac{\pi i h}{l}\right), \quad \sigma_i^* = \sqrt{g\kappa_i^*}, \quad i=1,2,\ldots,$$

where σ_i^* are the corresponding natural sloshing frequencies (see Sec. 4.3.1.1 in Ref. 11). Expression (3) introduces symmetric (even, $i=2k$) and antisymmetric (odd, $i=2k-1$) modes. Inserting a slat-type screen at the tank middle does not change the symmetric natural modes, but the antisymmetric modes become discontinuous at the slats (So_0) and, therefore, cannot be described by expression (3).

Passage to Sn=1 leads to the central rigid wall dividing the whole tank into two equal symmetrically situated compartments. The corresponding natural sloshing modes in $Q_0^{\pm}$ are then defined by the formulas

$$\varphi_i^{\pm} = \varphi_i^{**\pm} = C_i \cos\left(\frac{\pi i}{a}(y \mp a)\right)\cosh(\pi i(z+h)/a), \qquad (4)$$

$$\kappa_i = \kappa_i^{**} = \frac{\pi i}{a}\tanh\left(\frac{\pi i h}{a}\right), \quad \sigma_i^{**} = \sqrt{g\kappa_i^{**}}, \quad i=1,2,\ldots.$$

Because $l=2a$, $\sigma_i^{**}=\sigma_{2i}^*$, the case Sn=1 leads to vanishing of the natural sloshing frequencies responsible for the antisymmetric modes of the case Sn=0.

Faltinsen and Timokha[12] describe evolution of the antisymmetric natural sloshing modes from Eq. (3) to Eq. (4) as Sn changes from 0 to 1 with finite nondimensional depth h/l. These modes remain very close to Eq. (3) for $0<Sn\lesssim 0.5$. The principal changes in the natural modes are detected in the range $0.5\lesssim Sn<1$.

2. Resonant steady-state response for a clean rectangular tank

Damping of liquid sloshing in a clean tank without wave breaking is small and mainly caused by the viscous boundary layer. Finite resonant harmonically excited liquid sloshing is mainly due to nonlinear transfer of energy between primary excited and higher modes. A review on the resonance steady-state wave amplitude response can be found in Chap. 8 of Ref. 11. According to asymptotic theory of nonlinear resonant steady-state sloshing, the *primary* resonance is only possible at the odd (antisymmetric) modes, i.e., when $\sigma\to\sigma^*_{2k-1}$. The corresponding response curves are schematically illustrated in Fig. 3. Depending on the nondimensional liquid depth, h/l, one can arrive at the soft-spring type response curves in the panel (a), or at the hard-spring type response curves in the panel (b). This change for the first resonance $\sigma\approx\sigma_1^*$ happens for asymptotically small η_{2a}/l at the critical depth $h/l=0.3368\ldots$. Nonlinear effects can also cause *secondary* resonances meaning that multiples of the forcing frequency is equal to a natural sloshing frequency.

B. Linear sloshing problem and the corresponding linear modal equations

1. Boundary value problem

Henceforth in our theoretical analysis, we *assume* that the liquid is inviscid and incompressible with irrotational flow except in a small vicinity of the screen where flow separation (or a jet flow) occurs. Let equation $z=\zeta(y,t)$ describe the free-surface elevations and $\Phi(y,z,t)$ be the absolute velocity potential defined in the tank-fixed coordinate system Oyz. The linear sloshing theory involves the Laplace equation and the boundary conditions coupling Φ and ζ:

$$\nabla^2\Phi = 0 \quad \text{in} \quad Q_0 = Q_0^+ \cup Q_0^-, \qquad (5a)$$

$$\frac{\partial\Phi}{\partial y} = \dot{\eta}_2(t) \quad \text{on} \quad S_{0w}^{\pm}, \qquad (5b)$$

$$\frac{\partial\Phi}{\partial z} = 0 \quad \text{on} \quad S_{0b}^{\pm}, \qquad (5c)$$

$$\frac{\partial \Phi}{\partial z} = \frac{\partial \zeta}{\partial t} \quad \text{on} \quad \Sigma_0 = \Sigma_0^+ \cup \Sigma_0^-, \tag{5d}$$

$$\frac{\partial \Phi}{\partial t} + g\zeta = 0 \quad \text{on} \quad \Sigma_0 = \Sigma_0^+ \cup \Sigma_0^-, \tag{5e}$$

$$\int_{\Sigma_0} \zeta dy = 0. \tag{5f}$$

Geometric notations are explained in Fig. 1. The horizontal displacement of the tank is $\eta_2(t)$ and g is the gravity acceleration. Equations (5d) and (5e) are the linearized *kinematic* and *dynamic* boundary conditions formulated on the mean free surface $\Sigma_0 = \Sigma_0^- \cup \Sigma_0^+$.

The linear boundary problem Eq. (5) should be completed by appropriate boundary conditions on the screen Sc_0. When we *neglect* flow separation (or a jet flow) at the screen and, thereby, postulate the potential flow of an incompressible liquid everywhere in Q_0 including the openings Op_0, one should add the following linear boundary condition:

$$\frac{\partial \Phi}{\partial y} = \dot{\eta}_2 \quad \text{on} \quad \mathrm{So}_0 \tag{6}$$

implying that the solid screen slats move horizontally together with the rectangular tank.

The problem Eqs. (5) and (6) require initial conditions which can be defined as

$$\zeta(y,0) = \zeta_0(y), \quad \frac{\partial \zeta}{\partial t}(y,0) = \zeta_1(y),$$

where ζ_0 and ζ_1 are the initial free-surface shape and velocity, respectively.

2. Linear modal solution when neglecting viscous screen effect

The linear sloshing problem Eqs. (5) and (6) have the following modal solution (see details in Chap. 5 of Ref. 11):

$$\zeta(y,t) = \sum_{i=1}^{\infty} \beta_i(t) f_i(y), \tag{7}$$

$$\Phi(y,z,t) = \dot{\eta}_2(t) y + \sum_{i=1}^{\infty} R_i(t) \varphi_i(y,z), \tag{8}$$

where $\varphi_i(y,z)[f_i(y) = \varphi_i(y,0)]$ are the natural sloshing modes appearing as the nontrivial eigensolution of the following spectral boundary problem:

$$\nabla^2 \varphi_i = 0 \quad \text{in} \quad Q_0; \quad \frac{\partial \varphi_i}{\partial n} = 0 \quad \text{on} \quad S_0 = S_{0w}^{\pm} \cup S_{0b}^{\pm} \cup \mathrm{So}_0; \tag{9}$$

$$\frac{\partial \varphi_i}{\partial z} = \kappa_i \varphi_i \quad \text{on} \quad \Sigma_0.$$

The spectral parameter $\kappa_i > 0$ determines the natural sloshing frequencies

$$\sigma_i = \sqrt{g\kappa_i}, \quad i = 1,2,\ldots. \tag{10}$$

According to general theorems on the spectral boundary problem Eq. (9) (see, e.g., Refs. 16–18), the natural sloshing modes are orthogonal on Σ_0, i.e.,

$$\int_{\Sigma_0} f_i f_j dy = 0, \quad i \neq j; \quad f_i(y) = \varphi_i(y,0). \tag{11}$$

An accurate approximate eigensolution of the spectral problem Eq. (9) was constructed by Faltinsen and Timokha.[12] Analyzing this solution shows that the natural frequencies and modes are far from σ_{2i-1}^* for $0.5 \lesssim \mathrm{Sn} < 1$. This means that, in contrast to earlier TLD analysis, we cannot adopt the eigensolution (3) for these solidity ratios.

The modal solution Eqs. (7) and (8) automatically satisfy all the relations of Eqs. (5) and (6) except the kinematic and dynamic boundary conditions Eqs. (5d) and (5e). Due to the orthogonality condition Eq. (11), the kinematic condition Eq. (5) couples $R_i(t)$ and $\beta_i(t)$ as follows:

$$R_i(t) = \frac{\dot{\beta}_i(t)}{\kappa_i}, \quad i = 1,2,\ldots. \tag{12}$$

After adopting Eq. (12) in the modal solution Eq. (8) and substituting this modal solution in the dynamic boundary condition Eq. (5d), the orthogonality condition Eq. (11) leads to the linear ordinary differential equations with respect to $\beta_i(t), i = 1,2,\ldots$, the so-called *linear modal equations*. For the considered tank shape, these modal equations take the form

$$\mu_k[\ddot{\beta}_{2k-1}(t) + \sigma_{2k-1}^2 \beta_{2k-1}(t)] + \lambda_k \ddot{\eta}_2(t) = 0, \quad k = 1,2,\ldots; \tag{13a}$$

$$\ddot{\beta}_{2k}(t) + \sigma_{2k}^2 \beta_{2k}(t) = 0, \quad k = 1,2,\ldots, \tag{13b}$$

where

$$\mu_k = \frac{1}{\kappa_{2k-1}} \int_{-a}^{0} f_{2k-1}^2 dy, \quad \lambda_k = \int_{-a}^{0} y f_{2k-1} dy, \quad k \geq 1. \tag{14}$$

We see that the η_2-forcing term is present only in Eq. (13a) responsible for antisymmetric modes, i.e., only antisymmetric modes are primary, directly excited. Symmetric modes depend in the linear approximation only on initial conditions. The hydrodynamic coefficients σ_{2i-1}, μ_k, and λ_k differ from similar coefficients in linear modal equations for sloshing in a clear rectangular tank (Chap. 5 in Ref. 11). Our hydrodynamic coefficients are now functions of Sn, the number of the submerged screen slots and their position.

C. Modification of the modal solution due to the pressure drop condition

The linear modal Eq. (13) must be modified to account for viscous cross-flow at the screen. The corresponding modification can be done by using a pressure drop condition at the screen. We will show, that this will lead to additional quadratic terms in the modal Eq. (13a) associated with the

antisymmetric modes. Because the symmetric modes do not cause cross-flow through the screen, the modal Eq. (13b) for symmetric modes will remain homogeneous within the framework of the linear sloshing theory.

1. Pressure drop condition

The pressure drop condition at the screen can be formulated as (see, e.g., Ref. 6)

$$P_- - P_+ = \tfrac{1}{2}\rho K u|u| \quad \text{on } \mathrm{Sc}_0, \tag{15}$$

where K is an empirical pressure drop coefficient, ρ is the liquid density, u is the so-called *approach* velocity to the screen, and $(P_- - P_+)$ is the *pressure drop*. The pressure drop formulation Eq. (15) is based on that both sides of the screen are wetted. It does not apply in the free-surface zone where, due to different elevations at the screen sides, liquid goes through the openings to the dry screen side with further fall out. The falling liquid will then impact on the underlying free surface and thereby cause an extra dissipation.

The pressure drop coefficient K depends on the solidity ratio Sn. It may also depend on the Reynolds and Keulegan–Carpenter numbers. For slat-type screens, the pressure drop coefficient weakly depends on the Reynolds number (see details in Ref. 6, p. 314). Following Tait *et al.*[3] who referred to formulas by Baines and Peterson[19] and Weisbach,[20] we will adopt the following approximation of the empirical pressure drop coefficient

$$K = \left(\frac{1}{Cc(1-\mathrm{Sn})} - 1\right)^2, \qquad Cc = 0.405\exp(-\pi \mathrm{Sn}) + 0.595 \quad \text{for } \mathrm{Sn} \geq 0.3. \tag{16}$$

According to experimental studies by Tait *et al.*[3] for slat-type screens with Sn=0.42, different excitation frequencies close to the first natural sloshing frequency, and for intermediate and shallow liquid depths, formula (16) gives satisfactory approximation of K for the Keulegan–Carpenter number $KC = u_m T/D > 15$ where u_m is the amplitude of u, T is the oscillation period, and D is a characteristic length (here, the slot height). The pressure drop condition was originally formulated in the literature for uniform, coordinate-independent $u=u(t)$ and $P=P(t)$.

2. The horizontal approach velocity

The linear modal solution Eq. (8) based on the screen-modified natural sloshing modes following from the linear analysis by Faltinsen and Timokha[12] is assumed a first-order approximation of the relative horizontal velocity at the screen, i.e.,

$$U(y,z,t) = u(y,z,t) + \tilde{u}(y,z,t) = \sum_{i=1}^{\infty} \frac{\dot{\beta}_{2i-1}(t)}{\kappa_{2i-1}} \frac{\partial \varphi_{2i-1}}{\partial y}(y,z), \quad y \neq 0, \tag{17}$$

where φ_{2i-1} are the corresponding antisymmetric natural sloshing modes. Because dealing with the linear natural screen-modified sloshing modes by Faltinsen and Timokha[12] leads to a singular velocity field at the slot edges, the restriction $y \neq 0$ is important; formally, U is infinite at these edges.

In expression (17), $\tilde{u}$ is the singular horizontal velocity component and u is the regular horizontal velocity component. The latter should be continuous at $y=0$ so that $u(0,z,t)$ is associated with the approach velocity in formula (15). Because the natural sloshing modes are defined within an arbitrary nonzero multiplier C_{2i-1}, following Faltinsen and Timokha[12] leads to the expression

$$\varphi_{2i-1}(y,z) = C_{2i-1}(\phi_i(y,z) + \tilde{\phi}_i(y,z)), \quad i \geq 1, \tag{18}$$

where the functions $\tilde{\phi}_i$ and ϕ_i are associated with $\tilde{u}(y,z,t)$ and $u(y,z,t)$, respectively. Furthermore, Ref. 12 shows that the functions $\phi_i(y,z)$ and $\tilde{\phi}_i(y,z)$ can be presented in a standard expansion adopted in many problems of the linear wave theory[13] and, therefore, take the form

$$\phi_i(y,z) = \mp \cosh(k_0^{(i)}(z+h)/a)\cos(k_0^{(i)}(y \mp a)/a), \tag{19a}$$

$$\tilde{\phi}_i(y,z) = \mp \sum_{j=1}^{\infty} A_j^{(i)} \cos(k_j^{(i)}(z+h)/a) \frac{\cosh(k_j^{(i)}(y \mp a)/a)}{\cosh(k_j^{(i)})} \quad \text{in } Q_0^{\pm}, \tag{19b}$$

where $\{k_0^{(i)}, i \geq 1\}$ and $\{k_j^{(i)}, i \geq 1, j \geq 1\}$ are the roots of the equations

$$k_0^{(i)} \tanh(k_0^{(i)} h/a) = \kappa_{2i-1} a \quad \text{and} \quad k_j^{(i)} \tan(k_j^{(i)} h/a) = -\kappa_{2i-1} a, \quad i \geq 1, \quad j \geq 1. \tag{20}$$

Here, κ_{2i-1} are the eigenvalues of the spectral problem Eq. (9) in which the screen effect is included so that they are not equal to κ_{2i-1}^* in Eq. (3).

The terms associated with $\tilde{\phi}_i$ are evanescent terms exponentially decaying away from the screen; they capture the local singular character of the linear natural sloshing modes at the slot edges. The "wave components" of the natural sloshing modes, ϕ_i determines the surface wave profile and, thereby, the corresponding wave number $k_0^{(i)}$. It is very important that the wave numbers $k_0^{(i)}$ are mathematically not equal to the wave number of the corresponding clean tank, $\pi(2i-1)/l$. Faltinsen and Timokha[12] studied the screen effect on κ_{2i-1}, $k_0^{(i)}$, and $k_j^{(i)}$ as well as on the natural sloshing modes Eqs. (18) and (19). It follows from their analysis that the values $k_0^{(i)}$ are less than $\pi(2i-1)/l$ and $k_0^{(i)}$ monotonically decreases from $\pi(2i-1)/l$ to $2\pi(i-1)/l$ as Sn increases from 0 to 1. The values $k_0^{(i)}$ remain close to $\pi(2i-1)/l$ only for $\mathrm{Sn} \lesssim 0.5$, i.e., for a TLD-case. Furthermore, the values $k_j^{(i)}$ for lower natural sloshing modes rapidly tend to $\pi j/h$ as $j \to \infty$ providing almost zero flux through the screen associated with the function $\tilde{\phi}_i$.

The approach velocity u should represent the velocity flux through the screen without representing the local flow details (here, singularities at the edges) at the screen. This means that the approach velocity should be well approximated in terms of the "wave component" functions ϕ_i expressed by Eq. (19a). It follows from Eq. (17) that the approach velocity can then be determined by

$$u(z,t)=\sum_{i=1}^{N_m}\frac{\dot{\beta}_{2i-1}}{\kappa_{2i-1}}U_i(z),\quad -h<z<0, \tag{21}$$

where N_m is the required number of antisymmetric modes ($N_m\to\infty$) and

$$U_i(z)=\left.\frac{\partial\phi_i}{\partial y}\right|_{y=0}=-\frac{C_{2i-1}}{a}\cosh(k_0^{(i)}(z+h)/a)\sin(k_0^{(i)}). \tag{22}$$

3. The pressure drop condition and the modified modal equations

Using the linear modal solution Eq. (8) in expression for the dynamic pressure

$$p=-\rho\frac{\partial\Phi}{\partial t} \tag{23}$$

formally leads to a linear pressure drop at the slats, namely, $p_- - p_+ \neq 0$ on So_0 due to the discontinuous antisymmetric natural sloshing modes φ_{2i-1}. However, the difference $P_- - P_+$ in the pressure drop condition Eq. (15) has another physical nature. This pressure drop appears due to flow separation (or a jet flow) which is not captured by the linear modal solution.

We should first insert the approach velocity Eq. (21) into the pressure drop condition and find the corresponding pressure correction p_2. When expressing p_2, we use an analytical continuation of the irrotational flow to the whole liquid domain. Formally, this suggests the modified velocity potential

$$\Phi(y,z,t)=\dot{\eta}_2 y+\sum_{i=1}^{\infty}\frac{\dot{\beta}_i(t)}{\kappa_i}\varphi_i(y,z)\mp\frac{1}{\rho}\int_{t_0}^{t}p_2(y,z,t_1)\mathrm{d}t_1 \quad \text{in } Q_0^{\pm}. \tag{24}$$

Now, we should substitute Eqs. (7) and (24) into the problem Eq. (5) and satisfy the Laplace equation, the body-boundary condition, and the pressure drop condition $p_{2-} - p_{2+} = (1/2)\rho K u|u|$. Furthermore, we should also account for Eqs. (7) and (24) into kinematic Eq. (5d) and dynamic Eq. (5e) boundary conditions. The latter conditions (see Appendix A) give

$$\frac{\partial p_2}{\partial n}=0 \quad \text{on } \Sigma_0^{\pm}, \tag{25a}$$

$$\ddot{\eta}_2 y+\sum_{i=1}^{\infty}\frac{\ddot{\beta}_i(t)+g\kappa_i\beta(t)}{\kappa_i}f_i(y)\mp\frac{1}{\rho}p_2(y,0,t)=0 \quad \text{on } \Sigma_0^{\pm}. \tag{25b}$$

It may look unphysically that, as the derivations in Appendix A show, the pressure-correction term p_2 satisfies the Neumann boundary condition Eq. (25a) on the mean free surface. However, one should remember the specific definition of p_2 in the modified velocity potential Eq. (24) implying that the integral over p_2 is also a correction of the velocity potential. The latter gives Eq. (A3) following from the kinematic condition Eq. (5d), and because Eq. (A3) is true for any instant t, one mathematically gets the zero-Neumann condition Eq. (25a) for the pressure-correction term.

Using Eq. (25a) together with relations in Eq. (A1) and the pressure drop condition leads to the boundary value problem

$$\nabla^2 p_2=0 \quad \text{in } Q_0^{\pm};$$

$$\frac{\partial p_2}{\partial n}=0 \quad \text{on } S_{0b}^{\pm}\cup S_{0w}^{\pm}\cup\Sigma_0^{\pm}; \tag{26}$$

$$p_2=\pm\frac{1}{4}\rho K u|u| \quad \text{on } \mathrm{Sc}_0.$$

This problem has the following solution

$$p_2=\pm\rho\frac{K}{4h}\left(\Omega_0+2\sum_{k=1}^{\infty}\Omega_k\cos\left(\frac{\pi k}{h}z\right)\frac{\cosh(\pi k(y\mp a)/h)}{\cosh(\pi k a/h)}\right), \tag{27}$$

where

$$\Omega_k=\int_{-h}^{0}u|u|\cos\left(\frac{\pi k}{h}z\right)\mathrm{d}z,\quad k\geq 0. \tag{28}$$

One must note that when introducing the approach velocity via Eq. (21) we neglect the evanescent terms exponentially decaying away from screen which are responsible for a singular character of the linear natural sloshing modes at the slot edges. We see that similar exponentially decaying terms appear in solution Eq. (27) associated with $\Omega_k, k\geq 1$. These terms do not contribute to the screen averaged pressure, but are only responsible for a local nearly screen change of the pressure field by p_2. This local change has no physical meaning, especially for larger k because the local field at the screen is in reality viscous. Excluding these exponentially decaying terms means an averaged (over the mean screen height) pressure drop which will furthermore be adopted. The modified velocity potential Eq. (24) should then be approximated by

$$\Phi(y,z,t)=\dot{\eta}_2 y+\sum_{i=1}^{\infty}\frac{\dot{\beta}_i(t)}{\kappa_i}\varphi_i(y,z)\mp\frac{K}{4h}\int_{t_0}^{t}\left(\int_{-h}^{0}u(z,t_1)|u(z,t_1)|\mathrm{d}z\right)\mathrm{d}t_1 \quad \text{in } Q_0^{\pm}, \tag{29}$$

where u is given by Eq. (21).

Let us consider the dynamic Eq. (25b) and use the orthogonality Eq. (11). This gives the modified modal equations with respect to β_{2i-1}

$$\mu_k(\ddot{\beta}_{2k-1}(t)+\sigma_{2k-1}^2\beta_{2k-1}(t))+\lambda_k\ddot{\eta}_2(t)-\frac{K\alpha_k}{4h}\int_{-h}^{0}\left(\sum_{i=1}^{N_m}\frac{\dot{\beta}_{2i-1}}{\kappa_{2i-1}}U_i(z)\right)\left|\sum_{i=1}^{N_m}\frac{\dot{\beta}_{2i-1}}{\kappa_{2i-1}}U_i(z)\right|\mathrm{d}z=0,\quad k=1,2,\ldots,N_m, \tag{30}$$

where N_m is the required number of antisymmetric modes [also see Eq. (21)], and

$$\alpha_k = \int_{-a}^{0} f_{2k-1}(y)\mathrm{d}y. \tag{31}$$

Other hydrodynamic coefficients are expressed by Eqs. (10) and (14). The symmetric modes are governed by Eq. (13b), i.e., they are not excited by the horizontal forcing $\eta_2(t)$ within the framework of the linear free-surface theory.

Based on studies by Faltinsen and Timokha[12] for a uniformly slotted screen with $0.5 \lesssim \mathrm{Sn} < 0.95$ and relatively small number of the openings $N \lesssim 50$, the natural sloshing frequencies and modes and, therefore, the hydrodynamic coefficients κ_i, σ_i, μ_i, λ_i, and α_i become strongly dependent on the geometric dimensions of the mean liquid domain, h and l, and, in addition, on the *two independent* screen parameters Sn and N. The hydrodynamic coefficients can also change with the position of the slot nearest to the mean free surface, i.e., due to the fact that the slot goes in and out of the mean free surface. When $0 < \mathrm{Sn} \lesssim 0.5$, the natural sloshing modes and frequencies are close to those for the clean tank and the latter additional dependencies can be neglected.

Henceforth, we consider steady-state liquid sloshing occurring due to the harmonic sway excitation $\eta_2(t) = \eta_{2a}\cos(\sigma t)$, where η_{2a} is the forcing amplitude, and σ is the forcing frequency. The emphasis will be on the η_{2a}-scaled wave elevations which, according to the modal presentation Eq. (7), is described by the formula

$$\zeta^*(y,t) = \sum_{i=1}^{\infty} \beta_i^*(t) f_i(y), \quad \beta_i^*(t) = \beta_i(t)/\eta_{2a}. \tag{32}$$

When l (tank width) is the characteristic size and $1/\sigma$ is the characteristic time, the modal Eqs. (30) can be rewritten to the nondimensional form with respect to $\beta_i^*(t)$:

$$\bar{\mu}_k(\ddot{\beta}^*_{2k-1}(t) + \bar{\sigma}^2_{2k-1}\beta^*_{2k-1}(t)) - \bar{\lambda}_k \cos t - [K\bar{\eta}_{2a}]\frac{\bar{\alpha}_k}{4\bar{h}}\int_{-\bar{h}}^{0}\left(\sum_{i=1}^{N_m}\frac{\dot{\beta}^*_{2i-1}}{\bar{\kappa}_{2i-1}}\bar{U}_i(\bar{z})\right) \times \left|\sum_{i=1}^{N_m}\frac{\dot{\beta}^*_{2i-1}}{\bar{\kappa}_{2i-1}}\bar{U}_i(\bar{z})\right| \mathrm{d}\bar{z} = 0, \quad k = 1,2,\ldots,N_m, \tag{33}$$

where we have introduced the nondimensional parameters

$$\bar{\sigma}_i = \sigma_i/\sigma, \quad \bar{\eta}_{2a} = \eta_{2a}/l, \quad \bar{U} = lU,$$

$$\bar{\kappa}_i = \kappa_i l, \quad \bar{h} = h/l, \quad \bar{z} = z/l,$$

$$\bar{\mu}_i = \mu_i/l^2, \quad \bar{\lambda}_i = \lambda_i/l^2, \quad \bar{\alpha}_i = \alpha_i/l.$$

When σ/σ_1^* and h/l are constant values, $0.5 \lesssim \mathrm{Sn}$, and $N \lesssim 50$, the steady-state solution of Eq. (33) strongly depends on the nondimensional parameter $[K\bar{\eta}_{2a}]$ (in the front of the integral term), the independent parameters Sn, N, and, generally, the position of the slot closest to the mean free surface. This is because, as we remarked above, all these input parameters can change the hydrodynamic coefficients in the modal equations. A simplification comes for *smaller solidity ratios*, $0 < \mathrm{Sn} \lesssim 0.5$ and $10 \lesssim N$ when (Ref. 12) the natural sloshing modes and frequencies (and the corresponding hydrodynamic coefficients) are close to those for the clean tank and, therefore, the steady-state solution of Eq. (33) is only function of σ/σ_1^*, h/l, and the nondimensional parameter $[K\bar{\eta}_{2a}]$. Another simplification is possible for a *porous-media screen* implying the *limit case* $N \to \infty$. During preparation of Ref. 12, the authors established that, whereas $100 \lesssim N$ and $0.5 < \mathrm{Sn} < 0.95$, the natural sloshing frequencies and modes become only functions of Sn [or K because one can define $\mathrm{Sn} = \mathrm{Sn}(K)$ by inverting the monotonic function Eq. (16)]. Thus, the porous media limit implies that the steady-state solution of Eq. (33) depends on the independent nondimensional input parameters σ/σ_1^*, h/l, $K\bar{\eta}_{2a}$, and K.

The periodic steady-state solution has been found from the system Eq. (30) by numerical time-integration following a fifth-order Runge–Kutta method with arbitrary initial conditions associated with initial free-surface shape and velocity. This becomes possible because the modal equations imply a dissipative mechanical system, i.e., transient waves die out with increasing time.

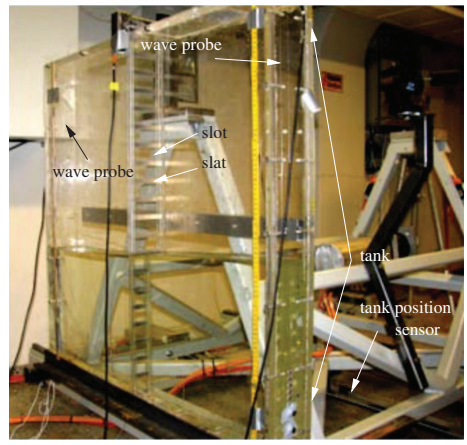

FIG. 4. (Color online) Experimental set-up and equipments.

III. EXPERIMENTS

A Plexiglas-made rectangular tank was installed in a rig located at the Marine Technology Center in Trondheim, Norway. The tank's internal dimensions are 1.0 m × 0.98 m × 0.1 m (width × height × breadth). The setup photograph is shown in Fig. 4. The tank has been equipped with two resistant wave probes. The measurement accuracy of the wave elevations is about 1 mm. The measurement probes have been installed at 1 cm away from the two opposite vertical walls. Two considerations determined our choice of the tank breadth. One is that we wanted to achieve two-dimensional flow conditions and, hence, the breadth-to-width ratio has to be small. The other criterion is that the tank breadth must be clearly larger than the boundary layers at the tank walls and the thin side-screen bracings "B" of 0.005 m (see Fig. 5).

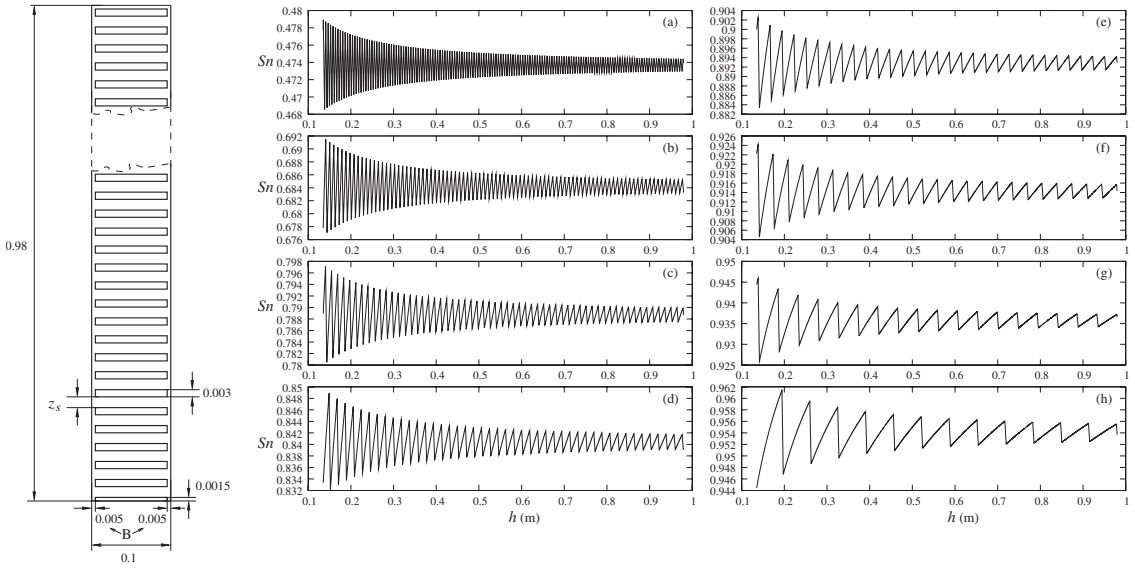

FIG. 5. Geometric parameters of the perforated plate (screen). All the numerical values are in meters. The plate thickness is 5 mm. The distance between the two nearest slots, z_s, takes the values z_s=0.0027 m (screen a), 0.0065 m (screen b), 0.0112 m (screen c), 0.0158 m (screen d), 0.025 m (screen e), 0.032 m (screen f), 0.0437 m (screen g), and 0.0623 m (screen h). Due to technical limitations in the drilling of the slots, the minimum possible slot height 3 mm was used for all the screens. This causes eight different solidity ratios which, generally, change with the liquid depth as shown in panels (a)–(h). Effect of the rigid side-screen bracings B of 0.005 m width is neglected in our analysis.

Meniscus effects occur at the intersection between the tank walls and the free surface leading to three-dimensional waves with very small wave height and wavelength relative to the gravity waves. The error due to meniscus effects is believed negligible.

The plate with perforated slots is mounted in the tank middle (see Fig. 4). The plate thickness is 5 mm which is neglected in our theoretical model. The geometric structure of the perforated plate is illustrated in Fig. 5. Due to technical limitations in the drilling of the slots, the minimum possible slot height 3 mm was used for all the screens (a)–(h). It has been controlled that the slot height is very close to constant through the screen. If that was not the case, it could cause a bias in the sloshing in the two compartments. The latter fact was observed by originally using wrongly manufactured screens. For larger solidity ratios, there is only a limited number of slots below the free surface.

Forced lateral harmonic tank motion $\eta_2=\eta_{2a}\cos(\sigma t)$ is studied. The steady-state wave elevation at the walls is recorded for different forcing frequencies in specified frequency intervals. Because the shallow-liquid sloshing is not adequately described by the linear sloshing theory except for very small excitation amplitudes, our focus in the present paper is on finite liquid depths. The frequency range is [≈0.6 Hz, ≈1.7 Hz] which includes the required resonance frequencies $\sigma_1^*/2\pi$, $\sigma_2^*/2\pi$, and $\sigma_3^*/2\pi$ [see Eq. (3)] of the corresponding clean tank for the tested liquid depths 0.4 and 0.35 m. An important consideration was to avoid tank roof impact which would lead to an extra energy dissipation (see Chap. 11 in Ref. 11). The latter fact implied that η_{2a}/l was limited to slightly higher than 0.01 in tests with the 0.4 m liquid depth.

In the experiments, the model tests started with the largest test frequency. The forcing frequency was subsequently decreased and kept fixed for a certain time interval. The reason for decreasing the forcing frequency is to detect the maximum wave elevation. The latter fact follows from the possible soft-spring type nonlinear steady-state response for a smooth two-dimensional rectangular tank with the tested finite liquid depths (see Fig. 3). Each experimental series with a fixed forcing frequency lasted, normally, for about 300 cycles. Some isolated tests were made with 400–500 cycles to confirm that the experimentally found steady-state conditions remain stable on a long-time scale. The wave elevation usually reached the experimental steady-state condition after about 80–200 cycles and then the maximum wave-elevation in the steady-state region is found. Then the forcing frequency switched to a lower value and, again, to reach the next steady-state responses. The step of frequency changes is smaller around the peak points of the response in order to have the precise value of the resonance frequencies. The wave elevation is recorded with a sampling rate of 100 Hz and measured relative to the unperturbed free surface.

IV. COMPARISON WITH EXPERIMENTS

For screens (a)–(h) in Fig. 5 and h/l=0.4, the corresponding solidity ratios are computed to be Sn=0.4725, 0.6825, 0.786 25, 0.838 75, 0.891 25, 0.913 75, 0.936 25, and 0.951 25 with N=70, 42, 29, 22, 15, 12, 9, and 7, re-

spectively. Formula (16) gives the corresponding pressure drop coefficients, $K=3.09862$, 15.2292, 41.4063, 79.8816, 191.550, 315.503, 597.750, and 1045.40. The forcing amplitudes were $\eta_{2a}/l \approx 0.001$ and 0.01.

The larger forcing amplitude $\eta_{2a}/l=0.03$ was used for the model tests with $h/l=0.35$. For this liquid depth, the solidity ratios are Sn=0.472857, 0.687 143, 0.790, 0.841 429, 0.892 857, 0.914 286, 0.935 714, and 0.952 857 with $N=62$, 37, 25, 19, 13, 10, 8, and 6, respectively. The pressure drop coefficients are then evaluated by formula (16) to be $K=3.10666$, 15.8448, 43.1960, 82.9828, 197.846, 319.727, 587.348, and 1120.55, respectively.

The tested forcing frequency range covers the lower natural sloshing frequencies σ_1^*, σ_2^* and σ_3^*. For $h/l=0.4$, the ratios between these frequencies are $\sigma_2^*/\sigma_1^*=1.524$ and $\sigma_3^*/\sigma_1^*=1.878$ with $\sigma_1^*=5.119$ (rad/s). For $h/l=0.35$, $\sigma_2^*/\sigma_1^*=1.561$, and $\sigma_3^*/\sigma_1^*=1.933$ with $\sigma_1^*=4.966$ (rad/s).

For all the experimental input parameters, the Runge–Kutta integrations by Eq. (30) showed a fast convergence in terms of the modal system dimension N_m. Four modal equations of Eq. (30), $N_m=4$, provided stabilization of four-five significant figures of the numerical steady-state wave elevations. This means that, according to the quasilinear modal theory, the global liquid motions are well described by the four lower antisymmetric sloshing modes for the considered frequency range.

A. Experiments with the lowest forcing amplitude $\eta_{2a}/l \approx 0.001$ and $h/l=0.4$

Comparison of the measured maximum steady-state wave elevations at the walls (1 cm away) and our theoretical prediction by the modal system Eq. (30) is shown in Fig. 6. The solid circles (●) denote the experimental values, but the solid lines represent the corresponding theoretical values. In the figure, these values are scaled by the forcing amplitude η_{2a}. Generally, the experimental forcing amplitudes were different (up to a 10%-change) for different forcing frequencies. This is illustrated by the narrow horizontal graphs beneath the panels (a)–(h) in Fig. 6. The calculations by our quasilinear theoretical model Eq. (30) accounted for the actual experimental values of η_{2a}.

Results by the quasilinear theory is in very good agreement with experiments in the panels (b)–(g) of Fig. 6. A flat-type experimental response for certain frequency ranges in the panels (e)–(f) may be due to the measurement error of about 1 mm. In these frequency ranges, variations of the theoretical response curves are comparable with this error.

In the panels (a)–(f), we see the two resonant peaks associated with the natural frequencies σ_1 and σ_3 (and the corresponding modes φ_1 and φ_3) which remain relatively close to σ_1^* and σ_3^*. The theoretical peak at σ_3 is always higher than the similar peak at σ_1. This is explained by the fact that the natural sloshing mode φ_3 [see its dominant component Eq. (19a)] provides a faster decay from the mean free surface to the bottom and, thereby, leads to a lower cross-flow. The lower cross-flow through the screen for $\sigma \approx \sigma_3^*$ implies a lower damping due to flow separation (or jet flow) and a larger wave amplitude response is, therefore, expected.

Figure 6(a) shows discrepancies for the smallest tested solidity ratio Sn=0.4725. First, we see a drift of the experimental peaks to the left of their theoretical expectations. Second, as we have explained above by the decreased cross-flow through the screen, the theoretical wave elevations at $\sigma \approx \sigma_3$ should be higher of those at $\sigma \approx \sigma_1$ but the experimental values do not confirm that. Because the experimental and theoretical maximum wave elevations at the resonant peaks are, at least, 25-times larger than the forcing amplitude, the discrepancies can be explained by the free-surface nonlinearity leading to a soft-spring type response outlined in Sec. II A 2. Furthermore, effect of the free-surface nonlinearity is more important at $\sigma \approx \sigma_3$ because, as we stated, the screen-caused damping is of less importance for the second primary-excited resonance.

The free-surface nonlinearity mechanism explains also the difference between the quasilinear theoretical prediction and experimental measurements in the panel (h) with Sn=0.95125 ($K=1045.45$). For this solidity ratio, the screen almost (but not completely) prevents the cross-flow between compartments Q_0^+ and Q_0^- so that the free-surface motions are similar to those in Fig. 2(c), i.e., they occur almost independently in Q_0^+ and Q_0^- alike in the two corresponding clean tanks with the liquid depth-to-width ratio $h/a=0.8$. The nonlinear soft-spring behavior of the response curves is then expected (see Sec. II A 2). However, sloshing in the panel (h) cannot be modeled as fully *independent* resonant wave motions in two compartments Q_0^+ and Q_0^- with a rigid wall between them. Assuming independent sloshing in the compartments with *zero* cross-flow at the screen implies that $\sigma_3 \approx \sigma_2^*$ and, therefore, we should expect the linear response peak at $\sigma/\sigma_2^* \approx 1.524$ and the nonlinear resonance peak should, due to the soft-spring behavior, be to the left of this value. The panel (h) does not confirm such positions of these peaks. This means that cross-flow is still not completely zero and we arrive at the situation where both the cross-flow and the free-surface nonlinearity matter.

The theoretical-and-experimental results in Fig. 2 help judging on the general trends of the steady-state resonance response curves with increasing Sn in the range $0.5 \lesssim \mathrm{Sn} \lesssim 0.95$:

- For the smaller solidity ratios Sn=0.4725, 0.6825, 0.786 25, and 0.83875, the steady-state resonance response in panels (a)–(d) shows two clear resonance peaks associated with the two lowest antisymmetric modes. The peaks remain close to $\sigma/\sigma_1^* \approx 1$ and $\sigma/\sigma_1^* \approx 1.878$, i.e., they occur in a neighborhood of the natural sloshing frequencies Eq. (3). Furthermore, the maximum nondimensional wave elevations in the considered frequency range becomes smaller with increasing Sn. This means that increasing Sn between ≈0.5 and ≈0.85 increases the global damping in the mechanical system.
- Figures 6(e) and 6(f) with Sn=0.891 25 and 0.913 75 shows that further increase of the solidity ratio leads to an increase of the global damping at $\sigma/\sigma_1^* \approx 1$, but the theoretical and experimental steady-state resonance response at the second resonance peak (associated with

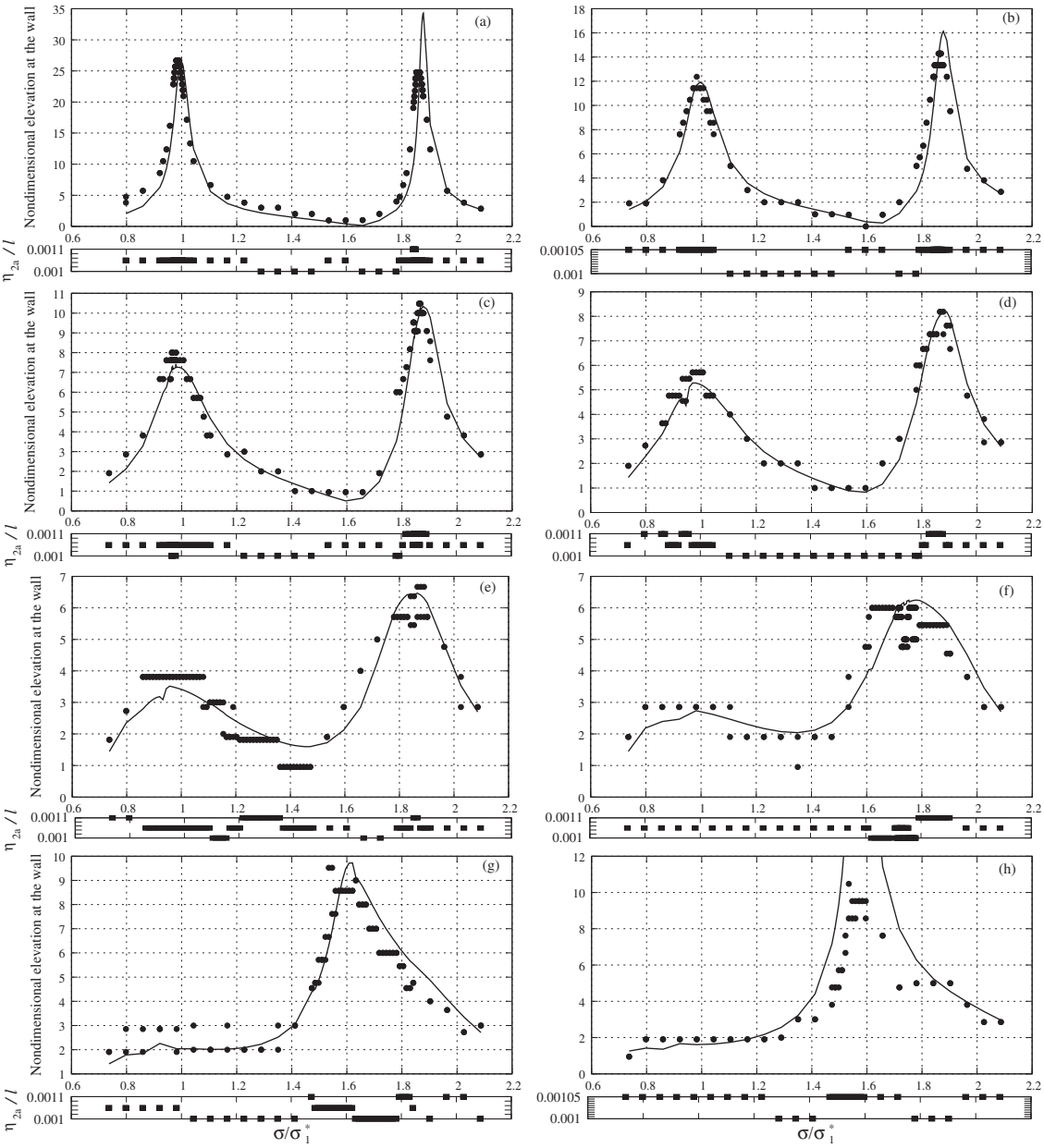

FIG. 6. The nondimensional experimental (●) and theoretical (solid line) maximum steady-state wave elevations at the vertical wall (at the two measurement probes situated 1 cm away from the wall) vs the forcing frequency; $h/l=0.4$. The wave elevations are scaled by the forcing amplitude η_{2a}, but the forcing frequency σ is scaled by the lowest natural sloshing frequency for the clean tank (3). The nondimensional forcing amplitude η_{2a}/l is about 0.001. Change of η_{2a}/l vs σ/σ_1^* for experimental series is shown. The change is accounted for in the computations by the modal Eqs. (30). (a) Sn=0.4725, $N=70$, $K=3.09862$, (b) Sn=0.6825, $N=42$, $K=15.2292$, (c) Sn=0.78625, $N=29$, $K=41.4063$, (d) Sn=0.83875, $N=22$, $K=79.8816$, (e) Sn=0.89125, $N=15$, $K=191.550$, (f) Sn=0.91375, $N=12$, $K=315.503$, (g) Sn=0.93625, $N=9$, $K=597.750$, (h) Sn=0.95125, $N=7$, $K=1045.40$.

the second antisymmetric mode) remains almost the same. Furthermore, we see a drift of this second resonance peak to the left of $\sigma/\sigma_1^* \approx 1.878$, i.e., from 1.87 to 1.75.

- Changing the solidity ratio to 0.936 25 in the panel (g) leads to vanishing of the first resonance peak, but the second resonance peak occurs at $\sigma/\sigma_1^*=1.6$. The largest tested solidity ratio 0.951 25 in the panel (h) theoretically shows a clear linear resonance at $\sigma/\sigma_1^*=1.59$. The maximum theoretical η_{2a}-scaled wave el-

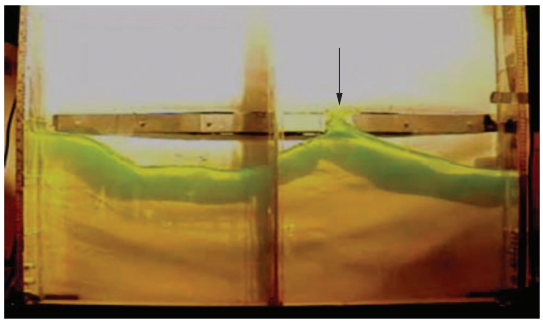

FIG. 7. (Color online) Typical wave breaking occurring for all the tested solidity ratios $\mathrm{Sn} \lesssim 0.9$ in the range of $1.25 < \sigma/\sigma_1^* < 1.78$ for the model tests with $h/l = 0.4$ and $\eta_{2a}/l \approx 0.01$. The photograph and video recording are for the screen (a) with $\mathrm{Sn} = 0.481\,25$ and the forcing frequencies $\sigma/\sigma_1^* = 1.71$ and 1.75, respectively (enhanced online). [URL: http://dx.doi.org/10.1063/1.3562310.1]

evation is computed to be about 40; it is not shown in the panel. Instead, experiments give much lower values with a local peak at $\sigma/\sigma_1^* = 1.54$ which has earlier been explained by a complex effect due to nonlinear soft-spring type behavior and non-negligible cross-flow through the screen.

B. Increasing the forcing amplitude to $\eta_{2a}/l = 0.01$ with $h/l = 0.4$

Increasing the forcing amplitude to $\eta_{2a}/l = 0.01$ leads to a set of specific free-surface phenomena documented by means of photographs and videos in Figs. 7–12 These phenomena are mainly observed in the frequency range $1.25 < \sigma/\sigma_1^* < 1.78$ and, for the screen (a) with the smallest tested solidity ratio 0.4725, in the range $0.92 \lesssim \sigma/\sigma_1^* \lesssim 1.04$. The free-surface phenomena can be classified in the following way:

- *Wave breaking* (basically of spilling type) happens for all the tested solidity ratios $\mathrm{Sn} \lesssim 0.9$ in the range of $1.25 < \sigma/\sigma_1^* < 1.78$. It is most severe for lower Sn. Figure 7 exhibits the corresponding photograph and video for the screen (a) with $\sigma/\sigma_1^* = 1.71$ and $\sigma/\sigma_1^* = 1.75$, respectively. The wave breaking occurs periodically in the left and right compartments as a consequence of collision between cross-flow going from the screen and an incoming wave in the corresponding compartment. For the screen (a) with the lowest tested solidity ratio, a local wave breaking is also observed for $\sigma/\sigma_1^* \approx 0.98$ as it is seen in Fig. 8. The latter disappears for other screens with higher solidity ratios.
- For $0.7 \lesssim \mathrm{Sn} \lesssim 0.9$, we established *three-dimensional* wave motions in the frequency range $1.66 \lesssim \sigma/\sigma_1^* \lesssim 1.73$. Figure 9 displays the corresponding video for the screen (b) with $\mathrm{Sn} = 0.6825$ and $\sigma/\sigma_1^* = 1.72$. These three-dimensional waves are accompanied by a local wave breaking. We were not able to identify what kind of cross-wave resonance causes the observed three-

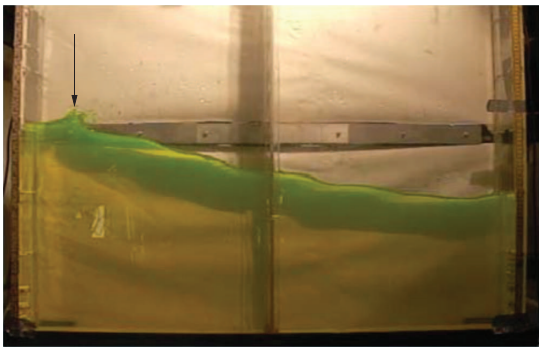

FIG. 8. (Color online) Local wave breaking occurring for the screen (a) with $\sigma/\sigma_1^* \approx 0.98$, $h/l = 0.4$, and $\eta_{2a}/l = 0.01$.

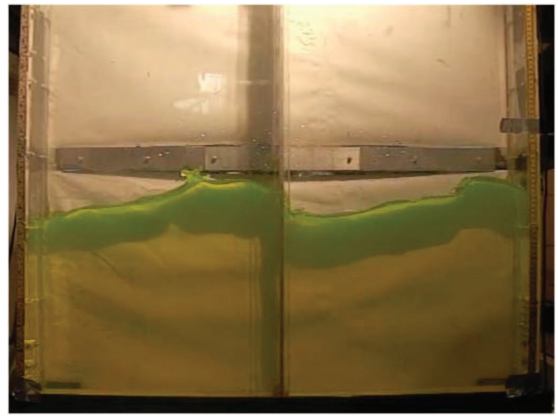

FIG. 9. (Color online) A typical three-dimensional perturbations of the free surface occurring for $0.7 \lesssim \mathrm{Sn} \lesssim 0.9$ and $1.66 \lesssim \sigma/\sigma_1^* \lesssim 1.73$; $h/l = 0.4$, $\eta_{2a}/l \approx 0.01$. The video is for the screen (b) with $\mathrm{Sn} = 0.6825$ and $\sigma/\sigma_1^* = 1.72$ (enhanced online).[URL: http://dx.doi.org/10.1063/1.3562310.2]

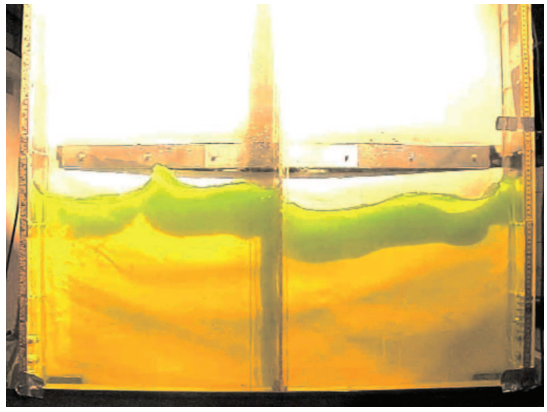

FIG. 10. (Color online) Video recording of a steep wave with the double superharmonics elevations at the walls (enhanced online).[URL: http://dx.doi.org/10.1063/1.3562310.3]

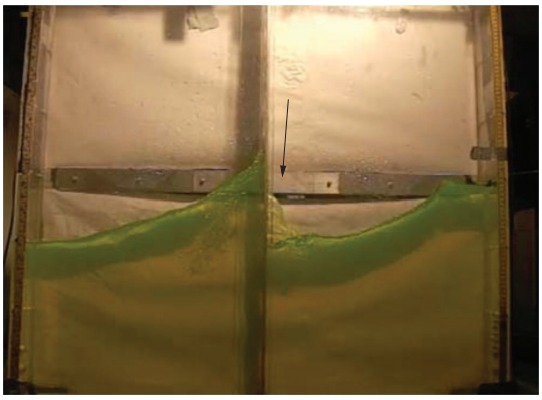

FIG. 11. (Color online) Photo of the liquid jet through the screen for Sn $=0.891\ 25$ and $\sigma/\sigma_1^*=1.48$.

dimensional waves. A dedicated study in the manner of Faltinsen *et al.* is needed.[21]

- The video in Fig. 10 illustrates the second Fourier harmonics for the nearly wall wave elevations established in our visual observations for the screens (b)–(d). In addition, these cases are characterized by steep wave patterns. The latter fact indicates an amplification of higher sloshing modes. Mechanism of this amplification in sloshing problems consists of the secondary resonance yielding the energy content from a primary-excited mode to higher modes via the free-surface nonlinearity (see Chap. 8 in Ref. 11).
- Liquid jets through the screen openings over the free surface with subsequent fallout on the opposite free surface happened for the screens (e)–(h) in a frequency range about $\sigma/\sigma_1^*=1.524$. Figure 11 shows the jet for the screen (c) and $\sigma/\sigma_1^*=1.48$.
- Runup with a detachment of a liquid portion along the screen happened for the solidity ratios $0.9\lesssim$ Sn. Figure 12 shows the corresponding photograph and video.

Even though the aforementioned surface phenomena indicate importance of the free-surface nonlinearity, we used the quasilinear modal theory to describe the steady-state wave elevations at the walls. The results are compared with experimental values in Figs. 13 and 14.

Figures 6(a)–6(d) and 13 demonstrate that increasing the forcing amplitude leads to the experimental response curves which cannot be fully quantified by the quasilinear theory. The reasons are (i) additional resonance peaks about the vertical dashed lines; (ii) a nonlinear soft-spring type behavior in a frequency range covering the natural sloshing frequency σ_3.

When considering Fig. 13(a) with the lowest tested Sn $=0.4725$ and comparing it with Fig. 6(a), a much clearer soft-spring behavior of the experimental amplitude response occurs at $\sigma\approx\sigma_3^*$. The experimental resonance peak at the first natural frequency, $\sigma\approx\sigma_1^*$, remains in these figures of a linear character. Recalling that the aforementioned lower cross-flow through the screen by the natural mode φ_3 (associated with exponential decay to the bottom) leads to a lower screen-caused damping clarifies a stronger effect of the free-surface nonlinearity which should yield for the tested liquid depth the soft-spring type response curve. Our quasilinear theory cannot capture this response as well as it cannot describe amplification of higher harmonics. However, it remains applicable for prediction of the first Fourier harmonics contribution in a local neighborhood of $\sigma\approx\sigma_1^*$ in Figs. 13 and 14. The vanishing of the first resonance peak with increasing *Sn* is reasonably well predicted. This occurs for Sn$=0.786\ 25$ [screen (c)] while the lower forcing amplitude detected this vanishing only for Sn$=0.936\ 25$ [screen (g)].

Figures 13 and 14 show that the quasilinear theory is, generally, not applicable in the frequency range $1.1\lesssim\sigma/\sigma_1^*\lesssim1.9$ for quantification of the steady-state amplitude response. It describes only a general trend of the maximum resonance peak position versus Sn. In the middle of this frequency range, $1.3\lesssim\sigma/\sigma_1^*\lesssim1.78$, experimental observations establish the aforementioned specific free-surface phenomena which are of a clear nonlinear nature. Being invalid in modeling the free-surface nonlinearity, the quasilinear theory shows in Fig. 14 a linear-type amplitude response about σ_3 (note that this natural sloshing frequency decreases from σ_3^* to σ_2^* as Sn tends to 1) while the experimental measurements show a soft-spring type response curves at the same frequency. For smaller forcing amplitude in Fig. 6, this kind of discrepancies was detected only for the maximum tested solidity ratio Sn$=0.951\ 25$.

Remembering the video in Fig. 10 detecting the double Fourier harmonics, we present in Figs. 13 and 14 the η_{2a}-scaled contributions of the first ($\triangle$) and second ($\triangledown$) Fourier harmonics components of the $2\pi/\sigma$-periodic measured steady-state signal. The sum of the first and second harmonics contributions in the figures gives approximately the actual wave elevation for almost all the experimental data and, therefore, relates appearance of the additional peaks to amplification of second harmonic response. Since the $(\cdot|\cdot|)$-nonlinearity can only yield odd harmonic terms, the existence of the second Fourier harmonics cannot be explained within the framework of the quasilinear theory. To explain amplification of the second Fourier harmonics, we

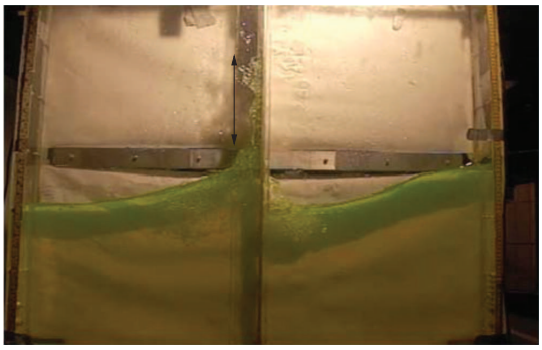

FIG. 12. (Color online) The photograph and video recording of the runup at the screen occurring for $0.9\lesssim$ Sn (enhanced online).[URL: http://dx.doi.org/10.1063/1.3562310.4]

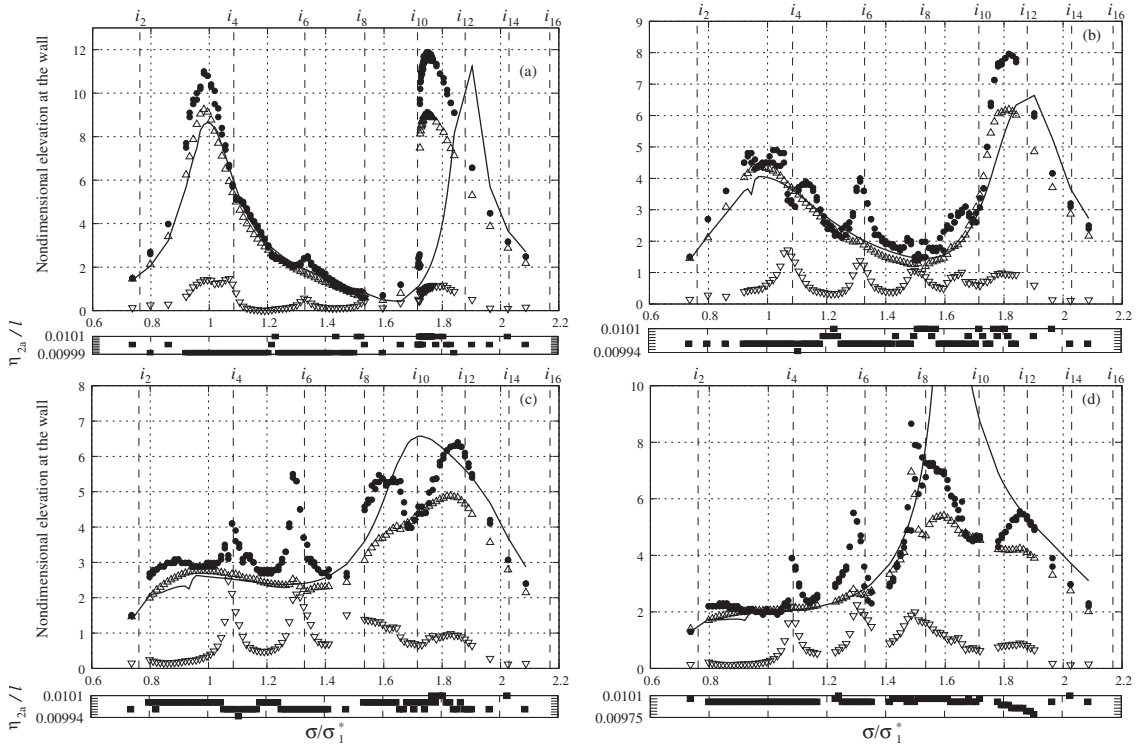

FIG. 13. The same as for the panels (a)–(d) in Fig. 6, but for the larger forcing amplitude $\eta_{2a}/l \approx 0.01$. Contribution of the first Fourier harmonics to the measured wave elevations (scaled by η_{2a}) is denoted by △, but ▽ denotes contribution of the second Fourier harmonics. The values $\sigma/\sigma_1^* = i_{2k}, k \geq 1$ [see Eq. (34) and the corresponding vertical dashed lines] indicate the frequencies where the secondary resonance due to the second-order free-surface nonlinearity is expected.

should implement the adaptive multimodal analysis elaborated by Faltinsen and Timokha.[5] According to this analysis, the second Fourier harmonics in the steady-state sloshing solution can only be resonantly excited due to the second-order free-surface nonlinearity when the forcing frequency is close to the one-half of the corresponding natural frequency of a symmetric mode, i.e., $2\sigma \approx \sigma_{2k}, k \geq 1$. The latter condition leads to

$$\frac{\sigma}{\sigma_1^*} \approx \frac{\sigma_{2k}^*}{2\sigma_1^*} = i_{2k}. \tag{34}$$

Figure 13 shows that the values $\sigma/\sigma_1^* = i_{2k}$, $k=1$, 2, 3, 4, and 5 well predict the frequencies of the resonance peaks associated with the second Fourier harmonics amplification.

C. Experiments with $\eta_{2a}/l=0.03$ and $h/l=0.35$

Increasing the forcing amplitude makes the previously described above free-surface phenomena much more severe. Along with very strong wave breaking and runup, we observed overturning waves and formation of gas pockets. A representative video is given in Fig. 15. Formation of gas pockets is demonstrated by the video in Fig. 16.

Even though strongly nonlinear free-surface phenomena are observed for the larger forcing amplitude $\eta_{2a}/l=0.03$ in our experimental model tests done with $h/l=0.35$, we attempted to compare our quasi-linear prediction and the corresponding experimental measurements of the steady-state maximum wave elevations at the walls. Results are reported in Figs. 17–19.

The measured signal was not exactly steady-state for several of the tested forcing frequencies. For the early-reported experimental results, standard deviations of the maximum wave elevation in the experimental steady-state condition were comparable with 1 mm, i.e., with the measurement error, but the experimental data for $\eta_{2a}/l=0.03$ with $h/l=0.35$ demonstrated standard deviations comparable with the forcing amplitude. The η_{2a}-scaled standard deviations of the measured signal are presented in Figs. 17–19 to identify the frequency ranges where they may matter. As it follows from the previous analysis for lower forcing amplitudes, the largest standard deviations are detected for σ between σ_2^* and σ_3^* where the free-surface nonlinearity is especially important. Just about these values of the forcing frequency, we observed most severe wave breaking. Furthermore, the change of the forcing amplitude for different forcing frequencies has been negligible for this experimental series, less than 1%, thus, we neglected it in our quasilinear modeling assuming $\eta_{2a}/l=0.03$.

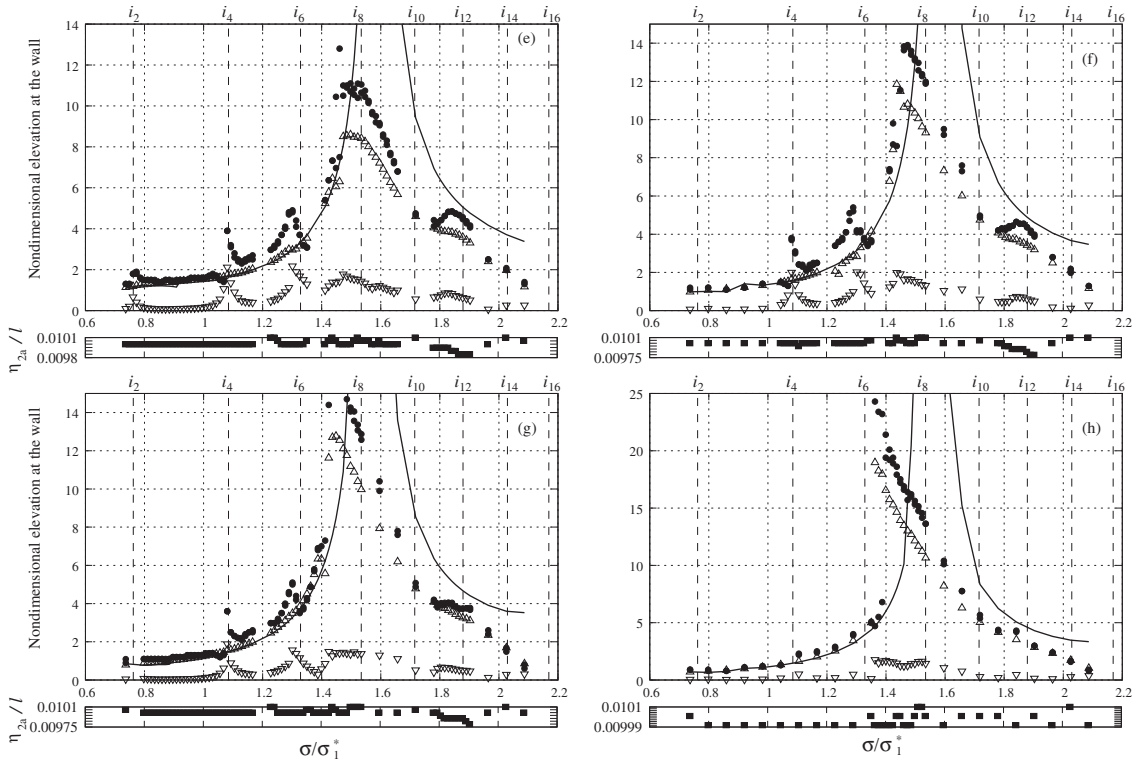

FIG. 14. The same as for the panels (e)–(h) in Fig. 6, but for the larger forcing amplitude $\eta_{2a}/l \approx 0.01$. Contribution of the first Fourier harmonics to the measured wave elevations (scaled by η_{2a}) is denoted by $\triangle$, but $\triangledown$ denotes contribution of the second Fourier harmonics. The values $\sigma/\sigma_1^* = i_{2k}, k \geq 1$ [see Eq. (34) and the corresponding vertical dashed lines] indicate the frequencies where the secondary resonance due to the second-order free-surface nonlinearity is expected.

We start our analysis with results in Fig. 17 which represents the case of the lower tested solidity ratios associated with the screens (a) and (b). The figure shows that the quasilinear theory does not satisfactorily quantify the free-surface elevations with increasing η_{2a}, but shows a correct trend in how resonance frequencies change. Furthermore, the case $\eta_{2a}/l = 0.03$ brings, from experimental point of view, several new physical phenomena. First of all, we note a

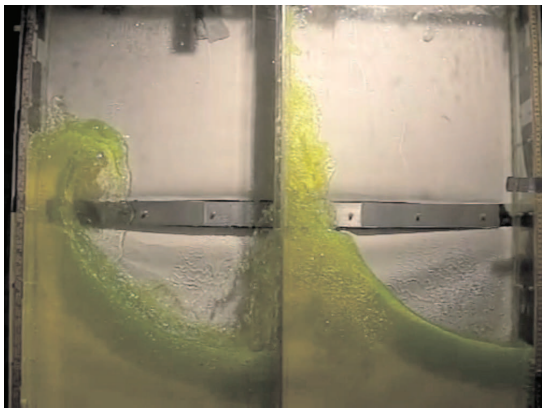

FIG. 15. (Color online) Representative video of the free-surface phenomena in experimental series with $\eta_{2a}/l = 0.03$ and $h/l = 0.35$. The video illustrates free-surface phenomena occurring for $\sigma/\sigma_1 = 1.328$ and Sn=0.914 286 (enhanced online).[URL: http://dx.doi.org/10.1063/1.3562310.5]

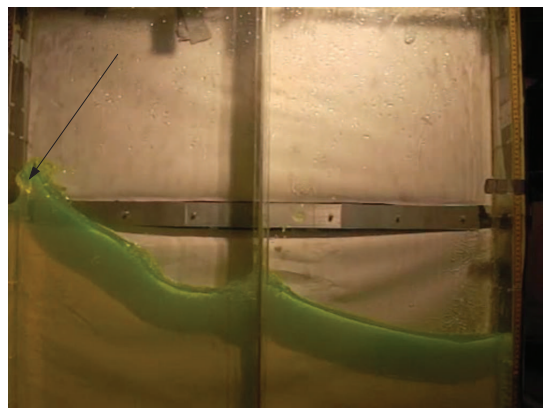

FIG. 16. (Color online) Formation of a gas pocket at the vertical walls occurring for $\eta_{2a}/l = 0.03$ and $h/l = 0.35$. The photograph and video is given for $\sigma/\sigma_1 = 0.96$ and Sn=0.472 857 (enhanced online).[URL: http://dx.doi.org/10.1063/1.3562310.6]

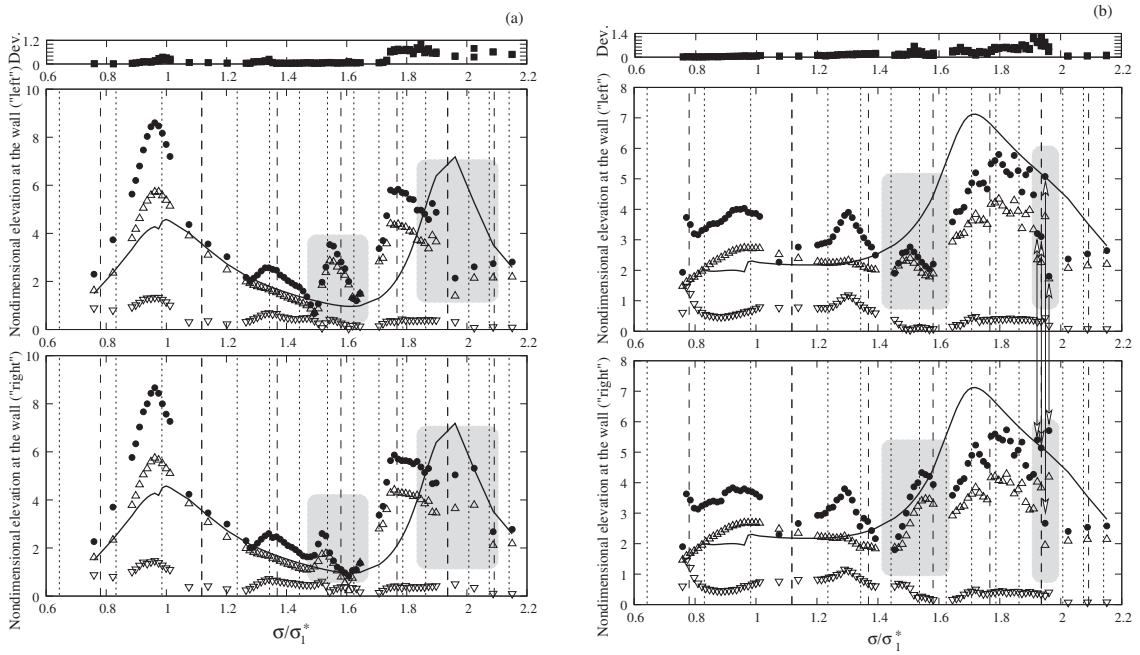

FIG. 17. The nondimensional experimental (●) and theoretical (solid line) maximum steady-state wave elevations at the "left" and "right" measurement probes (1 cm away from the wall) vs the forcing frequency; $h/l=0.35$ and $\eta_{2a}/l=0.03$. The wave elevations are scaled by the forcing amplitude η_{2a}, but the forcing frequency σ is scaled by the lowest natural sloshing frequency σ_1^* for the clean tank (3). "Dev." denotes the η_{2a}-scaled standard deviations of the measured maximum wave elevations in the experimental steady-state conditions. Contribution of the first Fourier harmonics to the measured wave elevations (scaled by η_{2a}) is denoted by △, but ▽ denotes the η_{2a}-scaled contribution of the second Fourier harmonics. The dashed lines indicate the frequencies where the secondary resonance due to the second-order free-surface nonlinearity is expected by Eq. (34). The dotted lines show the frequencies where the secondary resonance due to the third-order free-surface nonlinearity is expected by Eq. (35). The shadow zones (with arrows) indicate two different experimental steady-state solutions occurring in Q_0^+ and Q_0^-. (a) Sn=0.472 857, $N=62, K=3.106\,66$, (b) Sn=0.687143, $N=37$, $K=15.8448$.

multibranching of the experimental response curves which appears as different experimentally detected steady-state wave elevations at the opposite measurement probes (henceforth, "left" and "right" probes). We mark this by shadow zones in Fig. 17. A hysteresis with the corresponding soft-spring type multibranching (see Fig. 3) is possible in the two limit cases, Sn=1 and 0. This hysteresis can, therefore, be expected in the left of $\sigma/\sigma_1^*=1$, 1.524, and 1.878. According to Faltinsen and Timokha,[12] a central slat-type screen with the tested solidity ratios in Fig. 17 can slightly shift this hysteresis to the left of aforementioned frequencies, but it cannot move it in the right direction along the horizontal axis. The multibranching phenomenon in the shadow zone occurs in other frequency ranges and, therefore, it cannot be related to the nonlinear sloshing phenomena known for clean rectangular tanks.

Furthermore, similar to the cases with $\eta_{2a}/l=0.01$ and $h/l=0.4$, we see many additional experimental resonance peaks. Earlier, these peaks were well clarified by the secondary resonance with amplification of the second Fourier harmonics. However, Fig. 17 shows that it is not the case for the larger forcing amplitude. A reason is that the position of the additional peaks is not clearly at $\sigma/\sigma_1^*\approx i_{2k}$ and the actual wave elevations cannot, generally, be approximated by the sum of the first and second harmonics contributions. Because increasing forcing amplitude may lead to the secondary resonance by the third-order nonlinearity, we estimated the frequencies where this kind of the secondary resonance occurs. The corresponding condition $3\sigma\approx\sigma_{2k+1}$ gives

$$\frac{\sigma}{\sigma_1^*}\approx\frac{\sigma_{2k+1}}{3\sigma_1^*}=i_{2k+1},\quad k=1,2,\ldots. \tag{35}$$

The values of i_{2k+1} are marked by the vertical dotted lines in Fig. 17. Summarizing the dotted and dashed lines gives a 'net' of possible secondary resonances (due to the second- and third-order free-surface nonlinearities) in the studied frequency range. A dedicated study is required to quantify the reason for the experimentally detected multibranching and additional resonance peaks.

Figure 18 demonstrates the theoretical and experimental results for the screens (c)–(f) with larger solidity ratios. The quasilinear theory shows a clear linear resonance at $\sigma/\sigma_1^*=1.6$, but the experiments indicate a more complicated response. The multiple-peak response structure continuously disappears from the panels (c)–(f) with increasing the solidity ratio so that the experimental case (f) shows a clear soft-spring type behavior at the primary resonance $\sigma/\sigma_1^*=1.6$ with an extra jump at $\sigma/\sigma_1^*\approx i_4$. Similar response curves were detected by the adaptive modal sloshing theory for a

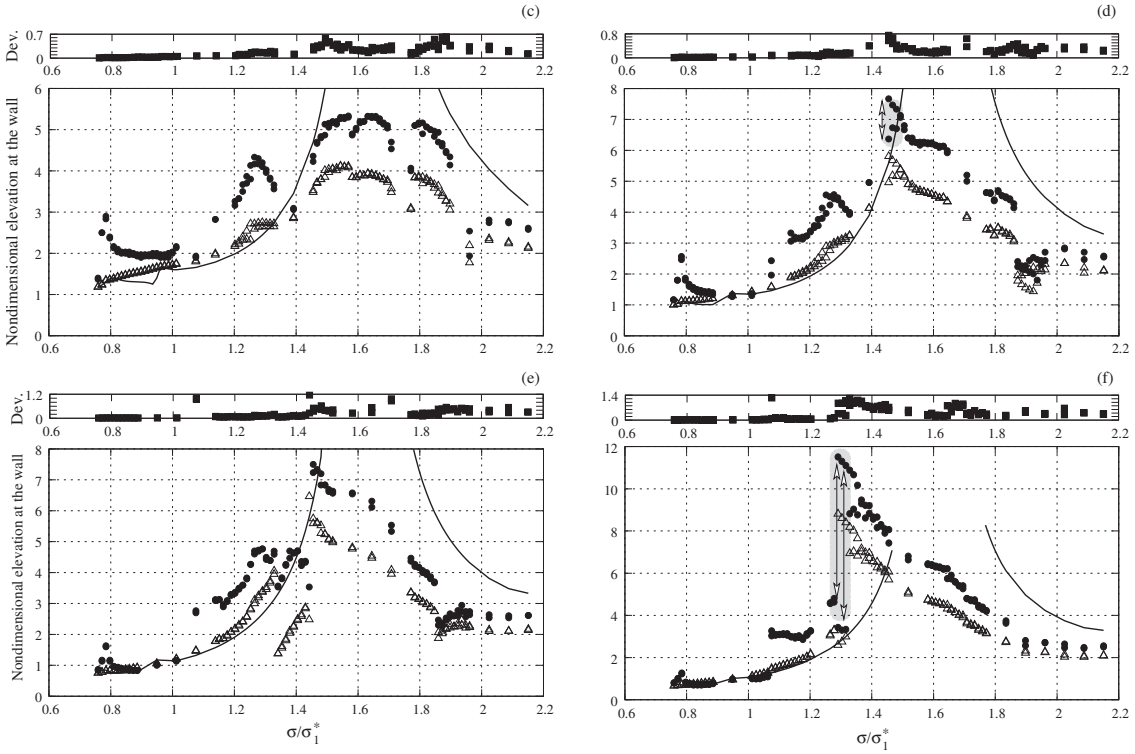

FIG. 18. The nondimensional experimental (●) and theoretical (solid line) maximum steady-state wave elevations at the 'left' and 'right' measurement probes (1 cm away from the wall) vs the forcing frequency; $h/l=0.35$ and $\eta_{2a}/l=0.03$. The wave elevations are scaled by the forcing amplitude η_{2a}, but the forcing frequency σ is scaled by the lowest natural sloshing frequency σ_1^* for the clean tank (3). Dev. denotes the η_{2a}-scaled standard deviations of the measured maximum wave elevations in the experimental steady-state conditions. The η_{2a}-scaled contribution of the first Fourier harmonics to the measured wave elevations is denoted by △. The shadow zones (with arrows) indicate different experimental steady-state elevations for opposite sides of the tank (for different measurement probes). (c) Sn=0.790, $N=25$, $K=43.1960$; (d) Sn=0.841 429, $N=19$, $K=82.9828$; (e) Sn=0.892 857, $N=13$, $K=197.846$; (f) Sn=0.914 286, $N=10$, $K=319.727$.

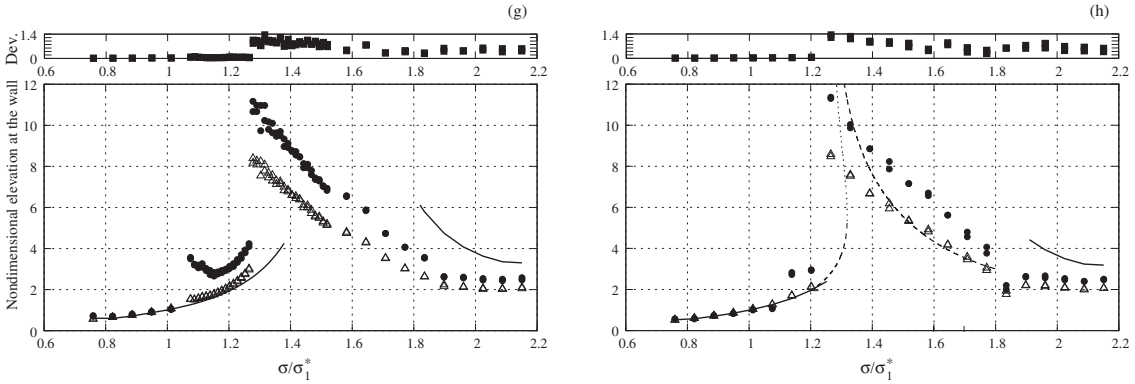

FIG. 19. The nondimensional experimental (●) and theoretical (solid line) maximum steady-state wave elevations at the measurement probes (1 cm away from the wall) vs the forcing frequency; $h/l=0.35$, $\eta_{2a}/l=0.03$. The wave elevations are scaled by the forcing amplitude η_{2a}, but the forcing frequency σ is scaled by the lowest natural sloshing frequency σ_1^* for the clean tank (3). Dev. denotes the η_{2a}-scaled standard deviations of the measured maximum wave elevations in the experimental steady-state conditions. The η_{2a}-scaled contribution of the first Fourier harmonics to the measured wave elevations is denoted by △. (g) Sn=0.935 714, $N=8$, $K=587.348$; (h) Sn=0.952 857, $N=6$, $K=1120.55$. The dashed line in (h) shows the first harmonics contribution by the single-dominant modal theory (Chap. 8 in Ref. 11) for Sn=1 (solid screen).

clean rectangular tank (see Sec. II). The trend continues in Fig. 19. This figure shows that the liquid sloshing dynamics becomes closer to that in the two compartments, Q_0^+ and Q_0^-, with a solid wall between them. One should remark that, starting with the case (f), the Runge–Kutta integration by the quasilinear modal theory becomes unstable in a neighborhood of the theoretical linear resonance $\sigma/\sigma_1^* \approx 1.6$.

V. CONCLUSIONS

Studies of resonant sloshing in a rectangular tank with screens are typically restricted to the screen solidity ratios $\mathrm{Sn} \lesssim 0.5$, the forcing frequencies close to the lowest natural frequency σ_1^* of the corresponding clean tank, and relatively small forcing amplitudes. For these input parameters, one can assume that the global liquid motions are close to those in the corresponding clean tank, and that the screen-induced flow separation (or a jet flow) plays the same role as a quadratic damping for linear oscillators (see a review on quadratic damping for linear oscillators in Ref. 15). Higher solidity ratios, $0.5 \lesssim \mathrm{Sn} \lesssim 0.95$, a limited number of the screen openings, $N \lesssim 50$, a wider range of the forcing frequencies, and increasing forcing amplitudes that are relevant for ship tanks with swash (perforated) bulkheads are studied in the present paper experimentally and theoretically.

New experimental model tests were performed for finite liquid depths, three forcing amplitudes $\eta_{2a}/l=0.001$, 0.01, and 0.03, and eight different slat-type screens installed at the middle of a rectangular tank. The primary emphasis has been placed on the two-dimensional steady-state sloshing and the corresponding experimental wave elevation at the opposite tank walls (1 cm away from the wall). The forcing frequency interval covered the three lowest natural frequencies of the clean rectangular tank, σ_1^*, σ_2^*, and σ_3^*. In our measurements of the steady-state maximum elevations, a larger number of tests with small changes of the forcing frequency σ was performed in local ranges where the experiments detected a local (resonance) peak.

In our theoretical analysis, we assumed the global flow to be described by an inviscid incompressible liquid model with irrotational flow. The screen-induced flow separation (or jet flow) effect on the global flow was modeled by a pressure drop condition. The formula for the empirical pressure drop coefficient was taken from the literature. This condition should be true not only for a porous media, but also, e.g., for orifice meter device with a single hole. The letter fact is important for higher solidity ratios of the experimental screens leading to a limit number of slots below the free surface. It is a matter of comparison with model test of, for instance, wave elevation that the empirical pressure drop condition makes sense. Our results for small excitation amplitude documented this fact. The multimodal method with linearized free-surface conditions was employed, i.e., we included into our theoretical model the screen-induced effect on the global flow, but neglected the free-surface nonlinearity.

Comparing the experimental and theoretical results for the three tested forcing amplitudes made it possible to estimate the effect of the free-surface nonlinearity. It is almost negligible for the lowest forcing amplitude $\eta_{2a}/l=0.001$ with $0.5 \lesssim \mathrm{Sn} \lesssim 0.95$. Noticeable discrepancies between theory and experiments due to the free-surface nonlinearity are only established for the limit tested values, $\mathrm{Sn}=0.4725$ and 0.951 25. An important conclusion for this forcing amplitude is that the larger amplitude response is found not at the primary resonance of the corresponding clean tank, σ_1^*, but rather at the natural frequency responsible for the second antisymmetric mode. According to Ref. 12, the natural sloshing frequency σ_3 for the screen-equipped rectangular tank monotonically decreases from σ_3^* to σ_2^* as Sn increases from 0.5 to 1. The reason is that the resonant excitations with σ away from σ_1^* cause a lower cross-flow through the screen. It is therefore understandable, that we should expect most severe nonlinear sloshing effects around σ_3 when η_{2a}/l increases. Experimental measurements and visual observations confirm this fact. Wave breaking, runups, transition to three-dimensional motions, and other specific free-surface phenomena were found just in a frequency range around σ_3. Photographs and videos are presented to illustrate them.

Analyzing the results for $\eta_{2a}/l=0.01$ made it possible to understand that the free-surface nonlinearity causes sufficient energy content to symmetric modes due to the secondary resonance. This is a novelty for the screen-equipped tanks relative to the corresponding clean tanks for which amplification of higher modes due to the secondary resonance requires, normally, larger forcing amplitude. A possible reason is that the symmetric modes do not lead to a cross-flow through the screen and, therefore, are almost undamped, in contrast to the antisymmetric ones. This implies that the same-order forcing of symmetric and antisymmetric modes should give a larger response of the symmetric modes. In order to describe the associated nonlinear sloshing, we should, in the future, employ the *adaptive nonlinear* multimodal method.[5,22]

Multibranch experimental response curves are detected for $\eta_{2a}/l=0.03$ in certain frequency ranges in a neighborhood of σ_2^* and σ_3^* where we cannot expect the soft-spring type behavior associated with nonlinear sloshing in a clean rectangular tank. Our quasilinear theory is not able to explain it. An explanation may come from analyzing possible secondary resonances due to the second- and third-order free-surface nonlinearities. Indeed, a few possibilities for the secondary resonance are detected at σ_1^* and, as a consequence, the quasilinear theory qualitatively well describes the main harmonics contribution of the actual wave elevations when $\sigma \approx \sigma_1^*$. However, there exist numerous possibilities for the secondary resonance in a frequency range covering σ_2^* and σ_3^* where the experiments detect the most severe free-surface phenomena and the multibranching occurs.

APPENDIX A: RELATIONS IN EQS. (25) AND (26)

Remembering that the natural sloshing modes φ_i satisfy the Laplace equation and the zero-Neumann condition on the wetted tank surface, inserting Eq. (24) into the time-independent relations Eqs. (5a)–(5c) gives

$$\nabla^2 p_2 = 0 \quad \text{in} \quad Q_0^{\pm}, \quad \frac{\partial p_2}{\partial n} = 0 \quad \text{on} \quad S_{0b}^{\pm} \cup S_{0w}^{\pm} \tag{A1}$$

for integrand p_2 in the modified velocity potential Eq. (24).

Inserting the modal solutions Eqs. (7) and (24) into the kinematic boundary condition Eq. (5d) and remembering that

$$\frac{\partial \varphi_i}{\partial z}(y,0) = \kappa_i \varphi_i(y,0) = \kappa_i f_i(y) \tag{A2}$$

due to the corresponding boundary condition on $\Sigma_0^{\pm}$ in the spectral problem Eq. (9) leads to the relation

$$\frac{1}{\rho}\int_{t_0}^{t} \frac{\partial p_2}{\partial z}(y,0,t_1)\mathrm{d}t_1 = 0 \tag{A3}$$

to be fulfilled for any instant t. The latter means that the integrand $\left(\frac{\partial p_2}{\partial z}\right)(y,0,t)$ should be zero, and we arrive at the zero-Neumann boundary condition Eq. (25a) which is further used in the boundary value problem Eq. (26).

Finally, inserting the modal solution Eqs. (7) and (24) into the dynamic boundary condition Eq. (5e) with relation Eq. (A2) gives the boundary condition Eq. (25b).

[1] J. Love and M. Tait, "Nonlinear simulation of a tuned liquid damper with damping screens using a modal expansion technique," J. Fluids Struct. **26**, 1058 (2010).
[2] S. Kaneko and M. Ishikawa, "Modelling of tuned liquid damper with submerged nets," ASME J. Pressure Vessel Technol. **121**, 334 (1999).
[3] M. Tait, A. El Damatty, N. Isyumov, and M. Siddique, "Numerical flow models to simulate tuned liquid dampers (TLD) with slat screens," J. Fluids Struct. **20**, 1007 (2005).
[4] P. Warnitchai and T. Pinkaew, "Modelling of liquid sloshing in rectangular tanks with flow-dampening devices," Eng. Struct. **20**, 593 (1998).
[5] O. M. Faltinsen and A. N. Timokha, "Adaptive multimodal approach to nonlinear sloshing in a rectangular tank," J. Fluid Mech. **432**, 167 (2001).
[6] R. D. Blevins, *Applied Fluid Dynamics* (Krieger Publishing Company, Malabar, FL, 1992).
[7] E. M. Laws and J. L. Livesey, "Flow through screens," Annu. Rev. Fluid Mech. **10**, 247 (1978).
[8] B. Molin, "On the added mass and damping of periodic arrays of fully or partially porous disks," J. Fluids Struct. **15**, 275 (2001).
[9] O. M. Faltinsen, R. Firoozkoohi, and A. N. Timokha, "Analytical modeling of liquid sloshing in a two-dimensional rectangular tank with a slat screen," J. Eng. Math. (in press).
[10] H. N. Abramson, "The dynamic behavior of liquids in a moving container," Technical Report SP-106, NASA, Washington, D.C., 1966.
[11] O. M. Faltinsen and A. N. Timokha, *Sloshing* (Cambridge University Press, Cambridge, 2009).
[12] O. M. Faltinsen and A. N. Timokha, "Natural sloshing frequencies and modes in a rectangular tank with a slat-type screen," J. Sound Vib. **330**, 1490 (2011).
[13] R. Porter and D. Evans, "Complementary approximations to wave scattering by vertical barriers," J. Fluid Mech. **294**, 155 (1995).
[14] D. Evans and P. McIver, "Resonant frequencies in a container with vertical baffles," J. Fluid Mech. **175**, 295 (1987).
[15] L. Cveticanin, "Oscillator with strong quadratic damping force," Publications de l'Institut Mathèmatique **85**, 119 (2009).
[16] M. Eastham, "An eigenvalue problem with parameter in the boundary condition," Q. J. Math. **13**, 304 (1962).
[17] S. F. Feschenko, I. A. Lukovsky, B. I. Rabinovich, and L. V. Dokuchaev, *Methods for Determining Added Fluid Mass in Mobile Cavities* (Naukova Dumka, Kiev, 1969) (in Russian).
[18] J. Morand and R. Ohayon, *Fluid structure interaction. Applied numerical methods* (Wiley, New York, 1995).
[19] W. D. Baines and E. G. Peterson, "An investigation of flow through screens," Trans. ASME **73**, 467 (1951).
[20] J. Weisbach, *Die Experimental-Hydraulik* (Engelehardt, Freiburg, 1855).
[21] O. Faltinsen, O. Rognebakke, and A. Timokha, "Resonant three-dimensional nonlinear sloshing in a square base basin," J. Fluid Mech. **487**, 1 (2003).
[22] O. Faltinsen, O. Rognebakke, and A. Timokha, "Transient and steady-state amplitudes of resonant three-dimensional sloshing in a square base tank with a finite fluid depth," Phys. Fluids **18**, 012103 (2006).

4. Faltinsen, O. M., Firoozkoohi, R., & Timokha, A. N. (2011). Effect of central slotted screen with a high solidity ratio on the secondary resonance phenomenon for liquid sloshing in a rectangular tank. Physics of Fluids , 23 (6), 13.

AIP | Physics of Fluids

Effect of central slotted screen with a high solidity ratio on the secondary resonance phenomenon for liquid sloshing in a rectangular tank

O. M. Faltinsen, R. Firoozkoohi, and A. N. Timokha

Citation: Phys. Fluids **23**, 062106 (2011); doi: 10.1063/1.3602508
View online: http://dx.doi.org/10.1063/1.3602508
View Table of Contents: http://pof.aip.org/resource/1/PHFLE6/v23/i6
Published by the American Institute of Physics.

Effect of central slotted screen with a high solidity ratio on the secondary resonance phenomenon for liquid sloshing in a rectangular tank

O. M. Faltinsen,[a] R. Firoozkoohi, and A. N. Timokha
Centre for Ships and Ocean Structures and Department of Marine Technology, Norwegian University of Science and Technology, NO-7091, Trondheim, Norway

(Received 20 March 2011; accepted 3 June 2011; published online 28 June 2011)

Mounting a screen with a high solidity ratio ($0.5 \lesssim Sn < 1$) at the center of a rectangular tank qualitatively changes the secondary resonance phenomenon for liquid sloshing. In contrast to the clean tank, the steady-state sloshing due to lateral excitation is then characterized by multi-peak response curves in a neighborhood of the primary resonance frequency. The present paper revises the adaptive nonlinear multimodal method to study the secondary resonance phenomenon for the screen-affected resonant sloshing with a finite liquid depth and, thereby, clarify earlier experimental results of the authors. © *2011 American Institute of Physics*. [doi:10.1063/1.3602508]

I. INTRODUCTION

Faltinsen *et al.*[1] studied experimentally and theoretically the steady-state resonant liquid sloshing in a rectangular tank with a slat-type screen installed at the tank middle. Their application in mind was sloshing in ship tanks with swash bulkheads. It has been extensively discussed in the introduction of Ref. 1, that, in contrast to the so-called Tuned Liquid Dampers (TLDs), the swash bulkheads are characterized by a relatively large solidity ratio *Sn* (the solidity ratio is the ratio of the area of the shadow projected by the screen on a plane parallel to the screen to the total area contained within the frame of the screen). A consequence of the higher solidity ratio of a central slotted (slat-type) screen in a rectangular tank is that the *antisymmetric natural sloshing modes and frequencies* change relative to those for a clean (without screen) rectangular tank. These changes were quantified by Faltinsen and Timokha[2] versus *Sn*, the number of the screen openings (slots) *N*, and the position of these openings.

In experiments by Faltinsen *et al.*,[1] the tank was forced horizontally with the forcing frequency σ in a frequency range covering the three lowest natural sloshing frequencies of the screen-equipped tank (henceforth, σ_i^* are the natural sloshing frequencies in the clean static tank, but σ_i are the natural sloshing frequencies in the screen-equipped tank and, according to Ref. 2, $\sigma_1 < \sigma_1^* < \sigma_2 = \sigma_2^* < \sigma_3 < \sigma_3^* < \sigma_4 = \sigma_4^* < \cdots$). It was ensured that no roof impact occurred. The focus was on the liquid depth-to-tank width ratio $h/l = 0.4$ and the two forcing amplitudes $\eta_{2a}/l = 0.001$ and 0.01 (l is the tank width). Eight different screens with solidity ratios from 0.47 to 0.95 were tested. Experimental measurements of the steady-state wave elevation at the tank walls and the corresponding video observations were documented. The theoretical analysis was based on the *linear multimodal method* assuming an incompressible liquid with irrotational flow everywhere except in a local neighborhood of the screen. An "integral" viscous effect of the nearly screen flow separation on the globally inviscid liquid was governed by a pressure drop condition.[3] The latter condition yielded the $(\cdot|\cdot|)$-nonlinear damping terms in the linear modal equations and, thereby, transformed the linear modal theory to a *quasi-linear* form. When the experimental forcing amplitude was sufficiently small, $\eta_{2a}/l = 0.001$, this quasi-linear theory agreed well with the experimental response curves of the maximum steady-state wave elevations. When $\eta_{2a}/l = 0.01$, the latter modal theory gave only a general trend in how the experimental response changed versus *Sn*. Failure of the quasi-linear theory could, in part, be related to specific free-surface phenomena appearing as

(i) breaking waves,
(ii) nearly wall (screen) run-up, and
(iii) cross-flow through screen's openings from water to air with jet flow impacting on the underlying free surface.

These phenomena were illustrated by photos and videos and extensively discussed. The majority of them were established for $\sigma > \sigma_2^*$, i.e., away from the (screen-modified) lowest natural sloshing frequency $\sigma_1 < \sigma_1^*$. When σ was close to the lowest natural sloshing frequency, the aforementioned free-surface phenomena were not strong.

Another important difference between the quasi-linear predictions and experiments in Ref. 1 appears as extra peaks on the experimental response curves at which the measured steady-state wave elevations were characterized by amplification of the double harmonics, 2σ. This amplification cannot be captured by the derived quasi-linear modal theory since the only $(\cdot|\cdot|)$-nonlinear quantities of this theory yield the odd harmonics. Amplification of the double harmonics is a necessary but not sufficient condition of the *secondary resonance phenomenon* in the nonlinear free-surface sloshing problem. Faltinsen and Timokha,[4] Hermann and Timokha,[5] Ockendon *et al.*,[6] Wu,[7] and Wu and Chen[8] (see, also extended review in Chap. 8 of Ref. 9) gave theoretical and experimental analysis of the phenomenon for the two-dimensional steady-state resonant liquid sloshing in a clean rectangular tank with finite, intermediate, and shallow liquid depths. Normally, the secondary resonance is studied for the

[a]Author to whom correspondence should be addressed. Electronic mail: odd.Faltinsen@marin.ntnu.no.

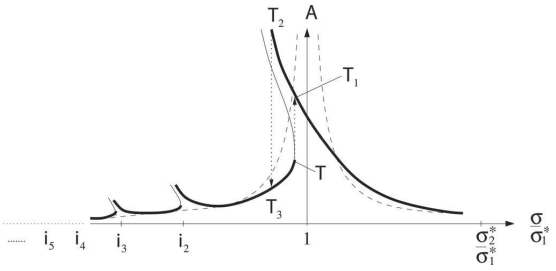

FIG. 1. The schematic response curves for a clean rectangular tank representing the maximum steady-state wave elevation A versus σ/σ_1^* for $0.3368\ldots < h/l$ due to lateral harmonic excitation. The dashed line shows results of the linear sloshing theory. The solid bold lines display stable nonlinear steady-state regimes. A hysteresis effect at $\sigma/\sigma_1^* = 1$ is possible and denoted by the points T, T_1, T_2, and T_3. The points i_2 and i_3 mark the most important secondary resonance points occurring as the forcing frequency satisfies the conditions $2\sigma = \sigma_2^*$ (amplification of the second mode) or $3\sigma = \sigma_3^*$ (amplification of the third mode), respectively. A hysteresis effect at i_2 and i_3 is also possible but, due to sufficiently large damping, it was detected in experiments[4] only for a relatively large forcing amplitude.

case when the tank is forced laterally and harmonically with the forcing frequency σ close to the lowest natural sloshing frequency σ_1^*. For the finite liquid depth (the depth-to-tank width ratio $0.2 \lesssim h/l$) and an asymptotically small forcing amplitude, the secondary resonances are mathematically expected at $2\sigma = \sigma_2^*$, $3\sigma = \sigma_3^*, \ldots, n\sigma = \sigma_n^*, n \geq 4$. These conditions imply amplification of the second, third, and higher harmonics as well as the corresponding natural modes. The harmonics are yielded by the free-surface nonlinearities of the corresponding polynomial orders. For $0.3368\ldots < h/l$ ($0.3368\ldots$ is the so-called critical depth where the soft-to-hard spring behavior of the response curves changes with $\sigma = \sigma_1^*$), the secondary resonance peaks on the steady-state response curves are situated away from the primary resonance $\sigma = \sigma_1^*$ as shown in Fig. 1. This fact and the liquid damping cause that the peaks associated with higher-order free-surface nonlinearities (fourth, fifth, etc.) are extremely narrow and practically not realized. In contrast, the second- and third-order nonlinearities matter[4] and lead to visible peaks on the experimental response curves, especially, with increasing the forcing amplitude. The situation changes with decreasing liquid depth when the natural sloshing spectrum becomes nearly commensurate. The passage to shallow liquid depth causes finger-type response curves which are discussed and quantified by Faltinsen and Timokha[10] by employing a Boussinesq-type fourth-order multimodal method.

Based on the experimental results by Faltinsen *et al.*,[1] the aforementioned free-surface phenomena (i)–(iii) and the multi-peak response curves indicate that the nonlinearity is important for sloshing in the screen-equipped tanks, especially, with increasing the forcing amplitude. A way to describe the nonlinear liquid sloshing can be Computational Fluid Dynamics (CFD).[11] The second author attempted to model experimental cases from Ref. 1 by interFOAM, which is an OpenFOAM code that solves the two-dimensional Navier-Stokes equations for incompressible laminar two-phase flow using the volume of fluid (VOF) method for free-surface capturing and the finite volume method (FVM) for the governing equations. In these calculations, the mesh number was about 150,000. Using the Intel(R) Core(TM) 2 Quad CPU (2.5 GHz) computer with parallel computations for four sub-domains of the main domain, a computational time of about 10^5 s was required to simulate 100 s of real-time sloshing and to reach nearly steady-state conditions. This means that, even though the CFD methods are generally applicable, using them for a parameter study of the nonlinear steady-state sloshing from experiments by Faltinsen *et al.*[1] is questionable. In the present paper, we show that an alternative could be analytically oriented (e.g., asymptotic multimodal) methods based on potential flow theory and employing a pressure drop condition to capture the viscous effect associated with flow separation at the screen. The *nonlinear* adaptive multimodal method is not able to describe the phenomena (i)–(iii). However, because the higher-order nonlinearities (higher than three) do not contribute to the secondary resonance phenomenon for the finite liquid depth, the method is applicable to describe the multi-peak response curves.

The nonlinear adaptive multimodal method requires derivation of the polynomial-type modal system, i.e., the system of ordinary differential equations which keeps only up to the third-order polynomial nonlinearities in the generalized coordinates responsible for amplification of the natural sloshing modes. The adaptive modal method is a generalization of the third-order Moiseev-type theory.[12–14] The method implicitly assumes an incompressible liquid with irrotational flow, but damping due to the boundary layer at the wetted tank surface, roof impact, etc., can generally be accounted for. Considering screens with a relatively small solidity ratio, Love and Tait[15] and Love *et al.*[16] adopted the polynomial-type modal system by Faltinsen and Timokha[4] with quadratic damping terms due to viscous flow separation at the screen. Because the latter approach assumes implicitly that the natural sloshing frequencies and modes of the screen-equipped tank remain the same as those for the corresponding clean tank, it is applicable only for relatively small solidity ratios. For slotted screens, Ref. 2 estimates this fact for $0 < Sn \lesssim 0.5$. Because the natural sloshing modes are modified by the screens for $0.5 \lesssim Sn < 1$, the polynomial-type modal system by Faltinsen and Timokha[4] should be *completely revised.* Such a *revision* is reported in the present paper (see Sec. II). The newly derived modal system couples the generalized coordinates β_i responsible for the screen-modified natural modes by Faltinsen and Timokha.[2] The multimodal method assumes an incompressible liquid with irrotational flow except locally at the screen. In addition, the method requires the normal representation of the free surface and, therefore, it cannot directly account for the free-surface phenomena (i–iii) described in experiments by Faltinsen *et al.*[1,14]

To include an "integral" viscous effect due to flow separation at the screen, we employ the $(\cdot|\cdot|)$-damping terms derived in Ref. 1 from the screen-averaged pressure drop condition. These damping terms involve an integral expression of the cross-flow at the mean submerged screen part and neglect the damping caused by the free-surface phenomenon (iii). Our formulation of the pressure drop condition implicitly assumes that the cross-flow dominates relative to the

tangential flow component at the screen. In addition, we neglect the fact that the tangential flow component implies a tangential drag on the screen.

Based on the results in Sec. II B, we derive in Sec. II C the required modal system keeping up to the third-order polynomial nonlinearities in terms of the generalized coordinates. Both antisymmetric and symmetric modes become coupled due to the free-surface nonlinearity. However, the screen-caused $(\cdot|\cdot|)$-damping terms appear only in modal equations responsible for the antisymmetric modes. The reason is that the antisymmetric modes determine the cross-flow, but the symmetric modes contribute to the tangential flow along the screen. In Sec. III B, the adaptive modal method by Faltinsen and Timokha[4] is generalized for the case of the screen-equipped rectangular tanks. This includes a generalization of the Moiseev asymptotic modal relationships and accounting for a larger number of the secondary resonances in a neighborhood of the lowest natural frequency. The steady-state solutions are found by combining a long-time simulations with the adaptive asymptotic modal systems and the path-following procedure along the response curves. Because the modal equations for the symmetric modes have no damping terms, we have to incorporate linear damping terms due to a viscous dissipative effect of the boundary layer flow at the mean wetted tank surface. A rough estimate of the corresponding damping rates are taken from Chap. 6 in Ref. 9. However, except for the lowest tested solidity ratio, the corresponding damping rates pass to zero in the final calculations from Sec. III.

The theoretical results in Sec. III agree well with the experimental measurements by Faltinsen *et al.*[1] for $h/l=0.4$ and the forcing amplitude $\eta_{2a}/l=0.01$. The theory is supported by the experimental fact that the secondary resonance peaks for $0.5\lesssim Sn<1$ are not only expected at i_2 and i_3 in Fig. 1, but also at

$$i_{2k}=\frac{\sigma}{\sigma_1^*}=\frac{\sigma_{2k}^*}{2\sigma_1^*}\quad(2\sigma=\sigma_{2k}^*)\qquad k=2,3,\ldots \tag{1}$$

(due to amplification of the double harmonics) and

$$3\sigma=\sigma_{2k+1};\quad \frac{\sigma}{\sigma_1^*}=\frac{\sigma_{2k+1}}{3\sigma_1^*}=i_{2k+1},\quad k=1,2,\ldots \tag{2}$$

(due to amplification of the third harmonics).

The multimodal method has to involve twenty natural modes to describe the secondary resonance modes associated with the experiments by Faltinsen *et al.*[1] for $h/l=0.4$ and forcing amplitude $\eta_{2a}/l=0.01$. Moreover, many of these modes, e.g., the 13th and 15th modes, should be considered as giving the lowest-order contribution (along with the first natural mode) to handle the secondary resonance sloshing with increasing the forcing frequency to $\sigma/\sigma_1^*\approx 1.3$ and higher. The experimental observations confirmed the locally steep wave profiles. The wavelength of the 20th natural mode for the experimental 1 m tank is 10 cm, namely, the theoretically involved modes have a wavelength larger than the rough upper bound 5 cm for when surface tension matters for linear propagating capillary-gravity waves. This means that we did not make an error neglecting the surface tension in our theoretical analysis.

A possible reason for quantitative differences between our nonlinear theory and experiments in certain frequency ranges for higher solidity ratios is the use of the simplified "integral"-type pressure drop condition which neglects specific nearly screen flows. In particular, higher solidity ratios lead to a jump in the free-surface elevation at the screen which causes a cross-flow from water to air. The latter cross-flow is associated with jet flows impacting on the underlying free surface. The water-water impact is likely to represent dissipation of the total energy. At the present time, we do not have a clear strategy how to estimate contribution of this and other specific nearly screen flows on the global liquid sloshing dynamics.

II. THEORY

An incompressible liquid with irrotational two-dimensional flow is assumed everywhere in the liquid domain $Q(t)$ *except* in a small neighborhood of a screen as shown in Fig. 2. The surface tension is neglected. The two-dimensional tank has vertical walls at the free surface $\Sigma(t)$. The tank is forced horizontally with displacements $\eta_2(t)$.

A. General modal equations

We follow the general scheme of the multimodal methods described, e.g., in Chap. 7 of Ref. 9 or in Ref. 17 implying the modal solution

$$z=\zeta(y,t)=\sum_{i=1}^{\infty}\beta_i(t)f_i(y), \tag{3a}$$

$$\Phi(y,z,t)=y\,\dot\eta_2+\sum_{i=1}^{\infty}R_n(t)\varphi_n(y,z) \tag{3b}$$

for the free-surface elevation and the absolute velocity potential, respectively. Here, β_i and R_n are the generalized coordinates and $\varphi_n(f_n(y)=\varphi_n(y,0))$ are the natural sloshing modes which are the eigenfunctions of the boundary spectral problem,

$$\nabla^2\varphi_n=0\ \text{ in }\ Q_0;\ \ \frac{\partial\varphi_n}{\partial n}=0\ \text{ on }\ S_0;$$
$$\frac{\partial\varphi_n}{\partial z}=\kappa_n\varphi_n\ \text{ on }\ \Sigma_0;\ \ \int_{\Sigma_0}\varphi_n\mathrm{d}y=0, \tag{4}$$

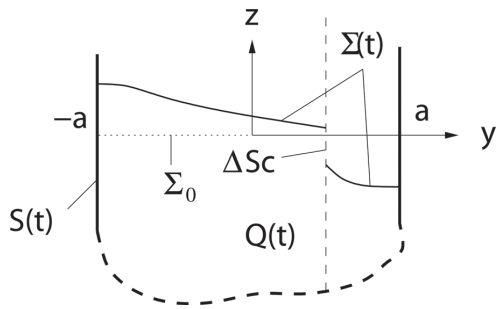

FIG. 2. A general two-dimensional tank with vertical walls near the free surface and, possibly, a perforated vertical screen. In our modal theory, the liquid cross-flow at the screen part ΔSc with subsequent fallout of the screen-generated liquid jet impact on the free surface is neglected; this cannot be described by the modal solution (3a).

where Q_0 is the mean liquid domain, S_0 is the mean wetted tank surface including the solid screen parts, and Σ_0 is the mean free surface. The natural sloshing frequencies are computed by the formulas $\sigma_n = \sqrt{g\kappa_n}$, $n = 1, 2, \ldots$ (g is the gravity acceleration).

The multimodal method employs the modal solution (3) with the normal presentation of the free surface (3a) and, thereby, *implicitly assumes* that there are no overturning waves. Since any breaking waves involve vorticity generation, they also cannot be described. Moreover, as it is shown in Fig. 2, the modal solution (3a) *cannot* model the liquid flow through the screen part ΔSc where one side of the screen is wetted, but another dry contacting the ullage gas. Experimental observations by Faltinsen *et al.*[1] reported a flow through ΔSc with forthcoming water fallout on the free surface. The multimodal method neglects this flow.

Chapter 7 in Ref. 9 shows that using the modal solution (3) together with the Bateman-Luke variational principle leads to the following general [modal] infinite-dimensional system of ordinary differential equations,

$$\sum_{k=1}^{\infty} \frac{\partial A_n}{\partial \beta_k}\ddot{\beta}_k = \sum_{k=1}^{\infty} A_{nk} R_k, \quad n = 1, 2, \ldots, \tag{5a}$$

$$\sum_{n=1}^{\infty} \frac{\partial A_n}{\partial \beta_\mu}\ddot{R}_n + \frac{1}{2}\sum_{n,k=1}^{\infty} \frac{\partial A_{nk}}{\partial \beta_\mu} R_n R_k + g\Lambda^{(0)}_{\mu\mu} + \lambda_{2\mu}\ddot{\eta}_2 = 0, \quad \mu = 1, 2, \ldots \tag{5b}$$

which couple the generalized coordinates β_k and R_n introduced by the modal solution (3). Here,

$$A_n = \int_{Q(t)} \varphi_n \mathrm{d}Q; \quad A_{nk} = \int_{Q(t)} \nabla\varphi_n \cdot \nabla\varphi_k \mathrm{d}Q;$$
$$\lambda_{2n} = \int_{\Sigma_0} y f_n \mathrm{d}S; \quad \Lambda^{(0)}_{nn} = \int_{\Sigma_0} f_n^2 \mathrm{d}S \tag{6}$$

so that A_n and A_{nk} are nonlinear functions of β_i.

Generally speaking, the fully nonlinear modal system (5) can be adopted for direct simulations. Going this way means the so-called Perko's[18,19] method. La Rocca *et al.*[20] used this method to describe nonlinear liquid sloshing in a clean rectangular tank. Simulations by the Perko method are less numerically efficient than the use of the adaptive modal method. However, the main problem of the Perko-type methods is that the system (5) becomes numerically stiff for strongly resonant sloshing. The latter fact has been discussed by Faltinsen and Timokha.[4,10]

B. The polynomial-type modal equations

In accordance with the adaptive multimodal method by Faltinsen and Timokha,[4] we assume that the nonlinear intermodal interaction is primarily determined by the second- and third-order polynomial terms in the generalized coordinates. This means that one can reduce (5) by keeping the third-order polynomial quantities. Using the Taylor series at $z = 0$

$$\varphi(y, \zeta, t) = f_n + (\kappa_n f_n)\zeta + \frac{1}{2}\left(\sum_{l=1}^{\infty} \alpha_{n,l} f_l\right)\zeta^2 + \cdots$$

in the expression

$$\frac{\partial A_n}{\partial \beta_k} = \int_{-a}^{a} \varphi(y, \zeta, t) f_k \, \mathrm{d}y$$

as well as in the expression on p. 173 of Ref. 4, i.e.,

$$A_{nk} = \kappa_n \Lambda^{(0)}_{nk} + \int_{-a}^{a} (\nabla\varphi_n \cdot \nabla\varphi_k)|_{z=0}\, \zeta \, \mathrm{d}y + \frac{1}{2}\int_{-a}^{a} \left.\frac{\partial(\nabla\varphi_n \cdot \nabla\varphi_k)}{\partial z}\right|_{z=0} \zeta^2 \, \mathrm{d}y + \cdots$$

gives the formulas

$$\frac{\partial A_n}{\partial \beta_j} = \Lambda^{(0)}_{nj} + \kappa_n \sum_{i=1}^{\infty} \Lambda^{(1)}_{nji}\beta_i + \frac{1}{2}\sum_{i,k=1}^{\infty}\left(\sum_{m=1}^{\infty} \alpha_{n,m}\Lambda^{(2)}_{mjik}\right)\beta_i\beta_k + \cdots, \tag{7}$$

$$A_{nk} = \kappa_n \Lambda^{(0)}_{nk} + \sum_{i=1}^{\infty} \Pi^{(1)}_{nk,i}\beta_i + \frac{1}{2}\sum_{p,q=1}^{\infty} \Pi^{(2)}_{nk,pq}\beta_p\beta_q + \cdots. \tag{8}$$

Here, we used the following relations:

$$f_n(y) = \varphi_n(y, 0); \quad \kappa_n f_n = \left.\frac{\partial\varphi_n}{\partial z}\right|_0; \quad \sum_{l=1}^{\infty} \alpha_{n,l} f_l = \left.\frac{\partial^2\varphi_n}{\partial z^2}\right|_0, \tag{9a}$$

$$\left.\frac{\partial f_n}{\partial y} = \frac{\partial\varphi_n}{\partial y}\right|_0; \quad \kappa_n \left.\frac{\partial f_n}{\partial y} = \frac{\partial^2\varphi_n}{\partial y \partial z}\right|_0; \quad \sum_{l=1}^{\infty} \alpha_{n,l}\frac{\partial f_l}{\partial y} = \left.\frac{\partial^3\varphi_n}{\partial y \partial z^2}\right|_0, \tag{9b}$$

where the coefficients $\alpha_{n,l}$ are introduced which imply a Fourier expansion of $\partial^2\varphi_n/\partial z^2|_{z=0}$ in terms of the orthogonal basis $\{f_n\}$;

$$\int_{-a}^{a} f_n f_k \, \mathrm{d}y = \Lambda^{(0)}_{nk}; \quad \int_{-a}^{a} f_n f_k f_i \, \mathrm{d}y = \Lambda^{(1)}_{nki};$$
$$\int_{-a}^{a} f_n f_k f_i f_j \, \mathrm{d}y = \Lambda^{(2)}_{nkij} \ldots, \tag{10}$$

$$\int_{-a}^{a} \frac{\partial f_n}{\partial y}\frac{\partial f_k}{\partial y} f_i \, \mathrm{d}y = \Lambda^{(-1)}_{nk,i}; \quad \int_{-a}^{a} \frac{\partial f_n}{\partial y}\frac{\partial f_k}{\partial y} f_i f_j \, \mathrm{d}y = \Lambda^{(-2)}_{nk,ij}, \ \ldots, \tag{11}$$

where, due to the orthogonality of the natural modes, $\Lambda^{(0)}_{nk} = 0$, $n \neq k$,

$$\Pi^{(1)}_{nk,i} = \Lambda^{(-1)}_{nk,i} + \kappa_n\kappa_k\Lambda^{(1)}_{nki}, \tag{12a}$$

$$\Pi^{(2)}_{nk,pq} = (\kappa_n + \kappa_k)\Lambda^{(-2)}_{nk,pq} + \sum_{m=1}^{\infty}\left[\alpha_{n,m}\kappa_k\Lambda^{(2)}_{mkpq} + \alpha_{k,m}\kappa_n\Lambda^{(2)}_{mnpq}\right]. \tag{12b}$$

The comma is used between indexes which disallow their position exchange. As long as there is no comma between the indexes, these indexes can commutate.

Substituting

$$R_k = \frac{\dot{\beta}_k}{\kappa_k} + \sum_{p,q=1}^{\infty} V^{2,k}_{p,q}\dot{\beta}_p\beta_q + \sum_{p,q,m=1}^{\infty} V^{3,k}_{p,q,m}\dot{\beta}_p\beta_q\beta_m + \cdots \tag{13}$$

in the kinematic equation (5a), one can compute the coefficients,

$$V^{2,n}_{k,i} = \frac{1}{\kappa_n \Lambda^{(0)}_{nn}} \left[-\frac{\Pi^{(1)}_{nk,i}}{\kappa_k} + \kappa_n \Lambda^{(1)}_{nki} \right], \tag{14a}$$

$$V^{3,n}_{k,p,q} = \frac{1}{\kappa_n \Lambda^{(0)}_{nn}} \left[-\frac{\Pi^{(2)}_{nk,pq}}{2\kappa_k} + \sum_{m=1}^{\infty} \left(\tfrac{1}{2} \alpha_{n,m} \Lambda^{(2)}_{mkpq} - \Pi^{(1)}_{nm,p} V^{2,m}_{k,q} \right) \right] \ldots. \tag{14b}$$

Finally, using Eqs. (7), (8), and (13) in the dynamic modal equation (5b), one can find the following asymptotic modal equation accounting for the third-order components in terms of the generalized coordinates β_i,

$$\sum_{n=1}^{\infty} \ddot{\beta}_n \left[\delta_{n\mu} + \sum_{i=1}^{\infty} d^{1,\mu}_{n,i} \beta_i + \sum_{i,j=1}^{\infty} d^{2,\mu}_{n,i,j} \beta_i \beta_j \right] + \\ + \sum_{n,k=1}^{\infty} \dot{\beta}_n \dot{\beta}_k \left[t^{0,\mu}_{n,k} + \sum_{i=1}^{\infty} t^{1,\mu}_{n,k,i} \beta_i \right] + \sigma^2_\mu \beta_\mu + P_\mu \ddot{\eta}_2 = 0, \\ \mu = 1, 2, \ldots, \tag{15}$$

where

$$\sigma^2_\mu = g\kappa_\mu; \quad P_\mu = \frac{\kappa_\mu \lambda_{2\mu}}{\Lambda^{(0)}_{\mu\mu}}, \tag{16a}$$

$$d^{1,\mu}_{n,i} = \kappa_\mu \left(V^{2,\mu}_{n,i} + \frac{\Lambda^{(1)}_{n\mu i}}{\Lambda^{(0)}_{\mu\mu}} \right); \quad t^{0,\mu}_{n,k} = \kappa_\mu V^{2,\mu}_{n,k} + \frac{\kappa_\mu \Pi^{(1)}_{nk,\mu}}{2\kappa_n \kappa_k \Lambda^{(0)}_{\mu\mu}}, \tag{16b}$$

$$d^{2,\mu}_{n,i,j} = \kappa_\mu \left(V^{3,\mu}_{n,j,i} + \frac{1}{\Lambda^{(0)}_{\mu\mu}} \sum_{m=1}^{\infty} \left[\kappa_m \Lambda^{(1)}_{m\mu i} V^{2,m}_{n,j} + \frac{1}{2} \frac{\alpha_{n,m} \Lambda^{(2)}_{m\mu ij}}{\kappa_n} \right] \right), \tag{16c}$$

$$t^{1,\mu}_{n,k,i} = \kappa_\mu \left(V^{3,\mu}_{n,k,i} + V^{3,\mu}_{n,i,k} + \frac{\Pi^{(2)}_{nk,\mu i}}{2\kappa_n \kappa_k \Lambda^{(0)}_{\mu\mu}} + \frac{1}{2\Lambda^{(0)}_{\mu\mu}} \sum_{m=1}^{\infty} \right. \\ \left. \times \left[2\kappa_m \Lambda^{(1)}_{m\mu i} V^{2,m}_{n,k} + \frac{\Pi^{(1)}_{mk,\mu} V^{2,m}_{n,i}}{\kappa_k} + \frac{\Pi^{(1)}_{nm,\mu} V^{2,m}_{k,i}}{\kappa_n} \right] \right). \tag{16d}$$

C. Modal equations for the case of a central slotted screen

The two-dimensional liquid sloshing is considered in a rectangular tank with width $l = 2a$ and a slotted screen installed at the tank middle as shown in Fig. 3. The figure introduces the geometric notations and the body-fixed coordinate system. The screen appears as a thin solid plate with a series of perforated horizontal slots. The screen thickness is neglected. When the liquid is at rest, the wetted screen part Sc_0 has N submerged slots. The *solidity ratio* of the submerged screen part is denoted by Sn which is a function of h and N.

Under assumptions of the previous section, we use the modal equations (15) in which the hydrodynamic coefficients

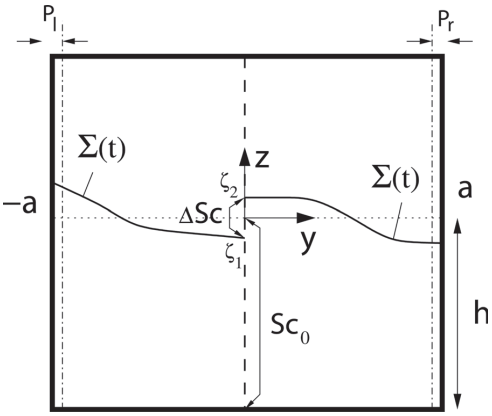

FIG. 3. A schematic picture of a rectangular tank with a slat-type screen in the middle. Basic geometric notations. Two measurement probes of wave elevation are located at small distances P_l and P_r from the walls. The mean wetted screen is Sc_0. For higher solidity ratios, the free surface $\Sigma(t)$ has a clear jump at the screen formed by the "wet-dry" area ΔSc (here, the interval (ζ_1,ζ_2)).

are computed based on the natural sloshing modes by Faltinsen and Timokha.[2] For $0.5 \lesssim Sn < 1$, these hydrodynamic coefficients are functions of Sn and N as well as slot positions. The modal equations do not account for a local viscous flow through the screen. Following Faltinsen *et al.*,[1] this can be done by employing an "integral" (averaged) version of the pressure drop condition[3] defined on the mean wetted screen as follows:

$$P_- - P_+ = \frac{1}{2} \rho K u|u| \quad \text{on} \quad Sc_0, \tag{17}$$

where K is an empirical pressure drop coefficient, ρ is the liquid density, u is the so-called lateral *approach* velocity to the screen, and $(P_- - P_+)$ is the *pressure drop*. A review on using this condition in sloshing problems can be found in Refs. 1, 9, and 21. This empirical condition comes from the steady-flow case[3] and, generally, can be employed for sloshing problems with many screens installed at different places. The space-averaged version of the pressure drop formulation (17) assumes that both sides of the screen are wetted, i.e. the jump $|\Delta Sc| = \zeta_2 - \zeta_1$ in Fig. 3 and the liquid flow through ΔSc are neglected. The pressure drop coefficient K depends on the solidity ratio Sn. It may also depend on the Reynolds and Keulegan-Carpenter (KC) numbers. For slat-type screens, the pressure drop coefficient weakly depends on the Reynolds number. There is negligible dependence on KC number for relevant KC numbers. Following Tait *et al.*[21] and Faltinsen *et al.*,[1] we will adopt the following approximation of the empirical pressure drop coefficient:

$$K = \left(\frac{1}{Cc\,(1 - Sn)} - 1 \right)^2, \quad Cc = 0405 \exp(-\pi Sn) + 0.595 \\ \text{for} \quad Sn \geq 03. \tag{18}$$

The formula (18) is applicable for different Sn-values. According to experimental values of K by Blevins,[3] its relative accuracy is less than 20% for $Sn \leq 0.9$, but may be larger for $Sn \geq 0.9$.

Faltinsen *et al.*[1] showed that the "integral" pressure drop condition leads to the following quantities:

$$KD_m(\dot\beta_{2i-1}) = -K\frac{\alpha'_m\kappa_{2m-1}}{4h\Lambda^{(0)}_{(2m-1)(2m-1)}}\int_{-h}^{0}\left(\sum_{i=1}^{\infty}\frac{\dot\beta_{2i-1}}{\kappa_{2i-1}}U_i(z)\right)\times\left|\sum_{i=1}^{\infty}\frac{\dot\beta_{2i-1}}{\kappa_{2i-1}}U_i(z)\right|\mathrm{d}z \tag{19}$$

to be incorporated into the modal equations for the antisymmetric modes (generalized coordinates β_{2m-1}) responsible for cross-flow through the screen. Here

$$\alpha'_m = 2\int_{-a}^{0} f_{2m-1}\mathrm{d}y,$$
$$U_i(z) = -\frac{1}{a}\cosh(k_0^{(i)}(z+h)/a)\sin(k_0^{(i)}),$$

with the constant $k_0^{(i)}$ being the roots of the equations,

$$k_0^{(i)}\tanh(k_0^{(i)}h/a) = \kappa_{2i-1}a.$$

Using the modal equations (15) and the pressure-drop "integral" terms (19) leads to the following modal equations:

$$\sum_{n=1}^{\infty}\ddot\beta_n\left[\delta_{n(2m-1)} + \sum_{i=1}^{\infty}D1^{2m-1}(n,i)\beta_i + \sum_{j=1}^{\infty}\sum_{i=1}^{j}D2^{2m-1}(n,i,j)\beta_i\beta_j\right] + \sum_{n=1}^{\infty}\sum_{k=1}^{n}\dot\beta_n\dot\beta_k\left[T0^{2m-1}(n,k) + \sum_{i=1}^{\infty}T1^{2m-1}(n,k,i)\beta_i\right] + KD_m(\dot\beta_{2i-1}) + \sigma^2_{2m-1}\beta_{2m-1} + P_{2m-1}\ddot\eta_2 = 0, \tag{20a}$$

$$\sum_{n=1}^{\infty}\ddot\beta_n\left[\delta_{n(2m)} + \sum_{i=1}^{\infty}D1^{2m}(n,i)\beta_i + \sum_{j=1}^{\infty}\sum_{i=1}^{j}D2^{2m}(n,i,j)\beta_i\beta_j\right] + \sum_{n=1}^{\infty}\sum_{k=1}^{n}\dot\beta_n\dot\beta_k\left[T0^{2m}(n,k) + \sum_{i=1}^{\infty}T1^{2m}(n,k,i)\beta_i\right] + \sigma^2_{2m}\beta_{2m} = 0, \quad m = 1,2,\ldots, \tag{20b}$$

where

$$D1^{\mu}(n,i) = d^{1,\mu}_{n,i}; \qquad D2^{\mu}(n,i,j) = \begin{cases} d^{2,\mu}_{n,i,i}, & i=j,\\ d^{2,\mu}_{n,i,j} + d^{2,\mu}_{n,j,i}, & i\neq j,\end{cases}$$

$$T0^{\mu}(n,k) = \begin{cases} t^{0,\mu}_{n,n}, & n=k,\\ t^{0,\mu}_{n,k} + t^{0,\mu}_{k,n}, & n\neq k,\end{cases}$$

$$T1^{\mu}(n,k,i) = \begin{cases} t^{1,\mu}_{n,n,i}, & n=k,\\ t^{1,\mu}_{n,k,i} + t^{1,\mu}_{k,n,i}, & n\neq k.\end{cases}$$

As we remarked above, the hydrodynamic coefficients in the modal equations (20) are computed by using the natural sloshing modes from Ref. 2.

When $0 < Sn \lesssim 0.5$, the natural sloshing modes are close to those for the clean tank, i.e., these are approximately governed by the trigonometric algebra implying

$$\varphi_k(y,z) \approx \cos\left(\frac{\pi k}{a}(y-a)\right)\frac{\cosh(\pi k(z+h)/l)}{\cosh(\pi kh/l)}, \tag{21}$$

in expressions of Sec. II B. As a consequence, many of the hydrodynamic coefficients at the polynomial-type terms of (20) are zero. In particular, the quadratic nonlinearity in β_1 (the generalized coordinate responsible for the first mode) is only present in the first equation of (20b) governing the first symmetric mode (β_2). Analogously, the cubic terms in β_1 exist only in the first and second equations of (20a). This means that the secondary resonance due to the second harmonics can only excite the second mode, but the third harmonics can only lead to the secondary resonance for the third mode.

When $0.5 \lesssim Sn < 1$, the trigonometric algebra representation for the natural sloshing modes (21) breaks down so that the screen-effected antisymmetric modes become, generally, non-continuous in the center of Σ_0 (see examples in Ref. 2). This fact leads to additional nonzero hydrodynamic coefficients causing a complex nonlinear energy redistribution between lower and higher modes. So, the nonzero quadratic quantities in β_1 appear now in all the equations for even modes (20b), i.e., all the symmetric modes can be amplified due to the second harmonics (the second-order nonlinearity) but the nonzero cubic terms in β_1 are present in all the equations (20a). As a consequence, the higher solidity ratios yield the secondary resonance due to the second and third harmonics not only at i_2 and i_3 but also at i_k, $k \geq 2$ defined by Eqs. (1) and (2).

Incorporating the $KD_m(\dot\beta_{2i-1})$-terms in modal equations (20a) adds a quadratic damping into a conservative mechanical system with infinite degrees of freedom. Because we operate with potential flow theory, the modal equations (20) do not contain other damping terms, e.g., due to laminar viscous boundary layer, tangential viscous drag at the screen, and wave breaking. Moreover, because the symmetric modes do not cause cross-flow through the central screen, the modal equations (20b) do not have any damping terms at all. As it will be explained in detail in Sec. III C, the latter fact can make it difficult to find the steady-state solution due to a continuous beating by these symmetric modes. Artificial small damping is therefore needed to reach the steady-state condition. For this purpose, it is standard procedure to incorporate the linear damping terms,

$$2\alpha_i\sigma_i\dot\beta_i \tag{22}$$

in the ith equation of (20) to account for other damping mechanisms and prevent the aforementioned beating in the computations. The actual values of α_i are unknown and, according to our theoretical model, should pass to zero in final calculations after the steady-state condition is achieved. A rough estimate of the initial α_i-values adopted for our steady-state calculations can be associated with the damping rates ξ_i for *linear sloshing* due to the laminar viscous boundary layer at the mean wetted tank surface for the clean tank evaluated in Secs. 6.3.1 and 6.11.1 of Ref. 9. The corresponding numerical procedure on the steady-state solution with decreasing α_i is explained in Sec. III C.

III. RESONANT STEADY-STATE SLOSHING DUE TO LATERAL EXCITATION WITH THE FORCING FREQUENCY AT THE LOWEST NATURAL SLOSHING FREQUENCY

A. Nondimensional formulation

We assume that $\eta_2(t)=\eta_{2a}\cos(\sigma t)$ with a relatively small nondimensional forcing amplitude η_{2a}/l and σ being close to the lowest natural sloshing frequency σ_1^* of the corresponding clean tank. The liquid depth is finite. Henceforth, we will introduce asymptotic relationship between the l-scaled generalized coordinates. This needs rewriting the modal equations (20) in a nondimensional form. Introducing the characteristic length $l=2a$ and the characteristic time $t_*=1/\sigma_1^*$, the normalization transforms the modal equations to the form,

$$\sum_{n=1}^{\infty}\ddot{\bar\beta}_n\left[\delta_{n(2m-1)}+\sum_{i=1}^{\infty}\bar D1^{2m-1}(n,i)\bar\beta_i+\sum_{j=1}^{\infty}\sum_{i=1}^{j}\bar D2^{2m-1}(n,i,j)\bar\beta_i\bar\beta_j\right]+\sum_{n=1}^{\infty}\sum_{k=1}^{n}\dot{\bar\beta}_n\dot{\bar\beta}_k\times\left[\bar T0^{2m-1}(n,k)+\sum_{i=1}^{\infty}\bar T1^{2m-1}(n,k,i)\bar\beta_i\right]+2\alpha_{2m-1}\bar\sigma_{2m-1}\dot{\bar\beta}_{2m-1}+K\bar D_m(\dot{\bar\beta}_{2i-1})+\bar\sigma_{2m-1}^2\bar\beta_{2m-1}-\bar\eta_{2a}\bar\sigma\cos(\bar\sigma t)=0, \tag{23a}$$

$$\sum_{n=1}^{\infty}\ddot{\bar\beta}_n\left[\delta_{n(2m)}+\sum_{i=1}^{\infty}\bar D1^{2m}(n,i)\bar\beta_i+\sum_{j=1}^{\infty}\sum_{i=1}^{j}\bar D2^{2m}(n,i,j)\bar\beta_i\bar\beta_j\right]+\sum_{n=1}^{\infty}\sum_{k=1}^{n}\dot{\bar\beta}_n\dot{\bar\beta}_k\left[\bar T0^{2m}(n,k)+\sum_{i=1}^{\infty}\bar T1^{2m}(n,k,i)\bar\beta_i\right]+2\alpha_{2m}\bar\sigma_{2m}\dot{\bar\beta}_{2m}+\bar\sigma_{2m}^2\bar\beta_{2m}=0,\quad m=1,2,\ldots. \tag{23b}$$

Here, we have incorporated the linear damping terms (22) and introduced the following nondimensional variables:

$$\bar\beta_i=\beta_i/l,\quad \bar\eta_{2a}=\eta_{2a}/l,\quad \bar\sigma=\sigma/\sigma_1^*,\quad \bar\sigma_i=\sigma_i/\sigma_1^*,$$
$$\bar D1^i=lD1^i,\quad \bar D2^i=l^2D2^i,\quad \bar T0^i=lT0^i,\quad \bar T1^i=l^2T1^i,$$
$$\bar D_m(\dot{\bar\beta}_i)=lD_m(l\dot{\bar\beta}_i)$$

B. Generalization of the adaptive asymptotic modal method

Working with the clean rectangular tank, Faltinsen and Timokha[4] proposed an adaptive asymptotic modal method for the resonant steady-state liquid sloshing. They assumed that the forcing amplitude is small, $\bar\eta_{2a}=O(\epsilon)$, $\epsilon\ll 1$ and that σ is in a neighborhood of σ_1^*. The method starts with the Moiseev[12–14] third-order asymptotic relationships,

$$\bar\beta_1=O(\epsilon^{1/3}),\bar\beta_2=O(\epsilon^{2/3}),\bar\beta_3=O(\epsilon),\bar\beta_k\lesssim O(\epsilon),k\geq 4, \tag{24}$$

considering them as *a priori* estimate of the generalized coordinates $\bar\beta_i$.

Based on the asymptotic relationships (24), one can derive the corresponding asymptotic modal equations by neglecting the $o(\epsilon)$-terms in the polynomial-type modal equations (23). This was done by Faltinsen *et al.*[14] Further, Faltinsen *et al.*[14] and Faltinsen and Timokha[4] showed that the asymptotic relations (24) are not satisfied when σ/σ_1^* in close to i_2 and i_3 (see Fig. 1) on the asymptotic scale $O(\epsilon^{2/3})$. The use of the asymptotic modal equations by Faltinsen *et al.*[14] leads then to unrealistic amplification of the generalized coordinates $\bar\beta_2$ and $\bar\beta_3$. When this happened, Faltinsen and Timokha[4] proposed *a posteriori* asymptotic relationships considering $\bar\beta_2$ and/or $\bar\beta_3$ to have the dominant order $O(\epsilon^{1/3})$. Neglecting the $o(\epsilon)$-terms in (23) makes it possible to derive the corresponding asymptotic modal equations based on these new asymptotic relationships. References 4 and 22 demonstrate that the same forcing amplitude and frequency can require different asymptotic modal systems (asymptotic ordering) for steady-state solutions belonging to different response curves.

According to the Moiseev asymptotics (24) for the clean tank, there is only one dominant mode $(\bar\beta_1)$ and only one mode $(\bar\beta_2)$ possesses the second asymptotic order. However, as we have already commented, the non-zero second-order polynomial terms in $\bar\beta_1$ appear for $0.5\lesssim Sn<1$ in all the modal equations (23b) but the nonzero cubic terms in $\bar\beta_1$ are now presented in (23a). This means that the Moiseev-type asymptotics (24) should in the studied case change to

$$\bar\beta_1=O(\epsilon^{1/3}),\quad \bar\beta_{2k}=O(\epsilon^{2/3}),\quad \bar\beta_{2k+1}=O(\epsilon),\quad k\geq 2 \tag{25}$$

and, in contrast to the clean tank with a finite liquid depth considering only two possible secondary resonances for $\bar\sigma$ close to the points i_2 and i_3, we should now expect the multiple secondary resonances as $\bar\sigma$ is close to values from the sets (1) and (2). Thus, we see that screens with $0.5\lesssim Sn<1$ change the Moiseev asymptotics (24) to (25) and, besides, the secondary resonances should now be expected at i_k, $k\geq 2$. These facts modify the adaptive modal method.

We start now with (25) as *a priori* asymptotics. When considering a frequency range $\bar\sigma_a<\bar\sigma<\bar\sigma_b$, we should further find out whether there are any i_k belonging (being close) to this range and change the ordering of the generalized coordinates $\bar\beta_k$ in Eq. (25) to $\bar\beta_k=O(\epsilon^{1/3})$ for the corresponding indexes k. This will be *a posteriori* asymptotics. To obtain the corresponding asymptotic modal system, we should exclude the $o(\epsilon)$-terms in modal equations (23). By using direct simulations with these *a posteriori* asymptotic modal equations, one must also validate whether we have included all the dominant generalized coordinates on the studied interval $\bar\sigma_a<\bar\sigma<\bar\sigma_b$. If not, more dominant modes should be added.

We must note that we have an extra term $K\bar D_m$ in Eqs. (23a) where, because $\bar D_m$ is of the quadratic character with respect to $\bar\beta_1$, $\bar D_m=O(\epsilon^{2/3})$. The asymptotic modal equations include the asymptotic quantities up to the order $O(\epsilon)$ and, therefore, our asymptotic scheme requires $\epsilon^{1/3}\lesssim K$. When the $K\bar D_m$-terms are of either comparable or lower order with respect to the dominant $\epsilon^{1/3}$, these terms give a leading contribution to the nonlinear resonant sloshing. This condition implies

$$O(\epsilon^{-1/3}) = \bar{\eta}_{2a}^{-1/3} \lesssim K. \tag{26}$$

C. Numerical steady-state solution

Normally, the numerical steady-state solution of the nonlinear adaptive asymptotic modal system is found by a long-time simulation with appropriate damping terms (see Refs. 1, 4, and 22). For the clean tank,[4] the linear damping coefficients (22) are used to get a numerical steady-state solution by means of these simulations. Nevertheless, the first approximation is found with $\alpha_i \geq \xi_i$ but next approximations follow from the long-time simulations with lower values of α_i and initial conditions following from the previous steady-state solution computed with a larger α_i. Faltinsen and Timokha[4] report that such a numerical procedure with a stepwise decrease of the damping ratios practically converges with $\alpha_i \lesssim \xi_i/100$ so that the corresponding numerical steady-state solution obtained with $\alpha_i \approx \xi_i/100$ can be considered as the steady-state solution of the corresponding asymptotic modal system without damping terms. Moreover, the experimentally established secondary-resonance jumps between the steady-state solutions for the clean tank (as in Fig. 1) were detected for $\alpha_i \lesssim \xi/100$. This means that, due to possible nonlinear character of damping, the adopted linear damping rates for nonlinear steady-state motions can be lower than ξ_i, but theserates should be higher for the resonance-type transients.

In the studied case, the subsystem for antisymmetric modes has, by definition, the unavoidable quadratic damping terms. However, the subsystem (20b) describing the symmetric modes has not any proper damping terms. This "disproportion" between symmetric and antisymmetric modes can affect the time-step simulations leading to a long-time non-decaying beating by the symmetric modes. As a consequence, whereas we can in the majority of cases postulate $\alpha_{2m-1} = 0$ in Eq. (23a), the damping ratios α_{2m} in Eq. (23b) should not be zero in simulations to describe the steady-state sloshing.

In the next section, we will typically take $\alpha_{2m-1} = 0$, $\alpha_{2m} = \xi_{2m}$ to get the first approximation of the steady-state solution. The next approximations will be obtained by long-time simulations with initial conditions following from the previous steady-state solution and lower values of α_{2m}. Except for the case of lower Sn with K that, generally, does not satisfy (26), this recursive procedure in α_{2m} for getting the numerical steady-state solution will practically converge with $\alpha_{2m} \lesssim \xi_{2m}/10$. Similar to numerical results by Faltinsen and Timokha[4] for the clean tank, the secondary-resonance jumps become detected after the procedure converges with a lower tested α_{2m}. The subsequent decrease of α_{2m} does not influence the result (difference is less that 0.1%), but may in some cases cause numerical instability on the long-time scale due to the stiffness of the ordinary differential equations. The Adams-Bashforth-Moulton predictor-corrector algorithm of orders 1 through 12 is involved in our computations. The algorithm handles mildly stiff differential equations.

The numerical recursive procedure in α_{2m} is combined with a path-following procedure along the response branches by a stepwise change of $\bar{\sigma}$ in positive and negative directions. This path-following procedure makes it possible to go along the steady-state response curves and, thereby, detect jumps between branches. However, it does not guarantee that no more branches exist.

D. Theoretical and experimental secondary-resonance response curves

Using the adaptive multimodal method we will study the secondary resonance phenomenon in a screen-equipped rectangular tank by considering the experimental case from Ref. 1 for $\bar{\eta}_{2a} = \eta_{2a}/l = 0.01$, $\bar{h} = h/l = 0.4$, and seven different screens. The screens' structure and experimental setup are in some detail described in Ref. 1. Even though Faltinsen *et al.*[1] tested the frequency range $0.7 < \sigma/\sigma_1^* < 2.2$, our primary focus will be on the interval $0.7 < \sigma/\sigma_1^* < 1.36$. The upper bond of the interval is chosen to be away from $1.52 = \sigma_2/\sigma_1^* < \sigma_3/\sigma_1^*$. The reason is that the experimental steady-state sloshing with $\sigma_2^*/\sigma_1^* \lesssim \bar{\sigma}$ (the forcing frequency exceeds the second natural sloshing frequency) is characterized by the free-surface phenomena mentioned in Introduction as (i-iii). The multimodal method is not able to describe them.

Within the framework of the experimental input parameters, the calculation by the adaptive modal method established stabilization of the numerical steady-state solution (error is less than 0.01%) by twenty generalized coordinates (describing amplification of ten symmetric and ten antisymmetric modes). Further, to cover the frequency range $0.7 < \sigma/\sigma_1^* < 1.36$, we needed four different adaptive modal systems (asymptotic orderings) whose domains of applicability are overlapped and shown in Figs. 4, 6, 8, 9, and 11.

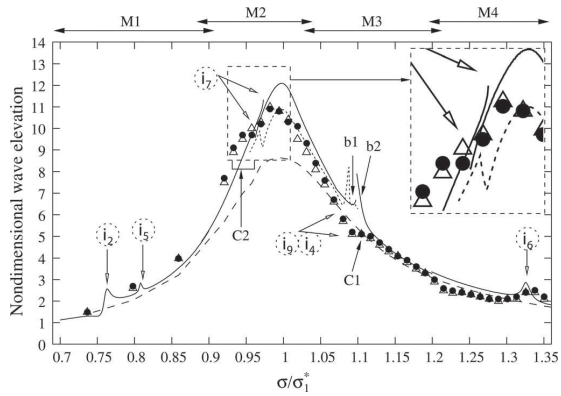

FIG. 4. The theoretical and experimental η_{2a}-scaled maximum wave elevation at the walls; $h/l = 0.4$ and $\eta_{2a}/l = 0.01$. The signs (•) and (Δ) denote the experimental measurements done at opposite walls (1 cm away from the walls, respectively). The submerged screen part has at rest 70 opening (slots), $Sn = 0.4725$ with $K = 3.09862$ (according to (18)). The solid lines denote results by the adaptive modal method involving four different asymptotic modal systems M1, M2, M3, and M4, whose frequency ranges are shown on the top. The modal systems involve $\alpha_{2m} = \xi_{2m}$ in Eq. (23b) and $\alpha_{2m-1} = 0$ in Eq. (23a). The dotted line in the middle shows the results with $\alpha_m = \xi_m$ in Eq. (23). The dashed line (quasi-linear modal theory) is taken from Faltinsen *et al.*[1] The values i_k are defined by Eqs. (1) and (2). They imply possibility of secondary resonance due to amplification of the second and third harmonics. The response curves are not connected between the branches b1 and b2 (a combined i_9-and-i_4 resonance) and in the zoomed zone caused by the secondary resonance at i_7.

A simple non-optimized FORTRAN code was written without any parallelization in computation. The computational time to reach a steady-state solution depended on the input physical parameters and the small nonzero damping rates α_{2m} which were employed to avoid beating in the symmetric modes. Normally, the damping rates $\alpha_{2m-1}=0$, $\alpha_{2m}=\xi_{2m}/10$ caused the computational time to be from 0.5 to 50 s to achieve a numerical steady-state solution within five significant figures (Intel(R) Core(TM) 2 Quad CPU (2.66 GHz) computer).

Our analysis starts with the experimentally lowest solidity ratio $Sn=0.4725$ leading to $K=3.09862$ according to formula (18). Comparing this value of K and $0.01^{-1/3}=4.6416$, one can conclude that condition (26) is satisfied *only* in an asymptotic sense. The adaptive modal method "feels" this fact. For the forcing frequencies close to $\sigma/\sigma_1^*=1$ simulations by the corresponding asymptotic modal systems were not able to get a clear steady-state solution with $\alpha_{2m-1}=0$ and $\alpha_{2m}<\xi_{2m}$. Physically, this means that other (in addition to the screen-induced one) damping mechanisms, including the viscous boundary layer at the wetted tank surface, matter for the present physical and geometric input parameters. The numerical results on the maximum steady-state wave elevation (1 cm at the wall) noted in Fig. 4 by solid lines were therefore obtained with $\alpha_{2m-1}=0$ and $\alpha_{2m}=\xi_{2m}$. These results are in a good agreement with experiments. For comparison, we present also the quasi-linear prediction from Ref. 1 by the dashed line.

For the case in Fig. 4, the adaptive modal method requires the four asymptotic modal systems M1, M2, M3, and M4 (see the ranges of their applicability on the figure top) to capture different *a posteriori* asymptotic relationships appearing on the whole interval $0.7<\sigma/\sigma_1^*<1.36$. These systems involve the following dominant modes: M1 = {1, 3, 5, 2}, M 2= {1, 5, 7, 9}, M3 = {1, 9, 11, 4}, and M4 = {1, 5, 7, 9, 11, 13, 15, 4, 6}. A requirement for being dominant is clarified by the secondary resonance as $i_3=0.625$, $i_2=0.762$, $i_5=0.808$, $i_7=0.956$, $i_9=1.084$, $i_4=1.085$, $i_{11}=1.198$, $i_{13}=1.303$, $i_6=1.328$, $i_{15}=1.400$, $i_{17}=1.491$. The dominant character of the corresponding modes was also checked by direct numerical simulations.

Appearance of the secondary resonances is clearly seen on the response curves at i_2, i_3, i_7, i_4, i_9, and i_6. Our primary attention is on the secondary resonance at i_7 where a hysteresis occurs with two non-connected branches (it is seen in the zoomed view) and to the combined i_9-and-i_4 resonance (the latter two resonances due to the second and third harmonics are situated very close to each other). The combined i_9-and-i_4 resonance leads to the two non-connected branches, b1 (lower) and b2 (upper). The branch b2 causes a narrow peak which is not experimentally supported for this solidity ratio while it is for higher solidity ratios, e.g., in Figs. 6 and 8, where appearance of the peak agrees with experimental measurements. Even though the experiments were performed by decreasing the forcing frequency after a steady-state sloshing with previous forcing frequency was reached, transients, most likely, caused the experimental values belonging to the lower branch to end at C1. There are no serious free-surface phenomena like (i–iii) (see, Introduction) in experimental observation at the frequency range close to C1, thus, the discrepancy cannot be related to the fact that the multimodal method does not capture specific free-surface motions. This cannot also be explained by accounting for the linear boundary layer damping for the antisymmetric modes. Indeed, including the non-zero linear damping terms ($\alpha_{2m-1}=\xi_{2m-1}$) in modal equations (23a) improves agreement with experiments for the forcing frequencies close to the primary resonance $\sigma/\sigma_1^*=1$, but these damping terms do not effect appearance of the theoretical peak.

Another interesting point is in the frequency range C2 (the i_7-zone with amplification of the third harmonics) where we have a quantitative discrepancy with experiments. The discrepancy can partly be explained by the local breaking waves which are found in experimental observations. Fig. 5 demonstrates a plunging wave breaker appearing near to the vertical walls for $\sigma/\sigma_1^*=0.9574$ belonging to C2.

Figs. 6–11 deal with the pressure drop coefficients K and $\bar{\eta}_{2a}$ for which condition (26) is satisfied. This means that the screen-induced damping should play the leading role for the antisymmetric modes. The linear damping terms play then a secondary role and are only needed in computations to reach the steady-state conditions. Later, they can pass to zero. Theoretical modeling of the experimental cases in Figs. 6–11 is therefore performed with $\alpha_{2m-1}=0$ and a decrease of α_{2m} from ξ_{2m} to $\alpha_{2m}<\xi_{2m}/10$ to get a numerical steady-state solution which is not affected by linear damping terms (as described in Sec. III C). Typically, the steady-state solution obtained with $\alpha_{2m-1}=0$ and $\alpha_{2m}=\xi_{2m}/10$ does not change (the difference is less than 0.1%) with subsequent decrease of α_{2m}. Furthermore, the same asymptotic modal systems M1, M2, M3, and M4 are used in these figures. These systems employ the modified Moiseev asymptotic ordering (25) revised due to the secondary resonance by the dominant ordering $O(\epsilon^{1/3})$ for the following modes: M1 = {1, 3, 5, 2, 4}, M2 = {1, 5, 7, 9, 2, 4}, M3 = {1, 5, 7, 9, 11, 13, 4}, and M4 = {1, 5, 7, 9, 11, 13, 15, 4, 6}. The frequency ranges for these models are shown in the figures.

The theoretical results for $Sn=0.6925(K=41.4063)$ are compared with experimental data in Fig. 6. For this screen,

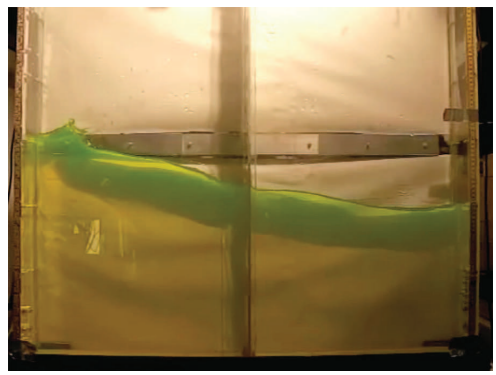

FIG. 5. (Color online) Video of the surface wave phenomena for the case in Fig. 4 with $Sn=0.4725$, $\eta_{2a}/l=0.01$ and $\sigma/\sigma_1^*=0.9574$. (enhanced online) [URL: http://dx.doi.org/10.1063/1.3602508.1]

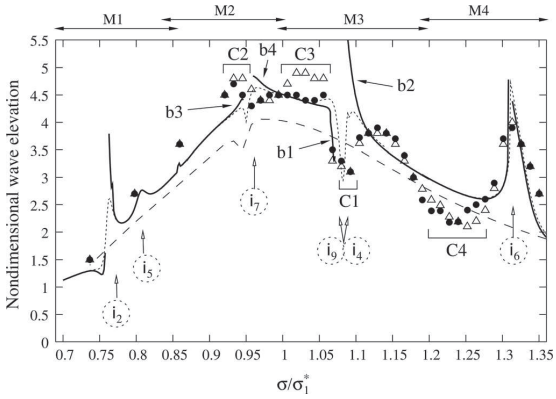

FIG. 6. The theoretical and experimental η_{2a}-scaled maximum wave elevation at the walls; $h/l = 0.4$, $\eta_{2a}/l = 0.01$. The signs (•) and (Δ) mark the experimental values. The submerged screen part has at rest 42 cross-openings (slots), $Sn = 0.6825$, and $K = 15.2292$ (due to (18)). The solid lines denote results by the adaptive multimodal method involving four asymptotic modal systems M1, M2, M3, and M4, whose frequency ranges are shown on the top. These adaptive modal systems employ the modified Moiseev asymptotic ordering (25) corrected due to the secondary resonance by the dominant ordering for the following modes: M1 = {1, 3, 5, 2, 4}, M2 = {1, 5, 7, 9, 2, 4}, M3 = {1, 5, 7, 9, 11, 13, 4}, and M4 = {1, 5, 7, 9, 11, 13, 15, 4, 6}. The asymptotic modal systems adopt $\alpha_{2m-1} = 0$ in Eq. (23a) but $\alpha_{2m} = \xi_{2m}/10$ in Eq. (23b) providing stabilization of the response curves as $\alpha_{2m} \to 0$. The dotted line shows the theoretical results with $\alpha_{2m} = \xi_{2m}$ in Eq. (23b). The dashed line (quasi-linear modal prediction) is taken from Faltinsen *et al.*[1] The values i_k are defined by Eqs. (1) and (2). They imply possibility of secondary resonance due to amplification of the second and third harmonics. The response curves are not connected between the branches b1 and b2 (a combined i_9-and-i_4 resonance), b3 and b4 (caused by the secondary resonance at i_7) as well as at i_6 and i_2.

the secondary resonances are expected at $i_3 = 0.624$, $i_2 = 0.762$, $i_5 = 0.807$, $i_7 = 0.955$, $i_9 = 1.084$, $i_4 = 1.085$, $i_{11} = 1.198$, $i_{13} = 1.303$, $i_6 = 1.328$, $i_{15} = 1.400$, and $i_{17} = 1.491$, i.e., they are almost the same as for the previous screen. Because we are able to test very small α_{2m}, our nonlinear modal theory shows four discontinuities (not two as in Fig. 4) in the response curves associated with the secondary resonances at i_2, i_7, i_9-and-i_4, and i_6. Agreement with experiments looks satisfactory. Experiments support the theoretical peaks at i_7,

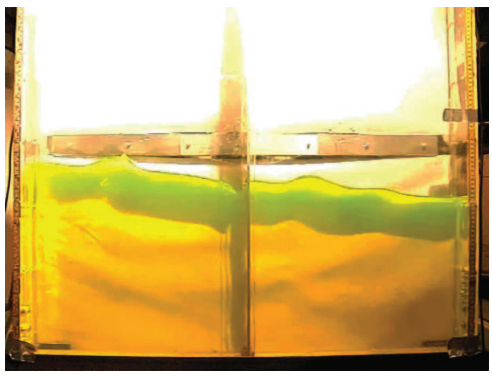

FIG. 7. (Color online) Video of the free-surface phenomena for the case in Fig. 6 with $Sn = 0.6825$, $\eta_{2a}/l = 0.01$ and $\sigma/\sigma_1^* = 1.043329$. (enhanced online). [URL:http://dx.doi.org/10.1063/1.3602508.2]

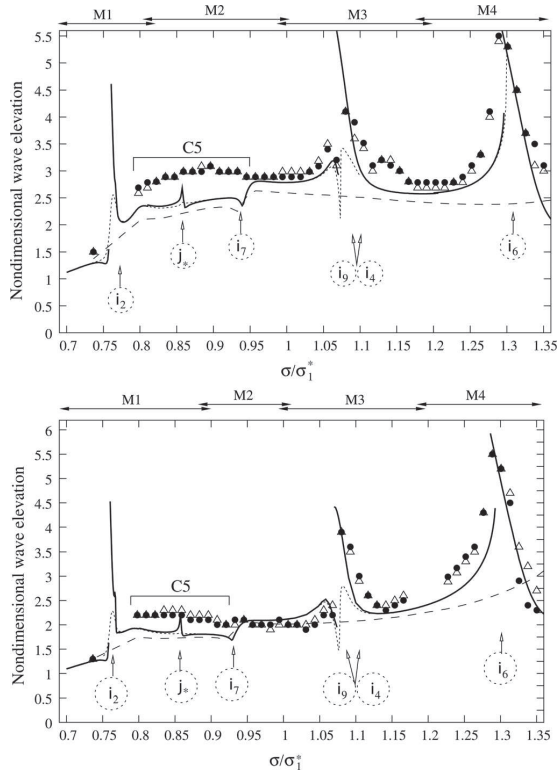

FIG. 8. The same as in Fig. 6 but for $Sn = 0.78625$, $K = 41.4063$, $N = 29$ (upper panel) and $Sn = 0.83875$, $K = 79.88.16$, $N = 22$ (lower panel). The frequency range C5 corresponds to the small-amplitude liquid sloshing where our nonlinear free-surface theory gives results close to the quasi-linear prediction, whereas both theoretical results on the maximum wave elevation at the walls are slightly lower than the experimental values.

i_9-and-i_4, and i_6. There are no appropriate experimental measurements at i_2. To demonstrate the damping effect on the symmetric modes due to the laminar boundary layer at the tank surface (the steady-state solution with $\alpha_{2m-1} = 0$, $\alpha_{2m} = \xi_{2m}$), we present the corresponding maximum theoretical wave elevations by the dotted line. This small damping does not modify the results from a qualitative point of view, but makes it possible to get fully connected response curves. Thus the mechanical system is *very sensitive* to the damping in a neighborhood of the secondary resonance points. Just around these points (see C1, C2, and C3) we see a quantitative discrepancy between our theory and experiments. As for a small frequency range C1 (see also, zone C1 in Fig. 4), the two experimental points in C1 do not belong to the theoretical branch b1 because this branch ends to the left of C1. Here, the linear damping due to the boundary layer at the wetted tank surface (dotted line, $\alpha_{2m-1} = 0$, $\alpha_{2m} = \xi_{2m}$) moves the branch end to the right. Thus, an improvement can be expected if we will be able to get a more accurate estimate of the global damping. The dotted lines show also a damping-related sensitivity in the zone C2. There is a discrepancy in the frequency range C3 where the measurements at the left and right measure probes differ from each other. In this

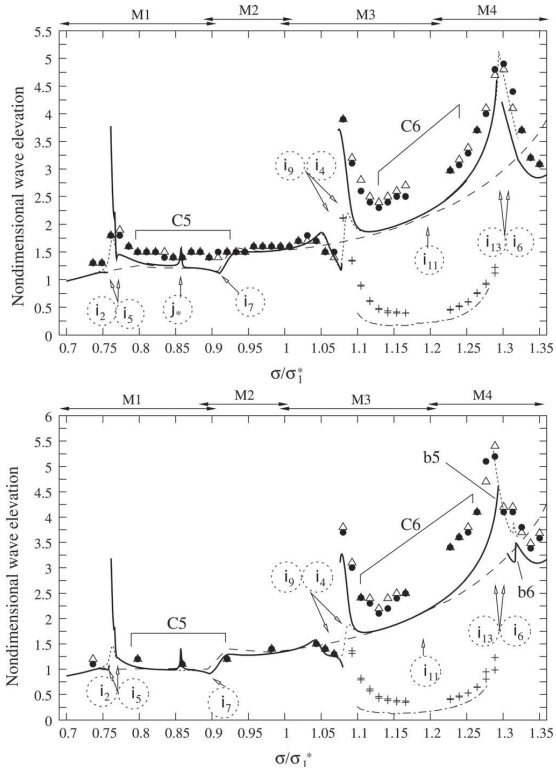

FIG. 9. The same as in Fig. 6 but for $Sn = 0.89125$, $K = 191.550$, $N = 15$ (upper panel) and $Sn = 0.91375$, $K = 315.503$, $N = 12$ (lower panel). The frequency range C5 corresponds to the small-amplitude sloshing where the nonlinear free-surface theory gives results on the steady-state wave elevations close to the quasi-linear prediction and both theoretical results are slightly lower than the experimental measurements. The frequency range C6 denotes a frequency range where a discrepancy occurs due to a larger double harmonics contribution to the measured signal (crests) relative to the theoretical prediction of this secondary harmonics (dashed-and-dotted line).

frequency range, the experiments show steep waves and a local breaking (see, video in Fig. 7). These phenomena may matter. A local wave breaking at the walls was also detected in the frequency range C4.

The theoretical results for $Sn = 0.78625$ and $Sn = 0.83875$ are compared with experimental measurements in the upper and lower panels of Fig. 8, respectively. For the screen with $Sn = 0.78625$, the most important secondary resonances are expected at $i_3 = 0.623$, $i_2 = 0.762$, $i_5 = 0.805$, $i_7 = 0.952$, $i_9 = 1.080$, $i_4 = 1.085$, $i_{11} = 1.194$, $i_{13} = 1.299$, $i_6 = 1.328$, $i_{15} = 1.400$, and $i_{17} = 1.491$. The screen with $Sn = 0.83875$ causes these secondary resonances at $i_3 = 0.621$, $i_2 = 0.762$, $i_5 = 0.803$, $i_7 = 0.950$, $i_9 = 1.078$, $i_4 = 1.085$, $i_{11} = 1.192$, $i_{13} = 1.296$, $i_6 = 1.328$, $i_{15} = 1.400$, and $i_{17} = 1.491$. For these two screens, we have, generally, a good agreement with experiments. A discrepancy appears in the frequency range C5, where the free-surface nonlinearity gives a minor contribution to the wave elevations except, very locally, at the point j_* so that the results by the adaptive modal method is the same as for the quasi-linear theory neglecting the free-surface nonlinearity. A narrow resonance at j_* is due to the fourth harmonics leading to the secondary resonance amplification of the tenth mode (theoretically, at $\sigma/\sigma_1^* = 0.8574252$). This amplification disappears when we include the linear damping terms with $\alpha_{2m-1} = 0$, $\alpha_{2m} = \xi_{2m}$ (dotted line). At the present time, we have no good explanation of the discrepancy at C5, but, because the results are almost the same as for the linear free-surface sloshing formulation in Ref. 1, this discrepancy cannot be explained by the free-surface nonlinearity. One interesting fact is a "knee" in the response curves at i_7 which is present for both linear and nonlinear free-surface theories. The "knee"-behavior is associated with the third harmonics yielded by the $(u|u|)$-nonlinearity in the pressure drop condition ($\bar{D}_m$-quantities in Eq. (23)) and, as we see, it is not influenced by the free-surface nonlinearity. The literature on the pressure drop condition does not give an answer on how precise this condition captures higher harmonics in the hydrodynamic pressure yielded by the viscous flow separation for the sinusoidal approach velocity. Normally, the literature discusses only the first harmonics and deals with the associated equivalent linearization. Furthermore, the terms $K\bar{D}_m$ come from Ref. 1 assuming an average over the mean wetted screen. This assumption may not be correct for higher solidity ratios causing a cross-flow through ΔSc (see Fig. 3).

Considering the experimental screens with higher solidity ratios leads to the results in Fig. 9. In the upper panel with $Sn = 0.89125$, $i_3 = 0.617$, $i_2 = 0.762$, $i_5 = 0.798$, $i_7 = 0.945$, $i_9 = 1.073$, $i_4 = 1.085$, $i_{11} = 1.187$, $i_{13} = 1.291$, $i_6 = 1.328$, $i_{15} = 1.399$, and $i_{17} = 1.491$, and the lower panel with $Sn = 0.91375$ implies $i_3 = 0.613$, $i_2 = 0.762$, $i_5 = 0.792$, $i_7 = 0.938$, $i_9 = 1.063$, $i_4 = 1.085$, $i_{11} = 1.176$, $i_{13} = 1.278$, $i_6 = 1.328$, $i_{15} = 1.398$, and $i_{17} = 1.490$. One can see that, because of the free-surface nonlinearity effect, the secondary resonance peak at i_6 moves to the left of its lowest-order prediction $i_6 = 1.328$ into the zone of the secondary resonance at i_{13}. This leads to a more complicated branch b6 (see also Fig. 11 to understand the tendency with increasing Sn) affected by a complex nonlinear interaction of the 6th and 13th modes. Including additional nonzero linear damping terms (here, $\alpha_{2m-1} = 0$, $\alpha_{2m} = \xi_{2m}$) gives a better agreement

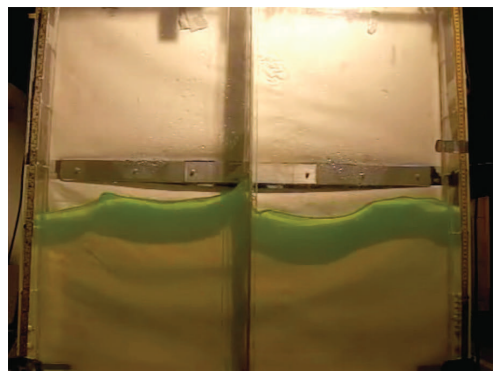

FIG. 10. (Color online) Video for the case in Fig. 9 (upper panel) with $Sn = 0.89125$, $\sigma/\sigma_1^* = 0.1288$. (enhanced online). [URL: http://dx.doi.org/10.1063/1.3602508.3]

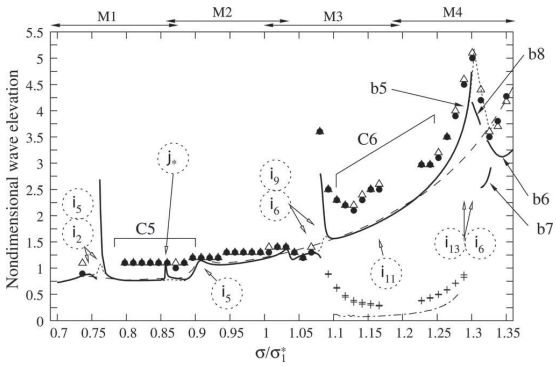

FIG. 11. The same as in Fig. 6 but for $Sn = 0.93625$, $K = 597.759$, and $N = 9$.

with experiments for the branch b6, but not for the branch b5. Fig. 10 shows the video for the steady-state sloshing associated with the top experimental point on the branch b5 in the upper panel of Fig. 9. The video demonstrates steep waves with local breaking and a pronounced jump in the free-surface profile at the screen. It is also clearly seen a flow from water to air through the screen area ΔSc. All these local free-surface phenomena may, generally, cause an extra dissipation which is not captured by the damping terms (22) with constant values of α_m.

The flow through ΔSc was also observed for the model tests conducted for the frequency range C6 (unfortunately, we do not have appropriate video). In this frequency range, the experimental signal (crests) contains a clearly larger second Fourier harmonics contribution relative to that by our nonlinear sloshing theory (dashed-and-dotted line). Our theory fully accounts for the quadratic free-surface nonlinearity which, from a mathematical point of view, is responsible for the second Fourier harmonics. Thus, we should look for other physical mechanisms generating this harmonics. For example, a dedicated analysis of the free-surface jump at the screen and related flow through ΔSc can, possibly, lead to the desirable second harmonics. We neglect the latter flow. In our pressure drop condition (19), the integration is not over the actual wetted screen (not from $-h$ to $\zeta_1(t)$ in Fig. 3) but over the mean wetted screen, i.e. from $-h$ to 0, which implies the lowest-order quantity in terms of small ζ_1 and ζ_2. If we speculatively integrate from $-h$ to ζ_1 in Eq. (19) and expand the obtained integral in a Taylor series by assuming $\zeta_1(t) = O\left(\epsilon^{1/3}\right)$, one gets

$$-K\frac{\alpha_m\kappa_{2m-1}}{4h\Lambda^{(0)}_{(2m-1)(2m-1)}}\left(\int_{-h}^{0}\left(\sum_{i=1}^{\infty}\frac{\dot\beta_{2i-1}}{\kappa_{2i-1}}U_i(z)\right)\times\left|\sum_{i=1}^{\infty}\frac{\dot\beta_{2i-1}}{\kappa_{2i-1}}U_i(z)\right|\mathrm{d}z-\underline{\left(\sum_{i=1}^{\infty}\frac{\dot\beta_{2i-1}}{\kappa_{2i-1}}U_i(0)\right)\left|\sum_{i=1}^{\infty}\frac{\dot\beta_{2i-1}}{\kappa_{2i-1}}U_i(0)\right|f_1(0-)\beta_1}+\cdots\right). \quad (27)$$

Because $\beta_1 = O\left(\epsilon^{1/3}\right)$ and β_1 contains the nonzero first Fourier harmonics, the underlined quantity in Eq. (27) yields the second harmonics to appear in the modal equations for the antisymmetric modes. A dedicated theoretical analysis of whether the screen-induced free-surface jump causes a second Fourier harmonics effect is therefore needed.

The same underprediction of the second harmonics in the frequency range C6 is seen for the larger solidity ratio 0.93625 in Fig. 11. Again, it cannot be related to the free-surface nonlinearity. Here, $i_3 = 0.604$, $i_2 = 0.762$, $i_5 = 0.779$, $i_7 = 0.921$, $i_9 = 1.063$, $i_4 = 1.085$, $i_{11} = 1.158$, $i_{13} = 1.262$, $i_6 = 1.328$, $i_{15} = 1.383$, and $i_{17} = 1.487$. The most interesting in the figure is the appearance of a non-connected branching at the i_6-and-i_{13} secondary resonance. Here, we see the non-connected branches b5, b6, b7, and b8, which, however, become connected and sufficiently modified when we include the linear damping terms for the symmetric modes ($\alpha_{2m-1} = 0$, $\alpha_{2m} = \xi_{2m}$).

IV. CONCLUSIONS

A theoretical approach was developed to describe secondary resonance in a rectangular tank with a central slotted screen of high solidity ratio. The secondary resonance is well known for two-dimensional steady-state resonant liquid sloshing in a clean tank when the forcing frequency σ is close to the lowest natural sloshing frequency (see Chap. 8 in Ref. 9). For the finite liquid depth, the secondary resonance leads to amplification of the second and third natural sloshing modes caused by quadratic and cubic free-surface nonlinearities, and the corresponding second and third harmonics (2σ and 3σ), respectively. Because of the trigonometric algebra for the natural sloshing modes, non-commensurate spectrum and damping, one can find only two forcing frequencies where the secondary resonance phenomenon occurs. These frequencies are situated away from the primary resonance frequency and, therefore, can matter only by increasing the forcing amplitude. Inserting a central slotted screen with a high solidity ratio, $0.5 \lesssim Sn < 1$, modifies the natural sloshing modes and, as a consequence, the secondary resonance phenomenon qualitatively changes. Because of the screen, the secondary resonance amplification can, depending on the input geometric and physical parameters, happen at a certain number of frequencies close to the primary resonance and, thereby, the resonance response curves would have a multi-peak shape. Higher natural sloshing modes (not only second and third) can now be excited. The present paper gives a qualitative and quantitative prediction of these facts.

Our theoretical approach is based on the nonlinear adaptive multimodal method which was first proposed by Faltinsen and Timokha[4] as a generalization of the Moiseev-type asymptotic approach for clean tanks. The adaptive modal method is an efficient numerical-and-analytical approach for parametric studies of the steady-state resonant sloshing and gives a rather accurate prediction and explanation of the multi-branching and multi-peaks of the response curves. The method requires derivation of a polynomial-type nonlinear modal system which is a base for asymptotic modal systems accounting for dominant contribution of higher modes to the resonant liquid sloshing for certain frequency domains. Such a polynomial-type modal system was

derived for two-dimensional and three-dimensional sloshing in rectangular tanks. The present paper revises the adaptive modal method for screen-equipped two-dimensional tanks. The revisions require changes in the Moiseev-type asymptotic ordering and a new prediction of the forcing frequencies at which the secondary resonance occurs. According to these revisions, a relatively large number of dominant modes should be included into the asymptotic analysis of steady-state resonance sloshing. The method assumes an incompressible liquid with irrotational flow except in a local neighborhood of the screen. Following Faltinsen *et al.*,[1] the viscous screen effect for the antisymmetric modes (which determines the cross-flow) is expressed by an "integral"-type pressure drop condition which leads to the corresponding integral quantities in the modal equations responsible for antisymmetric modes. This situation can, of course, change when using the proposed multimodal method and the pressure drop condition for a non-central location of the screen, or for several screens installed in the tank. Following Ref. 2 and the presented adaptive multimodal technique, one should then derive a revised nonlinear adaptive modal system where, depending on the number of screens and their position, the $(\cdot|\cdot|)$-integral quantities can appear in all the modal equations.

For the central screen case, the symmetric modes are theoretically not damped. This requires artificial linear damping terms in the modal equations responsible for the symmetric modes which help to reach steady-state solutions in our calculations. For the model tests case, decreasing the artificial damping rates α_{2m} leads to convergence of the numerical procedure with $\alpha_{2m} \lesssim \xi_{2m}/10$ (ξ_{2m} are the damping rates for *linear sloshing* due to the laminar viscous boundary layer at the mean wetted tank surface for the clean tank) so that, as for the clean tank case by Faltinsen and Timokha,[4] the secondary resonance jumps on the response curves are clearly detected with the damping rates lower then ξ_i. This means that laminar viscous layer plays a minor role in damping the symmetric modes in the studied case.

Even though the theoretical approach gives very good qualitative and, generally, good quantitative prediction of the experimental steady-state elevations, there is a discrepancy between theory and experiments in certain frequency ranges. This can partly be explained by the free-surface phenomena discussed in Ref. 1. Another possible reason for quantitative discrepancies is that the "integral"-type pressure drop condition cannot capture effects of specific flows at the screen with increasing solidity ratio when a free-surface jump between left and right screen sides occurs. Unfortunately, we were not able to measure this screen-caused jump ΔSc due to due to local phenomena at the screen region accompanied with the free-surface segmentation and jet flow through the holes. Our adaptive multimodal theory detects the maximum jump ΔSc at the primary resonance zone as well as at the secondary resonances by antisymmetric modes, i.e., when $\sigma/\sigma_1^* \approx i_{2k+1}$, $k \geq 1$. This is because of the central position of the screen which implies continuous symmetric modes. A dedicated study of these nearly screen flows is required. Furthermore, we need to express the damping due to tangential drag at the screen.

[1]O. Faltinsen, R. Firoozkoohi, and A. Timokha, Phys. Fluids **23**, 042101 (2011).
[2]O. M. Faltinsen and A. N. Timokha, J. Sound Vib. **330**, 1490 (2011).
[3]R. D. Blevins, *Applied Fluid Dynamics* (Krieger Publishing Company, Malabar, FL, 1992).
[4]O. M. Faltinsen and A. N. Timokha, J. Fluid Mech. **432**, 167 (2001).
[5]M. Hermann and A. Timokha, Math. Models Meth. Appl. Sci. **18**, 1845 (2008).
[6]J. R. Ockendon, H. Ockendon, and D. D. Waterhouse, J. Fluid Mech. **315**, 317 (1996).
[7]G. Wu, Ocean Eng. **34**, 2345 (2007).
[8]C.-H.Wu and B.-F. Chen, Ocean Eng. **36**, 500 (2009).
[9]O. M. Faltinsen and A. N. Timokha, *Sloshing* (Cambridge University Press, Cambridge, 2009).
[10]O. M. Faltinsen and A. N. Timokha, J. Fluid Mech. **470**, 319 (2002).
[11]M. Maravani and M. S. Hamed, Int. J. Numer. Methods Fluids **65**, 834 (2011).
[12]N. N. Moiseev, J. Appl. Math. Mech. **22**, 860 (1958).
[13]O. M. Faltinsen, J. Ship Res. **18**, 224 (1974).
[14]O. Faltinsen, O. Rognebakke, I. Lukovsky, and A. Timokha, J. Fluid Mech. **407**, 201 (2000).
[15]J. Love and M. Tait, J. Fluids Struct. **26**, 1058 (2010).
[16]J. Love, M. Tait, and H.Toopchi-Nezhad, Eng. Struct. **33**, 738 (2011).
[17]I. Lukovsky and A. Timokha, *Variational Methods in Nonlinear Problems of the Dynamics of a Limited Liquid Volume* (Institute of Mathematics of the National Academy of Sciences of Ukraine, Kiev, 1995) in Russian.
[18]R. E. Moore and L. M. Perko, J. Fluid Mech. **22**, 305 (1964).
[19]L. Perko, J. Fluid Mech. **35** (1), 77 (1969).
[20]M. La Rocca, M. Scortino, and M. Boniforti, Fluid Dyn. Res. **27**, 225 (2000).
[21]M. Tait, A. El Damatty, N. Isyumov, and M. Siddique, J. Fluids Struct. **20**, 1007 (2005).
[22]O. Faltinsen, O. Rognebakke, and A. Timokha, Phys. Fluids **18**, 012103 (2006).

Previous PhD theses published at the Departement of Marine Technology
(earlier: Faculty of Marine Technology)
NORWEGIAN UNIVERSITY OF SCIENCE AND TECHNOLOGY

Report No.	Author	Title
	Kavlie, Dag	Optimization of Plane Elastic Grillages, 1967
	Hansen, Hans R.	Man-Machine Communication and Data-Storage Methods in Ship Structural Design, 1971
	Gisvold, Kaare M.	A Method for non-linear mixed -integer programming and its Application to Design Problems, 1971
	Lund, Sverre	Tanker Frame Optimalization by means of SUMT-Transformation and Behaviour Models, 1971
	Vinje, Tor	On Vibration of Spherical Shells Interacting with Fluid, 1972
	Lorentz, Jan D.	Tank Arrangement for Crude Oil Carriers in Accordance with the new Anti-Pollution Regulations, 1975
	Carlsen, Carl A.	Computer-Aided Design of Tanker Structures, 1975
	Larsen, Carl M.	Static and Dynamic Analysis of Offshore Pipelines during Installation, 1976
UR-79-01	Brigt Hatlestad, MK	The finite element method used in a fatigue evaluation of fixed offshore platforms. (Dr.Ing. Thesis)
UR-79-02	Erik Pettersen, MK	Analysis and design of cellular structures. (Dr.Ing. Thesis)
UR-79-03	Sverre Valsgård, MK	Finite difference and finite element methods applied to nonlinear analysis of plated structures. (Dr.Ing. Thesis)
UR-79-04	Nils T. Nordsve, MK	Finite element collapse analysis of structural members considering imperfections and stresses due to fabrication. (Dr.Ing. Thesis)
UR-79-05	Ivar J. Fylling, MK	Analysis of towline forces in ocean towing systems. (Dr.Ing. Thesis)
UR-80-06	Nils Sandsmark, MM	Analysis of Stationary and Transient Heat Conduction by the Use of the Finite Element Method. (Dr.Ing. Thesis)
UR-80-09	Sverre Haver, MK	Analysis of uncertainties related to the stochastic modeling of ocean waves. (Dr.Ing. Thesis)
UR-81-15	Odland, Jonas	On the Strength of welded Ring stiffened cylindrical Shells primarily subjected to axial Compression
UR-82-17	Engesvik, Knut	Analysis of Uncertainties in the fatigue Capacity of

		Welded Joints
UR-82-18	Rye, Henrik	Ocean wave groups
UR-83-30	Eide, Oddvar Inge	On Cumulative Fatigue Damage in Steel Welded Joints
UR-83-33	Mo, Olav	Stochastic Time Domain Analysis of Slender Offshore Structures
UR-83-34	Amdahl, Jørgen	Energy absorption in Ship-platform impacts
UR-84-37	Mørch, Morten	Motions and mooring forces of semi submersibles as determined by full-scale measurements and theoretical analysis
UR-84-38	Soares, C. Guedes	Probabilistic models for load effects in ship structures
UR-84-39	Aarsnes, Jan V.	Current forces on ships
UR-84-40	Czujko, Jerzy	Collapse Analysis of Plates subjected to Biaxial Compression and Lateral Load
UR-85-46	Alf G. Engseth, MK	Finite element collapse analysis of tubular steel offshore structures. (Dr.Ing. Thesis)
UR-86-47	Dengody Sheshappa, MP	A Computer Design Model for Optimizing Fishing Vessel Designs Based on Techno-Economic Analysis. (Dr.Ing. Thesis)
UR-86-48	Vidar Aanesland, MH	A Theoretical and Numerical Study of Ship Wave Resistance. (Dr.Ing. Thesis)
UR-86-49	Heinz-Joachim Wessel, MK	Fracture Mechanics Analysis of Crack Growth in Plate Girders. (Dr.Ing. Thesis)
UR-86-50	Jon Taby, MK	Ultimate and Post-ultimate Strength of Dented Tubular Members. (Dr.Ing. Thesis)
UR-86-51	Walter Lian, MH	A Numerical Study of Two-Dimensional Separated Flow Past Bluff Bodies at Moderate KC-Numbers. (Dr.Ing. Thesis)
UR-86-52	Bjørn Sortland, MH	Force Measurements in Oscillating Flow on Ship Sections and Circular Cylinders in a U-Tube Water Tank. (Dr.Ing. Thesis)
UR-86-53	Kurt Strand, MM	A System Dynamic Approach to One-dimensional Fluid Flow. (Dr.Ing. Thesis)
UR-86-54	Arne Edvin Løken, MH	Three Dimensional Second Order Hydrodynamic Effects on Ocean Structures in Waves. (Dr.Ing. Thesis)
UR-86-55	Sigurd Falch, MH	A Numerical Study of Slamming of Two-Dimensional Bodies. (Dr.Ing. Thesis)
UR-87-56	Arne Braathen, MH	Application of a Vortex Tracking Method to the Prediction of Roll Damping of a Two-Dimension Floating Body. (Dr.Ing. Thesis)

UR-87-57	Bernt Leira, MK	Gaussian Vector Processes for Reliability Analysis involving Wave-Induced Load Effects. (Dr.Ing. Thesis)
UR-87-58	Magnus Småvik, MM	Thermal Load and Process Characteristics in a Two-Stroke Diesel Engine with Thermal Barriers (in Norwegian). (Dr.Ing. Thesis)
MTA-88-59	Bernt Arild Bremdal, MP	An Investigation of Marine Installation Processes – A Knowledge - Based Planning Approach. (Dr.Ing. Thesis)
MTA-88-60	Xu Jun, MK	Non-linear Dynamic Analysis of Space-framed Offshore Structures. (Dr.Ing. Thesis)
MTA-89-61	Gang Miao, MH	Hydrodynamic Forces and Dynamic Responses of Circular Cylinders in Wave Zones. (Dr.Ing. Thesis)
MTA-89-62	Martin Greenhow, MH	Linear and Non-Linear Studies of Waves and Floating Bodies. Part I and Part II. (Dr.Techn. Thesis)
MTA-89-63	Chang Li, MH	Force Coefficients of Spheres and Cubes in Oscillatory Flow with and without Current. (Dr.Ing. Thesis
MTA-89-64	Hu Ying, MP	A Study of Marketing and Design in Development of Marine Transport Systems. (Dr.Ing. Thesis)
MTA-89-65	Arild Jæger, MH	Seakeeping, Dynamic Stability and Performance of a Wedge Shaped Planing Hull. (Dr.Ing. Thesis)
MTA-89-66	Chan Siu Hung, MM	The dynamic characteristics of tilting-pad bearings
MTA-89-67	Kim Wikstrøm, MP	Analysis av projekteringen for ett offshore projekt. (Licenciat-avhandling)
MTA-89-68	Jiao Guoyang, MK	Reliability Analysis of Crack Growth under Random Loading, considering Model Updating. (Dr.Ing. Thesis)
MTA-89-69	Arnt Olufsen, MK	Uncertainty and Reliability Analysis of Fixed Offshore Structures. (Dr.Ing. Thesis)
MTA-89-70	Wu Yu-Lin, MR	System Reliability Analyses of Offshore Structures using improved Truss and Beam Models. (Dr.Ing. Thesis)
MTA-90-71	Jan Roger Hoff, MH	Three-dimensional Green function of a vessel with forward speed in waves. (Dr.Ing. Thesis)
MTA-90-72	Rong Zhao, MH	Slow-Drift Motions of a Moored Two-Dimensional Body in Irregular Waves. (Dr.Ing. Thesis)
MTA-90-73	Atle Minsaas, MP	Economical Risk Analysis. (Dr.Ing. Thesis)
MTA-90-74	Knut-Aril Farnes, MK	Long-term Statistics of Response in Non-linear Marine Structures. (Dr.Ing. Thesis)
MTA-90-75	Torbjørn Sotberg, MK	Application of Reliability Methods for Safety Assessment of Submarine Pipelines. (Dr.Ing.

		Thesis)
MTA-90-76	Zeuthen, Steffen, MP	SEAMAID. A computational model of the design process in a constraint-based logic programming environment. An example from the offshore domain. (Dr.Ing. Thesis)
MTA-91-77	Haagensen, Sven, MM	Fuel Dependant Cyclic Variability in a Spark Ignition Engine - An Optical Approach. (Dr.Ing. Thesis)
MTA-91-78	Løland, Geir, MH	Current forces on and flow through fish farms. (Dr.Ing. Thesis)
MTA-91-79	Hoen, Christopher, MK	System Identification of Structures Excited by Stochastic Load Processes. (Dr.Ing. Thesis)
MTA-91-80	Haugen, Stein, MK	Probabilistic Evaluation of Frequency of Collision between Ships and Offshore Platforms. (Dr.Ing. Thesis)
MTA-91-81	Sødahl, Nils, MK	Methods for Design and Analysis of Flexible Risers. (Dr.Ing. Thesis)
MTA-91-82	Ormberg, Harald, MK	Non-linear Response Analysis of Floating Fish Farm Systems. (Dr.Ing. Thesis)
MTA-91-83	Marley, Mark J., MK	Time Variant Reliability under Fatigue Degradation. (Dr.Ing. Thesis)
MTA-91-84	Krokstad, Jørgen R., MH	Second-order Loads in Multidirectional Seas. (Dr.Ing. Thesis)
MTA-91-85	Molteberg, Gunnar A., MM	The Application of System Identification Techniques to Performance Monitoring of Four Stroke Turbocharged Diesel Engines. (Dr.Ing. Thesis)
MTA-92-86	Mørch, Hans Jørgen Bjelke, MH	Aspects of Hydrofoil Design: with Emphasis on Hydrofoil Interaction in Calm Water. (Dr.Ing. Thesis)
MTA-92-87	Chan Siu Hung, MM	Nonlinear Analysis of Rotordynamic Instabilities in Highspeed Turbomachinery. (Dr.Ing. Thesis)
MTA-92-88	Bessason, Bjarni, MK	Assessment of Earthquake Loading and Response of Seismically Isolated Bridges. (Dr.Ing. Thesis)
MTA-92-89	Langli, Geir, MP	Improving Operational Safety through exploitation of Design Knowledge - an investigation of offshore platform safety. (Dr.Ing. Thesis)
MTA-92-90	Sævik, Svein, MK	On Stresses and Fatigue in Flexible Pipes. (Dr.Ing. Thesis)
MTA-92-91	Ask, Tor Ø., MM	Ignition and Flame Growth in Lean Gas-Air Mixtures. An Experimental Study with a Schlieren System. (Dr.Ing. Thesis)
MTA-86-92	Hessen, Gunnar, MK	Fracture Mechanics Analysis of Stiffened Tubular Members. (Dr.Ing. Thesis)

MTA-93-93	Steinebach, Christian, MM	Knowledge Based Systems for Diagnosis of Rotating Machinery. (Dr.Ing. Thesis)
MTA-93-94	Dalane, Jan Inge, MK	System Reliability in Design and Maintenance of Fixed Offshore Structures. (Dr.Ing. Thesis)
MTA-93-95	Steen, Sverre, MH	Cobblestone Effect on SES. (Dr.Ing. Thesis)
MTA-93-96	Karunakaran, Daniel, MK	Nonlinear Dynamic Response and Reliability Analysis of Drag-dominated Offshore Platforms. (Dr.Ing. Thesis)
MTA-93-97	Hagen, Arnulf, MP	The Framework of a Design Process Language. (Dr.Ing. Thesis)
MTA-93-98	Nordrik, Rune, MM	Investigation of Spark Ignition and Autoignition in Methane and Air Using Computational Fluid Dynamics and Chemical Reaction Kinetics. A Numerical Study of Ignition Processes in Internal Combustion Engines. (Dr.Ing. Thesis)
MTA-94-99	Passano, Elizabeth, MK	Efficient Analysis of Nonlinear Slender Marine Structures. (Dr.Ing. Thesis)
MTA-94-100	Kvålsvold, Jan, MH	Hydroelastic Modelling of Wetdeck Slamming on Multihull Vessels. (Dr.Ing. Thesis)
MTA-94-102	Bech, Sidsel M., MK	Experimental and Numerical Determination of Stiffness and Strength of GRP/PVC Sandwich Structures. (Dr.Ing. Thesis)
MTA-95-103	Paulsen, Hallvard, MM	A Study of Transient Jet and Spray using a Schlieren Method and Digital Image Processing. (Dr.Ing. Thesis)
MTA-95-104	Hovde, Geir Olav, MK	Fatigue and Overload Reliability of Offshore Structural Systems, Considering the Effect of Inspection and Repair. (Dr.Ing. Thesis)
MTA-95-105	Wang, Xiaozhi, MK	Reliability Analysis of Production Ships with Emphasis on Load Combination and Ultimate Strength. (Dr.Ing. Thesis)
MTA-95-106	Ulstein, Tore, MH	Nonlinear Effects of a Flexible Stern Seal Bag on Cobblestone Oscillations of an SES. (Dr.Ing. Thesis)
MTA-95-107	Solaas, Frøydis, MH	Analytical and Numerical Studies of Sloshing in Tanks. (Dr.Ing. Thesis)
MTA-95-108	Hellan, Øyvind, MK	Nonlinear Pushover and Cyclic Analyses in Ultimate Limit State Design and Reassessment of Tubular Steel Offshore Structures. (Dr.Ing. Thesis)
MTA-95-109	Hermundstad, Ole A., MK	Theoretical and Experimental Hydroelastic Analysis of High Speed Vessels. (Dr.Ing. Thesis)
MTA-96-110	Bratland, Anne K., MH	Wave-Current Interaction Effects on Large-Volume Bodies in Water of Finite Depth. (Dr.Ing. Thesis)
MTA-96-111	Herfjord, Kjell, MH	A Study of Two-dimensional Separated Flow by a Combination of the Finite Element Method and

		Navier-Stokes Equations. (Dr.Ing. Thesis)
MTA-96-112	Æsøy, Vilmar, MM	Hot Surface Assisted Compression Ignition in a Direct Injection Natural Gas Engine. (Dr.Ing. Thesis)
MTA-96-113	Eknes, Monika L., MK	Escalation Scenarios Initiated by Gas Explosions on Offshore Installations. (Dr.Ing. Thesis)
MTA-96-114	Erikstad, Stein O., MP	A Decision Support Model for Preliminary Ship Design. (Dr.Ing. Thesis)
MTA-96-115	Pedersen, Egil, MH	A Nautical Study of Towed Marine Seismic Streamer Cable Configurations. (Dr.Ing. Thesis)
MTA-97-116	Moksnes, Paul O., MM	Modelling Two-Phase Thermo-Fluid Systems Using Bond Graphs. (Dr.Ing. Thesis)
MTA-97-117	Halse, Karl H., MK	On Vortex Shedding and Prediction of Vortex-Induced Vibrations of Circular Cylinders. (Dr.Ing. Thesis)
MTA-97-118	Igland, Ragnar T., MK	Reliability Analysis of Pipelines during Laying, considering Ultimate Strength under Combined Loads. (Dr.Ing. Thesis)
MTA-97-119	Pedersen, Hans-P., MP	Levendefiskteknologi for fiskefartøy. (Dr.Ing. Thesis)
MTA-98-120	Vikestad, Kyrre, MK	Multi-Frequency Response of a Cylinder Subjected to Vortex Shedding and Support Motions. (Dr.Ing. Thesis)
MTA-98-121	Azadi, Mohammad R. E., MK	Analysis of Static and Dynamic Pile-Soil-Jacket Behaviour. (Dr.Ing. Thesis)
MTA-98-122	Ulltang, Terje, MP	A Communication Model for Product Information. (Dr.Ing. Thesis)
MTA-98-123	Torbergsen, Erik, MM	Impeller/Diffuser Interaction Forces in Centrifugal Pumps. (Dr.Ing. Thesis)
MTA-98-124	Hansen, Edmond, MH	A Discrete Element Model to Study Marginal Ice Zone Dynamics and the Behaviour of Vessels Moored in Broken Ice. (Dr.Ing. Thesis)
MTA-98-125	Videiro, Paulo M., MK	Reliability Based Design of Marine Structures. (Dr.Ing. Thesis)
MTA-99-126	Mainçon, Philippe, MK	Fatigue Reliability of Long Welds Application to Titanium Risers. (Dr.Ing. Thesis)
MTA-99-127	Haugen, Elin M., MH	Hydroelastic Analysis of Slamming on Stiffened Plates with Application to Catamaran Wetdecks. (Dr.Ing. Thesis)
MTA-99-128	Langhelle, Nina K., MK	Experimental Validation and Calibration of Nonlinear Finite Element Models for Use in Design of Aluminium Structures Exposed to Fire. (Dr.Ing. Thesis)
MTA-99-	Berstad, Are J., MK	Calculation of Fatigue Damage in Ship Structures.

129		(Dr.Ing. Thesis)
MTA-99-130	Andersen, Trond M., MM	Short Term Maintenance Planning. (Dr.Ing. Thesis)
MTA-99-131	Tveiten, Bård Wathne, MK	Fatigue Assessment of Welded Aluminium Ship Details. (Dr.Ing. Thesis)
MTA-99-132	Søreide, Fredrik, MP	Applications of underwater technology in deep water archaeology. Principles and practice. (Dr.Ing. Thesis)
MTA-99-133	Tønnessen, Rune, MH	A Finite Element Method Applied to Unsteady Viscous Flow Around 2D Blunt Bodies With Sharp Corners. (Dr.Ing. Thesis)
MTA-99-134	Elvekrok, Dag R., MP	Engineering Integration in Field Development Projects in the Norwegian Oil and Gas Industry. The Supplier Management of Norne. (Dr.Ing. Thesis)
MTA-99-135	Fagerholt, Kjetil, MP	Optimeringsbaserte Metoder for Ruteplanlegging innen skipsfart. (Dr.Ing. Thesis)
MTA-99-136	Bysveen, Marie, MM	Visualization in Two Directions on a Dynamic Combustion Rig for Studies of Fuel Quality. (Dr.Ing. Thesis)
MTA-2000-137	Storteig, Eskild, MM	Dynamic characteristics and leakage performance of liquid annular seals in centrifugal pumps. (Dr.Ing. Thesis)
MTA-2000-138	Sagli, Gro, MK	Model uncertainty and simplified estimates of long term extremes of hull girder loads in ships. (Dr.Ing. Thesis)
MTA-2000-139	Tronstad, Harald, MK	Nonlinear analysis and design of cable net structures like fishing gear based on the finite element method. (Dr.Ing. Thesis)
MTA-2000-140	Kroneberg, André, MP	Innovation in shipping by using scenarios. (Dr.Ing. Thesis)
MTA-2000-141	Haslum, Herbjørn Alf, MH	Simplified methods applied to nonlinear motion of spar platforms. (Dr.Ing. Thesis)
MTA-2001-142	Samdal, Ole Johan, MM	Modelling of Degradation Mechanisms and Stressor Interaction on Static Mechanical Equipment Residual Lifetime. (Dr.Ing. Thesis)
MTA-2001-143	Baarholm, Rolf Jarle, MH	Theoretical and experimental studies of wave impact underneath decks of offshore platforms. (Dr.Ing. Thesis)
MTA-2001-144	Wang, Lihua, MK	Probabilistic Analysis of Nonlinear Wave-induced Loads on Ships. (Dr.Ing. Thesis)
MTA-2001-145	Kristensen, Odd H. Holt, MK	Ultimate Capacity of Aluminium Plates under Multiple Loads, Considering HAZ Properties. (Dr.Ing. Thesis)
MTA-2001-146	Greco, Marilena, MH	A Two-Dimensional Study of Green-Water Loading. (Dr.Ing. Thesis)

MTA-2001-147	Heggelund, Svein E., MK	Calculation of Global Design Loads and Load Effects in Large High Speed Catamarans. (Dr.Ing. Thesis)
MTA-2001-148	Babalola, Olusegun T., MK	Fatigue Strength of Titanium Risers – Defect Sensitivity. (Dr.Ing. Thesis)
MTA-2001-149	Mohammed, Abuu K., MK	Nonlinear Shell Finite Elements for Ultimate Strength and Collapse Analysis of Ship Structures. (Dr.Ing. Thesis)
MTA-2002-150	Holmedal, Lars E., MH	Wave-current interactions in the vicinity of the sea bed. (Dr.Ing. Thesis)
MTA-2002-151	Rognebakke, Olav F., MH	Sloshing in rectangular tanks and interaction with ship motions. (Dr.Ing. Thesis)
MTA-2002-152	Lader, Pål Furset, MH	Geometry and Kinematics of Breaking Waves. (Dr.Ing. Thesis)
MTA-2002-153	Yang, Qinzheng, MH	Wash and wave resistance of ships in finite water depth. (Dr.Ing. Thesis)
MTA-2002-154	Melhus, Øyvin, MM	Utilization of VOC in Diesel Engines. Ignition and combustion of VOC released by crude oil tankers. (Dr.Ing. Thesis)
MTA-2002-155	Ronæss, Marit, MH	Wave Induced Motions of Two Ships Advancing on Parallel Course. (Dr.Ing. Thesis)
MTA-2002-156	Økland, Ole D., MK	Numerical and experimental investigation of whipping in twin hull vessels exposed to severe wet deck slamming. (Dr.Ing. Thesis)
MTA-2002-157	Ge, Chunhua, MK	Global Hydroelastic Response of Catamarans due to Wet Deck Slamming. (Dr.Ing. Thesis)
MTA-2002-158	Byklum, Eirik, MK	Nonlinear Shell Finite Elements for Ultimate Strength and Collapse Analysis of Ship Structures. (Dr.Ing. Thesis)
IMT-2003-1	Chen, Haibo, MK	Probabilistic Evaluation of FPSO-Tanker Collision in Tandem Offloading Operation. (Dr.Ing. Thesis)
IMT-2003-2	Skaugset, Kjetil Bjørn, MK	On the Suppression of Vortex Induced Vibrations of Circular Cylinders by Radial Water Jets. (Dr.Ing. Thesis)
IMT-2003-3	Chezhian, Muthu	Three-Dimensional Analysis of Slamming. (Dr.Ing. Thesis)
IMT-2003-4	Buhaug, Øyvind	Deposit Formation on Cylinder Liner Surfaces in Medium Speed Engines. (Dr.Ing. Thesis)
IMT-2003-5	Tregde, Vidar	Aspects of Ship Design: Optimization of Aft Hull with Inverse Geometry Design. (Dr.Ing. Thesis)
IMT-2003-6	Wist, Hanne Therese	Statistical Properties of Successive Ocean Wave Parameters. (Dr.Ing. Thesis)

IMT-2004-7	Ransau, Samuel	Numerical Methods for Flows with Evolving Interfaces. (Dr.Ing. Thesis)
IMT-2004-8	Soma, Torkel	Blue-Chip or Sub-Standard. A data interrogation approach of identity safety characteristics of shipping organization. (Dr.Ing. Thesis)
IMT-2004-9	Ersdal, Svein	An experimental study of hydrodynamic forces on cylinders and cables in near axial flow. (Dr.Ing. Thesis)
IMT-2005-10	Brodtkorb, Per Andreas	The Probability of Occurrence of Dangerous Wave Situations at Sea. (Dr.Ing. Thesis)
IMT-2005-11	Yttervik, Rune	Ocean current variability in relation to offshore engineering. (Dr.Ing. Thesis)
IMT-2005-12	Fredheim, Arne	Current Forces on Net-Structures. (Dr.Ing. Thesis)
IMT-2005-13	Heggernes, Kjetil	Flow around marine structures. (Dr.Ing. Thesis
IMT-2005-14	Fouques, Sebastien	Lagrangian Modelling of Ocean Surface Waves and Synthetic Aperture Radar Wave Measurements. (Dr.Ing. Thesis)
IMT-2006-15	Holm, Håvard	Numerical calculation of viscous free surface flow around marine structures. (Dr.Ing. Thesis)
IMT-2006-16	Bjørheim, Lars G.	Failure Assessment of Long Through Thickness Fatigue Cracks in Ship Hulls. (Dr.Ing. Thesis)
IMT-2006-17	Hansson, Lisbeth	Safety Management for Prevention of Occupational Accidents. (Dr.Ing. Thesis)
IMT-2006-18	Zhu, Xinying	Application of the CIP Method to Strongly Nonlinear Wave-Body Interaction Problems. (Dr.Ing. Thesis)
IMT-2006-19	Reite, Karl Johan	Modelling and Control of Trawl Systems. (Dr.Ing. Thesis)
IMT-2006-20	Smogeli, Øyvind Notland	Control of Marine Propellers. From Normal to Extreme Conditions. (Dr.Ing. Thesis)
IMT-2007-21	Storhaug, Gaute	Experimental Investigation of Wave Induced Vibrations and Their Effect on the Fatigue Loading of Ships. (Dr.Ing. Thesis)
IMT-2007-22	Sun, Hui	A Boundary Element Method Applied to Strongly Nonlinear Wave-Body Interaction Problems. (PhD Thesis, CeSOS)
IMT-2007-23	Rustad, Anne Marthine	Modelling and Control of Top Tensioned Risers. (PhD Thesis, CeSOS)
IMT-2007-24	Johansen, Vegar	Modelling flexible slender system for real-time simulations and control applications
IMT-2007-25	Wroldsen, Anders Sunde	Modelling and control of tensegrity structures. (PhD Thesis, CeSOS)
IMT-	Aronsen, Kristoffer Høye	An experimental investigation of in-line and

2007-26		combined inline and cross flow vortex induced vibrations. (Dr. avhandling, IMT)
IMT-2007-27	Gao, Zhen	Stochastic Response Analysis of Mooring Systems with Emphasis on Frequency-domain Analysis of Fatigue due to Wide-band Response Processes (PhD Thesis, CeSOS)
IMT-2007-28	Thorstensen, Tom Anders	Lifetime Profit Modelling of Ageing Systems Utilizing Information about Technical Condition. (Dr.ing. thesis, IMT)
IMT-2008-29	Berntsen, Per Ivar B.	Structural Reliability Based Position Mooring. (PhD-Thesis, IMT)
IMT-2008-30	Ye, Naiquan	Fatigue Assessment of Aluminium Welded Box-stiffener Joints in Ships (Dr.ing. thesis, IMT)
IMT-2008-31	Radan, Damir	Integrated Control of Marine Electrical Power Systems. (PhD-Thesis, IMT)
IMT-2008-32	Thomassen, Paul	Methods for Dynamic Response Analysis and Fatigue Life Estimation of Floating Fish Cages. (Dr.ing. thesis, IMT)
IMT-2008-33	Pákozdi, Csaba	A Smoothed Particle Hydrodynamics Study of Two-dimensional Nonlinear Sloshing in Rectangular Tanks. (Dr.ing.thesis, IMT/ CeSOS)
IMT-2007-34	Grytøyr, Guttorm	A Higher-Order Boundary Element Method and Applications to Marine Hydrodynamics. (Dr.ing.thesis, IMT)
IMT-2008-35	Drummen, Ingo	Experimental and Numerical Investigation of Nonlinear Wave-Induced Load Effects in Containerships considering Hydroelasticity. (PhD thesis, CeSOS)
IMT-2008-36	Skejic, Renato	Maneuvering and Seakeeping of a Singel Ship and of Two Ships in Interaction. (PhD-Thesis, CeSOS)
IMT-2008-37	Harlem, Alf	An Age-Based Replacement Model for Repairable Systems with Attention to High-Speed Marine Diesel Engines. (PhD-Thesis, IMT)
IMT-2008-38	Alsos, Hagbart S.	Ship Grounding. Analysis of Ductile Fracture, Bottom Damage and Hull Girder Response. (PhD-thesis, IMT)
IMT-2008-39	Graczyk, Mateusz	Experimental Investigation of Sloshing Loading and Load Effects in Membrane LNG Tanks Subjected to Random Excitation. (PhD-thesis, CeSOS)
IMT-2008-40	Taghipour, Reza	Efficient Prediction of Dynamic Response for Flexible amd Multi-body Marine Structures. (PhD-thesis, CeSOS)
IMT-2008-41	Ruth, Eivind	Propulsion control and thrust allocation on marine vessels. (PhD thesis, CeSOS)
IMT-2008-42	Nystad, Bent Helge	Technical Condition Indexes and Remaining Useful Life of Aggregated Systems. PhD thesis, IMT

IMT-2008-43	Soni, Prashant Kumar	Hydrodynamic Coefficients for Vortex Induced Vibrations of Flexible Beams, PhD thesis, CeSOS
IMT-2009-43	Amlashi, Hadi K.K.	Ultimate Strength and Reliability-based Design of Ship Hulls with Emphasis on Combined Global and Local Loads. PhD Thesis, IMT
IMT-2009-44	Pedersen, Tom Arne	Bond Graph Modelling of Marine Power Systems. PhD Thesis, IMT
IMT-2009-45	Kristiansen, Trygve	Two-Dimensional Numerical and Experimental Studies of Piston-Mode Resonance. PhD-Thesis, CeSOS
IMT-2009-46	Ong, Muk Chen	Applications of a Standard High Reynolds Number Model and a Stochastic Scour Prediction Model for Marine Structures. PhD-thesis, IMT
IMT-2009-47	Hong, Lin	Simplified Analysis and Design of Ships subjected to Collision and Grounding. PhD-thesis, IMT
IMT-2009-48	Koushan, Kamran	Vortex Induced Vibrations of Free Span Pipelines, PhD thesis, IMT
IMT-2009-49	Korsvik, Jarl Eirik	Heuristic Methods for Ship Routing and Scheduling. PhD-thesis, IMT
IMT-2009-50	Lee, Jihoon	Experimental Investigation and Numerical in Analyzing the Ocean Current Displacement of Longlines. Ph.d.-Thesis, IMT.
IMT-2009-51	Vestbøstad, Tone Gran	A Numerical Study of Wave-in-Deck Impact usin a Two-Dimensional Constrained Interpolation Profile Method, Ph.d.thesis, CeSOS.
IMT-2009-52	Bruun, Kristine	Bond Graph Modelling of Fuel Cells for Marine Power Plants. Ph.d.-thesis, IMT
IMT 2009-53	Holstad, Anders	Numerical Investigation of Turbulence in a Sekwed Three-Dimensional Channel Flow, Ph.d.-thesis, IMT.
IMT 2009-54	Ayala-Uraga, Efren	Reliability-Based Assessment of Deteriorating Ship-shaped Offshore Structures, Ph.d.-thesis, IMT
IMT 2009-55	Kong, Xiangjun	A Numerical Study of a Damaged Ship in Beam Sea Waves. Ph.d.-thesis, IMT/CeSOS.
IMT 2010-56	Kristiansen, David	Wave Induced Effects on Floaters of Aquaculture Plants, Ph.d.-thesis, CeSOS.
IMT 2010-57	Ludvigsen, Martin	An ROV-Toolbox for Optical and Acoustic Scientific Seabed Investigation. Ph.d.-thesis IMT.
IMT 2010-58	Hals, Jørgen	Modelling and Phase Control of Wave-Energy Converters. Ph.d.thesis, CeSOS.
IMT 2010- 59	Shu, Zhi	Uncertainty Assessment of Wave Loads and Ultimate Strength of Tankers and Bulk Carriers in a

		Reliability Framework. Ph.d. Thesis, IMT/ CeSOS
IMT 2010-60	Shao, Yanlin	Numerical Potential-Flow Studies on Weakly-Nonlinear Wave-Body Interactions with/without Small Forward Speed, Ph.d.thesis,CeSOS.
IMT 2010-61	Califano, Andrea	Dynamic Loads on Marine Propellers due to Intermittent Ventilation. Ph.d.thesis, IMT.
IMT 2010-62	El Khoury, George	Numerical Simulations of Massively Separated Turbulent Flows, Ph.d.-thesis, IMT
IMT 2010-63	Seim, Knut Sponheim	Mixing Process in Dense Overflows with Emphasis on the Faroe Bank Channel Overflow. Ph.d.thesis, IMT
IMT 2010-64	Jia, Huirong	Structural Analysis of Intect and Damaged Ships in a Collission Risk Analysis Perspective. Ph.d.thesis CeSoS.
IMT 2010-65	Jiao, Linlin	Wave-Induced Effects on a Pontoon-type Very Large Floating Structures (VLFS). Ph.D.-thesis, CeSOS.
IMT 2010-66	Abrahamsen, Bjørn Christian	Sloshing Induced Tank Roof with Entrapped Air Pocket. Ph.d.thesis, CeSOS.
IMT 2011-67	Karimirad, Madjid	Stochastic Dynamic Response Analysis of Spar-Type Wind Turbines with Catenary or Taut Mooring Systems. Ph.d.-thesis, CeSOS.
IMT - 2011-68	Erlend Meland	Condition Monitoring of Safety Critical Valves. Ph.d.-thesis, IMT.
IMT – 2011-69	Yang, Limin	Stochastic Dynamic System Analysis of Wave Energy Converter with Hydraulic Power Take-Off, with Particular Reference to Wear Damage Analysis, Ph.d. Thesis, CeSOS.
IMT – 2011-70	Visscher, Jan	Application of Particla Image Velocimetry on Turbulent Marine Flows, Ph.d.Thesis, IMT.
IMT – 2011-71	Su, Biao	Numerical Predictions of Global and Local Ice Loads on Ships. Ph.d.Thesis, CeSOS.
IMT – 2011-72	Liu, Zhenhui	Analytical and Numerical Analysis of Iceberg Collision with Ship Structures. Ph.d.Thesis, IMT.
IMT – 2011-73	Aarsæther, Karl Gunnar	Modeling and Analysis of Ship Traffic by Observation and Numerical Simulation. Ph.d.Thesis, IMT.
Imt – 2011-74	Wu, Jie	Hydrodynamic Force Identification from Stochastic Vortex Induced Vibration Experiments with Slender Beams. Ph.d.Thesis, IMT.
Imt – 2011-75	Amini, Hamid	Azimuth Propulsors in Off-design Conditions. Ph.d.Thesis, IMT.
IMT – 2011-76	Nguyen, Tan-Hoi	Toward a System of Real-Time Prediction and Monitoring of Bottom Damage Conditions During

		Ship Grounding. Ph.d.thesis, IMT.
IMT-2011-77	Tavakoli, Mohammad T.	Assessment of Oil Spill in Ship Collision and Grounding, Ph.d.thesis, IMT.
IMT-2011-78	Guo, Bingjie	Numerical and Experimental Investigation of Added Resistance in Waves. Ph.d.Thesis, IMT.
IMT-2011-79	Chen, Qiaofeng	Ultimate Strength of Aluminium Panels, considering HAZ Effects, IMT
IMT-2012-80	Kota, Ravikiran S.	Wave Loads on Decks of Offshore Structures in Random Seas. Ph.d.thesis, CeSOS.
IMT-2012-81	Sten, Ronny	Dynamic Simulation of Deep Water Drilling Risers with Heave Compensating Sysetm, IMT.
IMT-2012-82	Berle, Øyvind	Risk and resilience in global maritime supply chains, IMT.
IMT-2012-83	Fang, Shaoji	Fault Tolerant Position Mooring Control Based on Structural Reliability, CeSOS.
IMT-2012-84	You, Jikun	Numerical studies on wave forces and moored ship motions in intermediate and shallow water, CeSOS.
IMT-2012-85	Xiang ,Xu	Maneuvering of two interacting ships in waves, CeSOS
IMT-2012-86	Dong, Wenbin	Time-domain fatigueresponse and reliability analysis of offshore wind turbines with emphasis on wlded tubular joints and gear components, CeSOS
IMT-2012-87	Zhu, Suji	Investigation of Wave-Induced Nonlinear Load Effects in Open Ships considering Hull Girder Vibrations in Bending and Torsion, CeSOS
IMT-2012-88	Zhou, Li	Numerical and Experimental Investigation of Station-keeping in Level Ice, CeSOS
IMT-2012-90	Ushakov, Sergey	Particulate matter emission characteristics from diesel enignes operating on conventional and alternative marine fuels, IMT
IMT-2013-1	Yin, Decao	Experimental and Numerical Analysis of Combined In-line and Cross-flow Vortex Induced Vibrations, CeSOS
IMT-2013-2	Kurniawan, Adi	Modelling & geometry optimisation of wave energy converters, CeSOS
IMT-2013-3	Al Ryati, Nabil	Technical condition indexes doe auxiliary marine diesel engines, IMT
IMT-2013-4	Firoozkoohi, Reza	Experimental, numerical and analytical investigation of the effect of screens on sloshing, CeSOS
IMT-2013-5	Ommani, Babak	Potential-Flow Predictions of a Semi-Displacement Vessel Including Applications to Calm Water Broaching, CeSOS